Lehigh University
Lehigh Preserve

2014

Damage characterization strategies using local vibration measurements from wired and wireless sensor networks

Ruigen Yao
Lehigh University

Damage characterization strategies using local vibration measurements from wired and wireless sensor networks

by

Ruigen Yao

Presented to the Graduate and Research Committee

of Lehigh University

in Candidacy for the Degree of

Doctor of Philosophy

in

Structural Engineering

Lehigh University

September 2014

www.manaraa.com

Approved and recommended for acceptance as a dissertation in partial fulfillment
of the requirements for the degree of Doctor of Philosophy

_____

Date

_____

Dr. Shamim N. Pakzad

Dissertation Advisor

Associate Professor
of Civil and Environmental Engineering
Lehigh University

_____

Acceptance Date

Committee Members:

_____

Dr. John L. Wilson

Committee Chairperson

Professor of Civil and Environmental Engineering
Lehigh University

_____

Dr. Richard Sause

Member

Professor of Civil and Environmental Engineering
Lehigh University

_____

Dr. Henry S. Baird

External Member

Professor of Computer Engineering and Science
Lehigh University

_____

Dr. Parvathinathan Venkitasubramaniam

External Member

Assistant Professor of Electrical and Computer
Engineering
Lehigh University

iii

ACKNOWLEDGEMENTS

I would like to gratefully acknowledge the insight, guidance and support provided by my research advisor Shamim N. Pakzad throughout my PhD years. I also offer sincere thanks to Professors Wilson, Sause, Baird and Venkitasubramaniam for serving on my committee and providing valuable feedback to my research. Besides, in the process of deriving ideas for my research I have taken many courses both in and out of my department, and would like to express thanks to all the professors for their instruction and assistance as well.

I appreciate the contribution of the laboratory staff for helping me getting ready for the experiments, and fellow research students for the useful information exchange and beneficial collaboration.

Last but not least, I would like to thank my mother Ping Gao for her endless patience and support during my course of study.

TABLE OF CONTENTS

LIST OF TABLES

LIST OF FIGURES

ABSTRACT

The goal of this dissertation is to advance the state-of-art of data-driven structural monitoring (Figure 0.1), which is a promising way to automate the maintenance process of civil structures, thus benefitting their life-cycle management in both the economy and performance aspect. The availability of affordable electronic data acquisition systems enabled continuous monitoring of structures, and effective data compression algorithms are needed for structural state characterization/damage detection from the collected signals. Ideally, the data processing algorithms would provide information for all four levels of damage detection proposed by Rytter (1994): 1) damage existence; 2) damage location; 3) damage severity; 4) remaining service life prediction.

Damage detection in real-world structures is a complex problem because of the various possible forms of damage that can occur and the influences of operational/environmental variations on the observations/measurements made. The focus of this study will be the first three stages of damage detection using vibration measurements, which are commonly measured for structural health monitoring purposes. For damage existence identification time series analysis on single channel response will be used (**Part I of this document**), while higher-level damage detection is attempted by using multi-input-single-output subsystem modeling (**Part II of this document**). More detailed outlines of both subjects can be found in their respective introduction sections.

The specific contributions of this study are in the following technical areas: exploring the capabilities of different SHM vibration sensors, proposing and testing new indicators/thresholds for damage identification, cross-comparing the proposed indicators/thresholds with existing ones through applications to various civil structures,

and developing theoretical models regarding the validity/sensitivity/robustness of several damage features. All these efforts are for the search and development of optimal damage detection method in a certain application.

Farrar et al. (1999) proposed a statistical pattern recognition (SPR) paradigm for vibration-based structural health monitoring, which quite well generalized most damage detection procedures. The paradigm contains 4 steps: *1) Operational evaluation; 2) Data acquisition and cleansing; 3) Feature selection and data compression, and 4) Statistical model development.* Research conducted for this dissertation centers on the last three stages of this paradigm, with most of the technical contributions in the last two categories.
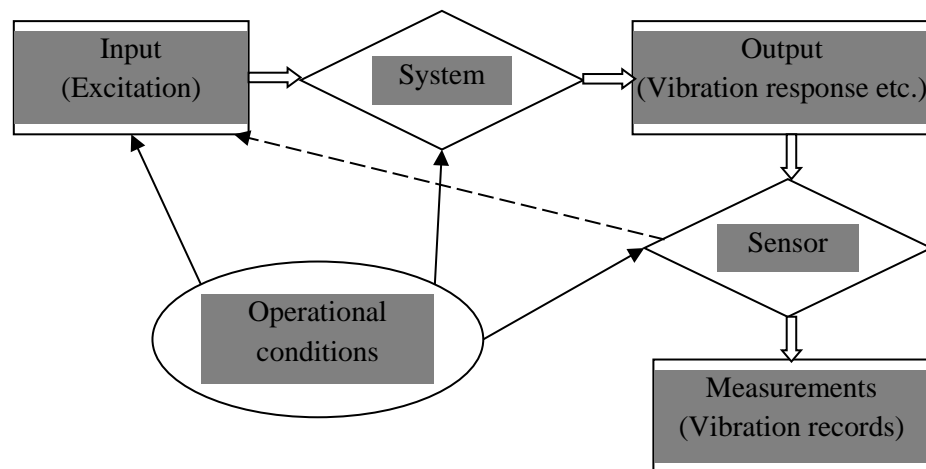
Figure 0.1   An illustration of data-driven monitoring.

Part I

Chapter 1 Introduction

1.1 OVERVIEW

Structural vibration monitoring has received a lot of attention from the research community in the past few years because of public safety concerns that arise from infrastructures deterioration. The objective is to create automatic structural assessment techniques that can be realized through programmed vibration analysis. Till now many vibration-based damage identification techniques have been proposed, and a majority of existing literature concerning vibration analysis is focused on system identification/modal realization as the main solution to this problem.

System identification (M. Chang and Pakzad, 2012; James III, Carrie, and Lauffer, 1993; Juang and Pappa, 1985; Overschee and Moor, 1994; Prevosto, 1982) can be based on input-output or output-only (by assuming that the input has certain probabilistic characteristics); it can operate in either time domain or frequency domain. Some examples of system identification methods include subspace identification (Overschee and Moor, 1994), eigensystem realization algorithm (Juang and Pappa, 1985), and complex mode indicator function (Prevosto, 1982). A number of studies have been conducted on using the extracted modal properties (natural frequencies, damping ratios, mode shapes) for structural damage detection through model updating (Brownjohn, Xia, Hao, and Xia, 2001; Duan, Yan, Ou, and Spencer, 2007; Friswell and Mottershead, 1995; Mottershead and Friswell, 1993) or statistical process control (Doebling and Farrar, 1998; Pakzad, Dryden, and Fenves, 2009). The drawback of system identification, however, is that it is innately a global approach. It processes the responses at different locations

simultaneously, and its output, modal properties, is a global transformation of the structural characteristics. As a result, it is reported to be computationally intensive, and not always effective for local damage evaluation (P. Chang, Flatau, and Liu, 2003; Doebling, Farrar, and Prime, 1998).

Univariate time series analysis (TSA) has been adopted for damage detection in many different contexts (Fassois and Sakellariou, 2007; Gul and Catbas, 2009; Haritos and Owen, 2004; Nair, Kiremidjian, and Law, 2006; Sohn and Farrar, 2001; Zhang, 2007). Its major advantage over system identification is computational efficiency, as only the response at one sensing node is needed and thus the algorithms can be implemented in a decentralized manner. Common frequency domain TSA methods include Fast Fourier Transform (FFT) and Power spectral analysis (Porat, 1994), while time domain TSA methods often involves mathematical modeling of the signal so that damage indicators can be functions of either model coefficients or model residuals (Brockwell and Davis, 2002). One notable merit of time domain techniques is that damage features can be generated in large quantities, thus making statistical processing of features for a more reliable damage detection result feasible.

1.2 RESEARCH OBJECTIVE

Scalar TSA based damage features, like many other families of damage indices, are influenced not only by structural condition but also by non-relevant environmental factors. Due to its inherent information limitation (i.e. depending only on single channel response), fluctuation of feature values can become quite prominent if the data are collected in a varying environment, negatively affecting decision making accuracy. To alleviate this problem, several tasks are identified and investigated herein:

4

1. Reliable damage threshold construction (**Chapter 3**)

2. New features with enhanced damage sensitivity/noise robustness (**Chapter 4**)

3. Theoretical sensitivity analysis of the TSA features with respect to damage/noise (**Chapter 6**)

To better appraising the damage detection potential of TSA features, they need to be compared to other types of damage indices. This topic is investigated in **Chapter 5**.

In the following section, the results of my research on the univariate TSA based damage detection literature will be explained in further details per chapter.

1.3 SUMMARY OF CONTENTS

In **Chapter 2**, brief descriptions of the sensors used in the studies for Part I of this dissertation are given. Also included are reviews of several related existing damage detection techniques. For better clarification of the concepts, these techniques are applied to a 3D steel truss structure instrumented with wireless accelerometers. Static tests are conducted to validate the properties of the structure and then dynamic test is used for extracting of modal properties and model updating of the system. Finally a local damage is simulated on the structure by adding weight to the midspan, and statistical process control on autoregressive (Brockwell and Davis, 2002) residuals from impulse response measurements modeling are employed to detect the structural change.

To truly automate the damage identification process, reliable damage threshold construction techniques are also need. In **Chapter 3**, two data-driven methods based on resampling and nearest neighbor rule are applied for threshold construction for damage features from autoregression (AR) analysis of vibration signals. Both threshold

5

calculation techniques are rooted in empirical feature probability estimation. The proposed thresholds are then tested on features extracted acceleration measurements collected from a 5 degree-of-freedom(DOF) test specimen. The resampling method is applied to Mahalanobis distance of AR model coefficients, while the nearest neighbor rule is used on a combination of coefficient distance feature and the residual autocorrelation feature. Both methods perform well in this case study.

Statistical pattern recognition has recently emerged as a promising set of complementary methods to system identification for automatic structural damage assessment. Its essence is to use well-known concepts in statistics for boundary definition of different pattern classes, such as those for damaged and undamaged structures. In **Chapter 4**, several statistical pattern recognition(Jain, Duin, and Mao, 2000) algorithms using autoregressive models, including statistical control charts and hypothesis testing, are reviewed as potentially competitive damage detection techniques. To enhance the performance of statistical methods, new feature extraction techniques using model spectra and residual autocorrelation, together with resampling-based threshold construction methods, are proposed. Subsequently, simulated acceleration data from a multi degree-of-freedom system is generated to test and compare the efficiency of the existing and proposed algorithms. Data from laboratory experiments conducted on a truss and a large-scale bridge slab model are then used to further validate the damage detection methods and demonstrate the superior performance of proposed algorithms.

Cross-comparison of the performances of damage detection algorithms on different types of structures is an important way to assess their merits and demerits. **Chapter 5** contains additional cross-comparison examples on a laboratory specimen, which is a

scaled two-bay steel frame subjected to random excitation at its left end. Damage is introduced by replacing two members near the right joint with more flexible ones. Three damage detection algorithms are used: the influence coefficient method (Labuz, Chang, and Pakzad, 2010; Labuz, Pakzad, and Cheng, 2011; Nigro, Pakzad, and Dorvash, 2014) and two AR methods. The influence coefficient method for damage detection is based on correlation analysis between responses measured at two different locations, while the autoregressive (AR) modeling method evaluates the change in coefficients and residual characteristics of the AR model estimated from response from only one sensor node. The damage existence identification and localization capability of each damage indicator is evaluated based on their separate application results.

While experiments and simulations are beneficial for performance evaluation of damage indices in a case-by-case manner, more rigorous derivations are needed for quantitative assessment on the effectiveness of these indices. One tool to help accomplish this objective is analytical sensitivity analysis, which has been successfully used to evaluate the influences of system operational parameters on observable characteristics in many fields of study. In **Chapter 6**, the sensitivity expressions of two damage features, namely the Mahalanobis distance of autoregressive coefficients and Cosh distance of autoregressive spectra, will be derived with respect to both structural damage and measurement noise level. The effectiveness of the proposed methods is illustrated in a numerical case study on a 10 DOF system, where their results are compared with those from direct simulation and theoretical calculation. During the sensitivity derivation process it is noticed that if autoregression is applied towards the auto-covariance function (ACovF) of the ambient vibration signal instead of the signal itself, then the coefficients

and residuals will not be affected by white noise. Thus also in **Chapter 6**, three autoregressive damage features extracted directly from the ambient vibration data and from the vibration signal autocorrelation will be presented. Two of the features are distance functions of AR model parameters and the third feature is a function of AR residuals. These features are then applied to acceleration measurements collected from a member of a truss bridge to detect a structural change, and their performances are compared and commented.

For clearer presentation of the materials, Figure 1.1 includes the feature extraction and threshold determination methods used in the researches described in Part I. Basically, new damage features and threshold evaluation techniques are proposed and compared with the existing ones through theoretical analysis, case simulation and laboratory/field experiments.

8
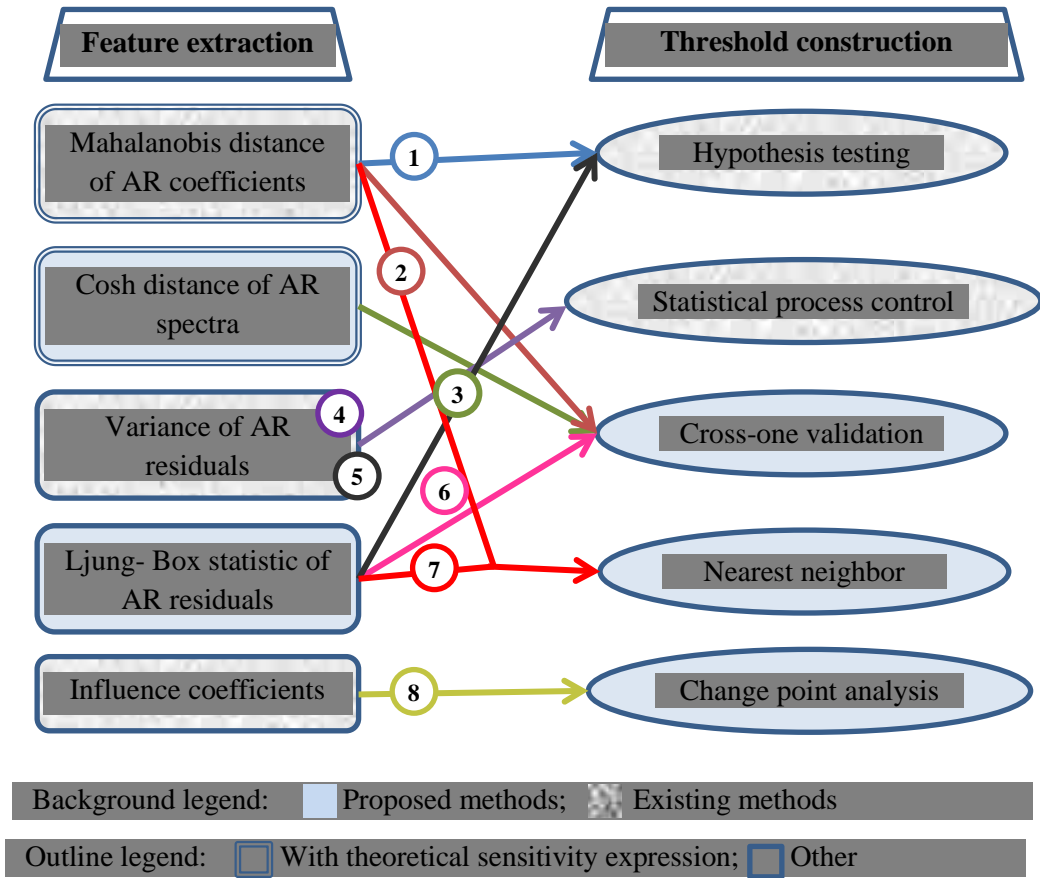
Figure 1.1   A summary of the damage feature extraction and threshold construction strategies employed in Part I.

Chapter 2   **Background**

Data-driven structural health monitoring needs sensors for data acquisition and data-processing algorithms for damage information extraction. In the following sections, descriptions of the structural sensing devices and existing damage detection algorithms related to this research will be given.

2.1 SENSORS AND DATA ACQUISITION SYSTEMS FOR SHM APPLICATIONS: PART I

Rapid development in digital data acquisition technologies has made continuous vibration monitoring of civil structures feasible (Lynch and Loh, 2006; Nagarajaiah et al., 2008; Pakzad and Fenves, 2009; Pakzad, 2010), and it is hoped that from the measurements a reliable assessment of the structural condition can be made. This is the main idea behind the data-driven structural health monitoring, where a sensor network is designed and implemented for a given structure and automatic programs are devised for extraction of structural information from the data.

Currently a variety of sensors is available for SHM applications. A few examples includes fiber optic systems, piezoelectric sensors, electromagnetic sensors, ultrasonic detectors, radar and millimeter wave technology, strain gauges, micro-electro-mechanical systems (MEMS), multifunctional materials and nanotechnology products for sensing and lasers. In the subsections below the sensors used in this study will be described.

2.1.1 'Stacked' wireless sensor

The wireless sensor adopted in this research consists of three sensor boards stacked together from bottom to top (Figure 2.1): the battery board, the processing board (Imote2) and the sensing board (SHM-A).

The Crossbow battery board (IBB2400CA), which has slots for three AAA battery cells, is used here to power the sensing unit. A description of the features of this board can be found in (Crossbow Technology Inc., 2006).

Imote2(Intel Corporation Research, 2005) contains Intel PXA271 CPU which has the ability of operation in low voltage (0.85V), low frequency (13MHz) mode. This feature provides very low power operation of the CPU. The processor's frequency can also be scaled from 13MHz to 416 MHz with dynamic voltage scaling which enables optimizing the power consumption. This platform also includes 256kB SRAM, 32 MB SDRAM and 32MB of FLASH memory which is distinguishable in compare with other smart sensor platforms. Besides, Imote2 integrates CC2420 IEEE 802.15.4 radio transceiver from Texas Instruments which supports a 250kb/s data rate with 16 channels in the 2.4GHz band. A 2.4GHz surface mount antenna is provided on the Imote2 platform. To enhance the communication reliability, an external antenna, Antenova Titanis 2.4 GHz Swivel SMA, is used in addition to Imote2's onboard antenna. Table 2.1 presents the general specifications of the Imote2 platform. The Imote2 has many I/O options which make this platform flexible to operate with different sensor boards.

Software platform, as well as hardware platform, influences the decentralized data-processing capability of wireless sensor nodes. TinyOS (2005) operating system is the main framework for programming the Imote2. This operating system is an open source, component oriented software which supports a wide range of WSN's applications. In addition, there is a need for some high-level components to cooperate with the framework and maintain the specific requirements of SHM. The Illinois Structural Health Monitoring Project (ISHMP)(2009) has developed a software package that works with

11

TinyOS for SHM applications. This is a package of applications satisfying the requirements for reliable monitoring of civil infrastructures. Remote Sensing application of ISHMP is used for data collection of this experiment. Two essential protocols in wireless data collection and transmission are time synchronization and reliable data transfer which both are employed in this program.

The sensing interface of this sensor is SHM-A sensor boards, developed by Rice and Spencer, Jr. (2008) in Smart Structures Technology Laboratory at Illinois University. Components of this unit are selected specifically for SHM applications. LIS3L02AS4 analog accelerometer manufactured by ST Microelectronics is used for SHM-A sensor board. LIS3L02AS4 is a low-cost, high sensitivity analog accelerometer with $50\mu g/\sqrt{Hz}$ Noise density which offers 3-axes of acceleration on one chip.

Table 2.2 presents the specifications of this accelerometer. Low-pass filter, Gain difference amplifier and Quickfilter 16-bit ADC are other components integrated on the sensor board. The Quickfilter QF4A512 Programmble signal conditioner is the key component of SHM_A sensor board (Rice and Spencer, Jr., 2008). It utilizes 4-channels with 16-bit resolution ADC which provides a reasonable sensitivity for most of SHM purposes. Figure 2.1 shows a unit of sensor boards and Imote2.

2.1.2 Conventional tethered sensors

Apart from wireless sensors, conventional wired data acquisition systems are also adopted for data acquisition in the experiments. Though they are less economical and scalable than the wireless counterparts, they are based on a more mature technology and often demonstrate better accuracy. Two different uniaxial accelerometer types were used in this study. One type of accelerometer is manufactured by PCB Piezotronics, Inc. A

12

high resolution capacitive uniaxial accelerometer model is used, specifically model 3701G3FA3G. This sensor has an acceleration range of ±3 g and a frequency response range of 0-100 Hz. More technical specifications of this sensor can be found in (PCB Piezotronics, 2009).

Another type of accelerometer is supplied by Silicon Designs, Inc. The model number is 2210-002. It is again a uniaxial sensor with a measurement range of ±2 g and a frequency response range of 0-300 Hz. For other technical parameters such as sensitivity and noise level, please refer to (Silicon Designs Inc., 2013).

Photographs of the two accelerometer types used for this research are shown in Figure 2.2 and Figure 2.3. Note that the measurement axis is normal to the top face of each sensor.

2.1.3 Data Acquisition Devices

Data acquired at wireless sensor nodes are first stored in the local memory of Imote2, and then transmitted back to the base station, which consists of an imote2 and an IIB2400 interface board (Figure 2.4) connected to a laptop. The Cygwin software is used to manage the wireless sensor network: one Cygwin window for sending commands, one Cygwin window for retrieving data. For more details, please refer to (Illinois Structural Health Monitoring Project, 2011).

For a test conducted on the 7 DOF mass-spring system, the data acquisition system was PDAQ Premium data acquisition system from DIGITEXX(2010) with 16 Channels for voltage input from different sensors types measuring acceleration, strain, wind speed/directi direction, temperature. This system integrates an analog filter with 24 bit

13

resolution. The software which retrieves and converts data is Digitexx. Figure 7.5 shows the data acquisition system.

In all other experiments mentioned in this dissertation using wireless sensors, acceleration responses were collected from the wired sensors using the CR9000, a modular, multiprocessor data acquisition (DAQ) system and PC9000 support software by Campbell Scientific, Inc. (2005, 2009). Figure 3.10 shows the DAQ system. The CR9000 has a 16-bit analog-to-digital converter and a peak sampling rate of 100 kHz.

2.2 EXISTING DATA PROCESSING METHODS FOR SHM: PART I

A lot of investigations have been carried out on the topic of structural state identification/damage detection from sensor data. Below several notable family of data processing algorithms for vibration measurements will be discussed. Note that most of these algorithms contain the steps of feature extraction and feature classification (corresponding to the last two stages of SPR damage detection paradigm presented at the end of the dissertation abstract). Some of the methods will be included for either comparison or validation purposes in the research presented in the following chapters.

2.2.1 Modal realization and model updating

Modal realization, in the SHM context, is often used interchangeably with the term 'system identification' as both refer to extraction of structural modal properties, which are important for global monitoring of structures. FE model updating is an excellent tool for higher level damage detection and for better understanding of the structural behavior. In the remainder of this subsection, their methodology will be presented and illustrated.

2.2.1.1 *Methodology review*

Some of the most widely used time domain difference models for structural system identification are autoregressive (AR), autoregressive moving average with exogenous input (ARMAX), and general state-space models. From a theoretical perspective, the difference models can be viewed as the discrete domain counterpart of the governing differential equations of dynamic systems. Also, there are a lot of system identification techniques using frequency domain representation of signals such as Fast Fourier Transform and spectrum estimate. Two of such examples are peak-picking (pp) and complex mode indicator function (CMIF) method (Peeters and Ventura, 2003). These algorithms are generally straightforward in methodology as structural frequency response has distinct peaks.

If a finite element (FE) model of the structure being investigated is available, the extracted modal properties, or other observations on structural behavior, can be used as input for FE model updating. Some commonly used model updating techniques include trial-and-error, sensitivity matrix method(Mottershead and Friswell, 1993), Bayesian probabilistic method(Beck and Katafygiotis, 1998), response surface method(Ren and Chen, 2010) etc. Since generally there are more model parameters than independent observations of the structure, the choice of updating variables is important for every model updating technique. Till now, this task is often accomplished based on experience and engineering judgment. Generally model updating processes are computationally intensive, but it can be an effective means for structural condition evaluation if properly done.

15

2.2.1.2 *Implementation example*

For better illustration of the concepts, an experimental example will be introduced here on modal properties extraction and model updating. Figure 2.7 shows the truss structure used in the experiment. To obtain an accurate value for the modulus of elasticity of the truss members, static tests are performed prior to dynamic tests (the step for modal properties extraction). Basically, deflections from the truss were compared with deflections of an analytical model constructed in SAP2000 under the same load for 10 loading configurations (which was set to be 1244 kips).

Modal properties extraction

During the dynamic test, fourteen sensor nodes were attached to the joints of the truss to measure the dynamic response of the structure. An additional sensor is fixed on the ground as a reference node to represent the sensor and environmental noise characteristics. Each sensor provides two set of acceleration data in two directions. Using 280 Hz sampling frequency, data from the reference node and one of the sensors attached to the truss are collected. Figure 2.8 shows the time-history and the power spectral density (PSD) of the output from these two sensors.

A low-pass digital filter with 35 Hz cut-off frequency is applied to the raw data to remove high frequency responses, which are more affected by circuitry noise. The dynamic excitation is ambient and therefore stochastic identification method is used to derive the modal properties. Stability diagram is used to determine the optimal model order for the system identification algorithm. Figure 2.9 shows this diagram for a limited frequency band-width which contains the major modes of the structure. The convergence tolerance for both frequency and damping ratio is 5%. When the modal assurance

criterion (MAC)(M. Chang and Pakzad, 2012) is greater than 95%, the mode shapes are deemed to have converged.

First three mode shapes of the structure are presented in Figure 2.10. It is observed that the first mode, which is significantly dominant, happens in the out-of-plane direction of the truss. This is also in agreement with the modal analysis of the analytical model.

SAP2000 Model updating

The aforementioned SAP2000 model is updated based on the extracted modal properties. The aim is to minimize the difference between frequencies of analytical and experimental models. Since the geometry and sectional properties of the structural members are known, connection stiffness is the major uncertain parameter which influences the dynamic behavior of the system. Thus the element end fixity, which is defined as a portion of the element's stiffness ($\alpha EI / l$), is chosen as the updating variable. Another consideration remains for the consistency of updated model with the result of static test (deformation). Therefore, an iteration process between the modal and static analysis of the model is performed. Figure 2.11 shows the comparison of first mode shape obtained from the system identification and the updated analytical model, which match very well.

2.2.2 Scalar time-series analysis and statistical pattern classification

Time series analysis (TSA) refers to the family of techniques to extract informative patterns from sequences of observations/measurements, and statistical pattern classification (SPC) denotes the process of decision making based on the patterns extracted. They are regarded as a more efficient alternative to modal extraction/model updating for damage detection.

TSA (Brockwell and Davis, 2009) for single channel acceleration measurements is one of the notable feature extraction techniques attempted in a number of vibration-based damage detection research articles (Atamturktur, Bornn, and Hemez, 2011; Gul and Catbas, 2009; Nair et al., 2006; Sohn and Farrar, 2001; Zhang, 2007), where algorithms such as scalar autoregressive (AR), autoregressive/autoregressive with exogenous input (AR-ARX), autoregressive with moving average (ARMA) modeling have been applied and functions of estimated model parameters used as damage features. Features, which are defined as functions of either the model residuals or the model coefficients, can often be generated in large quantities, thus facilitating statistical processing.

Statistical pattern recognition techniques (Figure 2.12) have long been applied to speech recognition (Ho & Baird, 1997), identifying logical information from image documents (Jelinek, 1976; Schurmann et al., 1992), reading DNA sequences in bioinformatics (Liew, Yan, & Yang, 2005) and problems in many other domains that require artificial cognitive assistance. Its essence is to use well-known concepts in statistics for boundary definition of different pattern classes, such as those for damaged and undamaged structures. Their ability to process large volumes of information produced via continuous and/or multichannel sensing is very beneficial, and in addition, the classification techniques are adaptable to most fields of applied science as they are basically mathematical tools. Application examples of the SPC techniques on damage detection can be found in (de Lautour and Omenzetter, 2010; Fugate, Sohn, and Farrar, 2001; Sakellariou and Fassois, 2006; Sohn, Farrar, Hunter, and Worden, 2001; Sohn, Worden, and Farrar, 2002), where hypothesis testing and clustering techniques are employed and satisfactory results are reported.

18

Several other studies further explored the effectiveness of TSA+SPC based damage detection schemes (Bodeux and Golinval, 2001; Fassois and Sakellariou, 2007; Lu and Gao, 2005; Noh, Nair, Kiremidjian, and Loh, 2009; Omenzetter and Brownjohn, 2006; Worden and Manson, 2007; Zheng and Mita, 2009) by making changes to data cleansing techniques, using various classification algorithms, and trying the methods on different types of simulated and real structures.

2.2.2.2 Implementation example

Here an application of the TSA+SPC to the same truss used in Section 2.2.1.2 above will be presented to illustrate the concept and the procedure. The example will use AR residuals for damage features and statistical process control (Stat-PC) for damage state identification.

Definition of AR model

Given a time series $x(t)$ (in this case acceleration measurements), an AR model with order p can be constructed as:

$$x(t) = \sum_{j=1}^{p} \varphi_j x(t-j) + e(t) \tag{2.1}$$

where φ_js are the model coefficients and $e(t)$ is the model residual. Once established, the model can be used to predict other time-series, and residuals are obtained as the error between prediction and real signal at different time points.

As long as the new measurements are similar to the baseline measurements to which this model is fitted, the prediction from the model should be close to new signal. However, if the incoming data is not acquired from the same structural condition under

19

which baseline measurements are collected, then the model will no longer be able to make precise prediction, and a substantial change in the distribution of residuals is expected. Based on this reason, analysis of residuals is a viable way to detect damage.

Model Order Selection

Akaike's Information Criterion (AIC) (Brockwell and Davis, 2002) is employed to select the proper model order. Its aim is to obtain a balance between the complexity of the model and accuracy of the prediction. According to this theory, the best model should be the one that minimizes the *AIC* value, which is the sum of the prediction error and a penalty term that increases with the number of parameters in the model.

Through AIC value comparison, the model order for this study is set at 28 lags. A series of trials also proved that higher order models do not yield a better performance.

Experimental set-up

Damage is simulated by adding two 45-lb weight discs at the mid-span on the lower cord of the truss. Free vibration tests are conducted for both damaged and undamaged states; for each case two sets of acceleration measurements are collected by the WSN. In each case, system vibration is introduced by pushing the structure from mid-span and then releasing it when the sensors start recording data. A low-pass Chebyshev filter with cutoff frequency of 40 Hz is applied to the data. The sampling rate after filtering is 80Hz, and every data set contains 4250 samples.

Statistical Process Control

Widely used in management of manufacture industries, Stat-PC's underlying assumption is that when a system deviates from its original state, a change will occur in

the statistical characteristics of the features monitored/charted. Generally, a control chart features a center line and two control limit lines (upper and lower bound).

Upper/Lower Control limits are drawn at points above/below which the likelihood for the features to occur is small. When the system is stable, the charted values should mostly remain inside the confidence region; otherwise, a significant amount of outliers will appear in the charts.

Only the last 2200 points of each data set is used here since the patterns shown by the first half are much affected by the initial load condition, which varies between different tests. The AR model is constructed using the first data set from undamaged state, and the other 3 are fitted to this model. The residual series (2200-28=2172 points) for all these four cases are then computed and divided into subgroups of size four, and control charts are used to detect the change in means and variances of residuals within each subgroup.

If the residuals are truly normally distributed random sequence, the subgroup mean should also have a normal distribution and the subgroup variance should have a chi-square distribution with degree of freedom three (Fugate et al., 2001). Hence, the control limits are $\pm z_{\alpha/2} s_p / \sqrt{n}$ for the mean $\bar{x}$ and $\overline{S}\sqrt{\chi^2_{1-\alpha/2,n-1}/(n-1)}$ / $\overline{S}\sqrt{\chi^2_{\alpha/2,n-1}/(n-1)}$ for standard deviation S, where $s_p / \overline{S}$ is the pooled variance/mean variance of baseline subgroups, α is the significance level (0.05 in this case) and n is the subgroup size (=4 here).

21

The $\bar{x}$ and S control charts, shown in Figure 2.13 & Figure 2.14, are constructed from measurements at node 4. Investigation of all other nodes also yields similar results and thus is not presented here. It can be seen that the x-bar chart gives a better performance than S chart which is because of the fact that the system is still within the linear range, so the variance change in the residuals is not very significant.

Table 2.1   Specifications of Imote2

Parameter	Value
Processor	Intel PXA271
SRAM Memory	256kB
SDRAM Memory	32MB
FLASH Memory	32MB
Power Consumption	44mW at 13MHz
	570mW at 416 MHz
Radio Frequency Band	2400.0 – 2483.5MHz
Dimensions	36mm×48mm×9mm

Table 2.2   Specifications of LIS3L02AS4 Accelerometer

Parameter	Value
Acceleration Range	$\pm 2g$
Avg. Noise Floor (X & Y)	0.3mg
Avg. Noise Floor (Z)	0.7mg
Resolution	0.66 V/g
Temperature Range	-40 to 85ºC

23

Figure 2.1   'Stacked' wireless sensor node
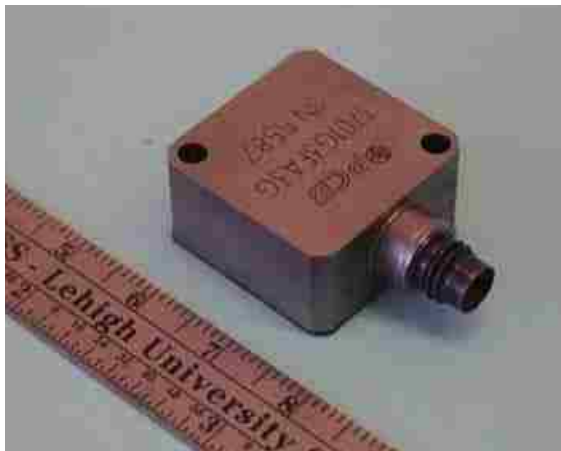
Figure 2.2   PCB wired sensor (courtesy of Mr. Ian C. Hodgson)

Figure 2.3   Silicon Designs wired sensor, mounted on a steel tube
(courtesy of Ms. Elizabeth L. Labuz)

Figure 2.4   Base-station of wireless sensor network: an interface board is
stacked on top of an Imote2

25

Figure 2.5   PDAQ Digetexx data acquisition system with the connecting
                     wires (last plot)

Figure 2.6   CR9000 data acquisition system: wire jack and user interface

26

Figure 2.7   3D steel truss of the experiment
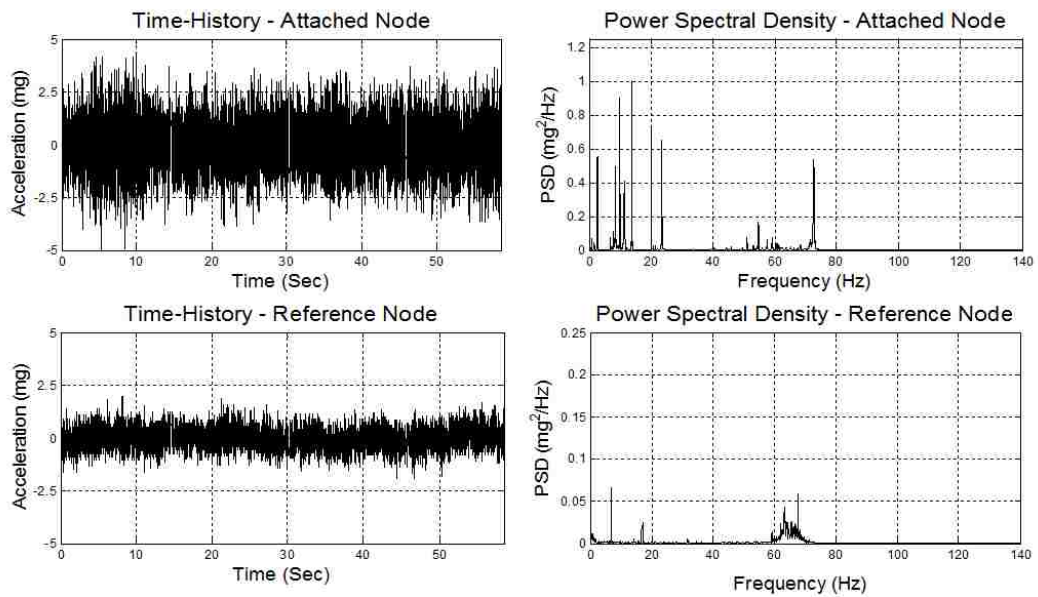
Figure 2.8   Comparison of the Outputs of Reference and Attached Nodes
                             in Time and Frequency Domains

27
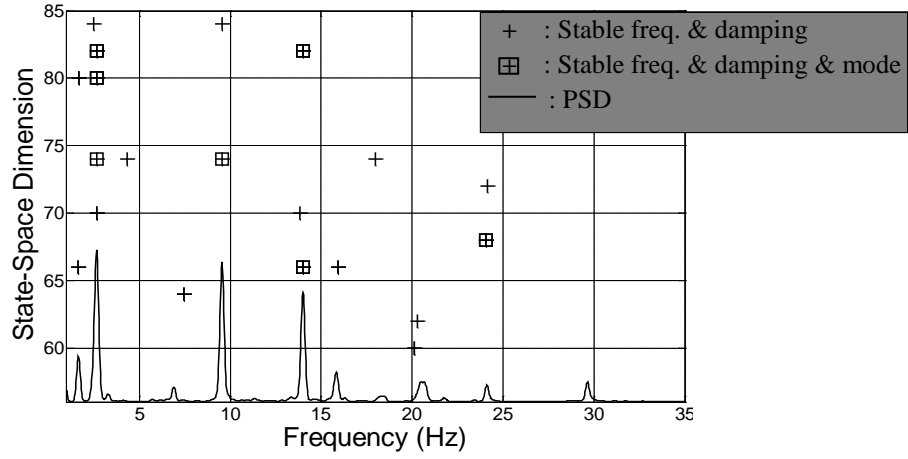
Figure 2.9   Stability Diagram for modal convergence and Power Spectral
                    Density of the response

28

First mode

Freq. = 2.648 Hz   ζ = 0.0064

Side view

Plan view

Second mode

Freq. = 9.54 Hz   ζ = 0.0041

Side view

Plan view

Third mode

Freq. = 14.00 Hz   ζ = 0.0036

Side view

Plan view
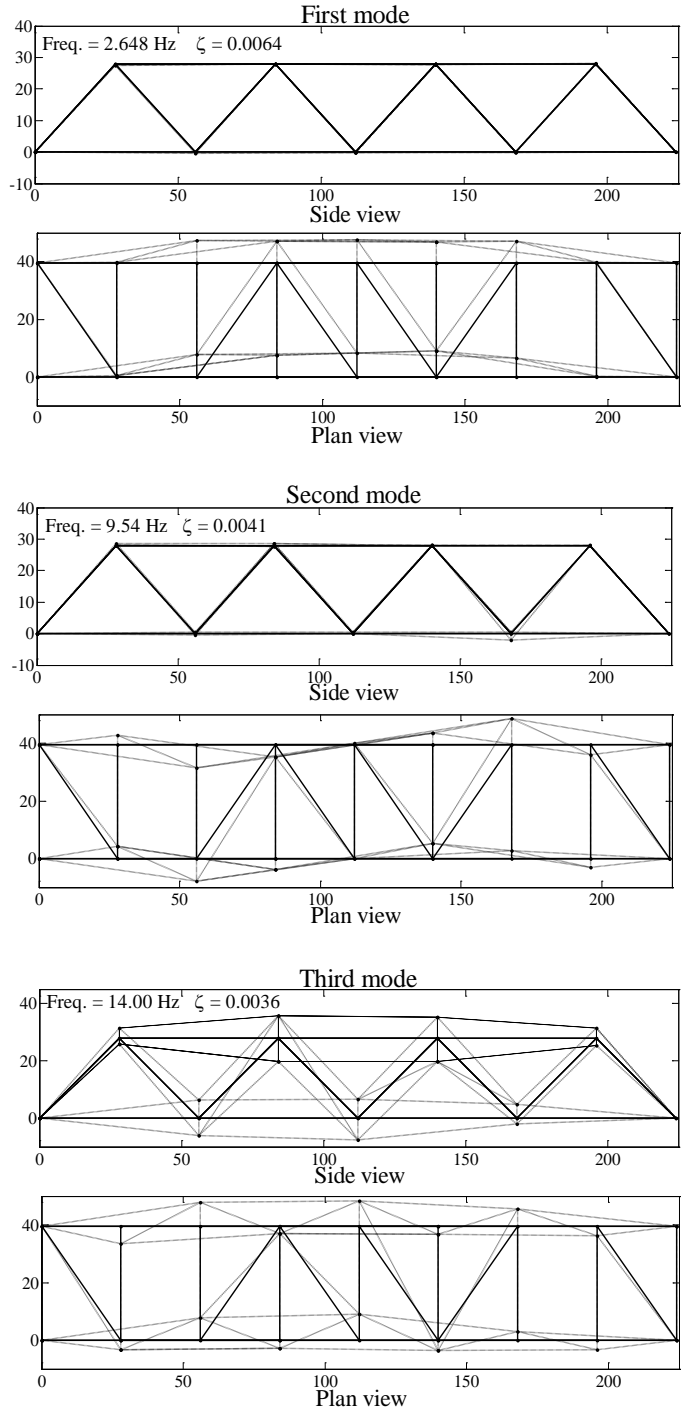
Figure 2.10   First 3 extracted mode shapes, frequencies and damping ratios

29
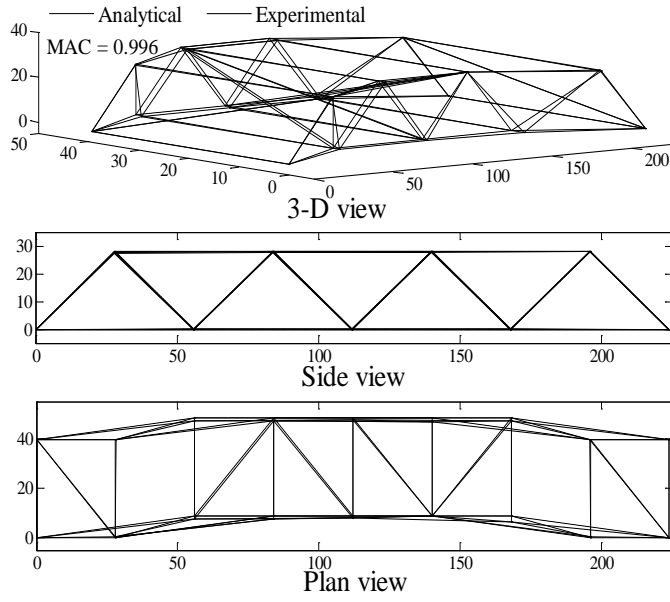
Figure 2.11   First mode shape: Experimental vs. Analytical result
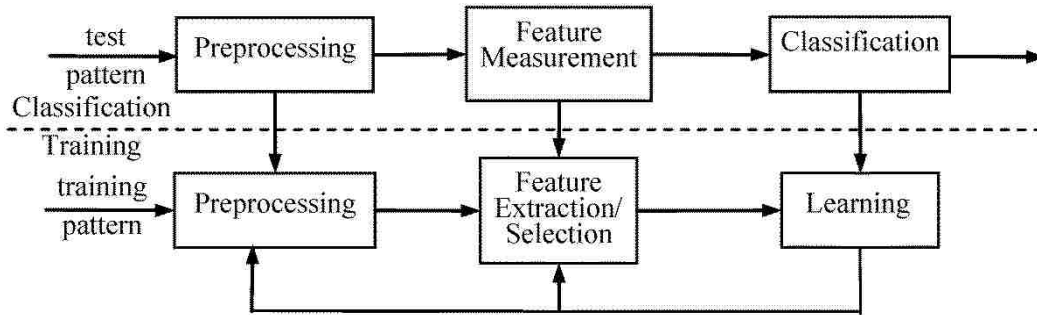
Figure 2.12   The general procedure of statistical pattern classification (Jain et al., 2000)
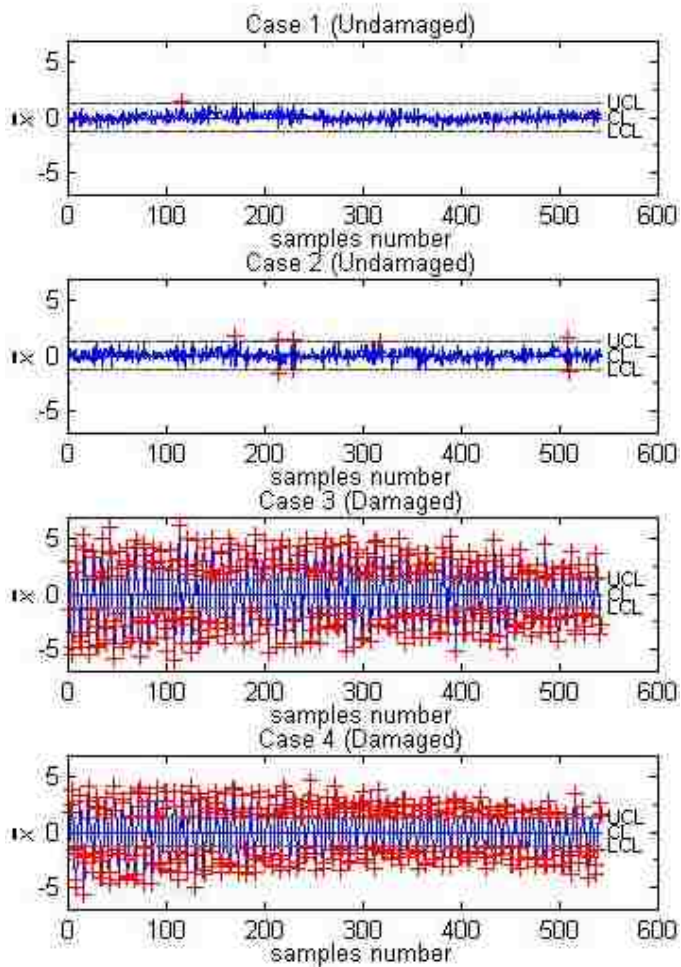
Figure 2.13 $\bar{x}$ control chart of the residuals
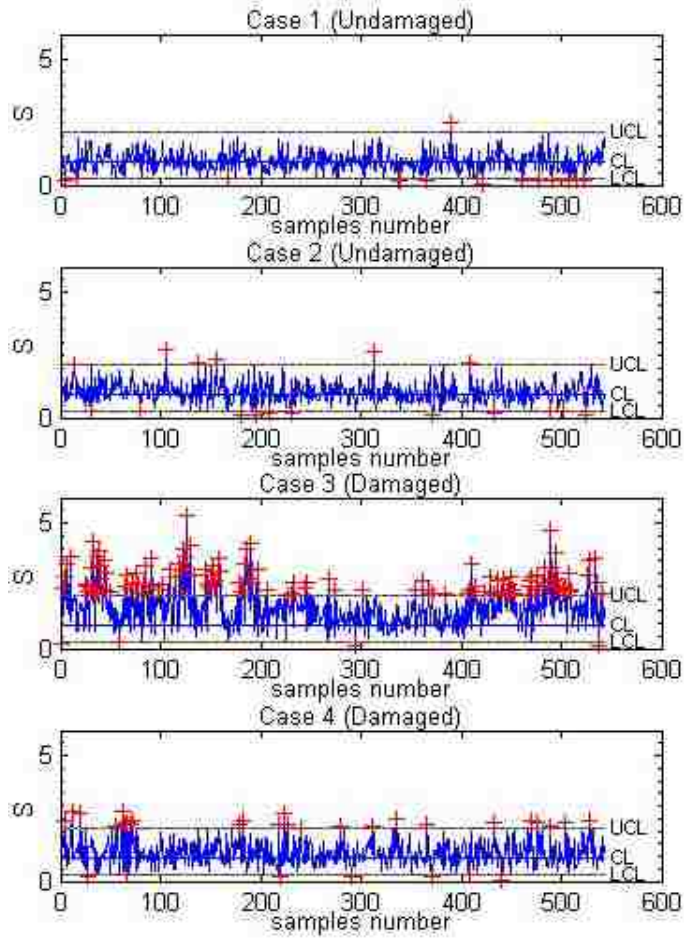
Figure 2.14 S control chart of the residuals

Chapter 3 Data-driven methods for threshold determination in auto-regression (AR) based damage detection

3.1 PRELUDE

As noted in the abstract, for years researchers have been working on automatic damage detection through SHM in the hope of reducing a structure's maintenance cost by minimizing human involvement in the process. The guiding philosophy of monitoring-based damage detection is to 'let the data speak for itself'. Most data-based damage detection algorithms include five steps: 1) obtain data from baseline/healthy state structure; 2) extract a statistical quantity/damage index Q from the data via time series analysis; 3) obtain data from current/unknown state structure; 4) extract the Q quantity from the data using the same method; 5) compare Q from the unknown state with that from baseline state using statistical testing. If the difference is statistically significant (i.e. exceeds a preset threshold), the system is deemed damaged.

The last step is important for automation of damage detection process because for almost all damage indices (modal properties, TSA features), their values will carry some fluctuations when extracted from datasets collected from the same structural state but different time intervals. Sometimes it is more because of the modeling error; sometimes environmental disturbances play a greater role. For reliable structural state identification, appropriate damage threshold construction schemes that take these variations into account are needed.

3.2 MOTIVATION AND ORGANIZATION

Statistical hypothesis testing (Koch, 1999) is the recognized standard approach for threshold determination. It assumes that the features follow a certain probability distribution, and the threshold is set at a point beyond which the chance for a feature value to occur is small. This approach is theoretically optimal as long as the assumed feature distribution is valid. Hypothesis testing may do well for fault identification in machinery, as the excitation force is well known and the damage types are well-defined. For civil engineering applications, **however**, there are more uncertainties. When the probability distribution of damage features are too complex to be accurately represented by analytical distribution functions available, threshold constructed using hypothesis testing will yield poor results in damage identification and an alternative approach is needed.

In this chapter a data driven threshold determination scheme using cross-validation and resampling techniques (Good, 2001) will be introduced and applied to the Mahalanobis distance (Mahalanobis, 1936) feature of AR coefficients described in Section 3.3.1. This feature is shown to have large variations, and its distribution is unknown. Yet the data-driven method still yields an effective threshold. Also the Mahalanobis distance feature is paired with the autocorrelation feature (Section 3.3.2) to improve the damage detection performance of time-series based methods. A nearest-neighbor approach (Duda, Hart, and Stork, 2012) is used to set an effective significance threshold for the feature pair.

The remaining content is organized into several sections:

- Section 3.3 presents the Mahalanobis distance of AR coefficients and Auto-correlation function of AR residuals, which are damage features used for this study.

- Section 3.4 introduces the proposed data-driven threshold construction techniques: cross-one validation and nearest-neighbor classification.

- Section 3.5 contains the application results of the new threshold evaluation techniques to a 5-DOF Plexiglas-aluminum system.

- Section 3.6 is the conclusion.

3.3 DAMAGE DETECTION METHODS USING TIME SERIES ANALYSIS

Autoregressive (AR) model is perhaps the most widely adopted time series analysis tool (Brockwell and Davis, 2002). The definition of a univariate AR model of order p is given in Eq. (2.1). This model basically attempts to express the value of signal at time t as a linear combination of its previous values up to lag p.

According to classical structural dynamics theory, the discretized structural response under random excitation can always be approximated by an AR process of large order. Damage features from AR modeling can be grossly divided into two categories; model coefficients based and model residual based. AR model coefficients can be estimated directly from the data using one of the standard algorithms, and the residual sequence can henceforth be obtained from Eq. (2.1). In the remainder of this section, two damage features, one from each category, will be presented.

3.3.1 Mahalanobis distance of AR model coefficients

It has been proved that if the signal is really an AR process, then any regular coefficients estimator $\{\varphi_j\}$ from the signal is asymptotically unbiased and normally

35

www.manaraa.com

distributed with covariance matrix $\sigma_e^2 \Gamma_p^{-1}$ (Brockwell and Davis, 2009). Therefore, a metric that represents the deviation in the probability space of normal distribution seems a good choice of damage feature. Mahalanobis distance is such a metric defined from the definition of multivariate normal distribution. The estimator of the Mahalanobis distance between a potential outlier vector x_ξ and baseline sample set can be obtained as

$$D_\zeta = \left(x_\xi - \overline{x} \right) \hat{\Sigma}^{-1} \left(x_\xi - \overline{x} \right). \tag{3.1}$$

where $\overline{x}$ is the average of the baseline sample feature vectors, and $\hat{\Sigma}$ the estimated covariance matrix. When applying this method: 1) the baseline signals are first segmented (often with large overlap) and for each segment an AR coefficient vector are estimated. 2) Signals from current structural state are processed likewise and for each coefficient vector obtained its Mahalanobis distance to the baseline coefficients set will be computed. 3) These Mahalanobis distance features are then compared with the Mahalanobis distances within baseline set. When the structural system is damaged, it is expected that the Mahalanobis distance feature for AR coefficients will increase significantly (Figure 3.1).

3.3.2 Auto-correlation function (ACF) of AR model residuals

It is clear from Eq. (2.1) that if the AR model used to filter the signal is the same as the model from which the signal is generated, the residual series should be a white noise. Otherwise, the residual series will carry certain identifiable patterns that can be captured by its autocorrelation function. ACF can be estimated from residual sequence as:

$$\hat{\rho}(\tau) = \frac{\sum_{i=1}^{i=N-\tau+1} \left[e(i+\tau) - \overline{e} \right] \left[e(i) - \overline{e} \right]}{\sum_{i=1}^{i=N} \left[e(i) - \overline{e} \right]^2}. \tag{3.2}$$

36

From the baseline signal a baseline AR model can be estimated, which will then be fitted to new signals from unknown structural state. If the structural condition is unchanged, the ACF will resemble a Dirichlet delta function. It can be shown that for large N the sample autocorrelations of a white noise sequence at nonzero lags are approximately identically and independently distributed $N(0,1/n)$ (Brockwell and Davis, 2009), hence the 95% confidence bounds can be drawn at $\pm 1.96/\sqrt{n}$, as 1.96 is the .025 quantile of the standard normal distribution. Accordingly, the system can be identified as damaged when the number of ACF function value outside the bounds become statistically significant (Figure 3.2).

3.4 THRESHOLD CONSTRUCTION SCHEMES FOR DAMAGE FEATURES FROM TIME SERIES ANALYSIS

A desirable threshold is one that strikes up a balance between false alarms and missed cases. Now in most engineering practices this value is determined in an *ad hoc* manner. Statistical hypothesis testing has been tried for automatic threshold construction, but its effectiveness is not guaranteed unless the actual feature distribution is the same as assumed. Here, two data-driven methods will be introduced for threshold construction.

3.4.1 Threshold calculated from resampling: the 'cross-one-out' method

From Figure 3.1 it is clear that the Mahalanobis distance feature suffers from large fluctuations within the baseline sample set. Also, when the baseline samples are extracted from vibration signal segments with overlap, the sample set is in fact not a very good representation of the actual feature probability space. Therefore, hypothesis testing exploiting the multivariate normal distribution will tend to yield a conservative threshold.

The first problem is perhaps resulted from environmental variations and statistical modeling and estimation deficiencies and cannot be helped; one solution to the second problem is to use vibration signals without overlap for feature extraction. However, when the data available is limited, this method is not practicable.

To address this problem here a 'cross-one-out' resampling technique is adopted. Figure 3.3 is a flow chart of this approach for the Mahalanobis distance feature. It can also be described in words as follows: First a segment is cut from the baseline signal at a random time point and reserved for testing, and sample segments of the same size are cut with a preset overlap from the remaining signal. The Mahalanobis distance between the AR model coefficients of left-out segment and those of the sample set is then computed and stored. This process is repeated for a large number of times and the value beyond which 5% of the tests occur is used as threshold in subsequent analysis. This is essentially an estimation of the feature distribution through recomputing the statistic for many a time by leaving out a certain portion of observation, and can be viewed as a combination of jackknife and cross-validation technique (Shao and Tu, 1995).

Other methods have been proposed for threshold determination of Mahalabnobis distance feature; a Monte Carlo method has been used (Sohn et al., 2001) to produce the desired threshold by calculating the 5% quantile of empirical feature distribution of simulated coefficient vectors whose components are drawn independently from standard normal distribution. However, as noted in previous text, the AR coefficients are not mutually independent and may not have a unit variance. The assumption of this simulation is not well-grounded, thereby this approach is not used here though reported successful in a couple of literatures.

38

3.4.2 Empirical density estimation for multiple features; the nearest neighbor rule

Threshold determination becomes complicated when there is more than one feature in the algorithm. Fortunately, the nearest neighbor rule (Figure 3.4) provides an intuitive way for empirical density estimation, from which damage threshold can be derived.

Suppose a dataset $\{x_i\}$ is generated from a certain probability distribution $p(x)$, then an empirical estimate of the probability density at x_i can be obtained exploiting the condition below

$$\hat{p}(x_i) \propto 1 / \min d^n \left(x_i, x_j \right) \, (i \neq j). \tag{3.3}$$

Here n stands for the feature vector dimension, and (x_i, x_j) is the distance between point x_i and x_j. It is clear that the larger the distance from a point to its nearest neighbor, the smaller is its probability to occur.

A decision strategy for multiple features can hence be established as follows; for each feature vector from unknown state, search for its nearest neighbor in the baseline feature set and record the squared Euclidean distance. When the number of feature vectors above threshold exceeds a certain amount, the system is identified as damaged.

Therefore, the only thing remains to be determined for applying this strategy is the threshold value and its corresponding significance level. In the application presented in Section 3.5, a 5% significance level threshold is used. The threshold value for the test (unknown state) sets is four times the distance value D^* that has 5% of within-baseline nearest neighbor distances above it. This decision is based on following considerations; assume that both baseline and test features follows a same unimodal distribution that decays exponentially with respect to the distance to feature mean, then around 2.5% of

39

the total features will be expected to have squared nearest neighbor distance beyond $2D^*$ given that the baseline and test set are of equal size. Since in the proposed decision strategy only baseline features are used for nearest neighbor search, this will increase the threshold to $4D^*$ because only half of the samples remain. To simply data processing, here the threshold is tested against 5% of the test features instead of 2.5% of the total features. It is but a slight relaxation of conditions, as few of the baseline features will go beyond this critical value.

3.5 APPLICATION OF THE PROPOSED THRESHOLD CONSTRUCTION SCHEMES

The damage detection algorithms are applied to acceleration measurements collected from a 5 degree-of-freedom structure (Figure 3.5) subjected to base excitation. Wired accelerometers are mounted to the shaking table and each floor. Damage is simulated by adding weight to the 4th floor. For each structural scenario, two sets of acceleration signals are recorded from two random excitation experiments. The sampling frequency is 100 Hz for all datasets.

3.5.1 Validation of the cross-validation threshold construction scheme

Figure 3.6 displays some of the results from Mahalanobis distance method. (a) is the result from 2nd floor response using threshold from proposed technique; (b) is the result from 4th floor response using threshold from proposed technique; (c) is the result from 4th floor response using threshold from hypothesis testing based on multivariate normal assumption. The significance level in all cases is 5%.

The AR model order adopted is 5, and 350-point segments are cut from acceleration signals with 300 overlap. It is obvious from Figure 3.6 (a) and (b) that the change in

المنارة للاستشارات

www.manaraa.com

feature value becomes more prominent at sensing locations more close to structural damage. Also, a comparison between Figure 3.6 (b) and (c) shows that the threshold determination technique proposed here does yield a superior performance to that of frequentist hypothesis testing. In all the plots in Figure 3.6 logarithmic scale is used for the y axis in order to decrease the oscillation of feature values.

Because in this case a controllable artificial excitation source is used in all the experiments, the overall statistical characteristic of Mahalanobis distance feature does not vary much over time. When this method is applied for damage detection from ambient vibration responses, this feature can have even more significant variantions. However, this resampling-based technique is still proved reliable in a couple of experiments on a space truss under ambient load, on the condition that there is enough data available.

3.5.2 Validation of the nearest-neighbor threshold construction scheme
Most of the current research on damage detection by time series analysis employs only a single feature, or a set of features from either residual analysis or model parameter analysis. More damage sensitive methods can probably be established by taking features from both categories into consideration, as they in some sense reflect different aspects of the vibration signals. Thus here the two features mentioned in Section 3.3 will be combined for damage identification.

To begin with, two feature pair sets of equal size are extracted from baseline and unknown signal, respectively. The extraction of Mahalanobis distance feature is still the same as before, i.e. for baseline signal feature values are generated using the 'cross-one-out' method introduced in Section 3.4, and for unknown state signal they are obtained using the routinely procedure described in Section 3.3. Note here that the logarithm of the

41

distance is used to reduce the oscillation of feature values. Correspondingly, the residual sequence of each signal segment is obtained by filtering each data segment with the AR model estimated from the whole baseline signal. The autocorrelation feature value is then computed from the formula below;

$$Q_2 = \sum_{i=-10}^{10} |\rho(i)| \tag{3.4}$$

Where $\rho(i)$ is the ACF of the residual sequence. The segment size and overlap length adopted are still 350 and 300.

Figure 3.7 contains two scatter plots of baseline and test feature clusters extracted from acceleration responses at 4th floor of the lab specimen aforementioned. Test features in the left plot come from healthy state, while those in the right one are from damaged state. It can be seen that when the structural condition remains same, the two clusters largely overlap each other; when damage has occurred, the test cluster will drift away from the baseline.

The nearest neighbor scheme is applied here to determine the damage threshold, and the results are summarized in Table 3.1. The value before the slash is the number of outliers, and after the slash is the decision on structural state. The notation in statistical hypothesis testing is used; H_0 denotes healthy state, while H_1 denotes damaged state. Feature variables are all normalized beforehand with respect to the corresponding baseline standard deviation so that contribution of the two features to damage identification is equal. In each comparison the size of both baseline and test set is 166, and the threshold value for the number of outliers is accordingly set at 9. For each sensor location different AR model order is used to better fit the data. The performance of this

42

algorithm is excellent in this case, with only one false alarm for the healthy state and perfect recognition for damaged case. It seems that the responses at 1st and 4th floor are most affected by the simulated damage.

3.6 CONCLUSION

For this case study presented here, thresholds based on data-driven techniques are proved successful. They tend to generate fewer false alarms than frequentist hypothesis testing, yet still correctly report damage for most tests. All of these techniques employ some sort of empirical density estimation. Although the procedure is somewhat computationally complex, it provides a relatively reliable way to construct thresholds for features with large variation or of unknown distribution and thus automate the process of damage detection.

However, it must be stated that neither improved schemes for threshold construction, nor combination of features, can replace the quest for features that are more stable and damage-sensitive. Features are always the most important topic in damage detection. Adjusting threshold determination methods and combining features can help well-chosen features to perform better, but they cannot save a bad feature from yielding bad performance. Such features based on autoregression on single node response are innately 'fragile' because the information is limited and can be affected by other factors. When the loading condition or operation environment of the structure monitored is subjected to change, features based on longer data or data from several sensing locations will probably be more reliable.

Table 3.1   Damage identification result using nearest neighbor scheme.

Sensor location　　Dataset num.	1st floor	2nd floor	3rd floor	4th floor	5th floor
1 (healthy state; baseline)					
2 (healthy state; validation)	$7/H_0$	$7/H_0$	$7/H_0$	$3/H_0$	$14/H_1$
3 (damaged state)	$126/H_1$	$78/H_1$	$32/H_1$	$161/H_1$	$88/H_1$
4 (damaged state)	$112/H_1$	$37/H_1$	$27/H_1$	$159/H_1$	$30/H_1$

44
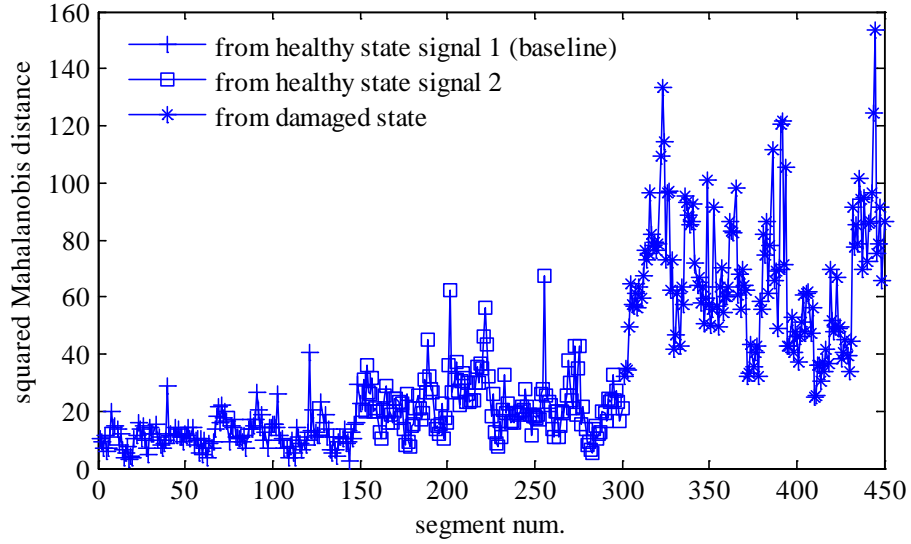
Figure 3.1   Mahalanobis distance of model coefficients. Segment size is

350. The overlap between consecutive segments is 300.
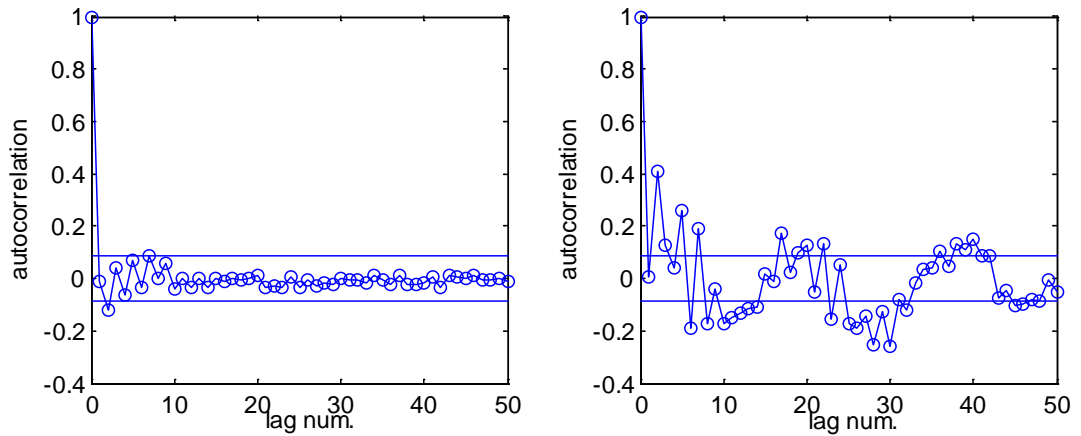
Figure 3.2   Residual autocorrelation as damage indicator; lots of outliers

appear when model no longer fit the data well. The length of

residual sequence is 520.

45
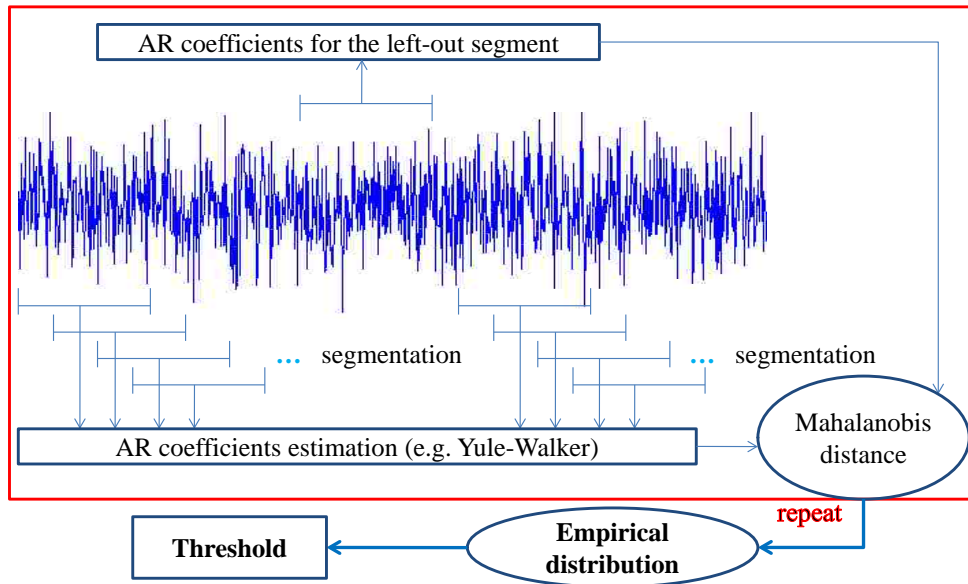
Figure 3.3   The 'cross-one-out' threshold evaluation method for Mahalanobis distance of model coefficients
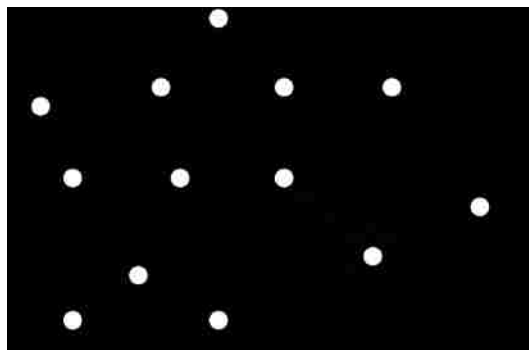
Figure 3.4   Illustration of the nearest neighbor rule

Figure 3.5   The Plexiglass 5-dof lab specimen
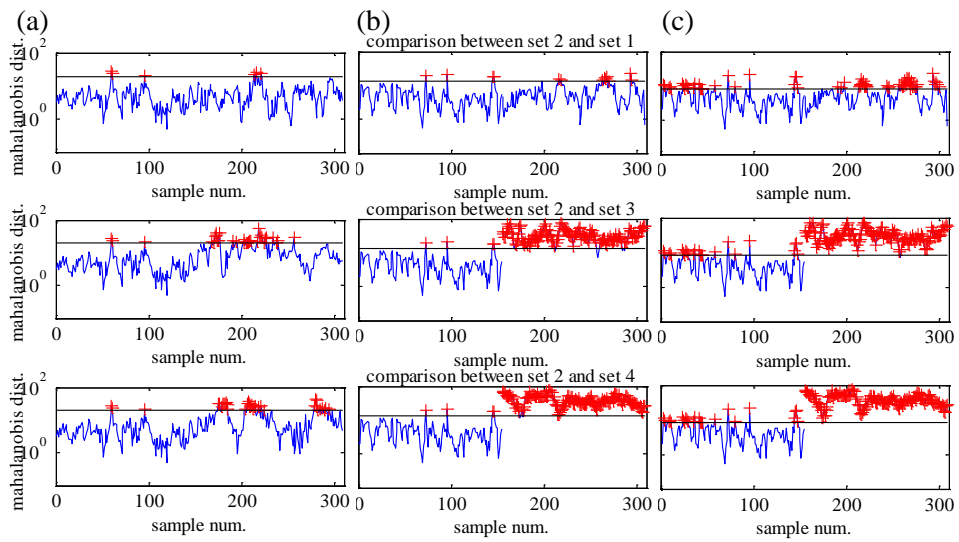
Figure 3.6   Damage detection using the Mahalanobis distance of AR

model coefficients

47
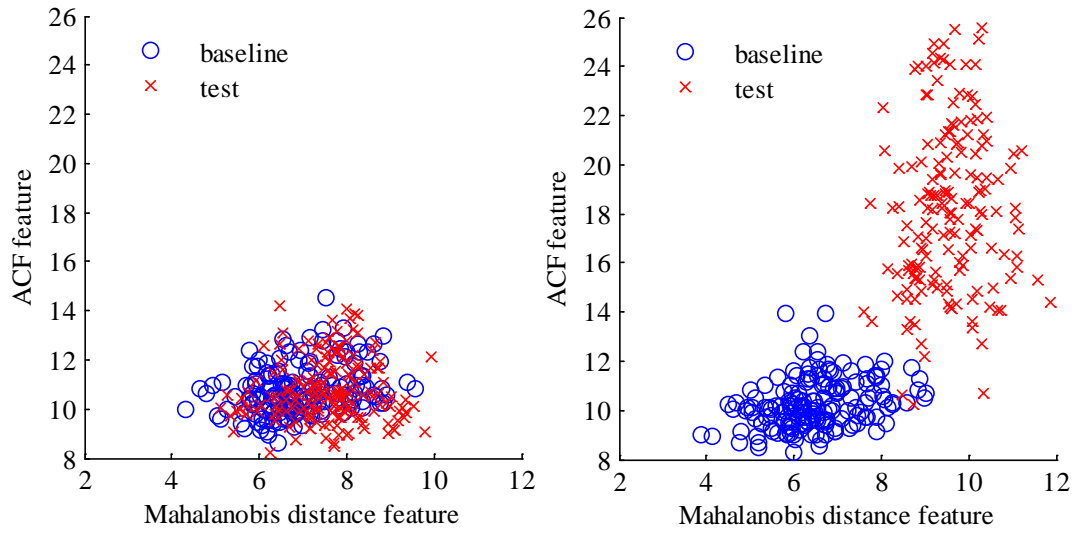
Figure 3.7   Scatter plots of damage feature pairs

Chapter 4　New AR features with enhanced performances

4.1 PRELUDE

As noted in the conclusion of the previous chapter, feature extraction plays a crucial role in the establishment of an effective damage detection scheme. Conventional damage feature extraction methods focus on direct estimation of structure's global physical parameters such as modal properties, which often require a numerical model of the structure (Abdel Wahab, de Roeck, and Peeters, 1999; Bernal, 2002; Doebling et al., 1998; Haritos and Owen, 2004). While these physical properties are easy concepts for interpretation, many of them are computationally intensive to estimate, and in some cases can fail to identify significant local damage even with a dense sensor network (Doebling et al., 1998). Recently, scalar TSA based damage features have received increasing attention as a more efficient alternative.

AR/ARX/ARMA models are some of the most common TSA tools adopted in the current literature. These features can somewhat reflect structural physics, e.g. the parameters of an input-output based ARX model for the LTI (linear time-invariant) systems represent the structural impulse response at an arbitrary location. Therefore, to provide more effective insight into the condition of the structure, scalar AR/ARX/ARMA based damage indicators are preferable features compared with those purely statistical indices of structural vibration responses such as kurtosis (a statistics measuring the sharpness of sample distribution) and principal components (a linear combination of observations from multiple channels such that the results possess maximum variance, therefore conveying the most information). TSA Damage indices are defined as functions

of TSA model parameters, and the selection of these parameters and functions matters significantly with regard to the damage detection performance.

4.2 MOTIVATION AND ORGANIZATION

The existing AR/ARX/ARMA methods for damage detection are based on monitoring of model residual variances and model parameter vectors (using Mahalanobis distance, Euclidean distance etc.). Though theoretically justified, they only reflect possible changes in certain aspects of the model, and may not be the most effective ways to apply AR/ARX/ARMA based damage detection.

In addition, their robustness to noise has been largely left unexamined. In this chapter a new AR model spectrum based damage feature and a new AR residual correlation based feature will be proposed along with a brief investigation into the damage sensitivity of AR model coefficients and residuals. The performance of new algorithms will be compared to that of the existing methods through numerical and laboratory experiments. The cross validation technique introduced in the previous chapter is used here for threshold construction of the AR model parameter based features.

The remainder of this chapter is organized into the following subsections.

- In Section 4.3, the formulations of several available TSA features (either coefficients based or residual based) are presented.

- In Section 4.4, the Ljung-Box statistic of AR residuals is proposed as a more sensitive damage feature than the AR residual variance, and the Cosh distance of AR model spectrum is introduced as a more stable damage index than the Mahalanobis distance of AR coefficients.

- In Section 4.5, two proposed damage features and two existing features are numerically validated on a 4-DOF system.

- In Section 4.6, two proposed damage features and two existing features are experimentally validated on a truss specimen and a bridge specimen.

- In Section 4.7, conclusions on the merits of AR damage features are made.

4.3 SPR ALGORITHMS USING AR/ARX BASED FEATURES

Many SPR algorithms only look at a certain aspect of AR/ARX models for input features. Two most commonly adopted features are model residuals and model coefficients.

4.3.1 Model residuals as damage indicator

Definition of AR model is already introduced in Section 2.2.2.2. An ARX model is similar to an AR model in structure, only there is an additional regression term on the right side of the equation for an external input:

$$x(t) = \sum_{i=1}^{a} \alpha_i x(t-i) + \sum_{j=0}^{b} \beta_j e(t-j) + \epsilon_x(t). \tag{4.1}$$

In this definition $e(t)$ *is used to denote the input, and* $\epsilon_x(t)$ *is the model residual term*. In application, damage indicators can be certain characteristics of the residuals obtained by fitting the model from baseline $x(t)$ to a dataset $y(t)$ collected from an unknown state.

$$\text{AR analysis: } e_y(t) = y(t) - \sum_{j=1}^{p} \varphi_{xj} y(t-j),$$

$$\text{ARX analysis: } \epsilon_y(t) = y(t) - \sum_{i=1}^{a} \alpha_i y(t-i) - \sum_{j=1}^{b} \beta_j e_y(t-j). \tag{4.2}$$

51

In (Sohn and Farrar, 2001), the ARX model residuals from strain gage data from a patrol boat are used to report damage. Note that since the input information is not available in this case, a two-stage analysis is adopted. First an $AR(p)$ model is fitted to all signal segments to obtain the residuals and AR coefficients. Then the baseline data segment $x(t)$ whose AR coefficients are closest to that of the unidentified data $y(t)$ is selected, and an $ARX(a,b)$ model is constructed from $x(t)$ using its AR residuals as exogenous input. Hence, ARX residual sequences ϵ_x and ϵ_y can be obtained respectively from $x(t)$ and $y(t)$ using the baseline model. The ratio $\sigma(\epsilon_y)/\sigma(\epsilon_x)$ is defined as the damage-sensitive feature in this case. Here $\sigma(\cdot)$ denotes the standard deviation of a sequence. An increase in the values of damage indicator is observed as the system became damaged.

In another study (Sohn et al., 2001) on damage identification in a mass-spring-damper system using acceleration response, similar methodology is used for feature extraction but a more statistically rigorous approach is employed for damage threshold construction. The selected damage index is $\sigma^2(\epsilon_y)/\sigma^2(\epsilon_x)$, which should follow an F -distribution under the Gaussian assumption of residuals. A modified hypothesis test is used to set the damage threshold.

A successful application of AR residuals in detecting structural change in a progressively damaged concrete bridge column is reported in (Fugate et al., 2001). Acceleration measurements are collected from a single sensor mounted on the model. A healthy-state dataset is used to train a baseline AR model, which is fitted to both training and unknown state data to produce AR residual sequences. These sequences are divided

52

into subgroups of size 4, and within-subgroup mean ($\bar{x}$) and standard deviation (S) are monitored using statistical process control chart. The upper/lower control limits of the charts are determined from baseline data residuals (Table 4.1); when the system is damaged, it is expected that a large portion of charted values will go beyond the limits.

4.3.2 AR coefficients as damage indicators

In the same paper (Sohn and Farrar, 2001) where AR-ARX residuals are used to capture damage, an outlier analysis is performed for the AR coefficients. The distance measure adopted for novelty evaluation is Mahalalobis distance, a metric that has been presented in Section 3.3.1.

Mahalanobis distance is defined from the deviation statistics; a normal Gaussian statistical population in $p-$variants is usually described by a $p-$dimensional frequency distribution:

$$f\left(x,\mu,\Sigma\right)=\frac{1}{\left(2\pi\right)^{p/2}\left|\Sigma\right|^{1/2}}\exp\left(\frac{1}{2}\left(x-\mu\right)^{T}\Sigma^{-1}\left(x-\mu\right)\right).\tag{4.3}$$

Where x is the p-dimensional Gaussian Random Vector, μ is its expectation, and Σ is its covariance matrix. When data from a structural state that differs from the baseline is tested, Mahalanobis distance value for AR coefficients is expected to increase substantially. Monte Carlo Simulation was employed for damage threshold construction: feature vectors with components drawn independently from a standard normal distribution are generated, and then their Mahalanobis distance values are computed and arranged in descending order. The threshold is set at the point beyond which 1% or 5% values occur.

53

Mahalanobis distance is also adopted for damage detection in an experimental research described in (Gul and Catbas, 2009), where AR modeling is applied to the free decay response produced via random decrement technique, instead of the raw ambient response.

4.4 PROPOSED DAMAGE DETECTION ALGORITHMS BASED ON TIME SERIES ANALYSIS

Though in several studies, AR models have been employed for feature extraction to detect structural damage, they mainly emphasized on development and validation of the SPR method and did not focus on examining their effectiveness for structural monitoring by sensitivity analysis. In this section the sensitivity of AR model properties as damage indicators will be inspected, and from the analysis result new autoregressive features based on model residuals and parameters are proposed.

Damage detection is essentially an inverse problem that attempts to diagnose the system using the input (excitation) and output (structural response) records. Since in most practical situations input information is difficult to obtain, a convenient, yet in most cases justifiable assumption is made that the excitation is white noise. Theoretically, the structural vibration response under such loading can be treated as an $ARMA(p,q)$ process, with a corresponding z-transfer function (Oppenheim and Schafer, 2009) as shown in equation (6):

$$X\left(z\right) = \frac{1 - \theta_1 z^{-1} - \theta_2 z^{-2} - \ldots - \theta_p z^{-q}}{1 - \alpha_1 z^{-1} - \alpha_2 z^{-2} \ldots - \alpha_p z^{-p}}. \tag{4.4}$$

In this equation, the auto regressive (AR) coefficients, $\{\alpha_i\}$, are determined by structural properties, and the moving average (MA) coefficients, $\{\theta_i\}$ are affected by both the structural condition and excitation. The location of the zeros of the process,

54

determined by the MA coefficients, can be easily affected by even a slight measurement noise content that introduces a rippled noise floor to the signal spectrum. In Figure 4.1, the two ARMA models have the same AR coefficients but different MA coefficients. The blue and red lines are the Welch's periodogram plots from data generated from the two models. The results are presented as an empirical proof that the zero positions (which is related to the MA coefficients) of a system cannot be reliably inferred from noise contaminated signals. As such, the ARMA models, despite their higher computational cost, do not always yield a performance superior to AR models in many applications. Therefore, using AR models is a preferable choice for constructing an efficient and effective damage detection algorithm that will work for online or distributed structural monitoring. In the remaining text of this chapter, the discussion will be limited to AR models.

4.4.1 Damage detection using autocorrelation function (ACF) of the residuals

From the definition of the AR model it is clear that if the autoregressive model used to filter an AR process is exactly the same as its underlying structure, then the produced model residuals should be the same as $\epsilon_x(t)$ in Eq. (1). Otherwise, the residual sequence will resemble an ARMA process instead of being a white noise.

Ljung & Box (1978) proposed a statistic to measure the difference between residual series and identically and independently distributed (i.i.d.) noise:

$$Q = n(n+2)\sum_{j=1}^{h} \frac{\rho_j^2}{n-j} \ , \tag{4.5}$$

where n is the sample size, h is the number of lags, and ρ_j is the autocorrelation at the jth lag. Since this Q – statistic follows a χ^2 distribution under the normality assumption

of the input, a statistical test can be devised at significance level α, by setting the rejection threshold at $\chi^2_{1-\alpha,h}$, which is the α – quantile of the χ^2 distribution with h degrees-of-freedom.

This so-called Ljung-Box test is yet a novel statistical approach in the civil engineering domain. Nonetheless, it seems an attractive alternative for damage detection to residual-variance based methods, and will be applied in conjunction with AR modeling in Sections 4.5 and 4.6. In the rest of this subsection, an analytical result will be provided on the sensitivity of residual ACF to structural damage. Here, structural damage is represented as a change in AR coefficients (indirect structural parameters), rather than parameters with a clear physical meaning (mass, stiffness, etc.).

Assume that the structural vibration response at a certain location can be described by a univariate $AR(p)$ model:

$$x(t) - \alpha_1 x(t-1) - \alpha_2 x(t-2) - \ldots - \alpha_p x(t-p) = e(t). \tag{4.6}$$

The corresponding z-transfer function is (p is always an even number, as the structural poles always appear in pairs as conjugates):

$$\begin{aligned}
\Phi(z) = \frac{E(z)}{X(z)} &= \frac{1}{1 - \alpha_1 z^{-1} - \alpha_2 z^{-2} \ldots - \alpha_p z^{-p}} \\
&= \frac{1}{\left(1 - a_1 z^{-1}\right)\left(1 - a_1^* z^{-1}\right)\left(1 - a_2 z^{-1}\right)\left(1 - a_2^* z^{-1}\right) \ldots \left(1 - a_{p/2} z^{-1}\right)\left(1 - a_{p/2}^* z^{-1}\right)},
\end{aligned} \tag{4.7}$$

which is an all-pole expression. It can be shown that the poles of a discretized MDOF structure are related to its eigenfrequencies (ω_i) and damping ratios (ζ_i) through the following expression (Nair et al., 2006):

$$a_i, a_i^* = e^{-\zeta_i \omega_i T_s \pm \omega_i \sqrt{1 - \zeta_i^2} T_s}, \quad \text{i:the mode order} \tag{4.8}$$

56

In Eq.(4.8), T_s is the data sampling frequency. Hence in the subsequent derivations, damage will be represented by a shift in the position of system poles. To simplify the discussion, suppose the model only differs from the data structure in the first pair of conjugate poles, a_1 and a_1^*, by a value of Δa_1 and Δa_1^*, where $\left(\Delta a_1\right)^* = \Delta a_1^*$. The z-transfer function of the residual sequence from the new structural state can be expressed as:

$$E'(z) = \frac{\left[1-\left(a_1+\Delta a_1\right)z^{-1}\right]\left[1-\left(a_1^*+\Delta a_1^*\right)z^{-1}\right]}{\left(1-a_1 z^{-1}\right)\left(1-a_1^* z^{-1}\right)}E(z).$$ (4.9)

Eq. (4.9) can be written in the time domain as

$$\left(1-a_1 B\right)\left(1-a_1^* B\right)e'(t) = \left[1-\left(a_1+\Delta a_1\right)B\right]\left[1-\left(a_1^*+\Delta a_1^*\right)B\right]e(t),$$

$$e'(t) = \sum_{n=0}^{\infty}\left(a_1 B\right)^n \sum_{m=0}^{\infty}\left(a_1^* B\right)^m \left[1-\left(a_1+\Delta a_1\right)B\right]\left[1-\left(a_1^*+\Delta a_1^*\right)B\right]e(t)$$

$$= e(t) + \left[\sum_{n=0}^{\infty}\left(a_1 B\right)^n\left(-\Delta a_1^* B\right) + \sum_{m=0}^{\infty}\left(a_1^* B\right)^m\left(-\Delta a_1 B\right)\right]e(t).$$

Here B stands for the backshift operator, i.e. $Bp[n] = p[n-1]$. Considering changes in all pole pairs,

$$e'(t) = e(t) + \sum_{k=1}^{p}\left[\sum_{n=0}^{\infty}\left(a_1 B\right)^n\left(-\Delta a_1^* B\right) + \sum_{m=0}^{\infty}\left(a_1^* B\right)^m\left(-\Delta a_1 B\right)\right]e(t).$$ (4.10)

This result is obtained under the assumption that the deviation of the model from its original state is very small.

From Eq.(4.10) it is clear that as the model deviates from the baseline, the residuals will be the sum of a white noise sequence and a number of attenuated auto-regressive terms. As a result, an increase will be observed in its standard deviation, and its

57

autocorrelation function will start showing non-zero values at different time lags. A

simple derivation leads to an expression for the ACF of $e^{'}(t)$:

$$R_{e^{'}}(t) = \sigma_e^2 \{\delta(t) + \sum_{k=1}^{p}\left(-\Delta a_1^* - \Delta a_1\right)\delta(t-1)$$

$$+ \sum_{k=1}^{p}\sum_{l=0}^{p}\left[\frac{\left(\Delta a_k \Delta a_l\right)^* a_l^t}{1-\left(a_k a_l\right)^2} + \frac{\Delta a_k \Delta a_l a_l^{*t}}{1-\left(a_k^* a_l^*\right)^2} + \frac{\Delta a_k^* \Delta a_l a_l^{*t}}{1-\left(a_k a_l^*\right)^2} + \frac{\Delta a_k \Delta a_l^* a_l^t}{1-\left(a_k^* a_l\right)^2}\right]\} \ , \quad (4.11)$$

where σ_e^2 is the noise variance. In Eq. (4.11) high order terms are not omitted because

the poles of a physical structure are generally close to the unit circle, thus making the

value of the denominators small. The damage detection methods that were examined in

Section 4.3 are based on mean and standard deviation control charts on grouped residuals

and F-test on residual variance. Eq. (4.11) suggests that more sensitive statistical features

can be found by taking into consideration the change of the entire ACF, instead of

focusing only on the change in residual standard deviation.

4.4.2 Damage detection using AR model spectrum

Corresponding spectrum plot can be constructed given an AR model (Figure 4.3):

$$S_{AR}^{(p)}(\omega) = \frac{\sigma_e^2}{\left|\phi\left(e^{j\omega}\right)\right|^2} = \frac{\sigma_e^2}{\left|\sum_{k=0}^{p}\phi_k e^{-j\omega k}\right|^2} \quad (4.12)$$

Here σ_e^2 is not calculated and set to 1, since its value can be determined by excitation

level.

It is proposed here that Cosh spectral distance (Haritos and Owen, 2004; Wei and

Gibson, 2000) based on AR spectrum estimates be used as a more stable damage index

than Mahalanobis distance of AR coefficients:

$$C\left(S,\bar{S}\right)=\frac{1}{2N}\sum_{j=1}^{N}\left[\frac{S\left(\omega_j\right)}{\bar{S}\left(\omega_j\right)}-\log\frac{S\left(\omega_j\right)}{\bar{S}\left(\omega_j\right)}+\frac{\bar{S}\left(\omega_j\right)}{S\left(\omega_j\right)}-\log\frac{\bar{S}\left(\omega_j\right)}{S\left(\omega_j\right)}-2\right]. \qquad (4.13)$$

In Eq. (4.13), $S\left(\omega_j\right)$ is the Power Spectral Density to be examined, and $\bar{S}\left(\omega_j\right)$ is the average of the spectra estimates from baseline samples. When the system is damaged, the Cosh distance value should increase. Since no theoretical probability distribution is available for this statistic, damage threshold will be determined using the cross validation technique (Section 3.4.1).

Structural damage will influence the values of the AR coefficients obtained from autoregressive modeling on the vibration responses. A desirable feature is one that is sensitive to the damage, but not very sensitive to other non-relevant factors. A theoretical solution on the feature sensitivity would require not only a thorough inspection of the numerical estimation algorithm used, but also evaluation of finite sample number effect and complicated statistical distributions. Therefore, numerical simulations are adopted to investigate this subject. Each simulation consists of 50 runs, in which sample data are generated from an ARMA (10, 6) process with white noise added. In Figure 4.2, the first row shows how the coefficient and spectrum estimates respond to the change in signal noise level, the second row shows how these estimates are affected by a slight variation in the positions of two zeros of the ARMA process (as reflected in the difference between the two thin blue lines), and the third row shows their responses to change in the values of two poles of the ARMA process. In all estimations the AR order is set at 16.

As can be seen in the second and third row of Figure 4.2, the signs and values of AR coefficients are sensitive to the change in position of zeros and noise ratio, and especially to the latter; when the noise level is raised slightly, substantial variation happens in the

59

value of first six AR coefficients. The Mahalanobis distance measure mentioned before is implicitly based on the assumption that the estimated coefficients are Gaussian random vectors, which is only true asymptotically when the underlying process is strictly $AR(p)$; see (Sakellariou and Fassois, 2006) for details. When such variations are considered, the general 'shape' of the coefficient cluster may be easily affected and thus render this feature not robust with respect to variation due to environmental factors.

Judging from the plots, the AR spectrum estimate seems a more reliable feature compared to the coefficients. This feature is not greatly affected by noise level change, and has the desired feature of being more sensitive to shift in poles than zeros (considering the logarithmic plot scale that magnifies the difference between small values). No explicit reasoning is available now to account for this phenomenon, but the interaction between polynomial coefficients and roots is complicated when the polynomial order is high; sometimes a slight change in one corresponds to great variation in the other.

4.5 NUMERICAL IMPLEMENTATION OF THE STATISTICAL ALGORITHMS

To examine the effectiveness of both the old and new algorithms, a four degree-of-freedom mass-spring-damper system (Figure 4.4), subjected to white noise excitation is simulated using MATLAB. Two sets of acceleration measurements are collected at all nodes from the healthy structure. Then damage is simulated by reducing the stiffness of the spring between nodes 3 and 4 by 20%, and two additional sets of acceleration measurements are obtained from the damaged structure. Figure 4.5 and Figure 4.6 display the results from different statistical algorithms. In all these statistical tests, one dataset (dataset 2) from the undamaged condition is used to establish the baseline, and the other

(dataset 1) for false-positive testing. The other two sets from the damaged state are used to demonstrate each method's damage detection performance. Each dataset consists of 3000 points. The order of AR models is determined by using Akaike's Information Criterion (AIC) (Brockwell and Davis, 2002).

Damage is clearly indicated by both the $\bar{x}$ control chart and $Q-$statistic trace plot (Figure 4.5). The AR model order used in control chart construction is 28, the subgroup size is 4. The maximum lag number for Q-statistic evaluation is 25. The significance level of the threshold is 5%. The classification result using $S-$control chart is not satisfactory, possibly due to the fact that the residuals are not completely uncorrelated. $Q-$statistic trace plots are the more sensitive features, where the values from the damaged state significantly increase as model order increases. Such large differences have compensated the imperfection of having the false positive trace lying above the threshold. Note that as the AR order increases, the model overfits dataset 2, thus making the difference in Q-statistic value obtained from dataset 1 and dataset 2 greater. Another interesting point observed is that as model order increases, the false positive trace becomes quite flat, while the two damaged state traces are fluctuating.

In Figure 4.6, The AR model order employed is 28, and each dataset is segmented into a group of 350-point long pieces with 300-point overlap between successive parts. The significance level of the threshold is 5%. The number of FFT (fast Fourier Transform) points is 256. It can be seen that the Mahalanobis distance feature is not robust with respect to variation due to environmental factors, and cross-validation technique is employed for threshold construction in both Mahalanobis distance plot and the AR spectrum distance plot presented herein.

4.6 EXPERIMENTAL VALIDATION OF THE STATISTICAL ALGORITHMS

For further verification of the statistical algorithms, they are also applied to acceleration data from two laboratory experiments. As in the numerical case, two acceleration datasets are obtained for either structural scenario.

4.6.1 Case study 1: truss model subjected to ambient vibrations.

Figure 4.7 shows a picture of the specimen tested, with 14 wireless sensors mounted on the connection nodes. The truss is 1 m wide, 0.707 m tall, and has in the longitudinal direction four spans (lower cord), each 1.414 m long. For additional information on the truss, please refer to Section 2.2. No additional excitation is applied except the ambient vibration, and two $20.4\,kg$ disks are added to the mid-span of the truss to approximate a loss of stiffness in the system. For the undamaged case, the fundamental frequency estimate of the truss is 2.33 Hz. For the damaged case, the first frequency is 2.05 Hz.

The statistical control charts have already been applied to free vibration data collected from the truss in Section 2.2. However, as the AR models were initially proposed as a tool to study stationary time series, it makes more sense to apply them to ambient vibration responses. Due to the measurement noise disturbances in the high frequency content of the acceleration signals collected, the data is preprocessed using a low-pass filter before SPR evaluation. The results from Ljung-Box test, Mahalanobis distance and Cosh spectral distance evaluation are shown in Figure 4.8 and Figure 4.9. In all applications, the first two datasets are from healthy state, the rest from damaged state. The significance level of all thresholds is 5%. The maximum lag number for Q-statistic evaluation is 25. For evaluation of the Mahalanobis distance and Cosh spectral distance features, the AR model order selected to be 22, and each dataset is segmented into a

62

group of 300-point long pieces with 250-point overlap between successive parts. The significance level of the threshold is 5%. The number of FFT (fast Fourier Transform) points is 256. Statistical control chart failed to yield a satisfactory classification result in this case. Again, the theoretical threshold of the Q-statistic generates false alarms.

4.6.2 Case study 2: bridge slab model subjected to white-noise excitation

The test specimen is a two-span reinforced concrete bridge model tested at the University of Nevada, Reno (Figure 4.10). The three bents are each placed on separate shaking tables. Clear column heights of 1.83 m, 2.44 m, and 1.52 m were chosen for Bents 1, 2, and 3, and the diameter for each column is 0.31 m. The width and the total length of the slab were 2.5 m and 20.5 m. The design prototype was an idealized two-span frame of a cast-in-place, post-tensioned reinforced concrete box girder bridge. As part of a larger NEES (Network for Earthquake Engineering Simulation) project (Johnson, Ranf, and Saiidi, 2008), the specimen was progressively damaged during various low-to-high amplitude level earthquake excitation tests, all of which were from the 90 degree and 180 degree components of the Century City Country Club North record from the 1994 Northridge, California earthquake. In the intervals between these tests, white noise excitation was applied to the structure. Minor cracks were first observed after the 13th earthquake test, and exposing of reinforcements occurred after 15th test, other details on the damage accumulation in bridge bents can be found in

Table 4.2. The data used here is the transverse acceleration measurements of the slab from white-noise tests collected from sensor AT3 (Figure 4.10). The names of the data files, as shown in Figure 4.11 to Figure 4.13, is a combination of the number of the earthquake tests before and after the white noise test, with common prefix 'WN'.

Postfixes are employed to distinguish data from different tests under same structural condition.

For all the results presented for this case study, the first three datasets are from the healthy state, the rest from the damaged state. Again, thresholds with a 5% significance level are used for all features. When evaluating the Mahalanobis distance and Cosh spectral distance, the AR model order used is 20, and each dataset is segmented into a group of 350-point long pieces with 300-point overlap between successive parts. The number of FFT (Fast Fourier Transform) points is 256. The AR model order used in control chart construction is 15, and the subgroup size is 10. It is observed that when the damage is small, features calculated from model coefficients are no less sensitive than those from residuals. But when the damage becomes severer, the value of latter increases much more rapidly than the former. This can be explained by the results presented in Section 4.4: the change in autocorrelation/variance is the sum of pole shifts and a number of second order terms with possibly small denominator values. The 'second order effect' will grow prominent when the damage becomes more substantial. The statistical control method performs quite well in this case, possibly because the excitation is a controlled white noise input.

Also, it can be observed in all of the numerical and experimental applications the Cosh distance outperforms the Mahalanobis distance in that the former is relatively more robust to excitation condition variations. The percentages of outliers/inliers of the application examples are provided in Table 4.3. Note that for all the figures the threshold is set at a 5% statistical significance level, which means damage is recognized when the outlier portion exceeds 5% of the total observations (or equivalently, when the inlier

64

portion falls below 95% of the total observations). It is clear that the Cosh spectral distance yields a more consistent performance for the baseline and false-positive testing datasets, while remains overall sensitive to structural damage.

It is worth noting that as the system becomes non-linear, many feature values stop reflecting the damage extent, due to the invalidity of LTI (linear time invariant) assumption for the system.

4.7 CONCLUSION

In this chapter, two time series-based structural damage detection algorithms using statistical pattern recognition are proposed and investigated. One of them uses the Ljung-Box statistic of AR model residual sequence as damage index; the other uses the Cosh spectral distance of the estimated AR model spectrum. Compared with existing algorithms based on AR model residual variance and coefficients distance, the Ljung-Box statistic provides a more accurate account of the structural damage by evaluating possible change in the entire ACF of residuals and Cosh spectral distance is less sensitive to changes in excitation sources as its value is largely determined by system poles, a property shared by most spectrum-based features. Subsequent applications to vibration data from simulation and lab experiments shows that the Ljung-Box statistic is indeed a more sensitive feature than residual variance in most cases, while Cosh spectral distance tends to be more stable than Mahalanobis distance of coefficients.

In all the applications presented, the theoretical threshold of Ljung-Box test is conservative (i.e. generates a large number of false positives). The available control chart method also suffers from similar threshold construction inaccuracies. This problem arises from the fact that the structural response is not precisely an AR process, and the residuals

65

obtained from the estimated model are not exactly white noise as assumed in the formulation of the Ljung-Box test. This discrepancy between the theoretical results and those from real data is inevitable because of statistical modeling errors. The data- driven resampling method proposed for threshold construction for Mahalanobis distance and Cosh spectral distance measure yields a better performance. Similar procedures may also be attempted for the residual based features in future research.

66

Table 4.1   Formulas for upper/lower bound calculation of the two control charts
(Fugate et al., 2001).

	Upper bound	Lower bound	Center line
$\bar{x}$ chart	$z_{\alpha/2}s_p / \sqrt{n}$	$-z_{\alpha/2}s_p / \sqrt{n}$	0
S chart	$\bar{S}\sqrt{\chi^2_{1-\alpha/2,n-1} / (n-1)}$	$\bar{S}\sqrt{\chi^2_{\alpha/2,n-1} / (n-1)}$	s_p

** s_p is the square root of pooled variance of subgroups in the baseline residual set, and z_α represents the α

quantile of the standard normal distribution.

** $\chi^2_{p,n}$ denotes the pth quantile of a Chi-square random variable with n degrees of freedom.

Table 4.2   Damage Progression Summary for Each Bent (Johnson et al., 2008)

		Observed damage	
Test	Bent 1	Bent 2	Bent 3
12	—	—	—
13	CRACK (0.08)	—	—
14	CRACK (0.08)	CRACK (0.08)	CRACK (0.08)
15	CRACK (0.25), FL	CRACK (0.08)	CRACK (0.25),SPAL (100)
16	CRACK (0.50),SPAL (125)	CRACK (0.17), FL	CRACK (0.33),SPAL (100), TranEXP
17	CRACK (0.50),SPAL (150), TranEXP	CRACK (0.25), FL	CRACK (0.50),SPAL (100), TranEXP
18	CRACK (0.50),SPAL (150), TranEXP	CRACK (0.50),SPAL (100)	CRACK (2.00),SPAL (140), TranEXP, LongEXP, InBUCK
19	CRACK (0.75),SPAL (150), TranEXP	CRACK (2.00),SPAL (115)	CRACK (2.00),SPAL (150), TranEXP, LongEXP,
			BUCK, TranFRAC
20	CRACK (0.75),SPAL (150),	CRACK (2.00),SPAL (125)	CRACK (2.00),SPAL (150), TranEXP, LongEXP,
	TranEXP, LongEXP		BUCK, TranFRAC, LongFRAC
21	CRACK (0.75),SPAL (150),	CRACK (2.00),SPAL (125)	CRACK (2.00),SPAL (150), TranEXP, LongEXP,
	TranEXP, LongEXP		BUCK, TranFRAC, LongFRAC, CORE
22	CRACK (0.75),SPAL (150),	CRACK (2.00),SPAL (200),	CRACK (2.00),SPAL (150), TranEXP, LongEXP,
	TranEXP, LongEXP, InBUCK	TranEXP, BUCK	BUCK, TranFRAC, LongFRAC, CORE

Notes: BUCK—buckling of longitudinal reinforcement, CORE—complete core degradation, CRACK—crack width in mm, InBUCK—incipient buckling,
LongEXP—the exposing of longitudinal reinforcement, LongFRAC—fracture of the longitudinal reinforcement, SPAL—spall height in mm,
TranEXP—the exposing of transverse reinforcement, TranFRAC—fracture of the transverse reinforcement.

67

Table 4.3 Comparison of the performances of Mahalanobis distance and Cosh distance feature; misclassified cases are marked in bold

		outlier percentage			inlier percentage			
		dataset 1	dataset 2		dataset 3	dataset 4		
Figure 6	Mahalanobis	0.00%	**9.26%**		27.78%	29.63%		
	Cosh	3.70%	**7.41%**		27.78%	46.30%		
		dataset 1	dataset 2		dataset 3	dataset 4		
Figure 8	Mahalanobis	0.00%	0.00%		0.00%	0.00%		
	Cosh	0.00%	2.44%		0.00%	0.00%		
		WN0709 B	WN0709 A	WN1112 A	WN141 5	WN171 8	WN181 9	WN192 0
Figure 11	Mahalanobis	0.00%	**38.71%**	37.63%	0.00%	0.00%	0.00%	0.00%
	Cosh	2.15%	**12.90%**	3.23%	22.58%	0.00%	0.00%	0.00%
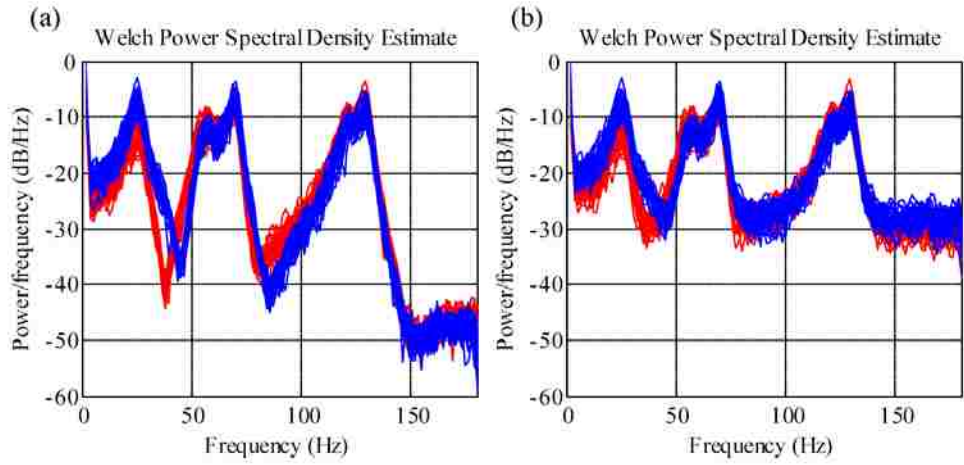
Figure 4.1   Sample spectrum plots from 50 simulations of two ARMA processes: a) constructed from noise-free samples; b) constructed from samples with 6.5% noise added.
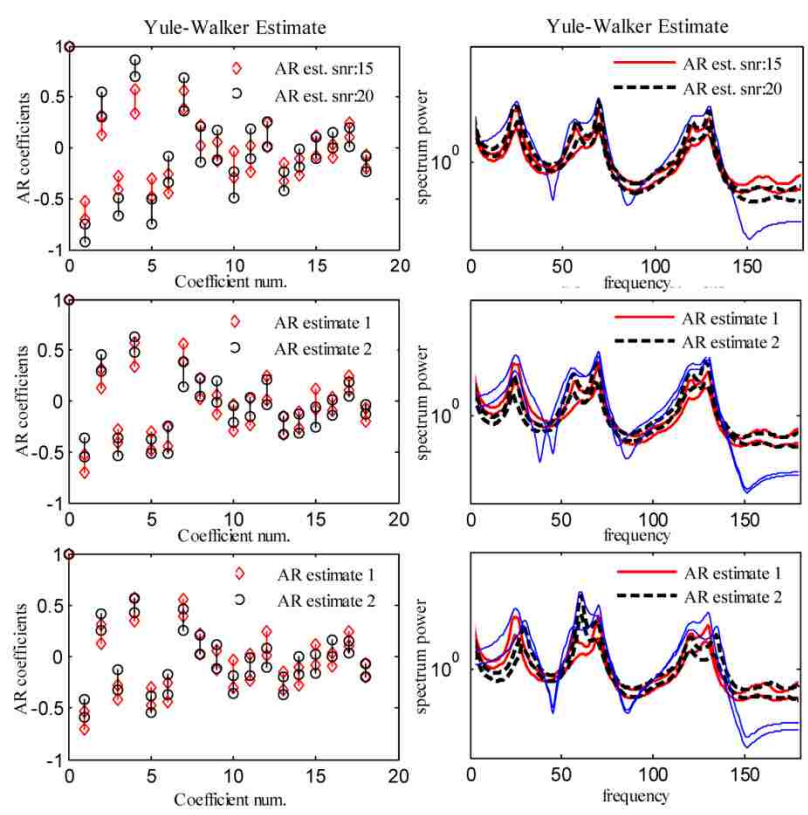
Figure 4.2   The estimation interval of AR coefficient and envelope of spectrum estimates over 50 simulations. 'snr' is the abbreviation for signal-to-noise ratio. In all the spectrum plots, the thin blue line(s) represents the spectrum of underlying model(s).
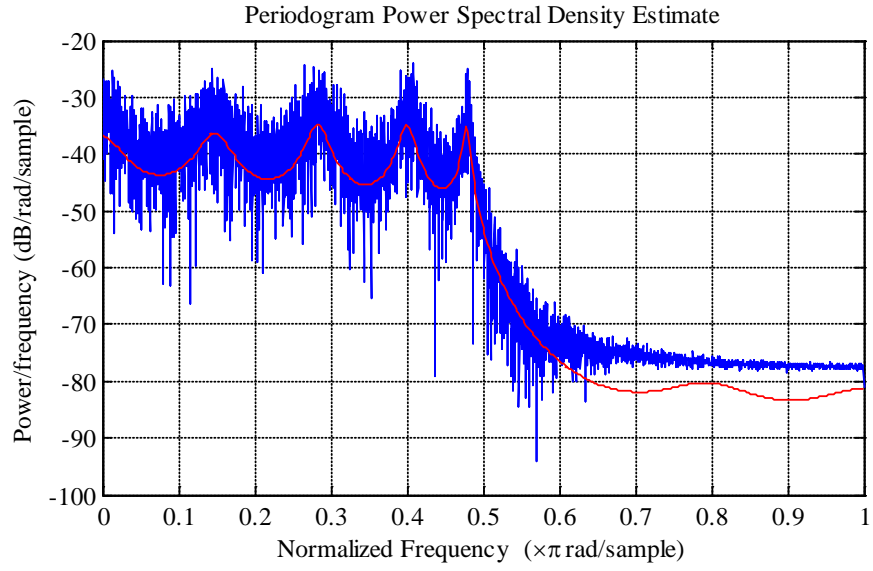
Figure 4.3   Comparison between an AR signal power spectrum density and the estimated AR model spectrum (the smooth red line)

70
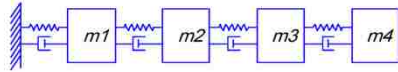
Figure 4.4   The simulated 4 DOF mass-spring-damper system
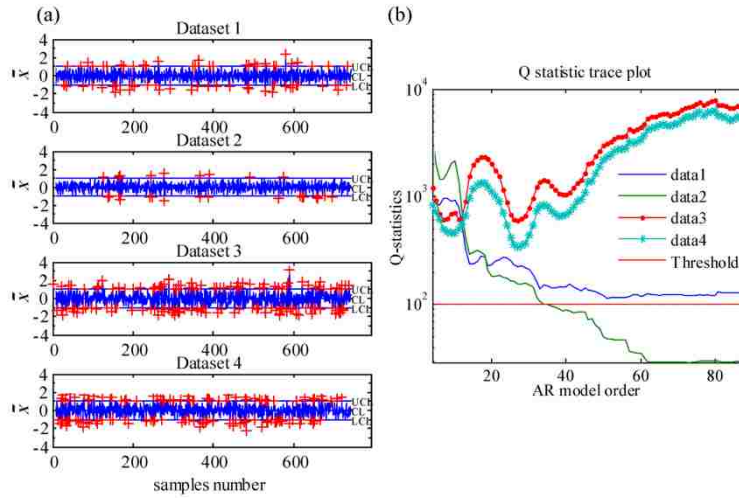
Figure 4.5   Damage classification results in the numerical case, by (a)
control chart and (b) Ljung-Box test statistic measure; all data
are acquired from node 3.
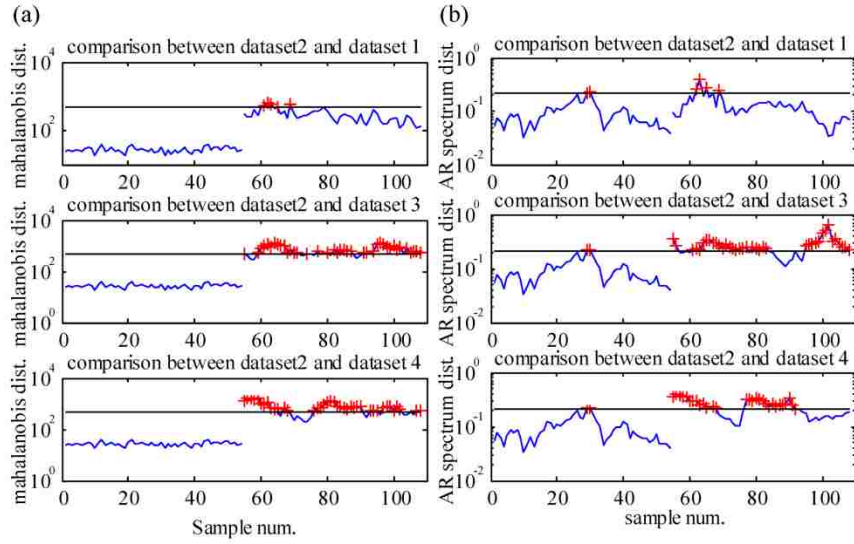
Figure 4.6   Damage classification results in the numerical case, by (a) Mahalanobis distance and (b) Cosh spectral distance measure.
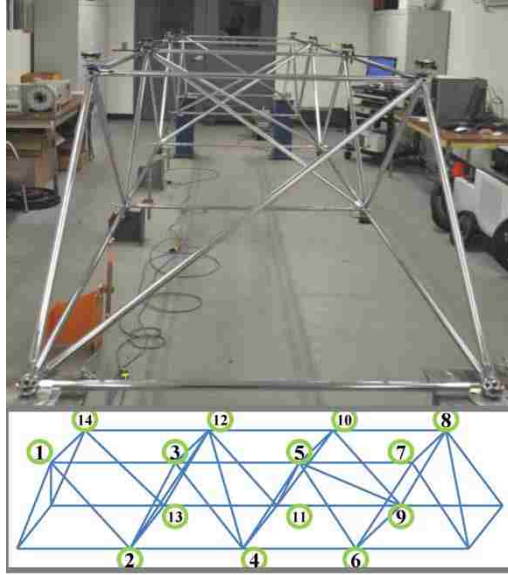
Figure 4.7   The space truss model with its sensor numbering scheme
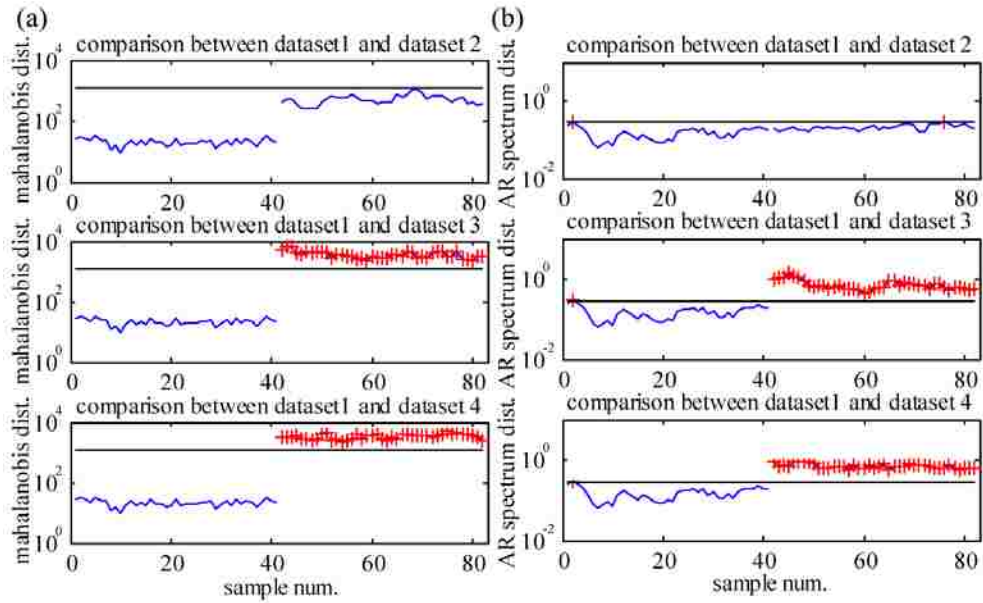
Figure 4.8   Damage classification results for the space truss by (a)
                    Mahalanobis distance and (b) Cosh spectral distance measure;
                    all data are acquired from truss node 4.
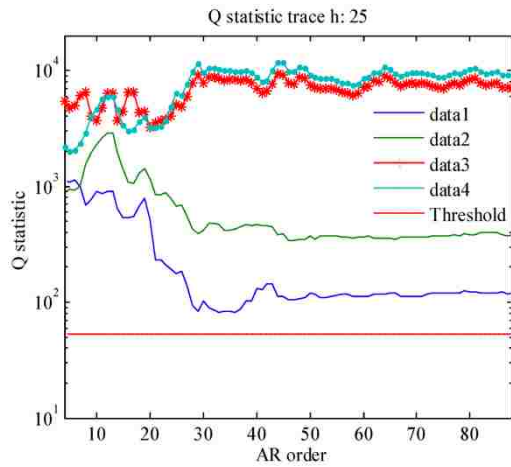
Figure 4.9   Damage classification results for the space truss using Ljung-
                    Box test statistic measure; All data are acquired from truss
                    node 4.

74
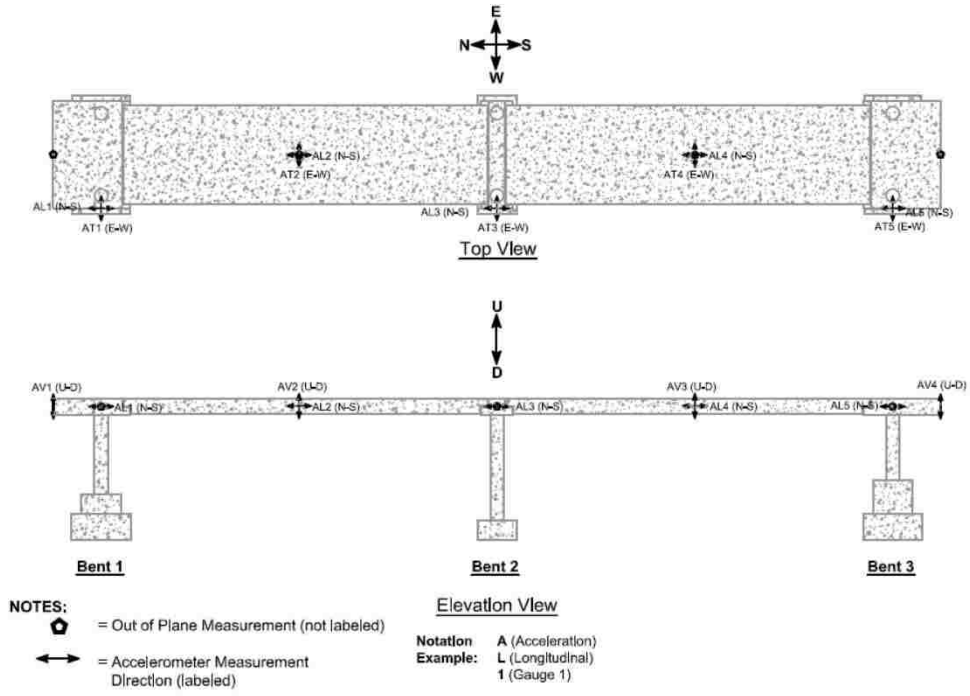
Figure 4.10   Implementation of accelerometers on the bridge slab model
                     (Johnson et al., 2008)
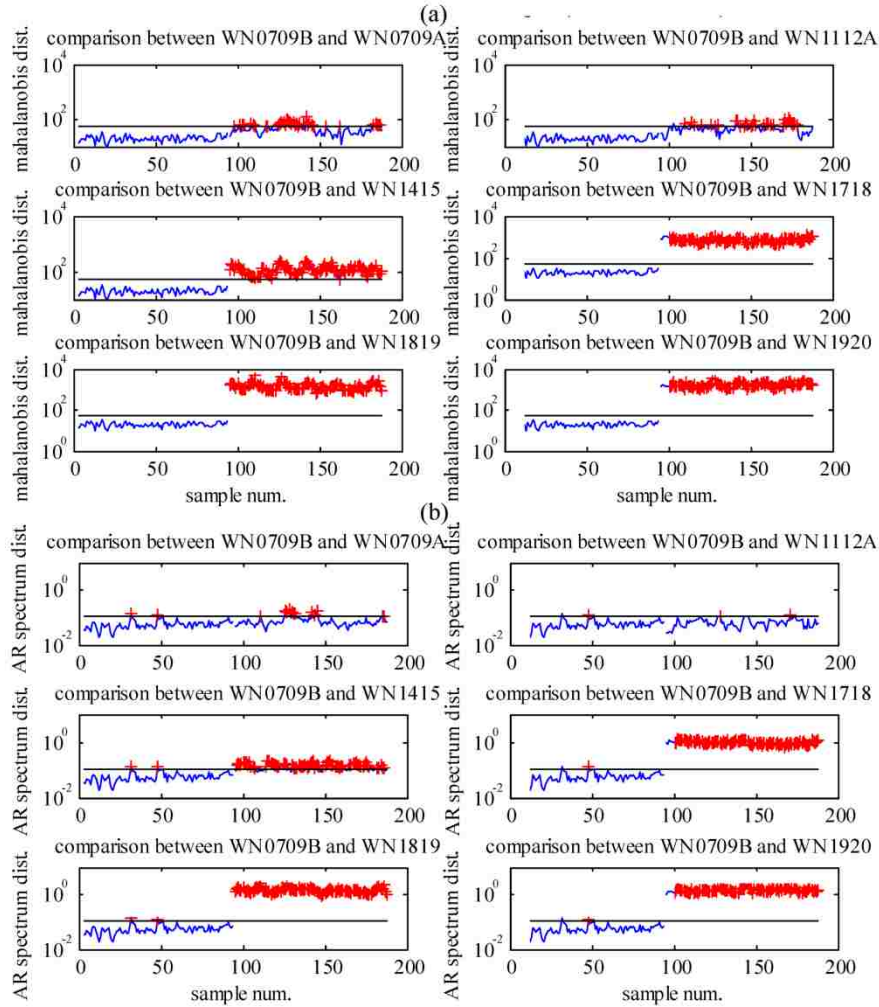
Figure 4.11   Damage classification results for the bridge slab model by (a) Mahalanobis distance and (b) Cosh spectral distance measure; all data are acquired from node 3.
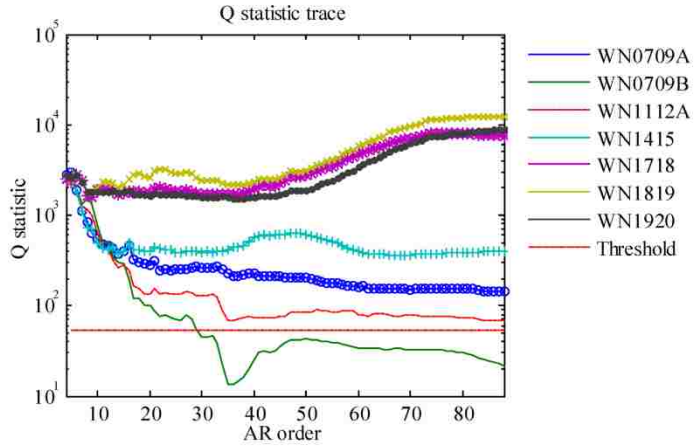
Figure 4.12   Damage classification results for the bridge slab model using Ljung-Box test statistic measure ; the maximum lag number for Q-statistic evaluation is 25.
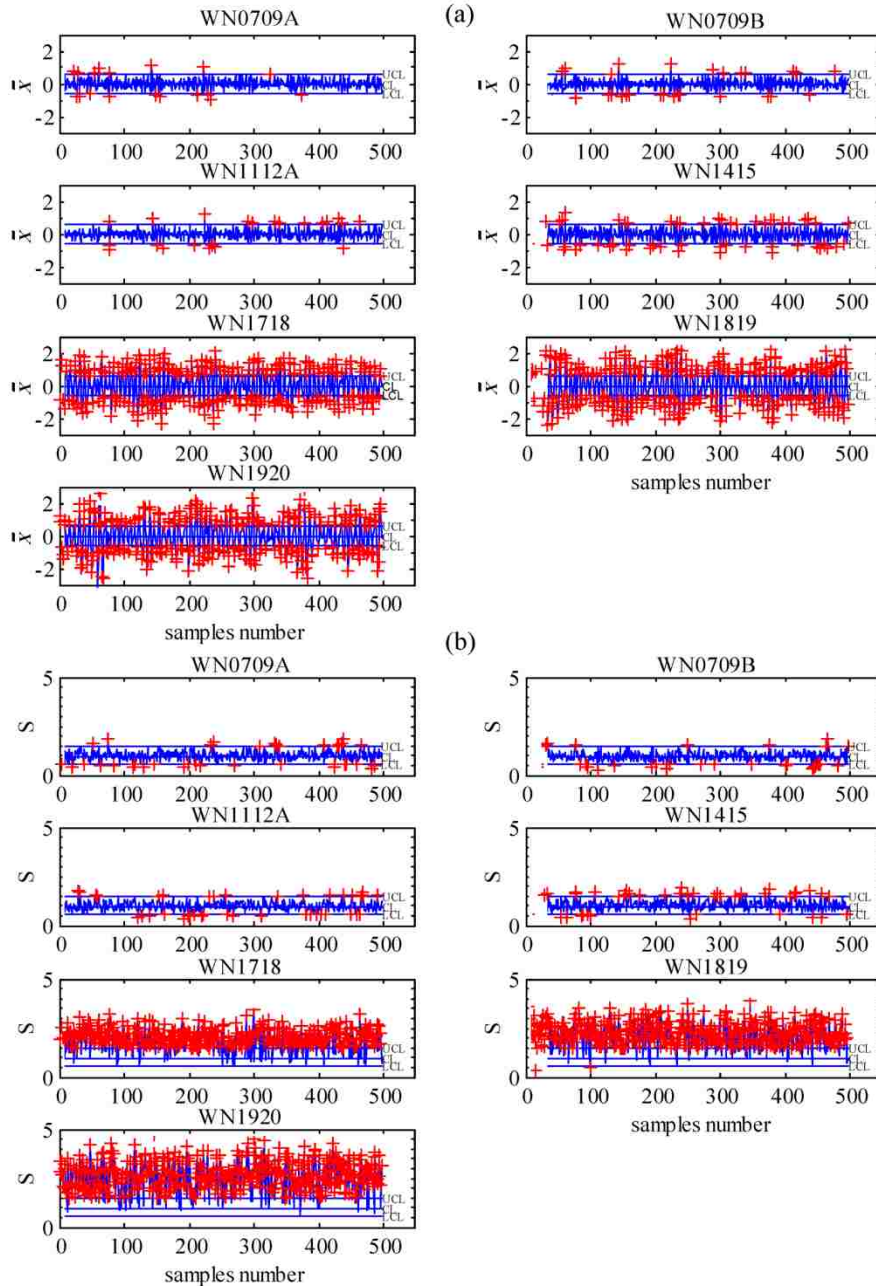
Figure 4.13   Damage classification results for the bridge slab model, by (a) control chart and (b) S control chart measure; data set WN0709B is employed as baseline here. all data are acquired from node 3.

Chapter 5   Cross comparison of AR features with other damage detection methods

5.1 PRELUDE

The aging and deterioration of civil structures are inevitable because of the natural and man-made hazards, and various damage forms (corrosion, fatigue, delamination etc.) has been found and defined for existing structures. Depending on the structural material, geometry, and operational condition, different structures will have different critical conditions and therefore different failure modes under excessive load, like the I-35W bridge in Minnesota and the Tacoma Narrows Bridge in Washington. As till now no theoretical/analytical methods can exactly model real-world structures and their interaction with the ambient environment, implementations of damage features on various types of real structures are important for their performance comparison. Cross-comparison between the performances of different features is an important way to help select the most appropriate feature for a particular application.

5.2 MOTIVATION AND ORGANIZATION

In the previous chapters several AR based damage detection techniques, either pre-existing or original, are presented and cross-compared. Here to better evaluate the potential of the family of AR features for damage identification, Mahalanobis distance of AR coefficients and Ljung-Box statistic of AR residuals are applied to identify damage in a scaled two-bay steel girder. The Influence Coefficients Method proposed by Labuz et al. (2010, 2011), which is a bi-channel time domain regression technique, is also applied to the same specimen. The threshold construction techniques for AR features are same as

79

adopted in Chapter 4, while change point analysis (CPA) is used for the influence coefficients.

The organization of the remaining content of this chapter is as follows:

- Section 5.3 reviews the influence coefficient based damage detection features.

- Section 5.4 reviews the damage features from Mahalanobis distance of AR coefficients and Ljung-Box statistic of AR residuals.

- Section 5.5 discusses the threshold construction process for the features.

- Section 5.6 contains the application results of the included damage detection methods.

- Section 5.7 presents the comments on the advantages of different damage detection methods used here.

5.3 STATISTICAL METHOD 1: LINEAR REGRESSION BETWEEN RESPONSES FROM TWO SENSOR NODES

If a linear structure is under static/quasi-static loading, then the structural response u at any two locations should be linearly correlated:

$$u_j\left(t_k\right) = \alpha_{j,i} \cdot u_i\left(t_k\right) + \epsilon_{ij}\left(t_k\right) \tag{5.1}$$

Here i and j indicate the response location, and k is a time label. The correlation coefficient is determined by both the force distribution and structural stiffness properties.

In practice, most structures are subjected to dynamic loads. However, if only a small part of the structure (with large stiffness and insignificant mass) is monitored, then it can be assumed that the local behavior could be captured by a static model.

80

This pair-wise regression method has been applied to detect damage in a beam column specimen and a simulated model of the steel frame here (Labuz et al., 2010, 2011). The feature extraction methodology can be summarized into the following steps; 1) for each pair of u_i and u_j, the correlation coefficients $\alpha_{i,j}$ and $\alpha_{j,i}$ and the corresponding residuals are evaluated using the least squares method (Figure 5.1); 2) to check the stability of estimation, two indices are calculated: accuracy factor EA $= \alpha_{i,j} \cdot \alpha_{j,i}$ and normalized estimation error $\gamma_{ij} = \sigma_{\alpha_{ij}} / \alpha_{ij}$; 3) correlation coefficients from those node pairs with EA close to 1 and γ_{ij} close to zero are selected as damage indicators.

This approach is straightforward in principle and efficient for computation. Also, the change in the values of regression coefficients can reflect to some extent the location of damage. However, when the dynamic response content becomes prominent (i.e. regression is performed for two far-apart nodes), the algorithm performance will degrade.

5.4 STATISTICAL METHOD 2: AUTOREGRESSIVE MODELING OF RESPONSE AT ONE LOCATION

Univariate autoregressive model (Brockwell and Davis, 2009) is among the most widely applied time series analysis tools. Its definition is presented as Eq. (2.1), which basically expresses the value of the signal at a certain time point as a linear combination of its previous values and a random error term. AR coefficients can be estimated from collected signals using one of the standard algorithms such like Yule-Walker and Burg (Porat, 1994), and model residuals/errors $e(t)$ can then be obtained as the difference between model prediction and the real signal. Autoregressive damage detection

algorithms can be based on either model coefficients or residual characteristics. In the remainder of this section, one example from either category will be presented.

5.4.1 The Mahalanobis distance of AR coefficients

This feature has been introduced in Section 3.3.1. Mahalanobis distance is a metric that represents the coefficients' deviation in the probability space of normal distribution, which is the asymptotic distribution of the estimated AR coefficient vector as signal length increases. When the system is damaged, the values of Mahalanobis distance feature will increase.

5.4.2 Ljung-Box statistic trace of AR model residuals

This feature is presented in Section 4.4.1. If the structural condition has undergone changes, then the baseline model will no longer provide a good fit to the new signals collected. As the result, the residual series, instead of resembling a white noise, shall carry some identifiable patterns over time.

The Ljung-Box statistic trace, as noted in previous applications, is a plot of the Ljung-Box statistic against the baseline AR model order (Figure 5.2). For undamaged state signal, a downward trend is expected in the plot. Thus if the trace is oscillating, stopping decreasing at short or going upward as the model order increase, the system is recognized as damaged.

5.5 THRESHOLD CONSTRUCTION METHODS

After feature selection, appropriate damage threshold construction schemes are needed to reach a decision on the current state of the structure being monitored. If the feature distribution can be assumed, then statistical hypothesis testing could be used for damage identification. However, in most cases the feature distribution is unknown and

cannot be approximated by an analytical function. As such, the damage threshold will be determined based on the data solely using one of the resampling techniques.

5.5.1 Change point analysis using cumulative sum

Change point analysis is used to find the point in a data sequence where the data characteristics change and the confidence level associated with this change point. It is an effective way of identifying thresholds and detecting subtle variations. A variety of approaches is available for performing change point analysis, such as cumulative sum, deviance reduction, and least squares. Here, the *cumulative sum* method (Taylor, 2000) will be adopted for damage threshold construction for the **influence coefficients features**.

The cumulative sum $\{S_i\}$ for a data sequence $\{x_i\}$ is calculated as below:

1) Subtract every value in this sequence by its mean $\overline{x}$.

2) Compute the cumulative sum at step i by adding up the values occurred before and at i. (i.e. $S_i = \sum_{j \leq i}(x_j - \overline{x})$)

Experienced individuals can identify the change point directly as the place where the trend of the cumulative sum plot changes. (Figure 5.3) But as our aim is automatic damage threshold construction, a bootstrap analysis is performed; the original signal sequence is randomly permuted for N times and each time the maximum absolute value of the cumulative sum of the new sequence is recorded. The threshold for the maximum absolute cumulative sum of a data sequence of constant properties is then set at the point

83

above which $N\alpha$ values occurred. The significance level α is set to 5% in all the applications in this chapter.

5.5.2 Cross validation

The theoretical distribution of **Mahalanobis distance feature** is hard to derive and the feature itself often exhibits large fluctuations even within the healthy state. Thus, a cross-validation approach introduced in Section 3.4.1 is used for its damage threshold construction. This method is shown to demonstrate more reliable performance to other threshold evaluation techniques such as hypothesis testing based on Gaussian assumption of model coefficients in Chapter 3.

5.6 EXPERIMENTAL RESULTS

The aforementioned influence coefficients and AR modeling method, together with their respective threshold evaluation approaches, are applied to detect damage in a scaled two-bay steel frame constructed from steel tubes. (Figure 5.4) The structure, instrumented with 21 accelerometers, is excited from the left beam-column joint by an electro-dynamic shaker (Figure 5.5). To simulate a structural damage, the potion between sensor S16 and S18 and that between S19 and S21 are switched out by 20% less stiff tubes. For each structural scenario, five random vibration tests are performed and the acceleration responses collected are used as input to the algorithms.

The first algorithm produces for each dataset $21 \times 20 = 420$ influence coefficients, each from a particular node combination. To facilitate the subsequent decision making process, only those coefficients with average evaluation accuracy factor $EA > 0.9$ and normalized estimation error $\gamma < 0.003$ are examined. Out of the 24 coefficients selected, the cumulative-sum-based change point analysis successfully identified damage for 21 of

84

them over the 10 tests. It is observed, however, that the 3 coefficients that failed to report damage are all from regression between distant nodes, which are by nature not quite reliable.

Figure 5.6 displays the estimation results from 4 influence coefficients, all indicating damage except for the one showed in the lower right corner. One interesting fact noticed is that though the nodes 5 and 6 are nowhere near damage, their corresponding influence coefficient value still increased abruptly as a result of structural change. This is probably because these correlation coefficients reflect the ratio of structural vibration 'shape function' values evaluated at two different locations, and those combinations with most affected coefficients are determined by not only the damage location but also the structural layout. Yet still, generally there will be a higher chance of observing changes near the damage for a properly restrained regular structure. Also if an analytical model of the structure is available, the influence coefficients can be used as input to a model updating scheme to find out the damage location.

The AR modeling based algorithms are also proved effective for damage detection in this case. While the influence coefficients capture the static behavior of the system, time series modeling deals with the structural dynamic effects. For has the system been all static, the response will only be a scaled white noise series with no distinguishable patterns for modeling. Figure 5.7 shows the results from AR coefficients based Mahalanobis distance method using data from sensor 2 and 17. To save space here, only two datasets per structural state are used. In both graphs dataset 3 is used as the baseline and 4 the false positive testing. Damage is clearly indicated in both plots, even though

85

one node is much farther from the damage location. It may thus be concluded that here the local damage does affect the global dynamic properties in a certain way.

Figure 5.8 is the Ljung-Box/Q statistic traces for node 2 and 17. The two damaged state traces float high above those undamaged ones as expected. The threshold from hypothesis testing is conservative for data from both sensors, suggesting that the theoretical assumptions do not quite represent reality here. Also, damaged state Q statistics from measurements at node 17 is much larger than that from node 2. After examining Q traces from all 21 nodes, it is found that the traces from nodes on the right beam show greatest change, indicating the damage location.

5.7 CONCLUSION

This chapter focuses on validating the performance of two types of statistical damage detection algorithms through their application to detect damage in an artificially excited two-bay steel frame using acceleration measurements collected. These algorithms are advantageous in that the decision on the structural state is made using well-established statistical concepts instead of human expertise, thereby eliminating possible individual biases. Besides, since they are mostly data driven, very few assumptions are needed regarding the physical structure.

The pair-wise regression and AR modeling method adopted here are complementary in the sense that while the former works on getting a static relation between signals from two different locations, the latter concerns itself with analyzing the dynamic pattern of the signal from a single sensor node. The damage features presented are influence coefficients from the 1st method, and Mahalanobis distance of model coefficients and Ljung-Box statistic of model residuals from the 2nd method. Their corresponding damage

86

threshold evaluation techniques are cumulative sum analysis, cross-one-out validation and hypothesis testing. It can be seen here that different types of features may need different ways to establish the damage threshold.

Judging from the results obtained in the previous section, both algorithms have successfully detected the existence of artificially introduced damage. It shall be noted, however, that the change in the influence coefficient values are not the ideal damage location indicator hinted in some earlier works(Labuz et al., 2010, 2011); they only suggest a possibility which need to be verified through other means of observation. The Mahalanobis distance is no fit for damage location detection in this case: at least as much change is observed from the features at node distant to damage as that from a nearby node. The Ljung-Box static from AR residuals seems to do better in this aspect, though no clear reasons can be provided for now. Also noticed is that the data-driven threshold evaluation methods based on resampling yield a superior performance to hypothesis testing, as they suffer less from statistical modeling errors.

To summarize, the statistical algorithms have been altogether effective for identifying damage existence in the lab specimen and two of them have been able to suggest the possible damage locations. Each feature extraction scheme and the associated threshold construction technique operate as a whole to bring forward the final result. To further investigate the capabilities of the algorithms, however, more experiments on various types of structures are needed.
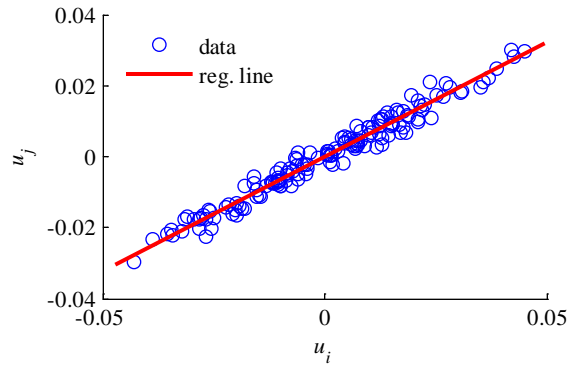
Figure 5.1   Regression for influence coefficients

88
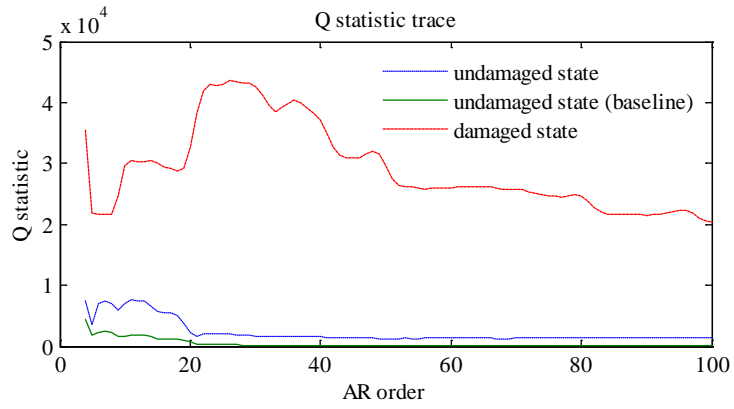
Figure 5.2   Ljung-Box statistic for structural damage identification
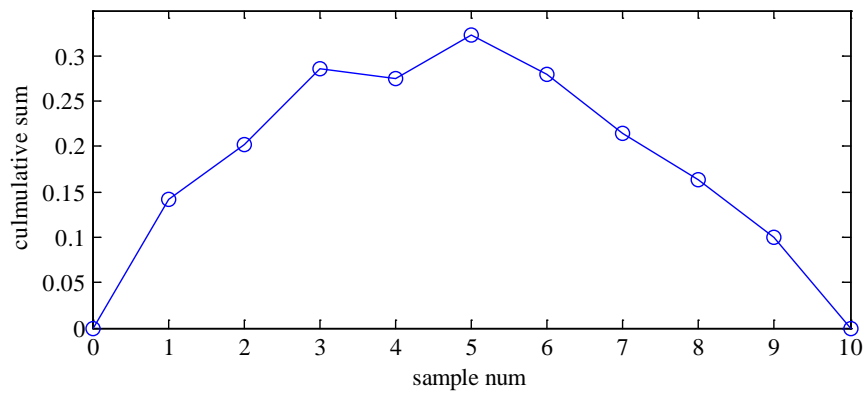
Figure 5.3   The cumulative sum plot from the implementation in Section 5.6.

Figure 5.4   The two-bay steel frame

Figure 5.5   A schematic plot of the girder mounted with accelerometers

90
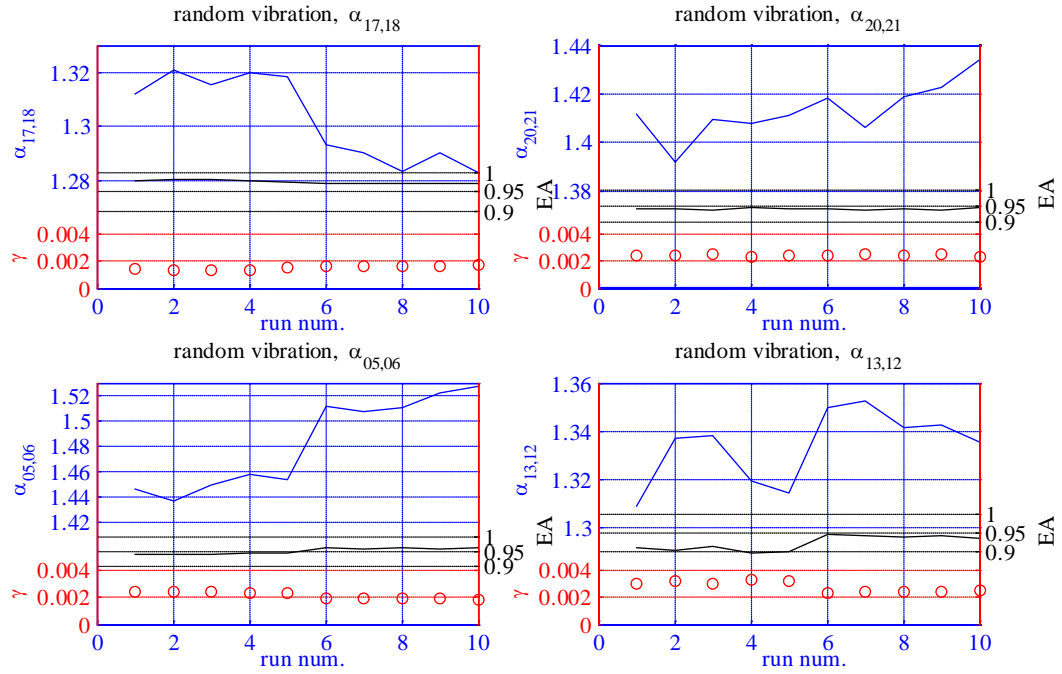
Figure 5.6   Influence coefficients from different node pairs

91
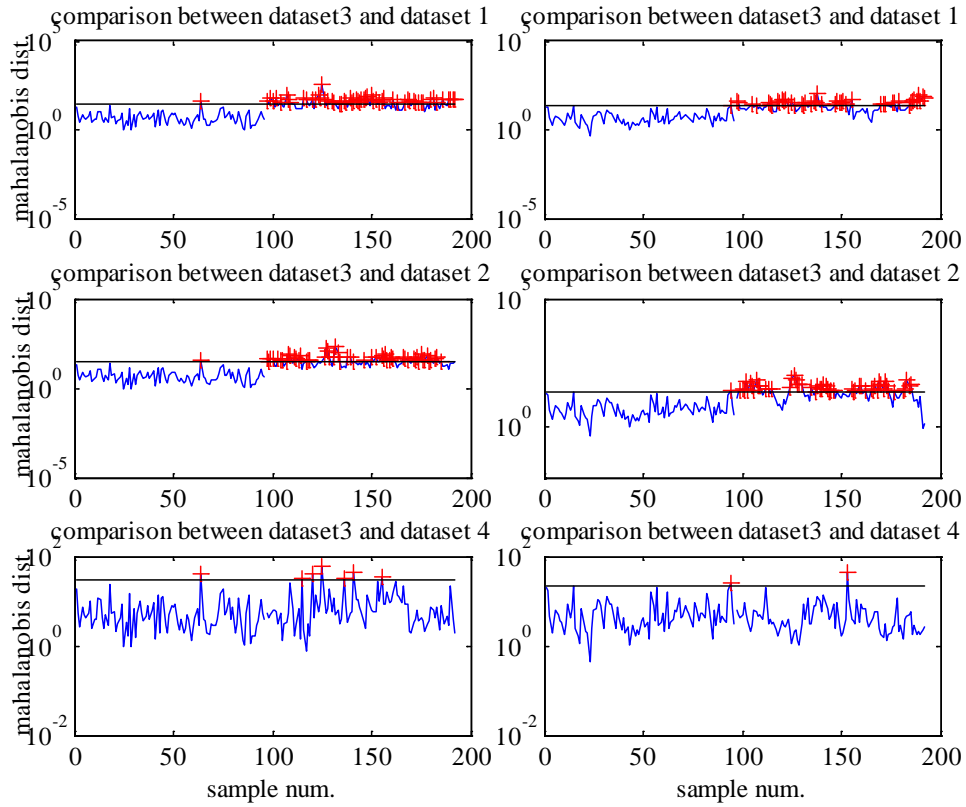
Figure 5.7   Mahalanobis distance from signals collected at node 2 (left)

and node 17(right)
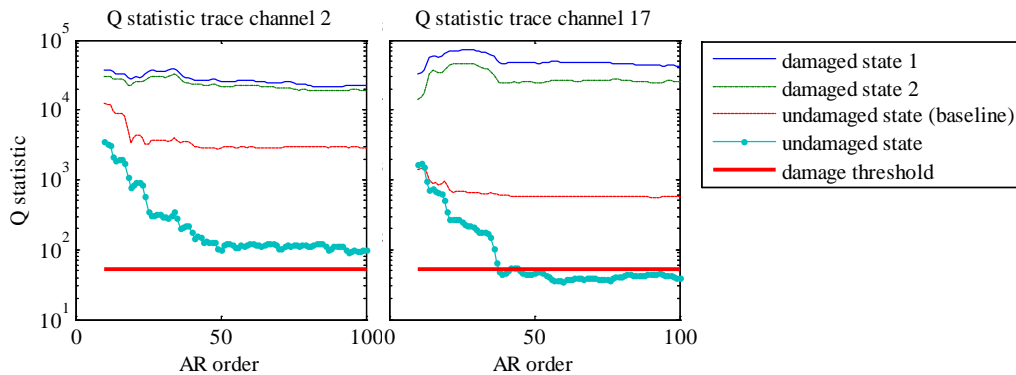
Figure 5.8   Ljung Box trace for damage detection

92

Chapter 6   Damage and noise sensitivity investigation of AR coefficient based features

6.1 PRELUDE

Damage detection is a very crucial part in the regular assessment and maintenance routine for civil infrastructure. Data-driven structural health monitoring (SHM) has been recently studied as a more economical alternative than traditional visual inspection method because of the lowering prices of sensing systems, and is expected to produces more accurate and reliable decisions that are free of human judgment bias or expertise. Moreover, SHM has the capability to reveal problems undetectable via 'naked-eye' inspection such as internal fracture and delamination.

Reliable damage detection requires reliable damage features. For vibration-based damage detection, features used include modal properties, scalar TSA features etc. Compared with modal properties, scalar TSA features are reported to be less complicated to compute and more sensitive to local damage in their respective applications. (Atamturktur et al., 2011; Zhang, 2007) provide comparisons on the effect of local damage on the modal frequencies/shapes and autoregressive features, and it is observed in both case studies that the latter shows a more noticeable change than the former. Also, AR-ARX method has demonstrated success in damage localization in (Zhang, 2007), and ARMA method has been used to indicate damage location and extent in (Nair et al., 2006). The AR methods, however, is not quite sensitive to damage location (Gul and Catbas, 2009). It is noted that univariate time series analysis methods are output-only, and damage indices of this type are often functions of structural signal autocovariance

93

functions, which are in turn determined by the structural stiffness properties, the structural geometry and excitation patterns. When the location of damage does not correspond well with where the largest damage-induced change in signal autoccovariancce functions occurs, damage localization based on time series analysis is likely to be very difficult. Still, these damage features have advantages such as being simple in concept, convenient for statistical processing as they can be generated in large quantities, and suitable for decentralized structural monitoring applications.

6.2 MOTIVATION AND ORGANIZATION

While it is important to propose and test new features to improve the state-of-the-art of structural damage detection, examination of the effect of structural change and environmental and operational factors on existing features in an analytically rigorous manner is also crucial for optimal feature selection for different practices. Previously, research has been conducted on evaluating the adverse effect of measurement noise on the accuracy of estimated modal parameters (Dorvash and Pakzad, 2012). In this chapter, the sensitivity of two damage features based on AR modeling due to damage level and measurement noise is studied and an analysis methodology is proposed. The two methods are the Mahalanobis distance (Mahalanobis, 1936) of AR coefficients and the Cosh distance (Gray Jr and Markel, 1976) of AR model spectra between the baseline state and the current state.

Sensitivity analysis reveals that ambient response based AR features are affected by measurement noise. To increase the noise robustness of feature values, AR modeling is applied to signal autocovariance function (ACovF) instead of the ambient signals itself. Theoretical justification is presented after the sensitivity derivation section.

94

The validity of sensitivity analysis methodology for Mahalanobis distance and Cosh distance features from ambient signals is supported by simulation results from a 10 DOF bridge model. Performances of the damage features from ambient acceleration series and those from ACovF of the series are compared through an application to vertical member of a steel truss bridge in western Pennsylvania.

The remaining content of this chapter is organized as follows:

- Section 6.3 gives an explanation of the theoretical relation between the structural acceleration response and the family of AR modeling, together with an examination of the properties of the scalar Yule-Walker AR coefficient estimators.

- Section 6.4 contains stepwise derivations regarding the analysis for the sensitivity with respect to damage level and measurement noise for both features.

- Section 6.5 introduces a way to reduce noise sensitivity by applying AR modeling to signal ACovF.

- Section 6.6 applies the sensitivity analysis procedure to a 10-DOF simulated model and the results are compared with those from direct simulation and theoretical calculation.

- Section 6.7 presents the comparison results between the damage detection performances of ambient signal based AR modeling and signal ACovF based AR modeling in a steel truss bridge.

- Section 6.8 is the conclusion on the feature performances/sensitivities.

6.3 AUTOREGRESSIVE MODELING FOR STRUCTURAL VIBRATION MEASUREMENTS

Sensor measurements do not reveal information concerning the structural state being monitored until they go through data-processing algorithms. Autoregressive (AR) modeling is one of the most effective time series analysis techniques, and has found applications in vibration monitoring of various types of structures (Nair et al., 2006; Worden, Manson, and Fieller, 2000; Zhang, 2007) that are instrumented with accelerometers. Here, different aspects of AR modeling are investigated in two subsections. Subsection 6.3.1 demonstrates the validity of AR modeling for structural vibration signals and presents a proof on a multi-input-multi-output (MIMO) ARX model between the excitation and acceleration response of a MDOF system. Since univariate AR estimators tend to behave differently from their multivariate counterparts because of the spatial correlation among structural responses, Subsection 6.3.2 investigates the characteristics of single-input-single-output (SISO) AR coefficient estimators from acceleration measurements to provide insight into the behavior of autoregressive features thus extracted.

6.3.1 Civil structural systems and AR/ARX model

An ARX model is a numerical tool that has been proved quite useful in describing causal systems subjected to series of external disturbances (Brockwell and Davis, 2002). In an effort to derive an explicit ARX model for a N degrees-of-freedom system between its excitation source and acceleration measurements, the system impulse response should be obtained, discretized and transformed. To start, calculate the acceleration impulse response of the i th mode by twice differentiating the Duhamel's integral of the displacement impulse response $h_i(t)$ (Chopra, 2006):

$$\ddot{h}_i(t) = \frac{\mathrm{d}^2\{\int_0^t h_i(t-\tau)\delta(\tau)d\tau\}}{\mathrm{d}t^2} = h_i(0)\delta'(t) + h_i'(t-\tau)\delta(\tau)|_{\tau=t} + \int_0^t \frac{\mathrm{d}^2}{\mathrm{d}t^2}\{h_i(t-\tau)\}\delta(\tau)d\tau,$$

(6.1)

$\delta(\tau)$ here stands for the dirac delta function. The acceleration impulse response may be written as the sum of the second-order derivative of the displacement impulse response and an impulse term:

$$\ddot{h}_i(t) = \frac{\mathrm{d}^2[h_i(t)]}{\mathrm{d}t^2} + \frac{1}{m_i}\delta(t)$$

$$= \frac{-\omega_{\mathrm{D}i}^2}{m_i\omega_{\mathrm{D}i}}\mathrm{e}^{-\zeta_i\omega_{ni}t}\sin\omega_{\mathrm{D}i}t + \frac{-2\zeta_i\omega_{\mathrm{D}i}\omega_{ni}}{m_i\omega_{\mathrm{D}i}}\mathrm{e}^{-\zeta_i\omega_{ni}t}\cos\omega_{\mathrm{D}i}t + \frac{\zeta_i^2\omega_{ni}^2}{m_i\omega_{\mathrm{D}i}}\mathrm{e}^{-\zeta_i\omega_{ni}t}\sin\omega_{\mathrm{D}i}t + \frac{1}{m_i}\delta(t).$$

(6.2)

where m_i, $\omega_{ni}, \omega_{\mathrm{D}i}$, and ζ_i are the modal mass, natural frequency, damped frequency and damping ratio of the i th mode, respectively. The discretized version of Eq. (6.2) is

$$a_i[n] = \frac{-\omega_{\mathrm{D}i}^2}{m_i\omega_{\mathrm{D}i}}\mathrm{e}^{-\zeta_i\omega_{ni}T_s n}\sin\omega_{\mathrm{D}i}T_s n + \frac{-2\zeta_i\omega_{\mathrm{D}i}\omega_{ni}}{m_i\omega_{\mathrm{D}i}}\mathrm{e}^{-\zeta_i\omega_{ni}T_s n}\cos\omega_{\mathrm{D}i}T_s n$$

$$+ \frac{\zeta_i^2\omega_{ni}^2}{m_i\omega_{\mathrm{D}i}}\mathrm{e}^{-\zeta_i\omega_{ni}T_s n}\sin\omega_{\mathrm{D}i}T_s n + \frac{1}{m_i T_s}\delta(n).$$

(6.3)

where n is the time label in the discrete domain and T_s is the sampling interval. Its corresponding z-transform can be obtained as:

$$\hat{a}(z) = \left(\frac{-\omega_{\mathrm{D}i}^2}{m_i\omega_{\mathrm{D}i}} + \frac{\zeta_i^2\omega_{ni}^2}{m_i\omega_{\mathrm{D}i}}\right)\frac{\mathrm{e}^{-\zeta_i\omega_{ni}T_s}z^{-1}\sin\omega_{\mathrm{D}i}T_s}{1 - 2\mathrm{e}^{-\zeta_i\omega_{ni}T_s}z^{-1}\cos\omega_{\mathrm{D}i}T_s + \mathrm{e}^{-2\zeta_i\omega_{ni}T_s}z^{-2}}$$

$$+ \frac{-2\zeta_i\omega_{\mathrm{D}i}\omega_{ni}}{m_i\omega_{\mathrm{D}i}}\frac{1 - \mathrm{e}^{-\zeta_i\omega_{ni}T_s}z^{-1}\cos\omega_{\mathrm{D}i}T_s}{1 - 2\mathrm{e}^{-\zeta_i\omega_{ni}T_s}z^{-1}\cos\omega_{\mathrm{D}i}T_s + \mathrm{e}^{-2\zeta_i\omega_{ni}T_s}z^{-2}} + \frac{1}{m_i T_s}.$$

(6.4)

97

Define the discretized modal input/output as $q_i[n]$ and $p_i[n]$, their relation can be expressed using an ARX model, by taking the inverse z-transform and rearranging Eq.(6.4):

$$q_i[n] - 2e^{-\zeta_i \omega_{ni} T_s} \cos \omega_{D_i} T_s q_i[n-1] + e^{-2\zeta_i \omega_{ni} T_s} q_i[n-2] = \left(\frac{1}{m_i T_s} - \frac{2\zeta_i \omega_{ni}}{m_i} \right) p_i[n]$$

$$+ e^{-\zeta_i \omega_{ni} T_s} \left[\frac{-2\cos \omega_{D_i} T_s}{m_i T_s} + \sin \omega_{Di} T_s \left(\frac{-\omega_{Di}}{m_i} + \frac{\zeta_i^2 \omega_{ni}^2}{m_i \omega_{Di}} \right) + \cos \omega_D T_s \frac{2\zeta_i \omega_{ni}}{m_i} \right] p_i[n-1]$$

$$+ \frac{e^{-2\zeta_i \omega_{ni} T_s}}{m_i T_s} p_i[n-2].$$

$$(6.5)$$

For notation simplicity the coefficient expressions will be omitted for now and Eq. (6.5) is denoted as:

$$A_i(B) q_i[n] = C_i(B) p_i[n], \qquad B\text{:the backshift operator}, \quad i.e. \ Bp[n] = p[n-1].$$

$$(6.6)$$

For the MDOF model discussed here, the matrix form of representation can be employed:

$$\mathbf{A}(B)\mathbf{q}[n] = \mathbf{C}(B)\mathbf{p}[n], \tag{6.7}$$

where $\mathbf{A}(B)$ and $\mathbf{C}(B)$ are diagonal matrices consisting of $A_i(B)$ and $C_i(B)$ terms, respectively. $\mathbf{q}[n]$ is the modal displacement vector and $\mathbf{p}[n]$ is the modal input vector. Their relationship with the nodal input vector $\mathbf{x}[n]$ and nodal displacement vector $\mathbf{y}[n]$ are as follows:

$$\mathbf{y}[n] = \mathbf{\Phi} \mathbf{q}[n], \ \mathbf{x}[n] = \mathbf{\Phi}^{T^{-1}} \mathbf{p}[n]. \tag{6.8}$$

98

$\boldsymbol{\Phi}$ here stands for the system eigenvector matrix. Therefore, the relation between the excitation and system acceleration response can be expressed as a multivariate ARX model:

$$\mathbf{A}'(B)\mathbf{y}[n] = \mathbf{C}'(B)\mathbf{x}[n],$$

$$\mathbf{A}'(B) = \boldsymbol{\Phi}\,\mathbf{A}(B)\,\boldsymbol{\Phi}^{-1}, \mathbf{C}'(B) = \boldsymbol{\Phi}\,\mathbf{C}(B)\,\boldsymbol{\Phi}^{T}. \tag{6.9}$$

Note that $\mathbf{A}'(0) = \boldsymbol{\Phi}\mathbf{A}(0)\boldsymbol{\Phi}^{-1} = \boldsymbol{\Phi}\boldsymbol{\Phi}^{-1} = \mathbf{I}$. For signals generated from the multivariate ARX system under random excitation, each scalar signal can be viewed as a sum of seemingly uncorrelated ARMA processes and modeled with a scalar ARMA process (Teräsvirta, 1977).

6.3.2 AR coefficient estimators for scalar acceleration signals

ARMA processes can be approximated with an AR process with a large model order (Porat, 1994). One main advantage of the latter method is its computational efficiency. The definition of a univariate AR model of order p is given in Eq. (2.1). Because of its concise form, the AR model has been widely adopted for time series analysis for different purposes. One of the frequently used AR coefficients estimators is Yule-Walker estimator (Porat, 1994), which is obtained from solving the following equation:

$$\begin{bmatrix} \hat{\varphi}_1 \\ \hat{\varphi}_2 \\ \hat{\varphi}_3 \\ \vdots \\ \hat{\varphi}_p \end{bmatrix} = \begin{bmatrix} R(0) & R(1) & R(2) & \cdots & R(p-1) \\ R(1) & R(0) & R(1) & \cdots & R(p-2) \\ R(2) & R(1) & R(0) & \cdots & R(p-3) \\ \vdots & \vdots & \vdots & \vdots & \ddots & \vdots \\ R(p-1) & R(p-2) & R(p-3) & \cdots & R(0) \end{bmatrix}^{-1} \begin{bmatrix} R(1) \\ R(2) \\ R(3) \\ \vdots \\ R(p) \end{bmatrix} = \Gamma^{-1}\boldsymbol{\gamma},$$

$$\tag{6.10}$$

where $R(\cdot)$ is the auto-covariance function (ACovF) of the time series and $\{\hat{\varphi}_j\}$ are the estimated AR coefficients.

When an AR model (which is an all-pole system) is constructed from the structural acceleration signal, spurious poles will be introduced because the model cannot properly parameterize possible zeroes in the underlying generating function, leading to a large AR order for an accurate model:

$$1-\beta z^{-1} \approx \frac{1-\beta z^{-1}}{1-\beta^{n+1}z^{-(n+1)}} = \frac{1}{1+\beta z^{-1}+\ldots+\beta^n z^{-n}}, \; (\left|\beta z^{-1}\right|<1)$$

$$1-\beta z^{-1} \approx \frac{-\beta z^{-1}\left(1-\beta^{-1}z\right)}{1-\beta^{-(n+1)}z^{n+1}} = \frac{-\beta^{n+1}z^{-(n+1)}}{1+\beta z^{-1}+\ldots+\beta^n z^{-n}}. \; (\left|\beta z^{-1}\right|>1) \qquad (6.11)$$

In either case the pole positions should be inside the unit circle to ensure a stable system. Poles thus generated tend to be uniformly distributed around the unit circle. Figure 6.1 shows the ACovF and the pole location plots in the z-plane of Yule-Walker estimators for structural displacement, velocity and acceleration signals. Compared with the poles of models based on the displacement and velocity, the poles of models based on the acceleration have a more balanced distribution inside the unit circle even at low AR orders. This is because the ACovF of acceleration measurements has a large impulse term at zero lag, which has a uniform frequency domain response and is a characteristic of white noise. Since AR model is a 'whitening' filter by definition (Brockwell and Davis, 2002), the poles from model estimated using such signal should have relatively evenly distributed poles around the origin to achieve a relatively 'flat' model spectrum. Also

100

note that as the model order increases, the pole positions move closer to the unit circle as the estimated system becomes less stable.

A brief explanation on this phenomenon is presented here: in the case of Yule-Walker estimation, the AR estimator of order $p+1$ is related to estimator of order p as:

$$\left[\hat{\varphi}_{1,p+1},\hat{\varphi}_{2,p+1},\ldots,\hat{\varphi}_{p+1,p+1}\right]=\left[\hat{\varphi}_{1,p},\hat{\varphi}_{2,p},\ldots,\hat{\varphi}_{p,p},0\right]-K_{p+1}\left[\hat{\varphi}_{p,p},\hat{\varphi}_{p,p},\ldots,\hat{\varphi}_{1,p},-1\right],$$

(6.12)

where $\hat{\varphi}_{i,p}$ denotes the i th estimated coefficient for an AR model of order p, and K_{p+1} is the $(p+1)$ th-order partial correlation coefficient (Porat, 1994) of the estimated signal. If the signal is strictly autoregressive up to lag p, then the expected value of K_{p+1} is zero. However, because the ambient structural vibration signals are ARMA processes, this condition generally can only be satisfied in the asymptotic sense. As such, the AR coefficient vector will vary as a whole as the model order increases, and so does the corresponding model spectra estimates:

$$\hat{S}_{AR}^{p}\left(\omega\right)=\frac{d_p}{\left|1-\sum_{k=1}^{p}\hat{\varphi}_{k,p}e^{-j\omega k}\right|^2}=\frac{d_p}{\left|\left(1-\alpha_{1,p}e^{-j\omega}\right)\ldots\left(1-\alpha_{p,p}e^{-j\omega}\right)\right|^2},$$

$$\hat{S}_{AR}^{p+1}\left(\omega\right)=\frac{d_{p+1}}{\left|1-\sum_{k=1}^{p+1}\hat{\varphi}_{k,p+1}e^{-j\omega k}\right|^2}=\frac{d_p\left(1-K_{p+1}^2\right)}{\left|\left(1-\alpha_{1,p+1}e^{-j\omega}\right)\ldots\left(1-\alpha_{p+1,p+1}e^{-j\omega}\right)\right|^2}$$

$$=\frac{d_p\left(1-K_{n+1}^2\right)}{\left|\left(1-\alpha_{1,p}e^{-j\omega}\right)\ldots\left(1-\alpha_{p,p}e^{-j\omega}\right)-K_{p+1}e^{-j\omega}\left(e^{-j\omega}-\alpha_{1,p}\right)\ldots\left(e^{-j\omega}-\alpha_{p,p}\right)\right|^2},$$

(6.13)

101

Here $\alpha_{i,p}$ stands for the i th pole of the AR model of order p. Note that the nominal

input power d_p decreases as model order increases, which lead to the shift of pole

positions to the unit circle so that the output amplitude can still remain at the same level

given a weaker input. It can be proved that the complex numbers

$\left(1-\alpha_1 e^{-j\omega}\right)\ldots\left(1-\alpha_p e^{-j\omega}\right)$ and $\left(e^{-j\omega}-\alpha_1\right)\ldots\left(e^{-j\omega}-\alpha_p\right)$ have the same magnitude, but

different phases (Oppenheim and Schafer, 2009). The expression for $\hat{S}_{AR}^{p+1}(\omega)$ is thus

further simplified as,

$$\hat{S}_{AR}^{p+1}(\omega) = \frac{d_p\left(1-K_{p+1}^2\right)}{\left|1-K_{p+1}e^{-j\Omega(\omega)}\right|^2 \left|\left(1-\alpha_1 e^{-j\omega}\right)\ldots\left(1-\alpha_p e^{-j\omega}\right)\right|^2} = \frac{\left(1-K_{p+1}^2\right)\hat{S}_{AR}^{p}(\omega)}{\left|1-K_{p+1}e^{-j\Omega(\omega)}\right|^2},$$

$$\Omega(\omega) = \angle \frac{\left(1-\alpha_{1,p}e^{-j\omega}\right)\ldots\left(1-\alpha_{p,p}e^{-j\omega}\right)}{e^{-j\omega}\left(e^{-j\omega}-\alpha_{1,p}\right)\ldots\left(e^{-j\omega}-\alpha_{p,p}\right)} = (p+1)\omega + 2\angle\left(1-\alpha_{1,p}e^{-j\omega}\right)\ldots\left(1-\alpha_{p,p}e^{-j\omega}\right).$$

$$(6.14)$$

When K_{p+1} is significantly small, the pole positions of the AR spectrum will not change

much as the model order increases and the spectrum shape will converge.

6.4 DAMAGE LEVEL AND MEASUREMENT NOISE SENSITIVITY FOR THE AR DAMAGE FEATURES

Distance measures between characteristics of undamaged and damaged structure

state are often adopted as damage features. Damage features examined in this chapter are

the Mahalanobis distance of AR coefficients (Chapter 3) and the Cosh distance of AR

model spectra (Chapter 4) extracted from structural acceleration measurements. For the

flow of derivations, their definitions are re-presented here. Mahalanobis distance is a

metric to evaluate the deviation within vectorial Gaussian sample groups (Mahalanobis, 1936):

$$D^2(\boldsymbol{\varphi}_u, \overline{\boldsymbol{\varphi}}_b) = \left(\boldsymbol{\varphi}_u^T - \overline{\boldsymbol{\varphi}}_b^T \right) \boldsymbol{\Sigma}_b^{-1} \left(\boldsymbol{\varphi}_u - \overline{\boldsymbol{\varphi}}_b \right). \tag{6.15}$$

where $\boldsymbol{\varphi}_u$ is the feature vector (in this case, the AR coefficients) from the unknown structural state and $\overline{\boldsymbol{\varphi}}_b / \boldsymbol{\Sigma}_b$ is the mean/covariance of feature vectors from baseline state. When the unknown vector $\boldsymbol{\varphi}_u$ is not generated from the baseline distribution, it is expected that the distance value will increase significantly.

From each vector of AR coefficients, corresponding AR spectrum plot can be constructed:

$$S_{AR}^{(p)}(\omega) = \frac{\sigma_e^2}{\left| \boldsymbol{\varphi}\left(e^{j\omega}\right) \right|^2} = \frac{\sigma_e^2}{\left| -\sum_{k=0}^{p} \varphi_k e^{-j\omega k} \right|^2}, \tag{6.16}$$

where $\varphi_0 = -1$. For feature extraction purposes model residual variance σ_e^2 is not calculated and set to unity, since its value is determined by excitation level. Cosh spectral distance based on AR spectrum estimates can be used as a frequency domain alternative to Mahalanobis distance of AR coefficients:

$$C\left(\mathbf{S}, \overline{\mathbf{S}}_b\right) = \frac{1}{2N} \sum_{j=1}^{N} \left[\frac{S\left(\omega_j\right)}{\overline{S}_b\left(\omega_j\right)} + \frac{\overline{S}_b\left(\omega_j\right)}{S\left(\omega_j\right)} - 2 \right]. \tag{6.17}$$

where $\overline{\mathbf{S}}_b$ is the baseline spectrum, $\mathbf{S}$ is the spectrum from the unknown state, and N is the length of each spectrum vector. An illustration of the procedures through which the features are generated is also given in Figure 6.2. The features are related to the structural damage through the autocovariance function of acceleration signals, which is determined

by structural stiffness properties and excitation characteristics. The analytical relation between the features and structural damage/measurement noise is explored in the remainder of this section, where noise/damage sensitivity of both indices are derived in 4 steps because the relation is not an evident one.

6.4.1 Sensitivity of structural response ACovF to damage

An AR model is an all-pole system. From Eq. (6.5) it is observed that the i th mode of a N -DOF system corresponds to a conjugate pair of system poles:

$$z_i, z_i^* = e^{-\zeta_i \omega_{ni} T_s \pm j\sqrt{1-\zeta_i^2} \omega_{ni} T_s}. \tag{6.18}$$

If it is assumed that the estimated AR model exactly captures all system poles, then an AR coefficient vector of size $(2N \times 1)$ can be computed by utilizing relations between polynomial coefficients and roots. However, simulation analysis reveals that there is a very large difference between the theoretical poles and those estimated from AR modeling (Figure 6.3). Also noted from Figure 6.3 is that AR spectrum does not converge to resemble the envelope of signal periodogram as the model order increases. Therefore, the damage sensitivity of system ACovF, from which the AR coefficient estimators are computed through Eq.(6.10), is investigated here as a first step towards obtaining accurate sensitivity estimates for both features.

To start, take the Laplace transform of the displacement impulse response of the i th system mode:

$$h_i(t) = \frac{1}{m_i \omega_{Di}} e^{-\zeta_i \omega_{ni} t} \sin \omega_{Di} t. \quad \overset{L.T.}{\Rightarrow} \quad \hat{h}_i(s) = \frac{1}{m_i(s^2 + 2\zeta_i \omega_{ni} s + \omega_{ni}^2)} \tag{6.19}$$

104

From the relationship between modal and nodal input/response in structural dynamics the impulse response matrix and the Laplace transfer function of the whole system can be obtained as:

$$\mathbf{H}(t) = \mathbf{\Phi} diag\left(h_i(t)\right)\mathbf{\Phi}^T, \ \ \hat{\mathbf{H}}(s) = \mathbf{\Phi} diag\left(\hat{h}_i(s)\right)\mathbf{\Phi}^T = (\mathbf{M}s^2 + \mathbf{C}s + \mathbf{K})^{-1},$$

$$\mathbf{u}(t) = \mathbf{H} \otimes \mathbf{p}(t), \ \hat{\mathbf{u}}(s) = \hat{\mathbf{H}}(s)\hat{\mathbf{p}}(s). \tag{6.20}$$

where $\mathbf{M}$, $\mathbf{C}$ and $\mathbf{K}$ are the mass, damping and stiffness matrices of the system, and $\otimes$ stands for the convolution operation. When the external excitation is a random process, the covariance of the response $\mathbf{u}$ can be represented as (Porat, 1994):

$$\mathbf{R}_u(\tau) = E\left(\mathbf{u}(t)\mathbf{u}(t+\tau)^T\right) = E\left([\mathbf{H}\otimes\mathbf{p}](t)[\mathbf{H}\otimes\mathbf{p}](t+\tau)^T\right) = \left[\mathbf{H}\oplus\mathbf{R}_p\otimes\mathbf{H}\right](\tau). \tag{6.21}$$

Here $\oplus$ represents the cross-correlation between two signals and $\mathbf{R}_p(\tau)$ is the covariance matrix of input excitation. From the convolution theorem, the Fourier Transform of the response covariance matrix, also known as the response power spectral density, is related to the excitation power spectral density through Eq. (6.22):

$$\therefore \hat{\mathbf{R}}_u(i\omega) = \hat{\mathbf{H}}^*(i\omega)\hat{\mathbf{R}}_p(i\omega)\hat{\mathbf{H}}(i\omega) = \mathbf{\Phi} diag\left(\hat{h}_i(i\omega)\right)^*\mathbf{\Phi}^T\hat{\mathbf{R}}_p(i\omega)\mathbf{\Phi} diag\left(\hat{h}_i(i\omega)\right)\mathbf{\Phi}^T. \tag{6.22}$$

In the case of white noise excitation, the ACovF between displacement responses at node i and node j is obtained by taking the inverse Laplace Transform of Eq.(6.22), (same result can be achieved through performing time domain convolution/correlation in Eq.(6.21))

$$\mathbf{R}_u(\tau)_{\{i,j\}} = \sum_{r=1}^{N}\frac{\phi_i^r}{m_r\omega_{Dr}}\sum_{s=1}^{N}\sum_{k=1}^{N}\sum_{l=1}^{N}\beta_{jkl}^{rs}\left(J_{rs}^2 + I_{rs}^2\right)^{-\frac{1}{2}}\exp\left(-\zeta_r\omega_{nr}\tau\right)\sin\left(\omega_{Dr}\tau + \gamma_{rs}\right),$$

105

$$\beta_{jkl}^{rs} = \frac{\mathbf{R}_p(0)_{\{k,l\}} \phi_k^r \phi_j^s \phi_l^s}{m_s}, \ I_{rs} = 2\omega_{\mathrm{D}r}\left(\zeta_r \omega_{\mathrm{n}r} + \zeta_s \omega_{\mathrm{n}s}\right),$$

$$J_{rs} = \left(\omega_{\mathrm{D}s}{}^2 - \omega_{\mathrm{D}r}{}^2\right) + \left(\zeta_r \omega_{\mathrm{n}r} + \zeta_s \omega_{\mathrm{n}s}\right)^2, \ \tan\gamma_{rs} = \frac{I_{rs}}{J_{rs}} . \tag{6.23}$$

where $(\cdot)_{\{k,l\}}$ refers to the term in k th row and l th column of the subscripted matrix and ϕ_i^r is the i th component of mode shape r. This formulation is very similar to that given by (James III et al., 1993); only that an additional dimension of summation is introduced to account for possible spatial correlation among inputs at system DOFs. The ACovF of acceleration measurements can be obtained by taking the 4$^{\text{th}}$ derivative of Eq. (6.23) and adding an impulse term to the expression,

$$
\begin{aligned}
\mathbf{R}_{\ddot{u}}(\tau)_{\{i,j\}} &= E\left(H^{'}(0)\, p(t)\, p(t)^T\, H^{'}(0)\right)_{\{i,j\}} + \frac{\mathrm{d}^4\left[\mathbf{R}_u(\tau)_{\{i,j\}}\right]}{\mathrm{d}\tau^4} \\
&= \Phi\Phi^T R_p \Phi\Phi^T{}_{\{i,j\}} + \sum_{r=1}^{N} \frac{\phi_i^r}{m_r \omega_d^r} \sum_{s=1}^{N}\sum_{k=1}^{N}\sum_{l=1}^{N} \beta_{jkl}^{rs}\left(J_{rs}^2 + I_{rs}^2\right)^{-\frac{1}{2}} \omega_{\mathrm{n}r}^4 \exp\left(-\zeta_r \omega_{\mathrm{n}}^r \tau\right) \\
&\quad \left\{\left[\left(1-7\zeta_r^2\right)\left(1-\zeta_r^2\right)+\zeta_r^4\right]\sin\left(\omega_{\mathrm{D}r}\tau + \gamma_{rs}\right) + 4\zeta_r\left(1-2\zeta_r^2\right)\left(1-\zeta_r^2\right)^{\frac{1}{2}}\cos\left(\omega_{\mathrm{D}r}\tau + \gamma_{rs}\right)\right\}.
\end{aligned}
\tag{6.24}
$$

Given the sensitivity of the modal properties to structural damage (derived in Subsection 6.4.2), sensitivity of the acceleration ACovF to structural damage can be readily obtained:

$$\mathrm{d}\mathbf{R}_{\ddot{u}}(\tau)_{\{i,j\}} = \sum_{l=1}^{N} \frac{\mathrm{d}\mathbf{R}_{\ddot{u}}(\tau)_{\{i,j\}}}{\mathrm{d}\omega_{\mathrm{n}l}}\, \mathrm{d}\omega_{\mathrm{n}l} + \sum_{k=1}^{N}\sum_{l=1}^{N} \frac{\mathrm{d}\mathbf{R}_{\ddot{u}}(\tau)_{\{i,j\}}}{\mathrm{d}\phi_k^l}\, \mathrm{d}\phi_k^l. \tag{6.25}$$

The complete time domain sensitivity formula is too long, but sensitivities for the spectral density can be obtained as:

106

$$\therefore \Delta \hat{\mathbf{R}}_u\left(i\omega\right) = \Delta\{\hat{\mathbf{H}}^*\left(i\omega\right)\hat{\mathbf{R}}_p\left(i\omega\right)\hat{\mathbf{H}}\left(i\omega\right)\}$$
$$= -\hat{\mathbf{H}}^*\left(i\omega\right)\Delta\mathbf{K}\hat{\mathbf{H}}^*\left(i\omega\right)\hat{\mathbf{R}}_p\left(i\omega\right)\hat{\mathbf{H}}\left(i\omega\right) - \hat{\mathbf{H}}^*\left(i\omega\right)\hat{\mathbf{R}}_p\left(i\omega\right)\hat{\mathbf{H}}\left(i\omega\right)\Delta\mathbf{K}\hat{\mathbf{H}}\left(i\omega\right).$$

(6.26)

Because Yule-Walker method is a time domain estimation method, the spectral density sensitivity will not be used for evaluation of the sensitivities of damage features. Still, this result is worth mentioning here as it provides a straightforward representation of the change in response ACovF as a function of the global stiffness variation.

6.4.2 Sensitivity of system eigenvalues and eigenvectors with respect to changes in global stiffness matrix

To calculate the sensitivity of the ACovF function to stiffness changes in the time domain, the sensitivity expressions for the natural frequencies and mode shapes to damage are needed. In this subsection the first-order sensitivities of modal properties with respect to a change in global stiffness matrix are presented.

If a N-DOF structure is classically damped, natural vibration frequencies and mode shapes are obtained through eigenvalue analysis of the mass matrix $\mathbf{M}$ and stiffness matrix $\mathbf{K}$:

$$\left(\mathbf{K} - \lambda_i\mathbf{M}\right)\phi_i = 0, \text{ where } \lambda_i = \omega_i^2.$$

(6.27)

Here λ_i and ϕ_i terms are the system eigenvalues and eigenvectors. Natural modal frequencies ω_i (angular) are the square roots of corresponding eigenvalues. To get the sensitivity of the modal properties to changes in stiffness matrix, first-order difference terms of both sides of Eq. (6.27) are calculated:

$$\Delta\left[\left(\mathbf{K} - \lambda_i\mathbf{M}\right)\phi_i\right] = \Delta\mathbf{K}\phi_i - \Delta\lambda_i\mathbf{M}\phi_i + (\mathbf{K} - \lambda_i\mathbf{M})\Delta\phi_i = 0,$$

107

$$(\mathbf{K} - \lambda_i \mathbf{M}) \Delta \phi_i = \Delta \lambda_i \mathbf{M} \phi_i - \Delta \mathbf{K} \phi_i, \tag{6.28}$$

Next all the eigenvectors are normalized with respect to the mass matrix and the change in eigenvectors are expressed as a weighted sum of the original normalized eigenvectors:

$$\Delta \phi_i = \sum_{k=1}^{N} d_{ik} \phi_k, \quad \text{where} \quad \phi_k^T \mathbf{M} \phi_k = 1. \tag{6.29}$$

Both sides of Eq. (6.28) are then premultiplied with ϕ_r^T $(r \neq i)$ and the mass/stiffness orthogonality between different modes is utilized to get the respective weight for each eigenvector:

$$\Delta \lambda_i \phi_r^T \mathbf{M} \phi_i - \phi_r^T \Delta \mathbf{K} \phi_i = -\phi_r^T \Delta \mathbf{K} \phi_i,$$

$$\sum_{k=1}^{N} d_{ik} \phi_r^T (\mathbf{K} - \lambda_i \mathbf{M}) \phi_k = d_{ir} \phi_r^T (\mathbf{K} - \lambda_i \mathbf{M}) \phi_r = d_{ir} \left(\phi_r^T \mathbf{K} \phi_r - \lambda_i \phi_r^T \mathbf{M} \phi_r \right) = d_{ir} \left(\lambda_r - \lambda_i \right),$$

$$d_{ir} \left(\lambda_r - \lambda_i \right) = -\phi_r^T \Delta \mathbf{K} \phi_i \Rightarrow d_{ir} = -\frac{\phi_r^T \Delta \mathbf{K} \phi_i}{\lambda_r - \lambda_i}. \tag{6.30}$$

When $r = i$, it can be proved that $d_{ir} = 0$. Therefore, the sensitivity of the i th eigenvector is orthogonal to itself and is computed as Eq.(6.31):

$$\Delta \left(\phi_i^T \mathbf{M} \phi_i \right) = 1 \Rightarrow \Delta \phi_i^T \mathbf{M} \phi_i = 0 \Rightarrow d_{rr} = \phi_i^T \mathbf{M} \Delta \phi_i / \phi_i^T \mathbf{M} \phi_i = 0,$$

$$\therefore \Delta \phi_i = \sum_{\substack{r=1 \\ r \neq i}}^{N} -\frac{\phi_r^T \Delta \mathbf{K} \phi_i}{\lambda_r - \lambda_i} \phi_r. \tag{6.31}$$

The sensitivity of the natural frequencies are obtained by premultiplying both sides of Eq. (6.28)with ϕ_i^T,

108

$$\phi_i^{\mathrm{T}} \left(\mathbf{K} - \lambda_i \mathbf{M} \right) \Delta \phi_i = \Delta \lambda_i \phi_i^T \mathbf{M} \phi_i - \phi_i^T \Delta \mathbf{K} \phi_i \Rightarrow \Delta \lambda_i = \phi_i^T \Delta \mathbf{K} \phi_i,$$

$$\because \lambda_i = \omega_i^2, \qquad \therefore \Delta \omega_i = \frac{\phi_i^T \Delta \mathbf{K} \phi_i}{2 \omega_i}. \tag{6.32}$$

Sensitivity of the acceleration signal ACovF to stiffness change can be calculated by substituting Eq.(6.31) and Eq.(6.32) into Eq.(6.25). Thus to obtain the damage sensitivity of the features, only their sensitivity with respect to the acceleration ACovF is needed.

6.4.3 Sensitivity of the AR coefficients/spectra to ACovF values

From Eq.(6.10), the sensitivity of the Yule-Walker AR estimators with respect to the changes in ACovF can be derived as:

$$\mathrm{d} \begin{bmatrix} \hat{\varphi}_1 \\ \hat{\varphi}_2 \\ \hat{\varphi}_3 \\ \vdots \\ \hat{\varphi}_p \end{bmatrix} / \mathrm{d}R(\tau) = \begin{cases} -\mathbf{\Gamma}^{-2} \boldsymbol{\gamma}, \ \tau = 0 \\ \mathbf{\Gamma}^{-1} \mathbf{e}_\tau - \mathbf{\Gamma}^{-1} toeplitz(\mathbf{e}_{\tau+1}) \mathbf{\Gamma}^{-1} \boldsymbol{\gamma}, \ 1 < \tau < p. \\ \mathbf{\Gamma}^{-1} \mathbf{e}_p, \ \tau = p \end{cases} \tag{6.33}$$

where $\mathbf{e}_\tau$ is a $(p \times 1)$ column vector with all elements equal to zero except for element τ, which equals to 1. For the AR spectrum, the definition here states that it is:

$$\hat{S}_{AR}^{(p)} \left(\omega \right) = \frac{1}{\left| \hat{\varphi} \left(e^{j\omega} \right) \right|^2} = \frac{1}{\left| \sum_{k=0}^{p} \hat{\varphi}_k e^{-j\omega k} \right|^2}, \tag{6.34}$$

In this definition, $\hat{\varphi}_0 = -1$. Its sensitivity to changes in coefficients can be computed as:

$$\frac{d\hat{S}_{AR}^{(p)} \left(\omega \right)^{-1}}{d\hat{\varphi}_k} = 2Re \left\{ e^{-j\omega k} \left(\sum_{n=0}^{p} \hat{\varphi}_n e^{j\omega n} \right) \right\}, \frac{d\hat{S}_{AR}^{(p)} (\omega)}{d\hat{\varphi}_k} = -2Re \left\{ e^{-j\omega k} \left(\sum_{n=0}^{p} \hat{\varphi}_n e^{j\omega n} \right) \right\} \hat{S}_{AR}^{(p)} \left(\omega \right)^2. \tag{6.35}$$

Thus by combining Eq. (6.33) and Eq. (6.35), the sensitivity of the spectrum to ACovF changes is calculated.

109

6.4.4 Sensitivity of the AR coefficients/spectra to the increase in the noise level

To compute the influence of noise on damage feature estimation, consider the signal

covariance sequence of contaminated signals. When white noise of standard deviation σ

is added to the signal, the expected signal ACovF sequence R_c will be

$$R_c(\tau) = R(\tau) + R_n(\tau) = R(\tau) + \sigma^2 \delta(\tau), \tag{6.36}$$

where $R_n(\tau)$ denotes the ACovF of white noise. Therefore, the sensitivity of the

estimated coefficients to the variance of additive Gaussian noise will be

$$\frac{d\left[\hat{\varphi}_1, \hat{\varphi}_2, \ldots, \hat{\varphi}_p\right]^T}{d\sigma^2} = \frac{d\left[\left(\boldsymbol{\Gamma} + \sigma^2 \mathbf{I}\right)^{-1} \boldsymbol{\gamma}\right]}{d\sigma^2} = -\boldsymbol{\Gamma}^{-2} \boldsymbol{\gamma}. \tag{6.37}$$

Sensitivity of the AR spectrum to the noise level can be derived through combining

Eq.(6.37) and Eq.(6.35) in the previous subsection. It should be noted that the above

formula only accounts for the extreme case (i.e. number of samples $N_s = \infty$). For the

finite sample scenario, the estimated noise correlation $\hat{\rho}_n(\tau)$ is asymptotically normally

distributed with variance n^{-1} at nonzero lags (Brockwell and Davis, 2009). As such,

$$\frac{d\left[\hat{\varphi}_1, \hat{\varphi}_2, \ldots, \hat{\varphi}_p\right]^T}{d\sigma^2} = -\boldsymbol{\Gamma}^{-1} \begin{bmatrix} 1 & \hat{\rho}_n(1) & \hat{\rho}_n(2) & \cdots & \hat{\rho}_n(p-1) \\ \hat{\rho}_n(1) & 1 & \hat{\rho}_n(1) & \cdots & \hat{\rho}_n(p-2) \\ \hat{\rho}_n(2) & \hat{\rho}_n(1) & 1 & \cdots & \hat{\rho}_n(p-3) \\ \vdots & \vdots & \vdots & \ddots & \vdots \\ \hat{\rho}_n(p-1) & \hat{\rho}_n(p-2) & \hat{\rho}_n(p-3) & \cdots & 1 \end{bmatrix} \boldsymbol{\Gamma}^{-1} \begin{bmatrix} R(1) \\ R(2) \\ R(3) \\ \vdots \\ R(p) \end{bmatrix}.$$

$$\tag{6.38}$$

The ACovF of the original signal is also affected by estimation errors and exhibits an

asymptotic Gaussian distribution (Brockwell and Davis, 2009). To avoid including

unnecessary statistical complexities and focus on the direct influence of structural damage/measurement noise level on damage features here it is assumed that the ACovF estimators are exact (the asymptotic case).

6.4.5 Sensitivity of the distance measures to changes in AR coefficients/spectra

The theoretical feature values under the null hypothesis will be needed for evaluation of relative sensitivity. The AR coefficient estimators from a scalar series of length N' are asymptotically unbiased and follow a multivariate Gaussian distribution with covariance matrix $\frac{\sigma_e^2}{N'}\mathbf{\Gamma}^{-1}$ ($\sigma_e^2 = R(0) - \boldsymbol{\gamma}^T\mathbf{\Gamma}^{-1}\boldsymbol{\gamma}$) (Brockwell and Davis, 2009). Under this assumption, the Mahalanobis distance feature for the undamaged structural state has a chi-square distribution with p degrees-of-freedom, and its statistical expectation is p. The expression for the expected value of the squared Mahalanobis distance for the general case is presented in Eq.(6.39).

$$
\begin{aligned}
E\left(D^2\right) &= E\left(\boldsymbol{\varphi}_u^T - \overline{\boldsymbol{\varphi}}_b^T\right)\mathbf{\Sigma}_b^{-1}\left(\boldsymbol{\varphi}_u - \overline{\boldsymbol{\varphi}}_b\right) \\
&= E\left[\left(\boldsymbol{\varphi}_u^T - \overline{\boldsymbol{\varphi}}_u^T\right)\mathbf{\Sigma}_b^{-1}\left(\boldsymbol{\varphi}_u - \overline{\boldsymbol{\varphi}}_u\right)\right] + \left[\left(\overline{\boldsymbol{\varphi}}_u^T - \overline{\boldsymbol{\varphi}}_b^T\right)\mathbf{\Sigma}_b^{-1}\left(\overline{\boldsymbol{\varphi}}_u - \overline{\boldsymbol{\varphi}}_b\right)\right] \\
&= trace\left[\mathbf{\Sigma}_b^{-1}\mathbf{\Sigma}_u\right] + \left[\left(\overline{\boldsymbol{\varphi}}_u^T - \overline{\boldsymbol{\varphi}}_b^T\right)\mathbf{\Sigma}_b^{-1}\left(\overline{\boldsymbol{\varphi}}_u - \overline{\boldsymbol{\varphi}}_b\right)\right],
\end{aligned}
$$

(6.39)

The first and second order sensitivities of $E\left(D^2\right)$ to signal covariance can then be computed. Note that for notation simplicity, θ is used to express the ACovF value at an arbitrary lag.

$$
\frac{dE\left(D^2\right)}{d\theta}\Big|_{\boldsymbol{\varphi}_u=\boldsymbol{\varphi}_b,\ \Sigma_u=\Sigma_b} = trace\left[\mathbf{\Sigma}_b^{-1}\frac{d\mathbf{\Sigma}_u}{d\theta}\right],
$$

(6.40)

111

$$\frac{d^2 E(D^2)}{d\theta^2}\Big|_{\varphi_u=\varphi_b, \Sigma_u=\Sigma_b} = trace\left[\Sigma_b^{-1}\frac{d^2\Sigma_u}{d\theta^2}\right] + 2\left[\frac{d\left(\overline{\varphi}_u^T - \overline{\varphi}_b^T\right)}{d\theta}\Sigma_b^{-1}\frac{d\left(\overline{\varphi}_u - \overline{\varphi}_b\right)}{d\theta}\right]. \quad (6.41)$$

The expressions for the first and second order sensitivity of Σ_u with respect to signal ACovF are presented in Appendix A; the contribution of these terms to the feature value is relatively small compared to the mean shift in the application described in the following section.

Under the Gaussian assumption, the AR spectral estimates also asymptotically follow a normal distribution; as p^3/N decreases, $\sqrt{\dfrac{N}{p}}(\overline{S}_b - S)/\overline{S}_b$ converges to a normal distribution with asymptotic variance equals to 4 at DC and 2 otherwise (Berk, 1974). Therefore the expected value for the Cosh distance of the baseline state can be written as the sum of moments of this Gaussian distribution:

$$E(C)|_{ES(\omega_j)=\overline{S}_b(\omega_j)} = \frac{1}{2N}\sum_{j=1}^{N}E\left[\frac{S(\omega_j)}{\overline{S}_b(\omega_j)} + \frac{\overline{S}_b(\omega_j)}{S(\omega_j)} - 2\right]$$

$$= \frac{1}{2N}\sum_{j=1}^{N}E\left[\frac{\overline{S}_b(\omega_j)}{S(\omega_j)} - 1\right] = \frac{1}{2N}\sum_{j=1}^{N}E\left[\frac{1}{\left(S(\omega_j)-\overline{S}_b(\omega_j)\right)/\overline{S}_b(\omega_j)+1} - 1\right],$$

The following is obtained after performing a geometric series expansion on $\left(S(\omega_j)-\overline{S}_b(\omega_j)\right)/\overline{S}_b(\omega_j)$ for the equation above:

$$E(C)|_{ES(\omega_j)=\overline{S}_b(\omega_j)} = \frac{1}{2N}\sum_{j=1}^{N}E\left[\sum_{l=1}^{\infty}\left(\frac{S(\omega_j)-\overline{S}_b(\omega_j)}{\overline{S}_b(\omega_j)}\right)^{2l}\right].$$

$$(6.42)$$

112

Since the normal assumption is valid only in the asymptotic sense, and higher order statistical moments are less significant in value and affected more by the deviation from this assumption, only the first two terms ($l = 1, 2$) will be considered in applications in this chapter.

The sensitivity expressions of Cosh distance are obtained in a similar manner as that for Mahalanobis distance,

$$
\frac{dE(C)}{d\theta}\Big|_{ES(\omega_j)=\overline{S}_b(\omega_j)} = \frac{1}{2N}\sum_{1}^{N}\left\{\frac{dES(\omega_j)}{d\theta}\frac{1}{\overline{S}_b(\omega_j)} + \frac{dE\left[S(\omega_j)^{-1}\right]}{d\theta}\overline{S}_b(\omega_j)\right\}
$$

$$
= \frac{1}{2N}\sum_{1}^{N}\left\{\frac{dES(\omega_j)}{d\theta}\frac{1}{\overline{S}_b(\omega_j)} + \frac{d\sum_{l=0}^{\infty}E\left(\frac{\overline{S}_b(\omega_j)-S(\omega_j)}{\overline{S}_b(\omega_j)}\right)^l}{d\theta}\right\} = 0,
\tag{6.43}
$$

$$
\frac{d^2E(C)}{d\theta^2}\Big|_{S(\omega_j)=\overline{S}_b(\omega_j)} = \frac{1}{2N}\sum_{1}^{N}\left\{\frac{d^2ES(\omega_j)}{d\theta^2}\frac{1}{\overline{S}_b(\omega_j)} + \frac{d^2\sum_{l=0}^{\infty}E\left(\frac{\overline{S}_b(\omega_j)-S(\omega_j)}{\overline{S}_b(\omega_j)}\right)^l}{d\theta^2}\right\}
$$

$$
= \frac{1}{2N}\sum_{1}^{N}\left(\frac{dS(\omega_j)}{d\theta}\right)^2\frac{2}{\overline{S}_b(\omega_j)^2}.
$$

$$
\tag{6.44}
$$

The damage/noise sensitivities of both features are found as the product of the sensitivities of features to ACovF and the sensitivities of ACovF to structural damage/measurement noise.

113

6.5 AUTOREGRESSIVE MODELING BASED ON SIGNAL ACovF

As indicated by the sensitivity analysis, the Mahalanobis distance and Cosh distance features based on ambient series modeling can be affected by noise level increase. This section explores the means to reduce model parameter based feature sensitivity.

The univariate AR model predicts the current value of a signal as a weighted combination of its previous values up to model order p. When prediction errors (model residuals) are small, the process becomes approximately deterministic.

Deterministic stable processes with a state-space representation are perfectly predictable from a finite number of past values (Porat, 1994). Here for structural vibration measurements from a single sensing location, their ACovF $R(t)$ after zero lag is essentially a sum of M exponentially decaying sinusoids (Eq. (6.23) (6.24)),

$$R(t) = \sum_{m=1}^{M} A_m e^{-\xi_m t} \sin(\omega_m t - \phi_m), \tag{6.45}$$

where ξ_m, ω_m are determined from system natural frequencies and damping ratios. It can be proved that $R(t)$ can be modeled using an exact AR model (i.e. without the residual term),

$$R(t) = -\sum_{k=1}^{2M} c_k R(t-k), \quad c(z) = \prod_{m=1}^{M} \left(1 - 2e^{-\xi_m} \cos \omega_m z^{-1} + e^{-2\xi_m} z^{-2}\right). \tag{6.46}$$

However, since in real applications there is always estimation and numerical errors, the residual term is retained to account for these effects. Thus the AR model for signal ACovF takes the same form as that for stationary time series. Forward covariance method (a variant of least squares) will be used for AR estimation from ACovF, and since the zero lag value of signal ACovF is not used, AR features thus produced will be less likely affected by noise contamination.

114

In Section 6.7, the Mahalanobis distance and the Cosh distance features based on ambient signals and signal ACovF are applied to detect structural change in a steel truss structure. Besides, Ljung-Box statistic of residual series from the two types of AR modeling is also presented alongside.

6.6 SIMULATION EXAMPLE: SENSITIVITY ANALYSIS FOR A 10-DOF STRUCTURE

To verify the sensitivity analysis scheme presented in the previous section, it is applied to a 10-DOF model with linear topology and simply supported at both ends (Figure 6.4). The mass of each node is 2 tons, the length of each element is 25 m and the section stiffness (EI) is $2.5 \times 10^5 \, kN \cdot m^2$. Damage is defined as a stiffness reduction in the inter-node elements, and a procedure to transform the local section stiffness change (ΔEI) to global stiffness change ($\Delta \mathbf{K}$) is developed in Appendix B.

Spatially and chronologically uncorrelated random excitation is applied at each node of the system. Acceleration signals are simulated from the system using Newmark's method, and both feature values are extracted from the signals during multiple runs of simulation. Each simulation returns a group of Cosh distance values and a group of Mahalanobis distance values, and feature mean and confidence interval can be henceforth obtained. Pooling results from all runs of simulation the average and confidence interval of means from respective feature groups can be calculated. These simulation results regarding effects of local damage/measurement noise on feature values are compared with theoretical analysis results and sensitivity analysis results. Here theoretical results refer to that computed directly from the theoretical ACovF (Eq. (6.24) and (6.36)) for each damage/measurement noise case, and sensitivity results are those obtained from

115

concatenating sensitivity expressions derived step-by-step in Section 6.4. For all

simulations and computations, the AR model order is set at 20. During each run of

simulation, 88 signal segments, each containing 5400 data points sampled at a frequency

of 50 Hz, are used to calculate the Mahalanobis distance and Cosh distance features. Two

figures are created to contrast the results, which are from calculations performed for

acceleration signals from node 4. For all the plots within each figure, star-marked solid

line with 95% confidence intervals, dashed line and thick solid line represent the results

from simulation, sensitivity analysis and theoretical analysis, respectively.

Figure 6.5 shows the trends of Mahalanobis distance and Cosh distance as the noise

level increases. Signals with 2% noise level are used as baseline and another case with

2% noise level is included for false positive testing (Gul and Catbas, 2009; Sohn and

Farrar, 2001). Because simulations that involve random vibration generation come with

uncertainty (i.e. yield different results on each run), it is beneficial to include results from

another set of signals collected under the same noise/structural state to demonstrate the

variation, which provides a reference on the amount of variation that can be confidently

identified by the features. Noise level in this application is defined as the ratio between

the standard deviation of measurement noise and that of the actual signal. In SHM

practice both the noise and signal strength vary depending on the application; noise

amplitude can be from tens to thousands μg and the sampled ambient vibration signal

amplitude can be in the order of few to hundreds mg (Dorvash and Pakzad, 2012; Pakzad,

Kim, Fenves, and Glaser, 2005; Wang, Lynch, and Law, 2007). Thus, the noise level

values investigated here (2%-30%) fall in the range of expected noise levels. The 3 lines

in the plots have relatively close values in comparison to the large confidence interval

from one simulation, with the average relative deviation from the theoretical to sensitivity analysis results with respect to the confidence interval length at 1.31% and 0.68% for the Mahalanobis and Cosh distance features, respectively, and that from simulation mean to sensitivity analysis results at 4.02% and 14.22% . There is a noticeable difference between the simulation and theoretical analysis because the derivations are based on the asymptotic theory, which is but an approximation for large-sample-base estimation. The confidence bounds generated through simulation for both features indicate positive skew in distribution, a fact compatible with the assumptions on their respective asymptotic distribution. The simulation mean for the Cosh distance is 8% higher than the computed theoretical value, but their increasing tendency are almost parallel. The baseline value estimation for Mahalanobis distance is more precise than Cosh distance because the value for latter is from a truncated series (Eq. (44)), and the sensitivity measure predicts the varying trend of Mahalanobis distance less exactly than that of Cosh distance because computation of the former uses the covariance matrix obtained from asymptotic theory, which adds in error. Sensitivity analysis values for both features start quite close to the theoretical results when deviation from the original/baseline state is small, yet their difference grows larger as the deviation increases because of higher-order effects that are neglected in the linearization step of sensitivity analysis. The average Cosh distance values from 50 simulations have a much reduced, yet still largely uniform, confidence interval (from $\pm50\%$ around the mean to $\pm10\%$ around the mean) over different cases, while the confidence interval for average Mahalanobis distance values is expanding along x axis. The sensitivity analysis in this case study underestimates the feature value for significant changes in structural state/signal noise level. Note here the distribution

117

variance terms ($trace\left[\mathbf{\Sigma}_b^{-1}\dfrac{d\mathbf{\Sigma}_u}{d\theta}\right]$ and $trace\left[\mathbf{\Sigma}_b^{-1}\dfrac{d^2\mathbf{\Sigma}_u}{d\theta^2}\right]$) are not considered as the

computation is complex and their relative influence is small.

   In applications the two damage features studied are often employed in a statistical

control style (Gul and Catbas, 2009; Sohn and Farrar, 2001). In other words, the features

will be extracted in large quantities and the system is identified as changed when the

number of feature values exceed a pre-set threshold becomes significant (i.e. more than a

certain proportion of the total number of feature samples). Table 6.1 shows the number of

outliers from simulation together with those predicted from theoretical and sensitivity

analysis as the noise level increases. Here for each feature the threshold is set at 5%

significant level and determined empirically from the baseline feature population.

Because the theoretical/sensitivity derivations involve only the mean shift of features, an

assumption is made that the higher moments of the feature distributions do not change

much over the different states. As such, outliers numbers can be predicted by adding the

mean deviations from theoretical/sensitivity analysis to the original baseline feature

values and then examining the number of outliers in the newly obtained feature group.

Results from the table indicate that for the Cosh distance feature the

theoretical/sensitivity approaches predict the outlier percentage change trend with good

accuracy; the simulation results are fluctuating around the predictions. For the

Mahalanobis distance feature the simulations produce higher outlier percentages than the

other two options, because the dispersion of this feature noticeably increased as noise

level rises (Figure 6.5). The sensitivity method gives a more conservative estimate on

outlier percentage increases as noise level rises than the theoretical method for both

118

damage features. Also, the outlier counts for the damage features do not vary significantly till noise level reaches 22%-26%.

Figure 6.6 presents their trends as a stiffness reduction between node 4 and 5 grows. The stiffness loss is expressed as a percentage of the original element stiffness, and measurements are assumed to contain 2% noise. The parabolic trends and relative positions of the lines are similar to those shown in Figure 6.5. This observation is not very surprising as both noise and structural damage affect the feature values through the acceleration signal ACovF. For both feature values, the 16% stiffness reduction produces about the same amount of mean shift as that done by an increase in noise level from 2% to a value between 26% and 30%. Since here the structure and a single type of damage are specified and excitation/noise characteristics are not varying, the feature values can directly reflect structural stiffness loss. In the general case, this is not feasible because the information based on which the features are extracted are limited (i.e., single channel acceleration).

Table 6.2 contains the outlier ratios as obtained from the three approaches. The number of outliers in each feature from theory/sensitivity analysis follows a similar procedure as that used in Table 6.1, where the baseline feature samples are involved in the computation. While the theoretical/sensitivity analysis predictions for Cosh distance agree with the simulation, those predictions for Mahalanobis distance are often well below the significance value since the feature dispersion increases as damage grows more severely (Figure 6.6). Again, the sensitivity method as a whole underestimates the outlier percentages at high damage levels because of the model error introduced by linearization, indicating that it produces a lower bound. Here the Mahalanobis distance responds to

damage at an earlier level (i.e., 8% stiffness reduction corresponds to a 10% outlier percentage from the simulation), while the Cosh distance only yields a significant change at a later stage (i.e., 12% stiffness reduction corresponds to a 10% outlier percentage).

Please note that all sensitivity expressions here are derived for the general case, except than the sensitivity of the local section stiffness change (ΔEI) to global stiffness change ($\Delta \mathbf{K}$), which is developed for this particular simulated structure. Results at other nodes also show agreement among curves from the three methods and due to space limitations are not presented here. Another observation worth mentioning for this case study is that as the measurement location moves away from the damage location, the change in damage feature values becomes less significant. In fact, the damage features are hardly reporting any noticeable changes at the first and last node.

6.7 EXPERIMENTAL VALIDATION OF AR FEATURES FROM ABMIENT SIGNALS AND SIGNAL ACovF

The features described in the previous section are applied to identify structural change for a vertical truss member in a steel truss bridge over the Allegheny River in western Pennsylvania. The bridge structure is a continuous deck truss with spans of 420 feet, 540 feet, and 420 feet, as shown in Figure 6.7. The truss is 40 feet in depth and is haunched to 84 feet at the two intermediate piers.

During an inspection in June 2010, it was found that vertical members at Panel Points (PP) 20' and 22 (Figure 6.7) on the north side of truss had excessive wind-induced vibration. The two members were then retrofitted by bolting a steel wide-flange member to each of them over their full height.

In a subsequent field test, transverse acceleration measurements are collected for Verticals 22 and 22'. These two members were identical before the retrofit of PP22. Each member is instrumented with eight accelerometers; four at the mid-span cross section and four at ¾ height. The damage indices will be applied to acceleration measurements from the two members in order to identify their difference. Since the indices are all extracted using single channel AR modeling, signals used here will be only from accelerometer 4, a sensor located on the inner flange tip of the middle section.

Sampling frequency for all acceleration measurements is 1000 Hz. Two datasets of 200,000 samples are collected for each member. Dataset 1, which is from the retrofitted PP22, will be used as baseline for all applications of damage detection presented in the following subsections.

6.7.1 Performance of AR features estimated from ambient acceleration data

The AR modeling is performed directly on ambient acceleration using Yule-Walker method, and AR order is set to 24 for all estimation processes. Each dataset is divided into segments of size 1,000 samples with no overlap, and from each segment a coefficient vector is obtained. As such, from each set of measurements a total of 200 features can be obtained. Figure 6.8 shows the damage identification (in this case, characterizing the difference between the two vertical members) results from application of Mahalanobis distance and Cosh distance features. In the plot titles, Dataset 1 and Dataset 2 are from the retrofitted PP22, while Dataset 3 and Dataset 4 are from the as-built PP22'. Damage thresholds for all plots correspond to a 5% significance level, and values beyond the thresholds are marked in the plots as crosses. For Dataset 2 more false alarms are observed for the Mahalanobis distance than the Cosh distance (26 vs. 12), and in turn the

121

former has less missed cases than the latter (i.e. points below the threshold) for Dataset 3 and Dataset 4. Thus, the feature based on AR spectra is more robust to environmental variations. For this case both features successfully identified the structural change in the form of a significant number of outliers.

The results of damage identification using the Q-statistic are contained in Figure 6.9. The baseline AR coefficients are estimated using one segment from Dataset 1 and used in computation of all residual series from both retrofitted and as-built state. The lag parameter, h, is set to 60. It can be observed that this feature is not prone to false positives, as the number of outliers for both Dataset 1 and Dataset 2 is no greater than 10. As expected, when the structural state changes, much more outliers appear in the Q-statistic chart.

6.7.2 Performance of AR features estimated from ACovF of acceleration measurements

The three features are also extracted using AR estimation from signal ACovF. The signal segmentation scheme, AR model order and threshold significance level adopted are the same as in the previous subsection. From each signal segment of length 1,000, an unbiased ACovF estimator of length 500 is obtained starting from lag 1 and up to lag 500. From each ACovF estimator an AR coefficient vector is computed. Although ideally only 2×24=48 (twice the AR order) ACovF samples are needed for determination of the AR coefficients, all 500 samples are used to account for ACovF estimation error and to get enough residual values for computation of the Q-statistic, which is a function of the ACovF of residuals.

Figure 6.10 includes the Mahalanobis distance and Cosh distance features from ACovFs of acceleration measurements. When compared with Figure 6.8, it can be seen

that the Cosh distance feature in this case generates slightly fewer false alarms (10 for dataset 2), yet retains the sensitivity to structural change. The Mahalanobis distance also yields more stable values for Dataset 2 (a total of 17 outliers), though the number of outliers reported for Dataset 3 and Dataset 4 is reduced. Again, both features have captured the structure change unambiguously.

Figure 6.11 is the Q-statistic control chart from AR estimation based on signal ACovF. The behavior of this feature here is similar to the case of direct AR modeling on vibration data (i.e. Figure 6.9), except that a larger magnitude of feature values for both retrofitted state (baseline) and as-built state is observed. This is most likely because when the AR coefficients no longer 'match' the current process the residual of sinusoids exhibit strong cyclic patterns, which will make the Q-statistic value increase since the statistic is defined as a measure between a series and white noise.

6.8 CONCLUSION

This research proposes a sensitivity analysis approach to investigate the effect of measurement noise and structural damage on two existing damage features, Mahalanobis distance of AR coefficients and Cosh distance of AR model spectra. It is found that both features values increase parabolically with respect to increases in local damage extent and measurement noise level. The approach is used to predict the feature values from a numerical 10-DOF bridge model in several damage/noise level cases, and the outcome is in good agreement with that from simulated acceleration signals and theoretical calculations. This observation supports the validity of the proposed approach, which is a more efficient way to examine the behavior (sensitivity and robustness) of damage features than repeating the simulation process for a number of times. The reason for that

www.manaraa.com

is because simulation requires generation of structural vibration signals and extraction of feature values for each noise/damage state, but the sensitivity values, once computed, can be applied to multiple states.

Since the approach introduced here involves using a structural FE model, modeling error can affect the procedure from two aspects: the baseline state signal estimation, which affects the noise and damage sensitivity estimation, and the relation between the structural measurements and local damage, which affects the damage sensitivity. For the first part of the problem, civil structures under ambient vibration are generally only well excited in a few low frequency modes. If the FE model can be tuned such that its modes match those measured from the real structure at the original state, then the structural baseline state response ACovFs can be estimated from the FE model with good accuracy. For the second part, there is no definite solution. However, ranges in which FE parameters vary can be assumed, and damage sensitivity expressions for certain parameter sets within the range can be computed to obtain the lower/upper bounds of damage feature sensitivity.

It is noted that the Mahalanobis distance and Cosh distance features respond not only to structural damage but also to increase in the noise level. This fact implies that both features are not completely robust to variations unrelated to structure change. This is partially due to the fact that these damage identification algorithms use only the response from a single channel, which is generated as a result of interaction between several components (structure, environment, and excitation). However, as shown in the simulation example above, it takes a significant increase in the noise level to produce a feature value change that matches that from a moderate reduction of stiffness for both AR

124

features. Thus, these damage indices are effective in monitoring a structure with reasonably stable operating conditions.

The variation of environmental conditions (temperature, humidity, etc.) often affects the damage features through their influence on the structural material properties (and hence the stiffness properties). The traffic variation will change the excitation amplitude, spatial pattern and frequency contents. AR based features will be robust to the excitation amplitude but affected by the other two excitation factors. These non-structural influences are not examined in an analytical manner unless the functional relationship between the environmental conditions and structural stiffness is known and the form of excitation variation is defined. The sensitivity terms can be derived by taking the derivative of signal ACovF with respect to these sources of influence. Further research is needed to address these issues.

A contrast between features from AR estimation directly on stationary time series and that estimated using the signal ACovF reveals that the noise robustness of Mahalanobis distance and Cosh distance features improved (though not to a great extent) for the latter modeling method. This is expected because ACovF computation is an averaging process and therefore should filter out some of the environmental uncertainties. Another more theoretical rationale, as presented in Section 6.5, is that the AR coefficients of ACovF of vibration signals of a multi-degree-of-freedom structure are functions of natural frequencies and damping properties only, which implies that the features will not be affected by changes in modal shapes (a sacrifice on the part of damage sensitivity) and also a number of non-structural-factors such as white measurement noise and excitation pattern variation. The results from Ljung-Box statistic using the two modeling methods

125

are similar. Yet it should be noted that the tests on this bridge are performed for a relatively short time span; the merits of the ACovF based modeling might become more clear for long-term monitoring of real-world structures subjected to a variety of operational conditions.

Table 6.1   Outlier percentages from simulation, theory, and sensitivity analysis as noise level increases

Feature Type	Outlier Percentage	Noise levels								
		0.02	**0.02**	**0.06**	**0.1**	**0.14**	**0.18**	**0.22**	**0.26**	**0.3**
C *	simulation	0.05	0.05	0.05	0.07	0.08	0.06	0.04	0.11	0.12
	theoretical	0.05	0.05	0.06	0.06	0.06	0.06	0.08	0.08	0.1
	sensitivity	0.06	0.06	0.06	0.06	0.06	0.06	0.06	0.08	0.09
D^2 *	simulation	0.05	0.05	0.05	0.06	0.07	0.08	0.09	0.13	0.21
	theoretical	0.05	0.05	0.06	0.06	0.06	0.06	0.06	0.08	0.1
	sensitivity	0.06	0.06	0.06	0.06	0.06	0.06	0.06	0.07	0.09

*: C -- Cosh distance; D^2 -- Mahalanobis distance

Table 6.2   Outlier percentages from simulation, theory, and sensitivity analysis as damage level increases

Feature Type	Outlier Percentage	Damage levels								
		0	**0.02**	**0.04**	**0.06**	**0.08**	**0.1**	**0.12**	**0.14**	**0.16**
C	simulation	0.05	0.06	0.05	0.06	0.08	0.07	0.1	0.11	0.16
	theoretical	0.05	0.06	0.07	0.08	0.09	0.1	0.11	0.13	0.13
	sensitivity	0.05	0.06	0.07	0.07	0.09	0.09	0.11	0.12	0.13
D^2	simulation	0.05	0.06	0.05	0.09	0.1	0.14	0.18	0.23	0.31
	theoretical	0.05	0.06	0.06	0.06	0.06	0.06	0.08	0.1	0.14
	sensitivity	0.05	0.06	0.06	0.06	0.06	0.06	0.06	0.08	0.1

128
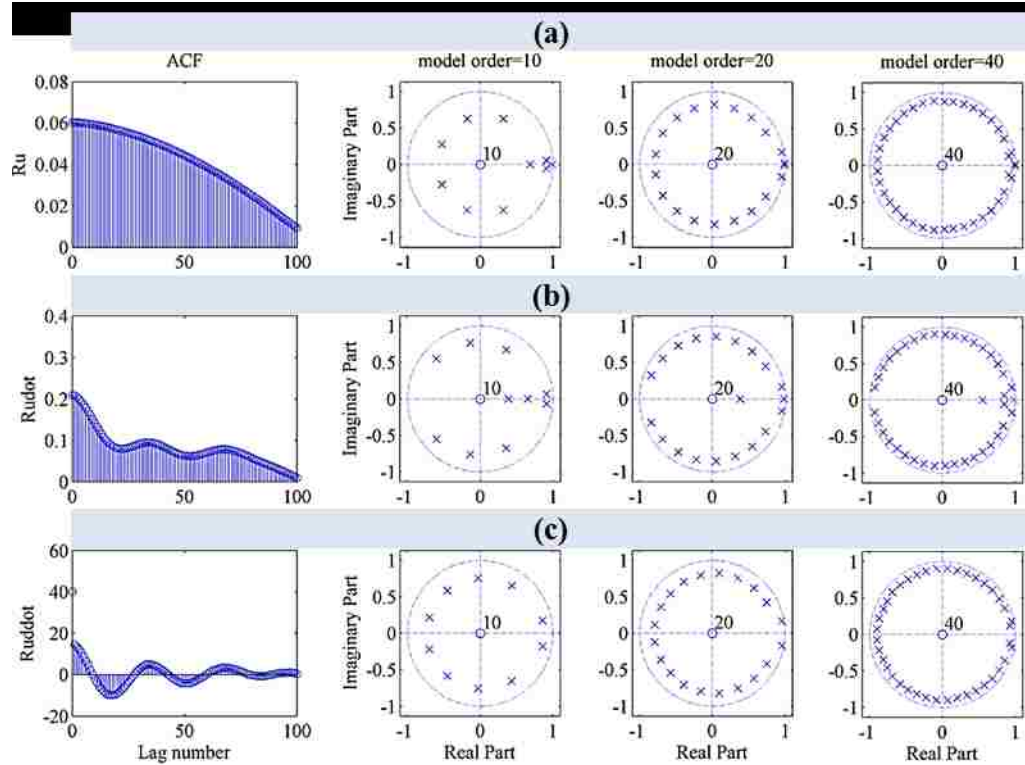
Figure 6.1   Pole positions of AR model estimated from structural

displacement (a), velocity (b), and acceleration (c) signals.

The first column of the subplots shows the ACovF values,

while the rest displays the pole positions of different models in

the z-plane.

129
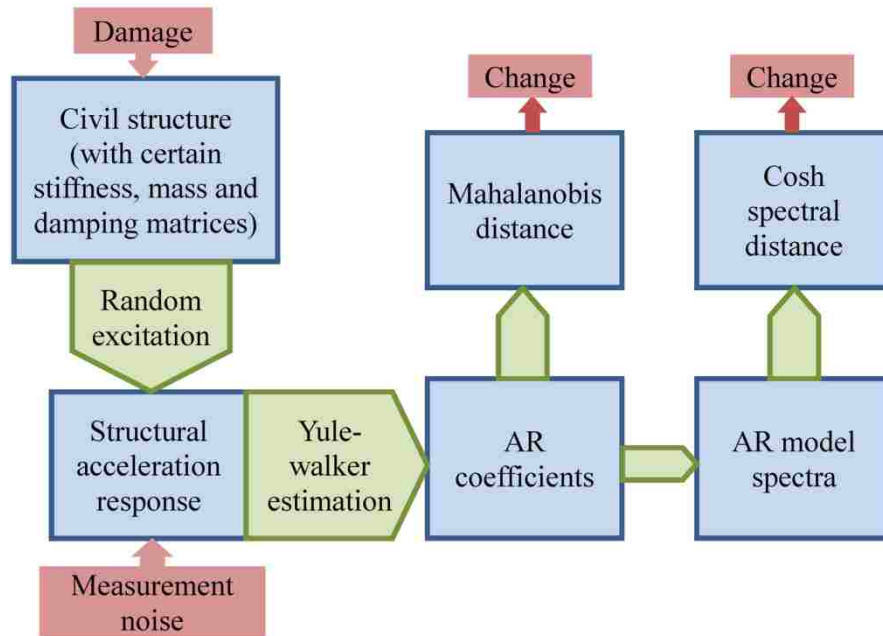
Figure 6.2   Illustration of the relation between structural

damage/measurement noise and AR-based damage features
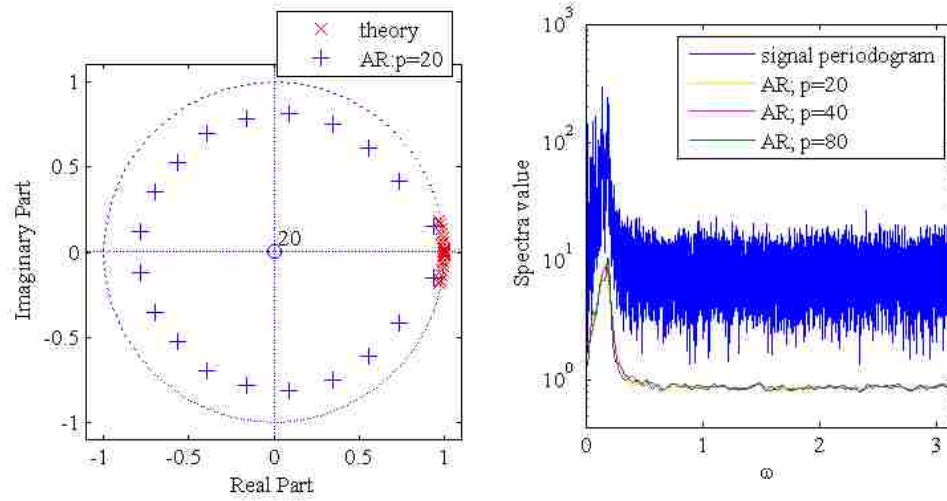
Figure 6.3   The contrast of the theoretical pole positions from digital

signal processing theory and those from estimated AR models

(left plot) and the comparison of the signal periodogram and

the AR model spectra of different orders (right plot)
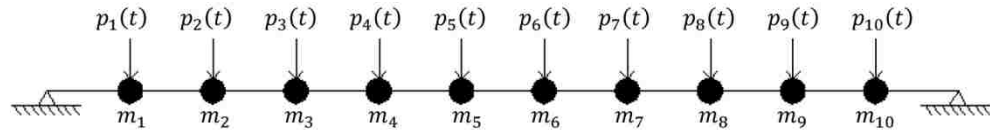
Figure 6.4   The simulated 10 DOF model
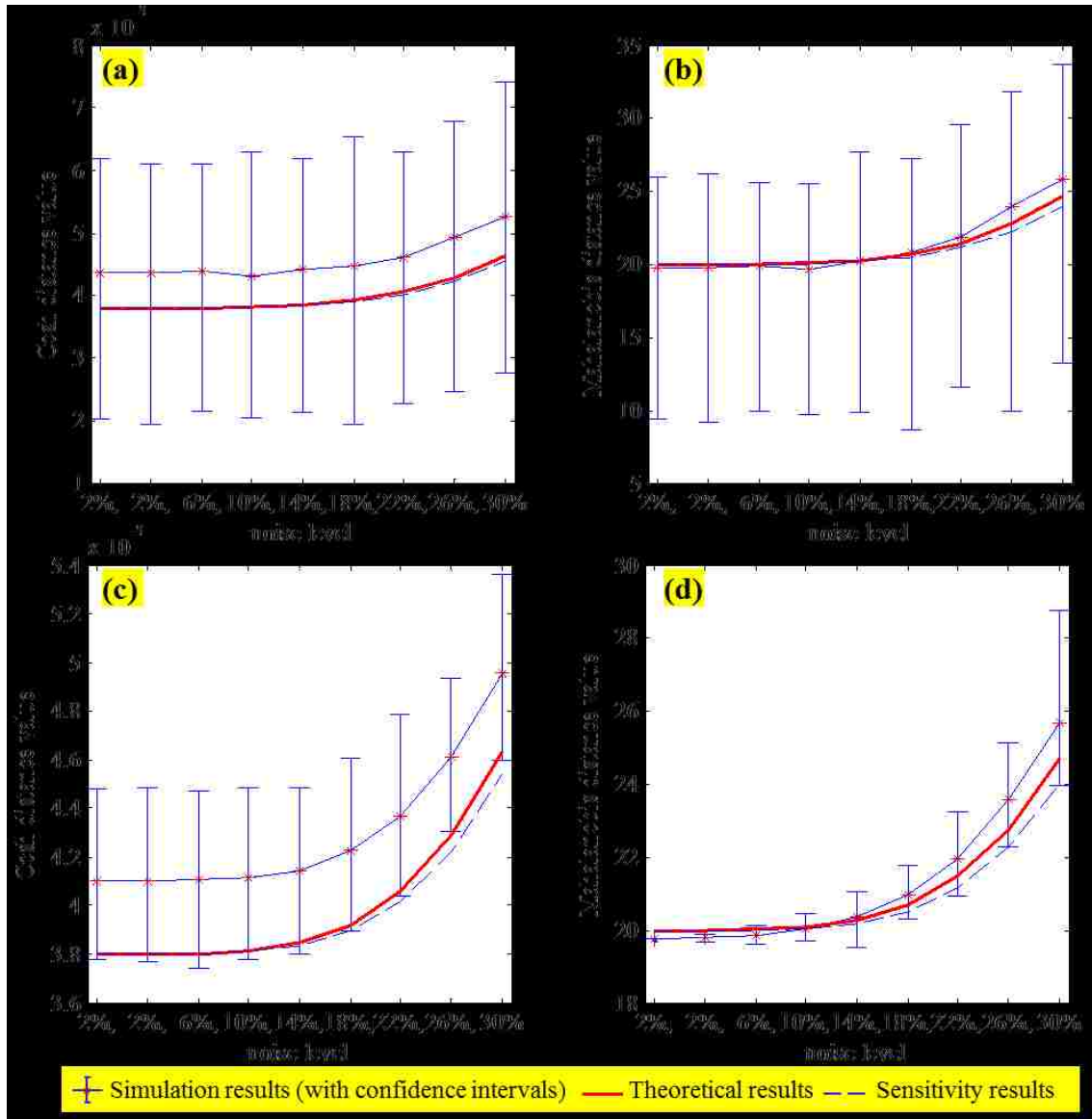
Figure 6.5   Plots of the Mahalanobis distance and Cosh distance damage

feature values as noise level increases. Plots (a) and (b) show

simulation results from one experiment, (c) and (d) show the

average simulation results from 50 runs (confidence intervals

are constructed based on average values).
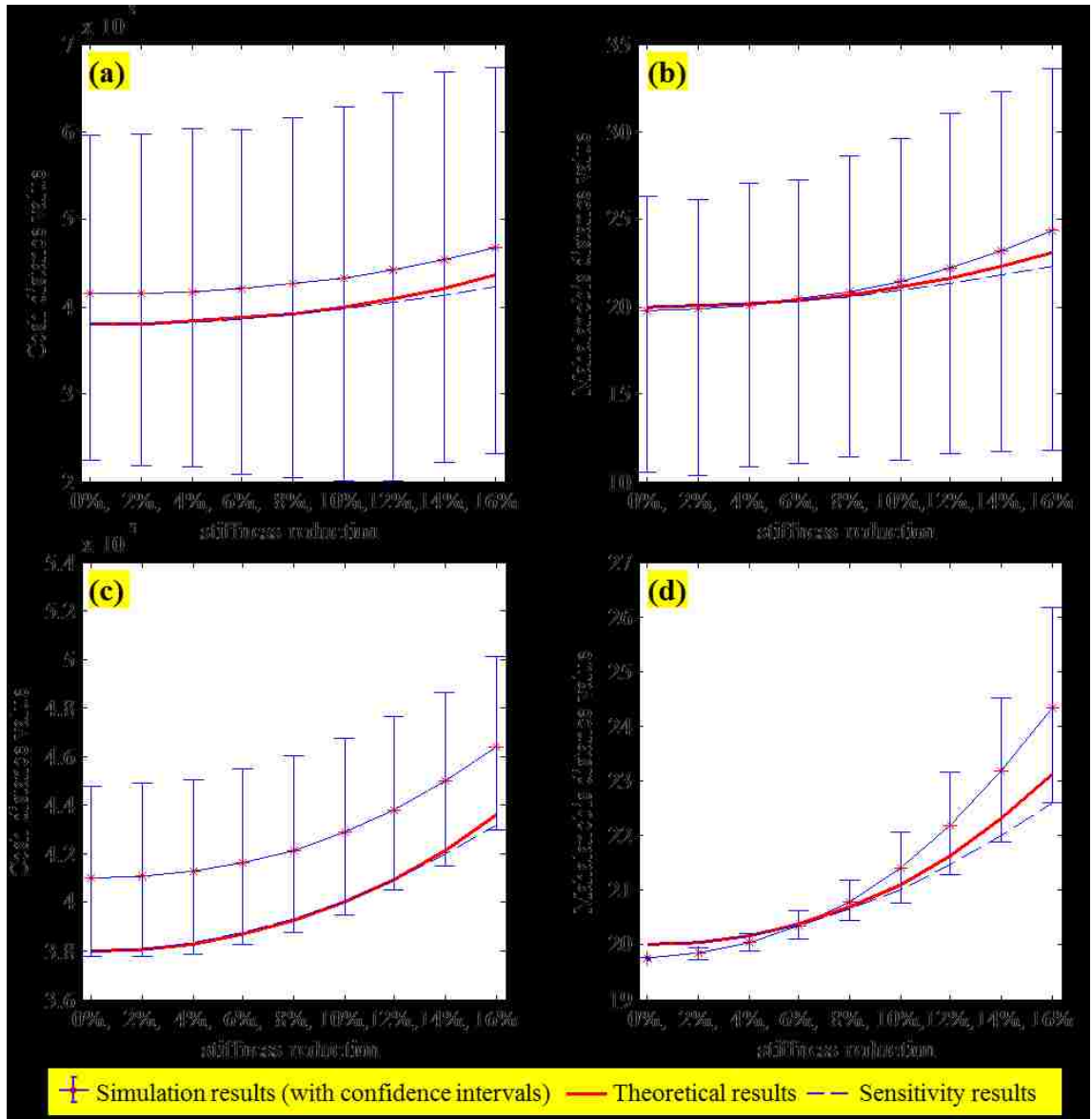
Figure 6.6   Plots of the damage feature values obtained as the stiffness of

the element between 4 and 5 decreases. Plots (a) and (b) show

simulation results from one experiment, (c) and (d) show the

average simulation results from 50 runs.
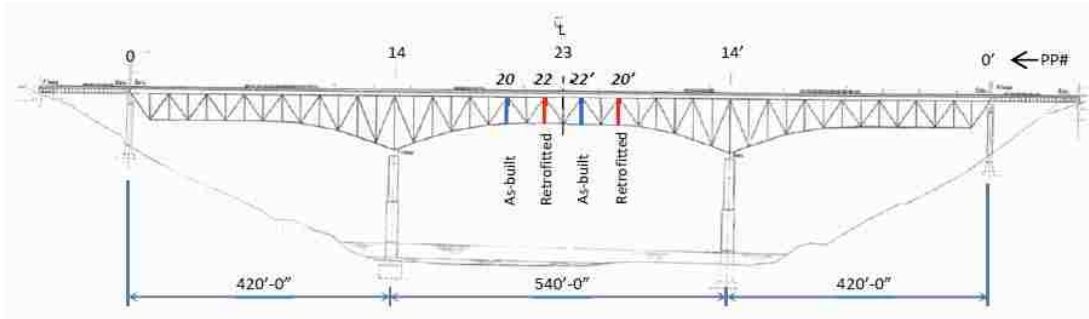
Figure 6.7   Side view of the truss bridge looking north (courtesy of Mr.

Ian C. Hodgson)
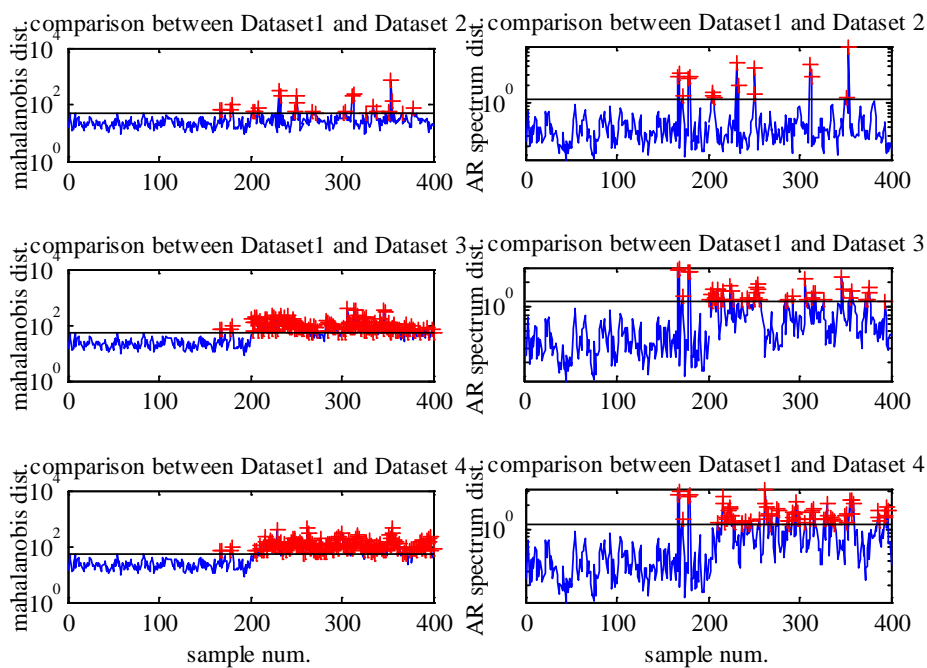
Figure 6.8   Mahalanobis distance and Cosh distance plots from AR

estimation using ambient acceleration

135
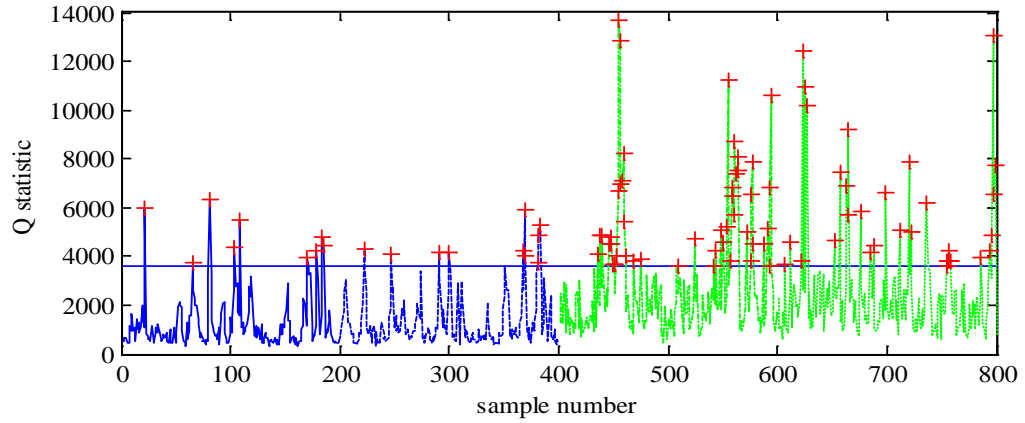
Figure 6.9   Ljung-Box statistic plot from AR estimation using ambient

acceleration
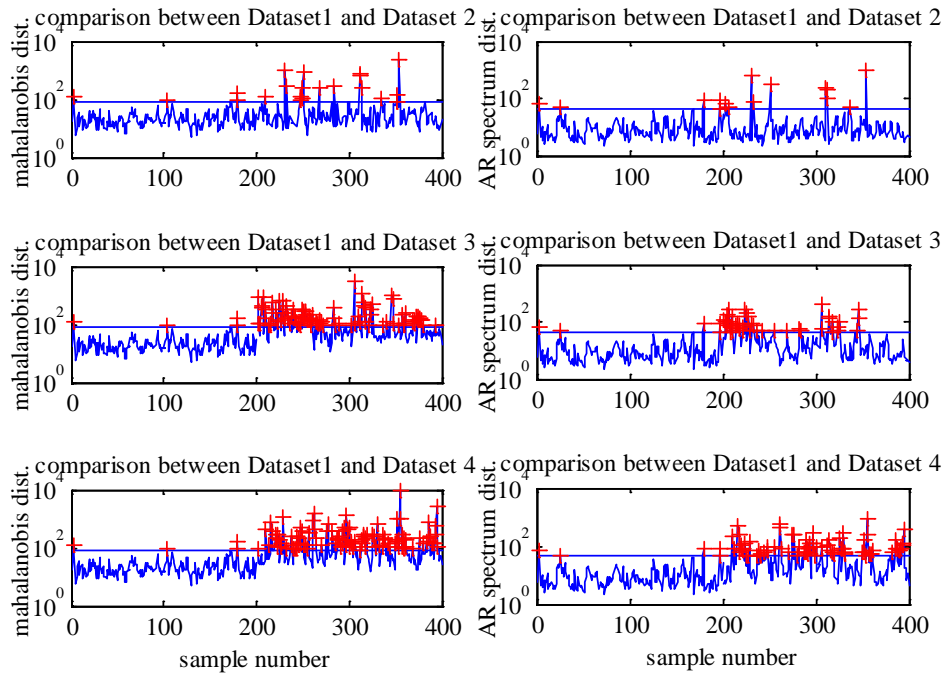
Figure 6.10   Mahalanobis distance and Cosh distance plots from AR

estimation using signal ACovF
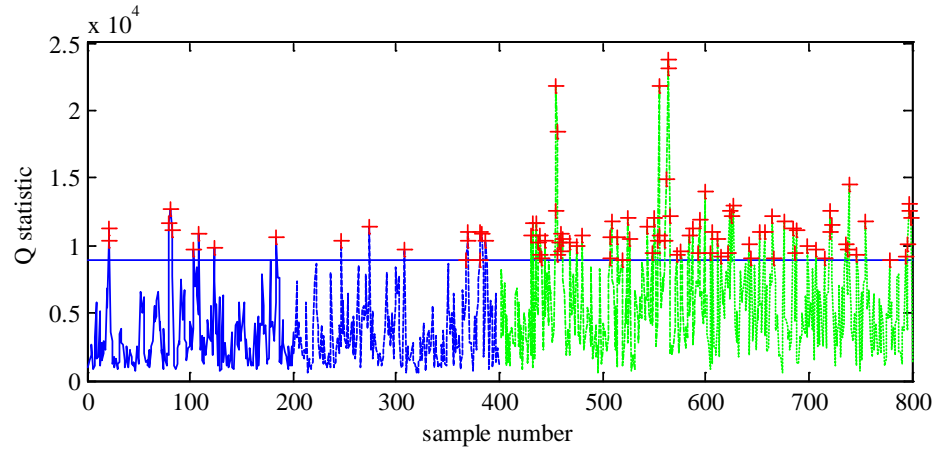
Figure 6.11   Ljung- Box statistic plots from AR estimation using signal

ACovF

Part II

Chapter 7 **Introduction**

7.1 OVERVIEW

In Part I, univariate TSA on vibration measurements have been successfully adopted for damage identification purposes in different applications. This method bears certain similarities to traditional system identification as both are concerned with numerical modeling, yet the former is more flexible because it uses various damage features that do not necessarily have an explicit physical meaning. Damage features can be functions of either model parameters or model coefficients, and well-known statistical concepts are applied to set the critical damage threshold for the features extracted. Since the method only utilizes responses from a single sensor node at each time, it is relatively sensitive to local damage. But for the same reason, the results produced become less reliable when the environmental condition is not stationary. Moreover, the damage location in general cannot be inferred from the value of the damage indices, confining the application of this method to preliminary damage detection.

In general, structural modal properties exhibit better stability than single channel TSA features. But as noted in Part I, modal realization/system identification methods can be computationally expensive to implement for large systems with a high number of sensing locations. Also, the estimated modal properties do not directly yield light on possible damage location and extent (P. Chang et al., 2003; Doebling et al., 1998). Though there are several methods that employ the modal properties for estimation of the stiffness matrix as the pseudo-inverse of the structural dynamic flexibility matrix

138

(Doebling, 1995; Salawu and Williams, 1993), these estimators are often not accurate enough as high order modes of civil structures, which contribute significantly to the structural stiffness matrix since they are associated with large system eigenvalues, are often outside the measured bandwidth. In (Bernal, 2002) a damage detection strategy using measured flexibility matrix is introduced, but its implementation requires an analytical model of the structure to be known beforehand. Thus for a general understanding of the structural vibration characteristics on a macro scale system identification techniques are useful, but for local structural damage identification more efficient methods are needed (Doebling et al., 1998).

Thus, in response to the robustness problem of scalar TSA damage features and the efficiency problem of modal property features, features from multi-input-single-output modeling based on sensor clusters have been investigated in several independent researches as a viable alternative for damage localization. Examples of such sub-structural analysis techniques include Chebyshev series expansion(Hernandez-Garcia, Masri, Ghanem, Figueiredo, and Farrar, 2010a, 2010b), iterative optimization(Hou, Jankowski, and Ou, 2011) and ARX modeling (Kuwabara, Yoshitomi, and Takewaki, 2013; Xing and Mita, 2012). This family of methods employs a smaller number of sensing channels than global system identification, and is more stable than single channel approaches as it utilizes responses along the substructural boundaries as the input to the subsystem.

7.2 RESEARCH OBJECTIVES
Many of the current substructural analysis methods are 'black-box' approaches that rely solely on numerical data-mining models, do not take into account the structural

topology, and produce outputs that do not have explicit physical interpretation. For those techniques that do consider the physical implications of substructural modeling parameters, often they are designed only for ideal structures such as shear frames. To expand the application scope and improve the efficiency/effectiveness of substructural approaches, the following tasks are identified and addressed herein:

1. Efficient heuristic MISO damage features formulation and validation (Chapter 8)

2. New substructural modeling techniques based on standard linear regression in time and frequency domain for stiffness estimation and damage detection in frame structures with relatively rigid floor/beam systems (Chapter 10)

3. Generalized time/frequency domain regression techniques using beam substructural elements for damage localization in more complex structures. (Chapter 11)

7.3 SUMMARY OF CONTENTS

Chapter 8 presents a summary of the strain gages used specifically for research presented in Part II (multivariate information fusion using substructural modeling), a literature review on the current substructural modeling techniques such as ARX modeling, neural networks etc. for high-level damage detection, and an illustrative example about the application of ARX modeling to a 3D steel truss. The truss structure is an elongated version of the truss described in Part I, with improved support conditions. For damage localization, ARX modeling operates on several adjacent sensing channels in a space truss structure. The damage features are extracted as variance ratios and Ljung-Box statistics of the residuals obtained via fitting the baseline model to data from the

140

current structure. It is shown that the damage indices extracted from the damaged substructure exhibit the most obvious change.

Chapter 9 includes some heuristic substructural modeling approaches. As the adjective indicates, these methods are based not on derivations but rather experience/intuition. One attempt for multivariate damage localization is the estimated mutual information statistic between data from adjacent sensing channels. The damage identification/localization results in the 3D truss obtained from this approach and the ARX modeling (Chapter 8) are then compared to those from univariate AR modeling to evaluate their relative pros and cons. Also presented in this Chapter are three substructural damage detection algorithms based on time domain memoryless regression. One of them is the Influence Coefficient method already described in Section 5.3, Chapter 5, and the rest two are enhanced version of the first one with more complex modeling schemes. They are then applied for damage identification in a two-span steel girder in the lab. They have different modeling complexities, and thus have different performance levels. Damage identification/localization/severity evaluation results obtained from these algorithms are compared and contrasted.

Current methods for obtaining insight into structural properties from vibration signals often either require responses from a large group of representative DOFs of the structure to produce accurate and consistent results (e.g. modal realization) or do not explicitly reflect possible structural damage locations and extent (e.g. 'black-box' substructural approaches). In **Chapter 10**, two novel regression-based techniques that use local acceleration responses of a frame structure to estimate its local stiffness are proposed. One employs displacement simulation methods; the other is based on spectral estimates.

141

Both methods are proven effective in their application to data collected from two laboratory specimens that are subjected to white noise excitation.

To apply the regression-based substructural approach to structures with more complex geometry, they should be generalized to substructures of different forms. In **Chapter 11**, multiple substructural damage identification models based on regression between internal responses and boundary responses of individual beam element in either plane or three-dimensional space are derived. Three damage indices are defined from regression model characteristics, and two change point analysis methods are adopted to capture changes in damage index sequences which are extracted from structural monitoring datasets from healthy and unknown states. Possible damage locations are identified as where the most significant changes in damage indices occur, and a voting scheme is used to synthesize results from different algorithms. This damage detection approach is straightforward and efficient, with the regression coefficients directly related to structural stiffness properties. Numerical and experimental application results show that the method successfully identifies and locates structural change for most of the cases.

142

Chapter 8   **Background**

The goal of SHM is to detect structural anomaly at an early stage so that proper repairs and retrofits can be implemented for normal operation of the structure (Farrar and Worden, 2007). The family of substructural damage detection approaches attempts to reach a balance between algorithm damage sensitivity and performance stability. Its computational complexity falls in between that of global modal realization and of single-channel TSA. However, because higher-level damage detection (damage localization and extent quantification) is involved, more detailed considerations will be needed for data acquisition and/or numerical model development. In the following text, brief accounts on the sensors used and existing substructural methods will be given.

8.1 SENSORS FOR SHM APPLICATIONS: PART II

Apart from the accelerometers mentioned in Section 2.1, strain gages are also employed in Part II to provide a different perspective on structural behavior. Two types of linear-pattern strain gages produced by Measurements Group Inc. are used in experimental investigations in later chapters (Vishay Precision Group, 2010a, 2010b).

The strain gages used on the frame in the laboratory are quarter-inch long model CEA-09-250UW-120. Before the gage is applied, the steel surface is rubbed and cleaned to ensure good contact between the gage and the frame. The gage is then glued to the surface and two wires are soldered on to the gage. A protective layer is then applied to cover the gage. The gage resistance is 120 ohms.

143

All strain gages installed on the steel truss bridge in western Pennsylvania were 0.25 inch gage length model LWK-06-W250B-350 (see Figure 3.1). These gages are uniaxial weldable resistance-type strain gages. Weldable-type strain gages were selected due to the ease of installation in a variety of weather conditions. The "welds" are point or spot resistance welds about the size of a pin prick. The probe is powered by a battery and only touches the foil on which the strain gage is pre-mounted by the manufacturer. This fuses the foil to the steel surface. It takes forty or more of these small "welds" to attach the gage to the steel surface. There are no arc strikes or heat affected zones that are discernible. There is no preheat or any other preparation involved other than the preparation of the local metal surface by grinding and then cleaning before the gage is attached to the member with the welding unit. There has never been an instance of adverse behavior associated with the use of weldable strain gages including their installation on extremely brittle material such as A615 Gr75 steel reinforcing bars. These strain gages were used in a quarter-bridge configuration. The gage resistance was 350 ohms and a bridge excitation voltage of 10 volts was used.

Pictures of the two strain gage models are presented as Figure 8.1 and Figure 8.2. The wired strain gages can share data acquisition systems with wired sensors.

8.2 EXISTING DATA PROCESSING METHODS FOR SHM: PART II
Here the discussions will revolve around substructural modeling for damage detection.

8.2.1 Substructural approaches for damage detection
Substructural approaches have been studied for damage identification from various aspects. Some researches centers on the evaluation of conditions for substrucural

144

identification, some form the relation between substructural properties and global system characteristics, and others concentrate on the performance evaluation of certain substructural methods through numerical/experimental applications. The remainder of this section focuses on the literature review and application of this family of approaches.

8.2.1.1 Methodology review

Substructural identification bears similarities with the standard system identification; only in the former case the boundary conditions/interactions need special conditions as they are often time-variant. Xie et al. (2010) presented a set of conditions under which a substructure is identifiable using measured excitation and response signals. Van den Hof et al. (1992) give a set of relaxed conditions for identifiability of closed loop systems. If the global system physics can be accurately inferred, they can be used to derive substructural parameters: Park, Reich, & Alvin (1998) presented a method to extracted subsystem flexibility matrices from global flexibility matrix. Different application examples of substructural approaches for damage detection can be found: In Yan et al. (2011) artificial neural network training is used to detect substructural damage within mass-spring and multi-story systems. Gul and Catbas (2010) applied autoregressive with exogenous input (ARX) modeling to measurements collected from clusters of sensors for damage localization in a numerical mass-spring system and a steel grid set up in a laboratory. To sum up, substructural approaches have received the attention of many researchers because of their potential for dencentralized damage localization.

8.2.1.2 Implementation example

As an illustration example of the substructural damage localization philosophy, in this subsection sensor-cluster based ARX modeling will be applied to a truss structure similar to that introduced in Section 2.2.1.2.

145

Definition of ARX model

The single-input-single-output (SISO) ARX model (L. Ljung, 1987) is defined as follows (note that this definition is different from that for AR-ARX analysis as in Eq. (4.2)):

$$x(t) = \sum_{i=1}^{a} \alpha_i x(t-i) + \sum_{j=1}^{b} \beta_j u(t-j) + e_x(t).$$

(8.1)

where $x(t)$ and $u(t)$ are the output and input signal, respectively. The parameter set (a,b) defines the order of the ARX model. Notice that this is also a linear regression model that associates the current response of a signal with its previous values and an exogenous input. If there are several exogenous inputs (multi-input-single-output case), each input will have its corresponding coefficient vector $\{\beta_j\}$.

Here when this model is applied for damage identification, the output signal will be from a certain sensor node (possibly at a potential damage location) and the input signals will be from its neighboring nodes. Here the damage indicators will be computed from residuals analysis, with the general procedure almost the same as that for univariate AR modeling. Model parameter based analysis will not be attempted here because it will require estimation of the multivariate model for many times, thereby resulting in high computational cost.

Modal order selection here can again use AIC/BIC(Brockwell and Davis, 2002)or other fitness indices, only that here optimal model order search would be bi-directional instead of unidirectional because there are two parameters (a and b) to be determined.

146

The algorithm described above is applied to acceleration measurements collected from a space truss in the lab (Figure 8.3). It consists of same members as the truss presented in Chapter 2 and Chapter 4, only it is two bars longer and has modified supports. The truss has its four corners fixed to sturdy I-beam sections, and 10 wireless sensors are mounted on the truss nodes in the midspan. Artificial damage is introduced by removing one interior diagonal member between sensor node 1 and 8. For each structural state(undamaged/damaged), two sets of data are collected at a sampling frequency of 280 Hz. As an effort to reduce the noise content, a low-pass filter is applied to all the data, which are subsequently downsampled to 70 Hz. The compressed data is then used as input to the damage detection algorithms, and dataset 1 is the selected baseline signal for all the implementations.

Damage detection results from ARX modeling

Here the acceleration measurements in the vertical direction from sensor node 3 and 8 are used as output in the ARX model, and measurements from their respective neighboring nodes will be used as the model input. Table 8.1 summarizes the normalized residual standard deviations and the log Ljung-Box statistic (Eq.(4.5)) of residuals computed from signals 1-4. In the first column of the table, the number before the slash represents the output sensor node, where those after the slash are the input nodes. And for the subscripts of these numbers, x stands for measurements in the vertical direction, and y the horizontal translational direction. Damage localization can be achieved by comparing results from models constructed with different output nodes (e.g. node 3 vs. 8), and/or models with different combinations of exogenous inputs; a more significant increase in feature values can be observed for models using the sensor 8 as the output

147

node, and for the models that include all neighboring node responses as inputs. Note that the artificial damage occurs between sensor 1 and 8. Because here only 10 truss nodes are instrumented with accelerometers, results from other nodes cannot be presented as the responses of several of their neighbor nodes are unknown.

Table 8.1   Results from the MISI ARX method. The standard deviations are all

normalized with respect to the baseline.

		dataset 1	dataset 2	dataset 3	dataset 4
$3_x/1_x,2_x,4_x,5_x,10_{x,y}$	normalized σ_e	1.000	0.962	1.576	1.460
	log Ljung-Box statistic	5.504	6.070	8.706	7.999
$8_x/1_x,6_x,7_x,9_x,10_{x,y}$	normalized σ_e	1.000	0.990	2.127	1.905
	log Ljung-Box statistic	5.107	5.873	9.596	9.696
$3_x/1_x,2_x,4_x,5_x$	normalized σ_e	1.000	0.937	1.257	1.254
	log Ljung-Box statistic	5.618	6.155	8.153	7.665
$8_x/6_x,7_x,9_x,10_{x,y}$	normalized σ_e	1.000	0.993	1.479	1.264
	log Ljung-Box statistic	5.210	6.148	9.563	8.602

Figure 8.1   strain gage model CEA-09-250UW-120, instrumented on the

2-bay frame
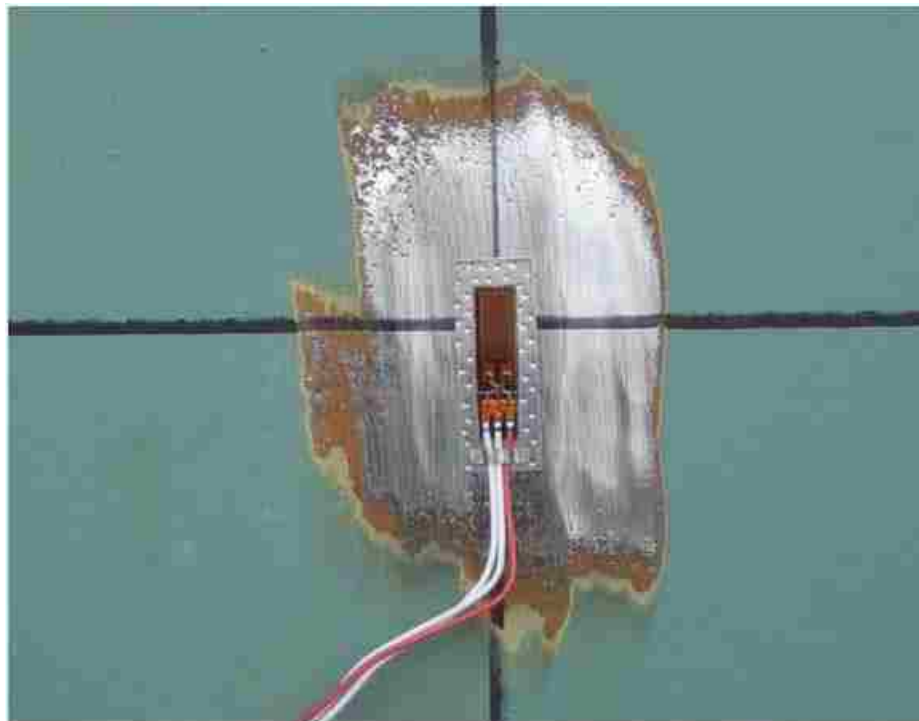
Figure 8.2   Strain gage model LWK-06-W250B-350, instrumented on the

truss bridge vertical (courtesy of Mr. Ian C. Hodgson)
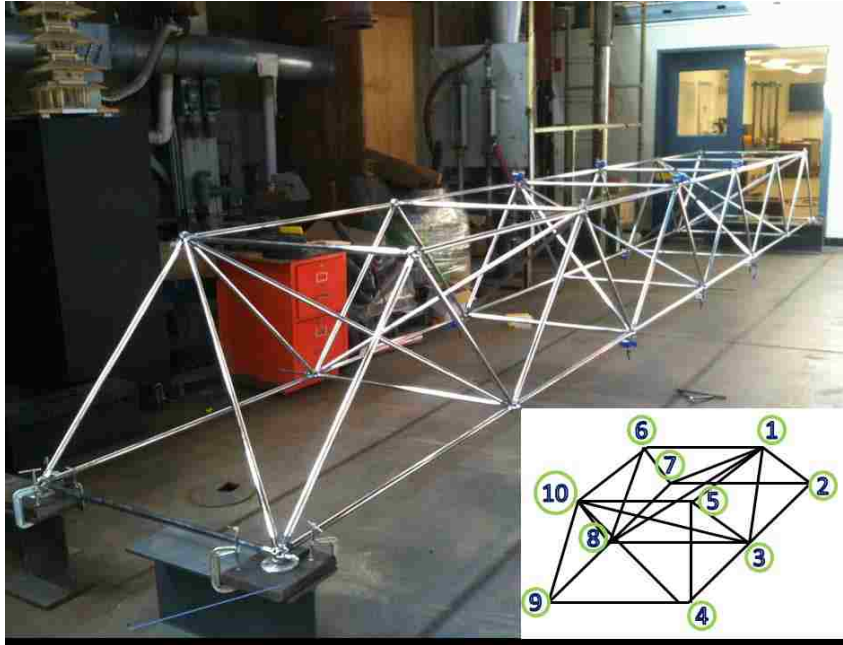
Figure 8.3   The space truss model with the sensor node numbers shown in

the lower right corner

Chapter 9 Heuristic multivariate approaches for high-level damage detection

9.1 PRELUDE

As noted in previous chapters, Substructural approaches attempts to combine the merits of univarite TSA and system identification, while trying to outperform both of them in the aspect of damage localization/extent quantification. Substructuring concept has already been used in Finite Element Methods to facilitate modeling for complex structures through condensing out the internal DOFs. It has recently been applied for damage localization by virtue of the need to quantify the interface reactions between the local system and the rest of the structure. Substructuring methods typically use responses from adjacent nodes to form an input-output damage identification model. In general, input-output methods are more reliable and accurate than output-only methods. Hence this family of approaches should be more robust to excitation variation than the 'single node' approaches, and still remain computationally efficient as they concerns mainly small-scale multivariate analysis.

For the consideration of high-level damage detection, the magnitudes of damage indices produced at different locations should reflect the amount of damage occurred that this locations. Ideally, the indices should carry some explicit interpretations pertaining to the structural physics. But to achieve this end, both methodological theoretical analysis of the structural behavior and the signal characteristics and detailed experimental calibration will be needed. Thus, it is advisable to examine a few multivariate numerical/heuristic modeling techniques to quickly evaluate the damage detection potential of substructural approaches before going into more complicated studies.

9.2 MOTIVATION AND ORGANIZATION

Heuristic approaches are not based on rigorous derivations; rather, they are brought forward by observation or experience. Intuitively, when damage occurs at some point in a structure, the correlation of signals collected at the two sides of the damage will reduce. Thus, the mutual information (Cover and Thomas, 2006) between two sensing channels is used for damage detection here. This statistic is expected to decrease in occurrence of damage between the locations of the two sensing channels.

The influence coefficients (IC) method, as mentioned in chapter 5, provides a viable way to identify change in relatively stiff structures/substructures but is not necessarily a good damage indicator. Here, multivariate regression coefficients between substructural intermediate response and substructural boundary responses are proposed: one is the improved influence coefficients (IIC), which are obtained by regressing a node's acceleration responses on those from all its adjacent nodes; the other is influence coefficients using hybrid vibration responses(ICHVR) that are from regression models that incorporate in the regressor matrix not only acceleration responses at neighbor nodes, but also strain data from close-by nodes. Compared with the original ICs, they are from more refined substructural models, and are expected to yield better damage localization performance.

The mutual information statistic, along with some of the univariate TSA damage indices, is applied to the same truss structure described in Section 8.2.1.2. The specimen is relatively flexible, and therefore is a good testbed for dynamic modeling algorithms. The damage detection performances of this method and ARX modeling are then compared with those of univariate TSA approaches. The IC, IIC and ICHVR are applied

153

to the frame structure first introduced in Section 5.6, which is a quite stiff structure. Their damage localization performances are then cross-compared.

The rest of this chapter will be organized as follows:

- Section 9.3 is a brief review of the univariate AR modeling method for damage identification.
- Section 9.4 presents the multivariate AR modeling method and the mutual information method.
- Section 9.5 gives a detailed description of the formulation of modified influence coefficients.
- Section 9.6 contains the application of the established and new temporal substructural modeling methods to acceleration measurements collected from the space truss structure (Figure 8.3) under ambient loading.
- Section 9.7 includes the experimental validation results of all three algorithms on the 2-bay truss structure (Figure 5.4).
- Section 9.8 concludes on the performances of different algorithms through cross-comparison for each case study.

9.3 UNIVARIATE AR TIME SERIES ANALYSIS FOR DAMAGE IDENTIFICATION: A REVIEW

Autoregressive models have long been successfully applied to model, validate and predict signals from various types of sources. The definition of a univariate AR model is introduced as Eq. (2.1) in Section 2.2.2.2 .

Univariate AR model parameters can be very efficiently estimated from a signal using one of the standard algorithms. According to the specific feature extraction process,

154

the damage features from AR model can be classified into two categories: model coefficients based and model residual based. In the remainder of this section, examples from both categories will be presented. For the first category, Mahalanobis distance of AR coefficients (Section 3.3.1) and Cosh distance of AR model spectrum (Section 4.4.2, Figure 4.3) will be used. And for the second category, the residual autocorrelation function (ACF, Section 3.3.2) will be adopted. When the system is damaged, the amplitudes of these features would increase.

9.4 DAMAGE IDENTIFICATION/LOCALIZATION USING MULTI-CHANNEL RESPONSES

Time series analysis on measurements from a single sensor node provides an efficient way for damage detection. However, applications have shown that their effectiveness as damage location indicator depends on the specific structural type. Also, due to the information limitation, this family of methods tends to suffer from false alarms when the environmental conditions are varying. Here in this section, the mutual information feature constructed from measurements from two adjacent sensors will be introduced in hope of improving algorithm stability and damage localization capability.

9.4.1 Mutual information between signals collected from adjacent nodes

Mutual information (Cover and Thomas, 2006) is a statistic defined to measure the mutual dependence/similarity between random variables (Figure 9.1). It is first proposed in communication theory to quantify the capacity of data transmission channels. Given the probability distributions of two random variables X and Y, their mutual information can be computed as:

$$I(X;Y) = \int_X \int_Y p(x,y) \log \frac{p(x,y)}{p(x)p(y)} dxdy. \tag{9.1}$$

155

$p(\cdot,\cdot)$ and $p(\cdot)$ here denote the joint and marginal probability distribution. It is clear that the value of this metric is always non-negative, and equal to zero only when X and Y are statistically independent. The definition can also be easily extended to the case where X and Y are random vectors.

If both X and Y are assumed to follow a Gaussian distribution, then the mutual information statistic can be obtained directly from their second-order statistical moments:

$$I(X;Y) = \frac{1}{2}\log\frac{|K\{X\}||K\{Y\}|}{|K\{X,Y\}|}. \tag{9.2}$$

where $K\{X\}$ stands for the variable covariance matrix and $|\cdot|$ is the matrix determinant. Mutual information can be more efficiently estimated from this formula than from the previous one, as it requires only the variance of the variables, instead of the complete distribution.

In the implementation section, mutual information between responses from two adjacent sensors will be employed as damage index. If damage (stiffness reduction) occurs between these two nodes, then it is expected that their mutual information value will decrease significantly. Since structural responses at any measured location are always correlated over time, they cannot be treated as single random variable. Rather, a time window of length L will be applied to each response signal and the estimated mutual information $\hat{I}(x_1(t); x_2(t))$ between two signals $x_1(t)$ and $x_2(t)$ becomes:

$$\hat{I}(x_1(t); x_2(t)) = I(x_1(t), x_1(t+1),...,x_1(t+L-1); x_2(t), x_2(t+1),...,x_2(t+L-1)) \tag{9.3}$$

Here the parameter L needs to be chosen with care so that the autocorrelation of signals after Lth lag will be close to zero.

9.5 LINEAR REGRESSION COEFFICIENTS AS DAMAGE INDICES

In this section time-domain linear regression based algorithms for damage identification are presented. These methods are computationally efficient and easy to implement, and thus effective for fast damage prognosis and on-line decision making regarding the current structural state. Three approaches will be included the remainder of this section; they follow the same principles, only with different modeling complexities.

9.5.1 The Influence Coefficients (IC)

If a linear structure is subjected to a static/quasi-static load, then the ratio between responses at any two arbitrary locations should be a constant as long as the structural condition and load pattern stay the same. Therefore, the linear regression coefficient $\alpha_{j,i}$ between responses collected at two nodes i and j can be used as a viable damage index (Labuz et al., 2010, 2011). A detailed description of the feature extraction and examination process can be found in Section 5.3.

When the load is actually dynamic, this method can still be applied to a local area of the structure, where the stiffness is large and the mass is comparatively small. In the subsequent section, this method will be applied to acceleration signals from a steel girder subjected to a white noise excitation.

9.5.2 The Improved Influence Coefficients (IIC)

It can be seen that influence coefficients are estimated from a very simple model. If the goal is just to detect the existence of major damage, they may suit the purpose. But if higher level damage detection (e.g. damage localization; damage severity assessment) is

needed, then the regression model needs to be refined to capture the local vibration behavior.

An improved influence coefficient approach is proposed here by incorporating, for responses from a given sensor node, all its neighboring nodes' responses. The mathematical expression for this algorithm can be expressed as follows:

$$u_j\left(t_k\right) = \sum_{i=1}^{n}\alpha_{j,i}u_i\left(t_k\right) + \varepsilon(t_k) \tag{9.4}$$

Here u_i stands for the vibration responses collected from a certain adjacent node of sensor j, and n is the total number of adjacent nodes of j. This algorithm is more complicated than the IC approach not only in the sense of an increased number of parameters, but also in that it actually takes into account the structural geometry and sensor network topology.

9.5.3 Influence Coefficients from Hybrid Vibration Responses (ICHVR)
If the end displacements and rotations of a Finite Element Model for a beam element are known, then the deformation at any point along the element can be computed using a set of interpolation functions. In practice, it is difficult to measure dynamic joint rotations; however, strains, which reflect end moments, can be measured through strain gages. With the end displacements and moments known, the complete behavior of a beam is known.

The regression model can be further modified to include the strain data from neighboring nodes:

158

$$u_j(t_k) = \sum_{i=1}^{n} \alpha_{j,i} u_i(t_k) + \sum_{l=1}^{m} \beta_{j,l} \phi_l(t_k) + \varepsilon(t_k) \qquad (9.5)$$

where ϕ_ls are the strain measurements from adjacent nodes of node j, and $\beta_{j,l}$ is the corresponding regression coefficients. This technique is the most complex of the three, and is expected to yield the most accurate performance on damage identification and prognosis.

Damage thresholds for the above three indices need to be created to determine if the variation in the estimated influence factors from an unknown structural state is significant enough to categorize it as damaged. It is also important to note at what confidence this level of damage has been identified, and also if multiple damage location have been detected. In order to make conclusions about these inquiries, a change point analysis (Taylor, 2000) that utilizes a combination of the cumulative sum method and bootstrapping (Good, 2001) is used here. A complete description of the procedure is given in Section 5.5.1. Only influence factor sequences with the maximum absolute cumulative sum S_{max} outside a 95% confidence level (Koch, 1999) were considered as from the damaged state.

9.6 EXPERIMENTAL VALIDATION OF THE TEMPORAL MODELING ALGORITHMS

The statistical algorithms described in Section 9.3 and 9.4 are applied to acceleration measurements collected from a space truss in the lab. Details on the experimental setup and signal collection can be found in Section 8.2.1.2. Dataset 1 is the selected baseline signal for all statistical damage detection implementations here.

159

9.6.1 Damage identification results from univariate AR coefficients based method

Figure 9.2 shows the model coefficient based Mahalanobis distance features and model spectrum based Cosh spectral distance features extracted from different datasets. The first two datasets are from the healthy state of the structure, and the last two datasets are from the damaged state. In application of both methods, the signals are divided into many short segments with large overlap among them so as to produce enough AR coefficient vectors from them for structural state evaluation. It can be seen from the plots that after the damage, a lot of outliers will appear. Also, the Mahalanobis distance method is not as stable as the Cosh spectral distance, i.e. more false alarms are observed in plots of the former. This is because spectral distance generally assigns more weight to the position of system poles than that of system zeros, and thus is less susceptible to noise disruptions. Both damage indices are ineffective damage location indicators in this case, as the magnitude of change in feature values as a result of damage is more or less the same for the two sensing locations, despite one is much closer to the damage than the other.

9.6.2 Damage identification results from univariate AR residuals based method

As stated in Section 2, damage detection can also be based on the autocovariance/ autocorrelation function of the residuals. Figure 9.3 contains the ACF plots of the residuals obtained from applying the AR modeling to measurements at sensor 4 and 8. After the structure is damaged, the absolute values of the ACF at non-zero time lags increase significantly. Accordingly, an increase in Ljung-Box statistic of the residual series will also be observed. Due to space limitations, however, its results are not presented here.

160

9.6.3 Damage identification results from mutual information method

The damage index based on mutual information, like the ARX based indices (Section 8.2.1.2), also succeeds to identify the damage existence and location. Figure 9.4 is a series of plots containing the estimated mutual information obtained from vertical acceleration measurements from pairs of adjacent nodes. Five estimates are computed from each dataset. In each of these plots, the features are normalized with the mean from the baseline sample group to facilitate cross-comparison. It can be observed that the damage features based on the node pairs located in the vicinity of damage exhibited the most significant change in their values. In addition, the estimates based on nodes that do not lie in the same vertical pane are more sensitive to damage than the rest, indicating that the damage occurs at the interior connections.

9.7 EXPERIMENTAL VALIDATION OF THE MEMORYLESSS REGRESSION ALGORITHMS

To test the accuracy of the three algorithms, three different damage scenarios were set up on a two-bay steel frame constructed from steel tubes first used in Chapter 5 (Figure 5.4). The frame is instrumented with 21 accelerometers and 9 strain gages. The first damage state is simulated by replacing the right beam end portion with a section of reduced stiffness, and 14 datasets were collected. The second damage mode consists of replacing the right bay, middle portion with a reduced stiffness member, with 20 datasets collected, and finally the third damage scenario consists of replacing the left bay, middle link with a reduced stiffness member, with an additional 20 datasets collected (Figure 9.5). For each case, half of the datasets are from the damaged case, and half are from the undamaged case.

Figure 9.6 shows the histograms of the change point locations. The most notable observation is that as the model complexity increases, the change point location indication becomes more exact. It can be seen that, for the first damage scenario, the IC method failed to identify the damage existence while the rest two succeeded. Also, for other damage cases, the histograms obtained from the IIC and ICHVR methods all have a sharper peak at the correct change point location than the established IC method.

Figure 9.7 are the damage localization results from different algorithms/scenarios. It can be observed that as the model complexity increases, the damage localization becomes more accurate. For all three damage scenarios, the IC method does not report change for the locations at/next to the damage, IIC method yield a more satisfactory performance, and the ICHVR identifies structural change at most places that are in the vicinity of actual damage. This further solidifies the point that the more complex the algorithm, the more accurately damage location is indicated. In addition, the sensors which reported only one regression parameter, has a higher likely hood of a false alarm. For more accurate results it is recommended to use regression models that report damage for multiple parameters.

Figure 9.8 contains plots of influence coefficients obtained from the node combinations at the damage location for the different damage scenarios. It is clear that as the model complexity increases, from algorithm 1 to algorithm 3, the difference between the undamaged data sets' average influence coefficients and damaged data sets' average influence coefficients becomes greater. Thus in this case study, adopting more complex and comprehensive models did help to better characterize the difference between the damaged and undamaged state, which is important for local/minor damage detection.

162

9.8 CONCLUSION

In this chapter, temporal and memoryless/instant-time substructural modeling approaches are devised and applied to separate specimens for their validation. Below are the conclusions drawn on the effectiveness of each family of methods.

9.8.1 Evaluation of the temporal substructural methods

A damage detection method using mutual information statistic on responses from two adjacent nodes is described and applied to acceleration measurements on a space truss model here. Its performance, together with the performance of MISO ARX modeling approach (Section 8.2.1.2), is then compared with those of the established damage identification techniques based on AR modeling of responses from a single sensing channel here. It is observed that the multivariate time series analysis produces viable damage indices and in the meanwhile is able to predict damage location with greater accuracy.

Univariate AR modeling algorithms has certain advantages when applied for damage identification; they are computationally efficient, suitable for on-sensor-board data processing, and sensitive to small scale damages. Their application to detect damage existence in the truss model is altogether successful. However, they are not always effective at damage localization. Moreover, since this family of algorithms monitors only the statistical properties of the measurements at a single sensor node, it is susceptible to changes in operation conditions that do not concern the structure itself. Such innate false-positive characteristic of these algorithms will make them unreliable for practice.

The MISO ARX modeling algorithm is slightly more sophisticated than the univariate AR method, as more parameters need to be estimated in the former case. But

then, the damage localization capability of the algorithm is visibly improved by adding

the neighbor nodes responses as external outputs in the model. Recognizing the increased

computational cost, the mutual information damage index is introduced and applied to the

specimen. This method is of a simpler formulation than the ARX algorithm, yet

nonetheless achieves the aim of damage detection/localization as shown in Section 9.6.

In summation, the multivariate time series analysis approach is proposed here as an

intermediate approach that seeks to combine the merits of traditional system

identification and univariate time series modeling. By including several responses from

adjacent nodes, model parameter estimation becomes less affected by excitation

variation; yet the model is still constructed on measurements from only a part of the

structure, thus retaining the sensitivity to local damage and algorithm computation

efficiency. The experimental application used here has confirmed the effectiveness of

proposed algorithms, and they will be further examined through implementation on

different types of structures in the future.

9.8.2 Evaluation of the instant-time substructural methods

Three regression-based damage detection algorithms are presented and applied for

damage diagnosis in a scaled two-bay steel frame specimen. The first algorithm, the

influence coefficients method, is an established node-pair-wise regression technique that

has been shown to be effective in several previous researches. The improved influence

coefficients method regresses responses from one node on those from all its adjacent

nodes. The influence coefficients using hybrid vibration responses further refines the

model by including strain data from neighboring nodes as regressors. It is demonstrate in

164

their application results that as the algorithm modeling complexity increases, so does their performance on damage identification and localization.

The research presented here addresses partly to the problem of optimal data collection and information compression and extraction in structural health monitoring applications. The quality of results on structural state diagnosis is directly related to the quantity of useful data and the truthfulness of the analysis model adopted. And when it comes to local damage identification, generally substructural analysis methods will be needed.

In finite element modeling, if there is a truss element in a structure, then to see if the element properties have changed, all that is needed is the displacements at the bar ends and the axial force. If further damage localization is desired, displacements at the midpoint of the member can be measured and used for analysis. The result will be exact as long as the data is accurate and the modeling assumption is correct, regardless of what the behavior of the rest of the structure is. If the data is contaminated by noise or if the real member is actually a beam element, then the result will become less reliable.

This simple example illustrates the general difficulties encountered when vibration-based damage identification is attempted: incomplete/ambiguous information and modeling error. For example, if the response at every location and the input at every location, and the basic constitutive relationship is known for a given structure, then damage identification is a simple task. But when only vibration responses from a limited number of sensors are available, damage identification, especially high level damage identification, becomes difficult. The performance of damage detection algorithms is largely dependent on the extent of the environmental and operational conditions, and the

165

validity of the assumptions. Still, the quest for automatic structural diagnosis system continues, and with the improvements of sensor technology and computing facilities, this goal is becoming more obtainable.

166
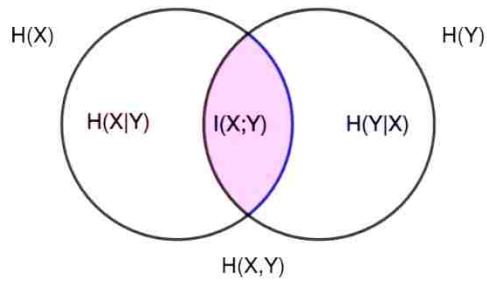
Figure 9.1   (Cover and Thomas, 2006) An illustration of the definition of mutual information as the sum of the separate entropies of two random variables X and Y subtracted by their joint entropy H(X,Y). Entropy is essentially a measure of uncertainty for random variables.

167
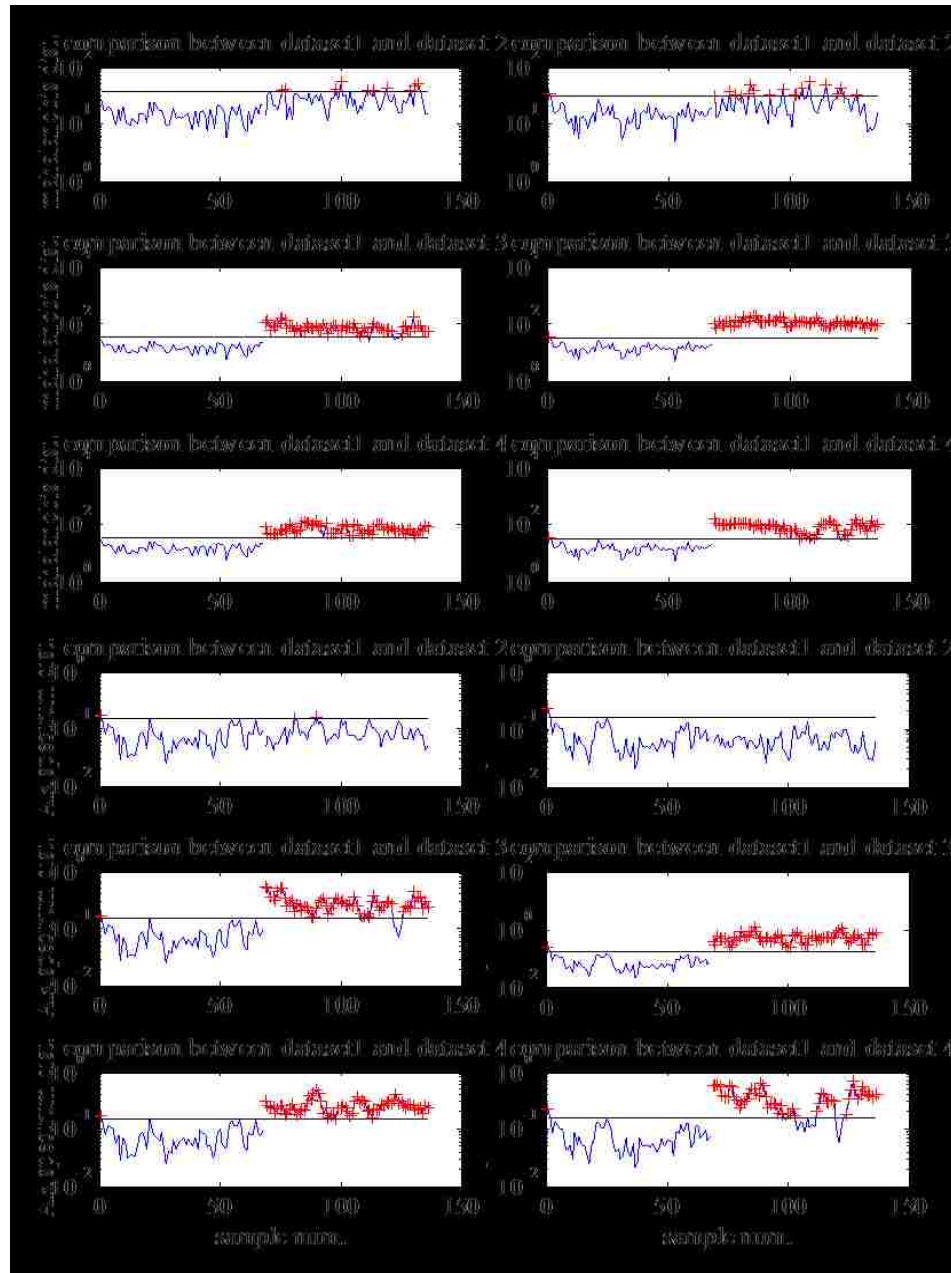
Figure 9.2   Damage identification results using AR coefficients based

method. (a) and (c) are the Mahalanobis distance and Cosh

spectral distance features obtained from measurements at

sensor 4, while (b) and (d) are those from sensor 8.
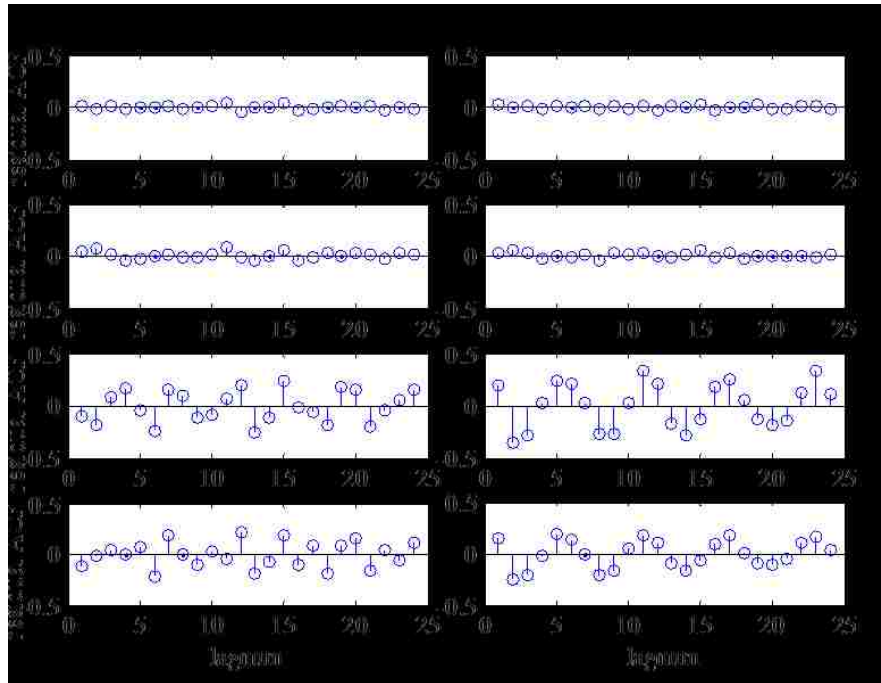
Figure 9.3   Damage identification results using AR residual based

method. (a) contains the residual autocorrelation function plots

obtained from measurements at sensor 4, with subplot 1-4

corresponding to dataset 1-4. (b) contains plots obtained from

sensor 8 using the same procedure. Dataset 1 is used as the

baseline here.

169
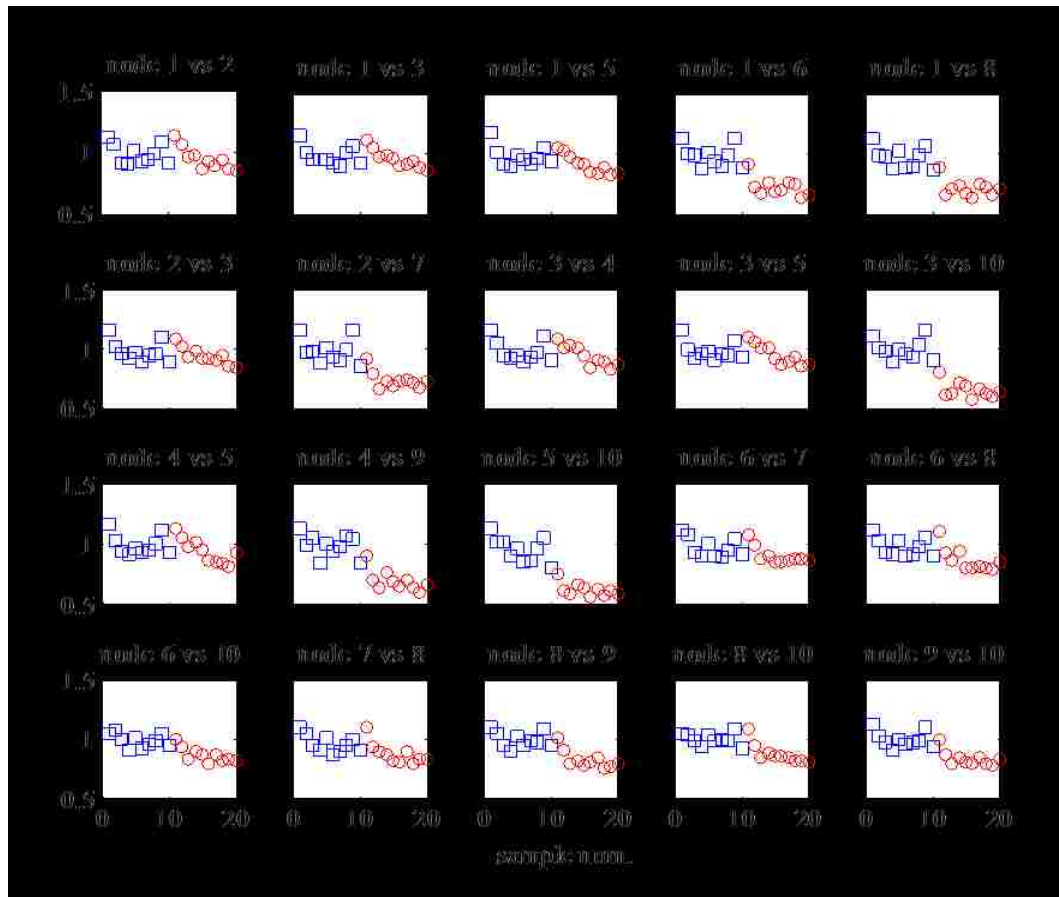
Figure 9.4   Damage identification results from mutual information

method. The blue squares are features from the undamaged

state, and the red circles are from damaged state.
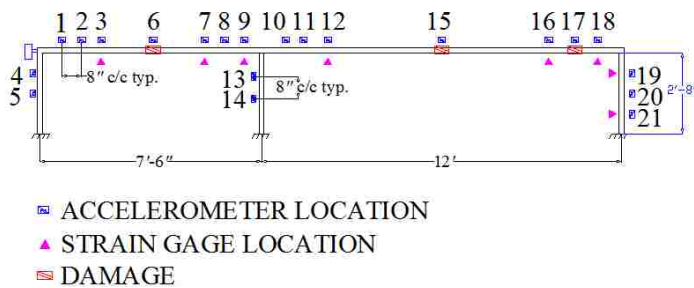
Figure 9.5   Two Bay Steel Frame Drawing with Strain Gauge and

Accelerometer Locations

170
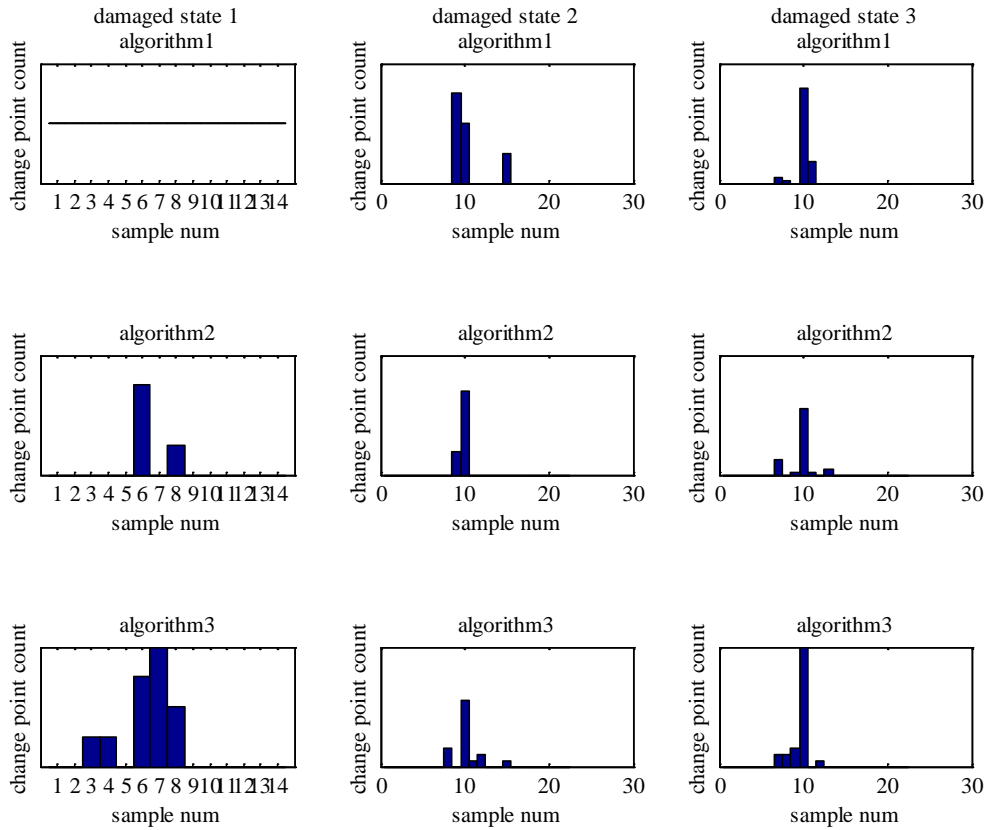
Figure 9.6   Histograms for the change point locations. Each sample

corresponds to a particular dataset. For each algorithm

implementation, there are a number of regression coefficients

sequences that report damage. Each histogram basically

pooled all these change point locations together.
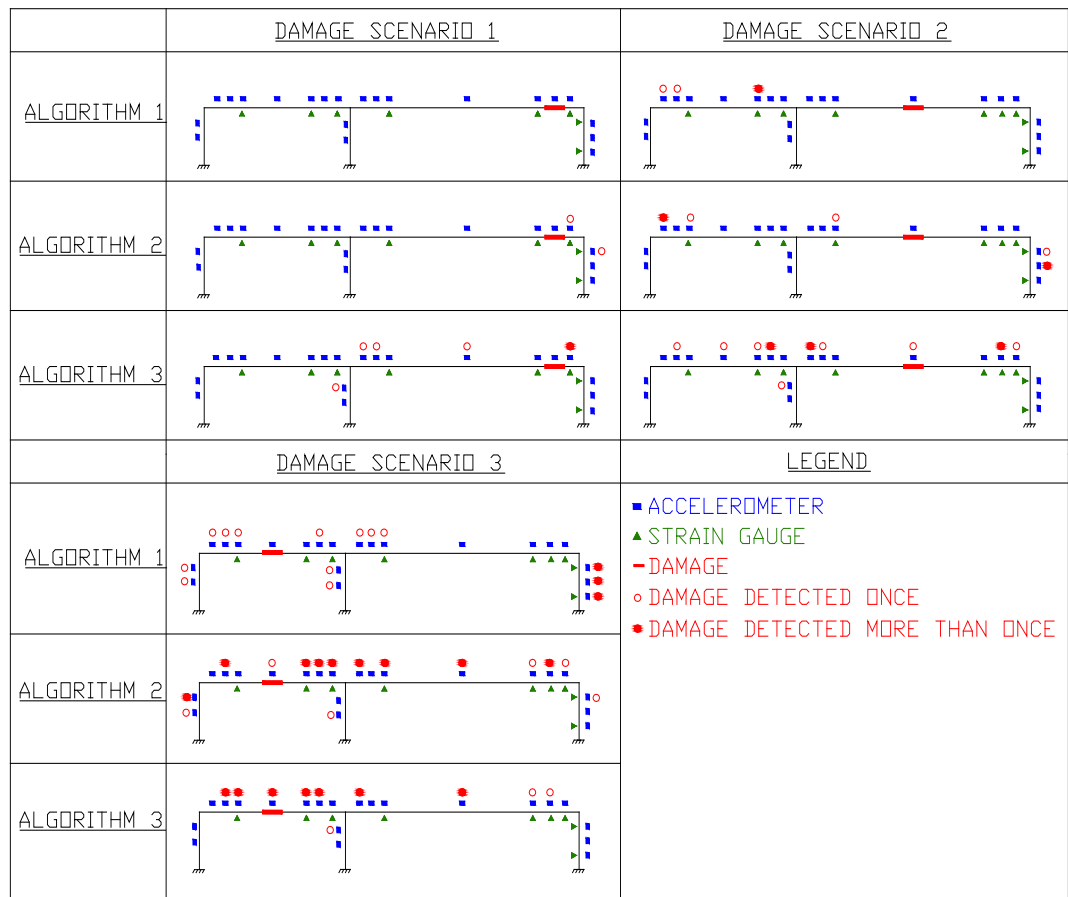
Figure 9.7   Examination of the damage localization capability of different

algorithms
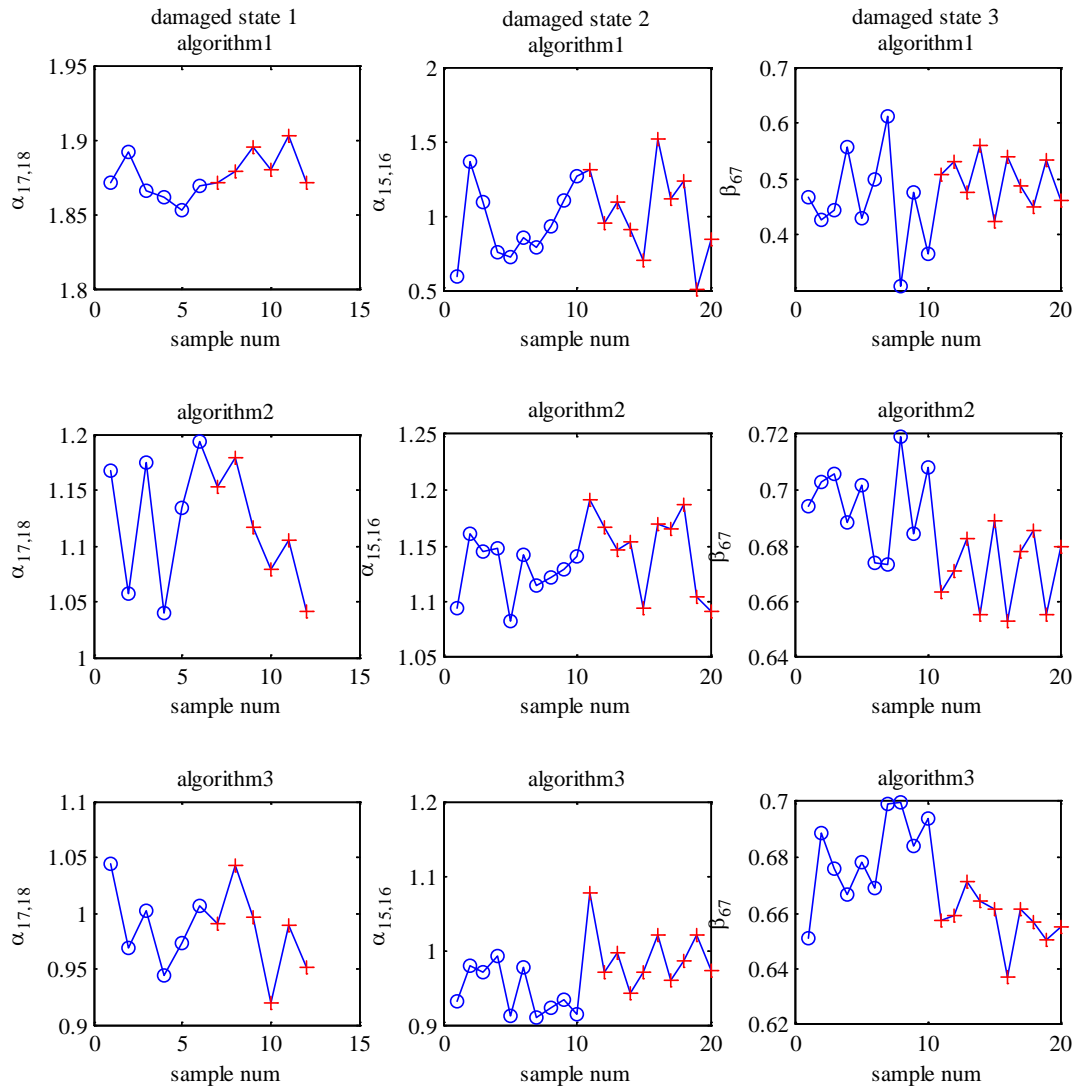
Figure 9.8   Plots of the influence coefficient values at the damage location

for different algorithms/damage scenarios. Each sample

corresponds to a particular dataset. The circles are influence

coefficient values from undamaged state, the crosses are from

the damaged state.

Chapter 10 Substructural approaches for stiffness estimation/damage detection in shear frames

10.1 PRELUDE

In sensing-based SHM, the structural properties are estimated from measurements (vibration etc.). This is an 'inverse problem', where conclusion on the underlying signal generator characteristics is drawn from observed data. As observed in previous chapter, for structural condition evaluation purposes it is preferred to have structural state/damage indices directly related to structural physics/local damage extent.

System identification techniques produce global modal properties, and tend to get computationally intensive as problem size increases (P. Chang et al., 2003; Dharap, Koh, and Nagarajaiah, 2006; Doebling et al., 1998; Rahai, Bakhtiari-Nejad, and Esfandiari, 2007; Saito, Mase, and Morita, 2005). Scalar TSA based statistical damage detection has been investigated in several recent studies (de Lautour and Omenzetter, 2010; Nair et al., 2006; Sohn et al., 2001). This type of methods provides more sensitive measures to local damage, yet the features often do not carry explicit physical meaning, and could be varying significantly when the excitation conditions are subjected to change.

Substructural approaches are generally small-to-medium scale multivariate approaches based on measurements from sensor clusters. If the algorithm formulation is done properly, it can produce local structural condition indicators. Moreover, the computation can be accomplished in a distributed manner. Following are a few examples for linear-topology structures to date: Hernandez-Garcia et al. (2010a, 2010b) proposed a structural decomposition approach that employs Chebyshev series expansion to model the mass-normalized interstory restoration force signal and then extract the structural

property information; In Yan et al. (2011) artificial neural network training is used to model the dynamics of substructures within mass-spring and multi-story systems, and standard F-test on model fit ratio is used to decide whether damage occurred for a substructure or not; Takewaki and Nakamura (2005) concluded that the DC component of a frequency domain function of system vibration responses is directly related to the system mass and stiffness and used it for damage identification in the top story of a frame model; in (Kuwabara et al., 2013; Xing and Mita, 2012) ARX modeling are adopted for the substructure system and functions of the extracted parameters are used for damage detection. Substructural physics and global structural mechanical properties are also interrelated: Barroso and Rodriguez (2004) introduce a transformational relationship between estimated modal properties and the mass-normalized interstory stiffness for multi-story structures.

10.2 MOTIVATION AND ORGANIZATION

While above presented substructural approaches have been successful in their respective simulation/ experimental applications, there is still room to improve in terms of computational efficiency and data interpretation. The contribution of the research included in this chapter is in formulation, efficiency evaluation and verification of two structural stiffness estimation algorithms that are based on linear regression methods. The algorithms are competent in the sense that they employ standard linear regression techniques and are easy to program and implement. They aim to detect stiffness loss in shear frame structures, which are widely used in civil design and construction practices. For all the shear frames discussed in this chapter, only the horizontal translational degrees-of-freedoms at each node are considered in the model. In this case, the linear

175

structural topology makes vibration-based structural diagnosis a well-defined problem (interstory stiffness loss). A major advantage of both algorithms proposed is that they are designed to operate using regression approaches on local structural acceleration responses, which is beneficial for real practice as the modeling process is computationally efficient and acceleration measurements are easy to obtain.

In the first algorithm, Time Domain Regression Method (TDRM), the acceleration at a node is regressed on simulated displacement responses from neighboring nodes. In the second algorithm, Frequency Domain Regression Method (FDRM), the autocorrelation spectrum from single node response is regressed on cross-correlation spectra with the neighboring node signals. Enhanced formulations of proposed algorithms are also introduced so than they can be used for evaluation of regular frames with joint rotational responses. Compared with established sub-structural analysis techniques that involve lengthier modeling and computation such as Chebyshev series expansion (Hernandez-Garcia et al., 2010a, 2010b), iterative optimization(Hou et al., 2011) and ARX modeling (Kuwabara et al., 2013; Xing and Mita, 2012), the regression coefficients provide a direct estimate of the local stiffness, and can be readily used as damage indicators. The case studies presented in later sections show that the algorithms yield excellent performance in identifying damage location and extent.

It is worth noting that for many traditional model updating methods (Brownjohn et al., 2001; Duan et al., 2007; Friswell and Mottershead, 1995; Mottershead and Friswell, 1993), the parameters of the initial numerical model are also updated to make the model's characteristics (e.g. modal properties, etc.) or response (e.g. deformation, etc.) match those measured from the real structure in the least squares sense. This family of methods

176

can perform effectively for damage identification when the numerical model is a suitable representation of the real system, but can produce erratic results when the numerical model is not well-defined (e.g. misrepresentation of boundary conditions or wrong choice of parameters). Compared to many model updating techniques, one of the significant advantages of the methods proposed in this paper is that an analytical finite element model describing the initial state of the structure itself is not needed; instead, regression is performed directly based on local vibration responses to obtain an estimation of the local structural property (stiffness).

The rest of the chapter is organized as follows:

- Section 10.3 gives a brief account of the dynamics theory, and then for the shear frame structure the linear relation between a single node acceleration response and its neighboring node displacement responses is presented.

- Section 10.4 introduces the time domain approach (TDRM) for stiffness estimation using reconstructed displacement response.

- Section 10.5 describes the frequency domain approach (FDRM) to evaluate system stiffness from signal periodograms.

- Section 10.6 offers an enhanced algorithm formulation of TDRM/FDRM, since for many structures the rotational responses at frame joints are not zero.

- Section 10.7 contains numerical validation results of both algorithms using a 5DOF system.

- Section 10.8 includes experimental validation results of both algorithms using two laboratory specimens.

177

- Section 10.9 is the conclusion on the effectiveness of the proposed substructural approaches.

10.3 GENERAL DYNAMIC SYSTEM SOLUTION AND LOCAL VIBRATION ANALYSIS OF A SHEAR FRAME

The response of a MDOF structure subjected to external excitation $\mathbf{p}(t)$ can be obtained by solving the second-order differential equation system:

$$\mathbf{m}\ddot{\mathbf{u}} + \mathbf{c}\dot{\mathbf{u}} + \mathbf{k}\mathbf{u} = \mathbf{p}(t). \tag{10.1}$$

In Eq.(10.1), $\mathbf{u}$ is the displacement response vector, and $\mathbf{m}$, $\mathbf{c}$, $\mathbf{k}$ are mass, damping, and stiffness matrices, respectively. This vibration analysis can be applied to continuous structures by choosing a finite set of representative DOFs, which is a valid approximation as long as there are enough parameters/DOFs in the model.

In this chapter local vibration measurements will be used to detect stiffness loss in a simulated shear frame model (Figure 10.1). In particular, linear regression models are formed using responses from local clusters of sensor nodes and the regression coefficients are used as damage features. Theoretical proofs are presented on the direct proportional relation between regression coefficients and structural stiffness, and thus the proposed features are more explicit when compared with damage detection techniques that employ multivariate time series analysis and other forms of complex modeling. The methods are further verified with simulation examples and experiments.

For the case of shear structures both $\mathbf{m}$ and $\mathbf{k}$ are 'banded matrices' and an associated term 'bandwidth' can be defined as the width of the diagonal band with nonzero entries in such a matrix. Under the assumption of classical Rayleigh damping ($\mathbf{c} = \mu\mathbf{m} + \lambda\mathbf{k}$, where μ and λ are constants), matrix $\mathbf{c}$ has bandwidth 3 as in this case $\mathbf{m}$

178

has bandwidth 1 and $\mathbf{k}$ has bandwidth 3. Therefore, the following equation holds for the response measurements of a shear frame model at floor i-1, i, and i+1:

$$m_i \ddot{u}_i = k_{i,i-1}\left(u_{i-1} - u_i\right) + k_{i,i+1}\left(u_{i+1} - u_i\right) - c_i \dot{u}_i - c_{i-1}\dot{u}_{i-1} - c_{i+1}\dot{u}_{i+1} + p_i. \qquad (10.2)$$

Here damping (c_{i-1}, c_i, c_{i+1}) is not assumed to be related to relative displacements/ velocities because part of the effect also comes from the system's interaction with the surrounding environment, which depends on the absolute displacements/velocities. Thus given the mass of the middle node m_i, its acceleration $\ddot{u}_i$, the displacement and velocity response at the three nodes, $u_{i-1}, u_i, u_{i+1}, \dot{u}_{i-1}, \dot{u}_i, \dot{u}_{i+1}$, and the excitation acting on the middle node, p_i, the local stiffness and damping parameters can be obtained through a linear least squares regression:

$$\mathbf{Y} = m_i \ddot{\mathbf{u}}_3 - \mathbf{p}_i,$$

$$\mathbf{X} = \left[\left(\mathbf{u}_{i-1} - \mathbf{u}_i\right), \left(\mathbf{u}_{i+1} - \mathbf{u}_i\right), \dot{\mathbf{u}}_i, \dot{\mathbf{u}}_{i-1}, \dot{\mathbf{u}}_{i+1}\right],$$

$$\hat{\boldsymbol{\beta}} = \begin{bmatrix} \hat{k}_{i,i-1} \\ \hat{k}_{i,i+1} \\ \hat{c}_i \\ \hat{c}_{i-1} \\ \hat{c}_{i+1} \end{bmatrix} = \left(\mathbf{X}'\mathbf{X}\right)^{-1}\mathbf{X}'\mathbf{Y}, \; \mathbf{e} = \mathbf{Y} - \mathbf{X}\hat{\boldsymbol{\beta}}. \qquad (10.3)$$

Where $\mathbf{Y}$ is the regressand, $\mathbf{X}$ are the regressors, $\hat{\boldsymbol{\beta}}$ is the estimated regression coefficients (the circumflex accent symbol means the empirical/estimated value) and $\mathbf{e}$ is the estimation error. This definition of regression model components will also be applied in subsequent model descriptions in Sections 10.4 and 10.5. In order to verify the performance of this method, this regression scheme is applied to random vibration responses collected from the simulated 5-DOF shear frame model (Figure 10.1). Table

179

10.1 and Figure 10.2 show the results from this implementation. Note that when this regression is performed for the first story, the dynamic response of the lower story (ground) is zero; and for the top story the upper story ($i+1$) contribution does not exist. The regression error is non-zero because instead of classical Rayleigh damping, modal damping (5% for each mode) is used. Still, the regression yields a good estimate for the stiffness. All the data used in this example are noise-free; when measurement noise is added to the data, the accuracy of the regression results is severely affected because the noise content of the vibration measurements actually gets amplified through the regression process. In the next two sections, this formulation will be further exploited to form the acceleration-output-only algorithms for local stiffness evaluation. These algorithms are shown to be relatively robust to noises.

10.4 TDRM: STIFFNESS ESTIMATION USING RECONSTRUCTED DISPLACEMENT RESPONSE FROM ACCELERATION MEASUREMENTS

In recent years, accelerometers have been most widely applied for general structural heath monitoring purposes. Therefore, the algorithm introduced here is designed to operate using only the acceleration response.

When a structure is operating in ambient environment, the commonly adopted assumption is that the excitation is white noise. In such case, the term $p(t)$ in Eq. (10.1) becomes the random error term in the regression model and can be removed from the regressor matrix $\mathbf{X}$. On the other hand, the displacement responses will be reconstructed from acceleration using the *regularized inverse central difference method* proposed by Lee et al. (Lee, Hong, and Park, 2010). Their solution is based on minimizing the following function $\Pi(\mathbf{u})$:

180

$$\min \Pi(\mathbf{u}) = \frac{1}{2} \left\| \mathbf{L}_a \mathbf{L}_c \mathbf{u} - (\Delta t)^2 \mathbf{L}_a \overline{\mathbf{a}} \right\|_2^2 + \underbrace{\frac{\lambda^2 \|\mathbf{u}\|_2^2}{2}}_{\text{regularization part}}, \qquad (10.4)$$

$$\underbrace{\phantom{\frac{1}{2}}}_{\text{central difference part}}$$

$$\operatorname{argmin}(\Pi(\mathbf{u}), \mathbf{u}) = \left(\mathbf{L}_c^T \mathbf{L}_a^T \mathbf{L}_a \mathbf{L}_c + \lambda^2 \mathbf{I} \right)^{-1} \mathbf{L}_c^T \mathbf{L}_a^T \mathbf{L}_a \overline{\mathbf{a}} (\Delta t)^2,$$

$$\mathbf{L}_c = \begin{bmatrix} 1 & -2 & 1 & & & & \\ & 1 & -2 & 1 & & & \\ & & & \ddots & & & \\ & & & 1 & -2 & 1 & \\ & & & & 1 & -2 & 1 \end{bmatrix}, \quad \mathbf{L}_a = \begin{bmatrix} \dfrac{1}{\sqrt{2}} & & & & \\ & 1 & & & \\ & & \ddots & & \\ & & & 1 & \\ & & & & \dfrac{1}{\sqrt{2}} \end{bmatrix}.$$

In Eq. (10.4), $\mathbf{u}$ is the reconstructed displacement, $\overline{\mathbf{a}}$ is the acceleration signal within a rectangular time window of length $(2k+1)$ (denoted using the macron accent symbol), Δt is the sampling interval, and λ is often referred to as regularization factor. The two coefficient matrices $\mathbf{L}_c$ and $\mathbf{L}_a$ are of dimensions $(2k+1) \times (2k+3)$ and $(2k+1) \times (2k+1)$, respectively. To improve the accuracy of this method, the displacement is reconstructed for a time window at a time and then the window is shifted forward one time step (Δt) and the displacement is reconstructed again. For each reconstruction, only the value from the time window center is retained for solution.

For the simulated 5-DOF shear frame model used in section 10.3 (Figure 10.1), local stiffness can now be estimated by regressing the middle node acceleration on the reconstructed displacement responses. The regular least squared scheme produces erratic results because of the large variation of the excitation force signal. An alternative method

181

with a derivation analogous to the Yule-Walker equation (Brockwell and Davis, 2009) is used for the regression. To start, multiply both sides of Eq. (10.2) with $\ddot{u}_i(t-\tau)$:

$$m_i\ddot{u}_i(t)\ddot{u}_i(t-\tau) = k_{i,i-1}\big(u_{i-1}(t)-u_i(t)\big)\ddot{u}_i(t-\tau) + k_{i,i+1}\big(u_{i+1}(t)-u_i(t)\big)\ddot{u}_i(t-\tau)$$
$$-c_i\dot{u}_i(t)\ddot{u}_i(t-\tau) - c_{i-1}\dot{u}_{i-1}(t)\ddot{u}_i(t-\tau) - c_{i+1}\dot{u}_{i+1}(t)\ddot{u}_i(t-\tau) + p_i(t)\ddot{u}_i(t-\tau).$$

(10.5)

Taking the expectation $E[\cdot]$ on both sides, and assuming that input excitation at node i is white noise:

$$m_iE\big[\ddot{u}_i(t)\ddot{u}_i(t-\tau)\big] = k_{i,i-1}E\big[\big(u_{i-1}(t)-u_i(t)\big)\ddot{u}_i(t-\tau)\big] + k_{i,i+1}E\big[\big(u_{i+1}(t)-u_i(t)\big)\ddot{u}_i(t-\tau)\big]$$
$$-c_iE[\dot{u}_i(t)\ddot{u}_i(t-\tau)] - c_{i-1}E[\dot{u}_{i-1}(t)\ddot{u}_i(t-\tau)] - c_{i+1}E[\dot{u}_{i+1}(t)\ddot{u}_i(t-\tau)] + E\big[p_i(t)\ddot{u}_i(t-\tau)\big],$$

$$\because E\big[p_i(t)\ddot{u}_i(t-\tau)\big] = 0 \ (\tau > 0),$$

$$m_iR_{\ddot{u}_i}(\tau) = k_{i,i-1}\big[R_{\ddot{u}_iu_{i-1}}(\tau) - R_{\ddot{u}_iu_i}(\tau)\big] + k_{i,i+1}\big[R_{\ddot{u}_iu_{i+1}}(\tau) - R_{\ddot{u}_iu_i}(\tau)\big]$$
$$-c_iR_{\ddot{u}_i\dot{u}_i}(\tau) - c_{i-1}R_{\ddot{u}_i\dot{u}_{i-1}}(\tau) - c_{i+1}R_{\ddot{u}_i\dot{u}_{i-1}}(\tau).$$

(10.6)

$R(\cdot)$ are the auto/cross correlation functions of the acceleration responses. When there is only one subscript, it stands for autocorrelation of that signal; when two subscripts are used, it stands for the cross-correlation between those signals. This convention regarding the subscripts is also used for $L(\cdot)$ (one-sided Laplace Transform) and $S(\cdot)$ (power spectral density), which are employed in the subsequent section. Since the civil structures are generally lightly damped systems (damping ratio< 5%), the velocity responses are also omitted from the regression model for an approximate solution on the structural stiffness. (Please refer to Section 10.7 for a numerical simulation example that shows for a lightly damped system, the method yields very consistent structural stiffness

182

estimates when the signal noise level is low.) Thus Eq. (10.6) is further simplified by

neglecting the damping terms and using the reconstructed displacements,

$$R_{\ddot{u}_i}\left(\tau\right) = k_{i,i-1}\,/\,m_i\left[R_{\ddot{u}_i\iint\{\ddot{u}_{i-1}\}}\left(\tau\right) - R_{\ddot{u}_i\iint\{\ddot{u}_i\}}\left(\tau\right)\right] + k_{i,i+1}\,/\,m_i\left[R_{\ddot{u}_i\iint\{\ddot{u}_{i+1}\}}\left(\tau\right) - R_{\ddot{u}_i\iint\{\ddot{u}_i\}}\left(\tau\right)\right]. \quad (10.7)$$

Here $\iint\{\cdot\}$ stands for the displacement reconstructed from the series within the bracket.

To perform this regression on discrete signals:

$$\mathbf{Y} = \mathbf{R}_{\ddot{u}_i}\left(\tau_j\right),\ j = 1,\ldots,N$$

$$\mathbf{X} = \left[\mathbf{R}_{\ddot{u}_i\iint\{\ddot{u}_{i-1}\}}\left(\tau_j\right) - \mathbf{R}_{\ddot{u}_i\iint\{\ddot{u}_i\}}\left(\tau_j\right) \quad \mathbf{R}_{\ddot{u}_i\iint\{\ddot{u}_{i+1}\}}\left(\tau_j\right) - \mathbf{R}_{\ddot{u}_i\iint\{\ddot{u}_i\}}\left(\tau_j\right)\right],$$

$$\hat{\boldsymbol{\beta}} = \left(\mathbf{X}'\mathbf{X}\right)^{-1}\mathbf{X}'\mathbf{Y} = \left[\hat{k}_{i,i-1}\,/\,m_i \quad \hat{k}_{i,i+1}\,/\,m_i\right]^{\mathrm{T}}. \quad (10.8)$$

In Eq. (10.8), N is the total number of sample points in time domain. This method

yields more accurate stiffness estimates than the regular linear regression, as the variance

of regression model error is much reduced. It is similar to the Natural Excitation

Technique (NExT) (James III et al., 1993) in system identification, which uses the cross

correlation matrix of system response under white noise excitation as a free-decay

response. Note that TDRM does not carry over the complete methodologies of Yule-

Walker method and NExT, which are separately used for AR model estimation and

modal realization. Rather, it is based on the same underlying idea as that of the Yule-

Walker equation and NExT; to remove random input excitation values from

consideration by multiplying both sides of the system dynamics equation with system

response at previous time points.

10.5 FDRM: STIFFNESS ESTIMATION USING ACCELERATION RESPONSE SPECTRA ESTIMATES

The interstory stiffness can also be estimated from the frequency domain representation of the acceleration signals. In this section we begin with taking the one-sided Laplace transform of Eq. (10.6):

$$m_i L_{\ddot{u}_i}(s) = k_{i,i-1}\left[L_{\ddot{u}_i u_{i-1}}(s) - L_{\ddot{u}_i u_i}(s) \right] + k_{i,i+1}\left[L_{\ddot{u}_i u_{i+1}}(s) - L_{\ddot{u}_i u_i}(s) \right]$$
$$-c_i L_{\ddot{u}_i \dot{u}_i}(s) - c_{i-1} L_{\ddot{u}_i \dot{u}_{i-1}}(s) - c_{i+1} L_{\ddot{u}_i \dot{u}_{i+1}}(s). \tag{10.9}$$

Where $L(\cdot)$ stands for the unilateral Laplace transform of the corresponding correlation function $R(\cdot)$ (i.e. $L(s) = \int\limits_0^{+\infty} R(\tau) e^{-s\tau} d\tau$). It can be shown that given responses from node i and j,

$$\dot{R}_{\ddot{u}_i u_j}(\tau) = \frac{\partial \int_{-\infty}^{+\infty} \ddot{u}_i(t) u_j(t+\tau) dt}{\partial \tau} = \int\limits_{-\infty}^{+\infty} \ddot{u}_i(t) \frac{\partial u_j(t+\tau)}{\partial \tau} dt = \int\limits_{-\infty}^{+\infty} \ddot{u}_i(t) \dot{u}_j(t+\tau) dt = R_{\ddot{u}_i \dot{u}_j}(\tau),$$

$$\therefore \ddot{R}_{\ddot{u}_i u_j}(\tau) = \frac{\partial R_{\ddot{u}_i \dot{u}_j}(\tau)}{\partial \tau} = \int\limits_{-\infty}^{+\infty} \ddot{u}_i(t) \frac{\partial \dot{u}_j(t+\tau)}{\partial \tau} dt = R_{\ddot{u}_i \ddot{u}_j}(\tau),$$

$$L_{\ddot{u}_i \ddot{u}_j} = \int\limits_0^{+\infty} R_{\ddot{u}_i \ddot{u}_j}(\tau) e^{-s\tau} d\tau = \int\limits_0^{+\infty} \frac{\partial R_{\ddot{u}_i \dot{u}_j}(\tau)}{\partial \tau} e^{-s\tau} d\tau$$

$$= s\int\limits_0^{+\infty} R_{\ddot{u}_i \dot{u}_j}(\tau) e^{-s\tau} d\tau - R_{\ddot{u}_i \dot{u}_j}(0) = sL_{\ddot{u}_i \dot{u}_j} - R_{\ddot{u}_i \dot{u}_j}(0),$$

$$L_{\ddot{u}_i \ddot{u}_j} = sL_{\ddot{u}_i \dot{u}_j} - R_{\ddot{u}_i \dot{u}_j}(0) = s\left(sL_{\ddot{u}_i u_j} - R_{\ddot{u}_i u_j}(0)\right) - R_{\ddot{u}_i \dot{u}_j}(0) = s^2 L_{\ddot{u}_i u_j} - sR_{\ddot{u}_i u_j}(0) - R_{\ddot{u}_i \dot{u}_j}(0),$$

$$L_{\ddot{u}_i \dot{u}_j} = \frac{L_{\ddot{u}_i \ddot{u}_j} + R_{\ddot{u}_i \dot{u}_j}(0)}{s}, \quad L_{\ddot{u}_i u_j} = \frac{L_{\ddot{u}_i \ddot{u}_j} + sR_{\ddot{u}_i u_j}(0) + R_{\ddot{u}_i \dot{u}_j}(0)}{s^2}. \tag{10.10}$$

Hence, an equation that contains only spectral density functions of acceleration responses $\ddot{u}_{i-1}$, $\ddot{u}_i$ and $\ddot{u}_{i+1}$ can be formed by substituting Eq. (10.10) into Eq. (10.9) and replacing s with $i\omega$ (thus going from the Laplace s-domain to the frequency domain):

$$
\begin{aligned}
m_i S_{\ddot{u}_i}(\omega) = {} & k_{i,i-1}\left[\frac{S_{\ddot{u}_i\ddot{u}_{i-1}}(\omega)+i\omega R_{\ddot{u}_i u_{i-1}}(0)+R_{\ddot{u}_i\dot{u}_{i-1}}(0)}{-\omega^2}+\frac{S_{\ddot{u}_i}(\omega)+i\omega R_{\ddot{u}_i u_i}(0)+R_{\ddot{u}_i\dot{u}_i}(0)}{\omega^2}\right] \\
& +k_{i,i+1}\left[\frac{S_{\ddot{u}_i\ddot{u}_{i+1}}(\omega)+i\omega R_{\ddot{u}_i u_{i+1}}(0)+R_{\ddot{u}_i\dot{u}_{i+1}}(0)}{-\omega^2}+\frac{S_{\ddot{u}_i}(\omega)+i\omega R_{\ddot{u}_i u_i}(0)+R_{\ddot{u}_i\dot{u}_i}(0)}{\omega^2}\right] \\
& -c_i\frac{S_{\ddot{u}_i}(\omega)+R_{\ddot{u}_i\dot{u}_i}(0)}{i\omega}-c_{i-1}\frac{S_{\ddot{u}_i\ddot{u}_{i-1}}(\omega)+R_{\ddot{u}_i\dot{u}_{i-1}}(0)}{i\omega}-c_{i+1}\frac{S_{\ddot{u}_i\ddot{u}_{i+1}}(\omega)+R_{\ddot{u}_i\dot{u}_{i+1}}(0)}{i\omega}.
\end{aligned}
$$
$$(10.11)$$

$S(\cdot)$ denotes unilateral auto/cross power spectral density, which is defined as the unilateral Fourier Transform of the signal cross-correlation function $R(\cdot)$ (i.e.

$S(\omega) = \int\limits_{0}^{+\infty} R(\tau)e^{-i\omega\tau}d\tau$). This replacement of s with $i\omega$ is performed for data processing

purposes as spectral density functions can be estimated from collected signals. Consider only the real part of Eq. (10.11) and rearrange the terms:

$$
\begin{aligned}
\omega^2\mathrm{Re}\left\{S_{\ddot{u}_i}(\omega)\right\} = {} & \frac{k_{i,i-1}}{m_i}\left[-\mathrm{Re}\left\{S_{\ddot{u}_i\ddot{u}_{i-1}}(\omega)\right\}+\mathrm{Re}\left\{S_{\ddot{u}_i}(\omega)\right\}\right]+\frac{k_{i,i+1}}{m_i}\left[-\mathrm{Re}\{S_{\ddot{u}_i\ddot{u}_{i+1}}(\omega)\}+\mathrm{Re}\left\{S_{\ddot{u}_i}(\omega)\right\}\right] \\
& -\frac{c_{i-1}}{m_i}\omega\mathrm{Im}\{S_{\ddot{u}_i\ddot{u}_{i-1}}(\omega)\}-\frac{c_i}{m_i}\omega\mathrm{Im}\left\{S_{\ddot{u}_i}(\omega)\right\}-\frac{c_{i+1}}{m_i}\omega\mathrm{Im}\left\{S_{\ddot{u}_i\ddot{u}_{i+1}}(\omega)\right\}+C', \\
C' = {} & k_{i,i-1}[-R_{\ddot{u}_i\dot{u}_{i-1}}(0)+R_{\ddot{u}_i\dot{u}_i}(0)]+k_{i,i+1}\left[-R_{\ddot{u}_i\dot{u}_{i+1}}(0)+R_{\ddot{u}_i\dot{u}_i}(0)\right].
\end{aligned}
$$
$$(10.12)$$

Under appropriate conditions (i.e. $E\left[p_i(t)\ddot{u}_i(t-\tau)\right]=0\;(\tau<0)$ relatively insignificant in value), two-sided spectra can be used instead of one-sided spectra to facilitate computation by using the periodogram.

185

$$\omega^2 S_{\ddot{u}_i}(\omega) = \frac{k_{i,i-1}}{m_i}\left[-\mathrm{Re}\left\{S_{\ddot{u}_i\ddot{u}_{i-1}}(\omega)\right\}+S_{\ddot{u}_i}(\omega)\right]+\frac{k_{i,i+1}}{m_i}\left[-\mathrm{Re}\{S_{\ddot{u}_i\ddot{u}_{i+1}}(\omega)\}+S_{\ddot{u}_i}(\omega)\right]$$
$$-\frac{c_{i-1}}{m_i}\omega\mathrm{Im}\{S_{\ddot{u}_i\ddot{u}_{i-1}}(\omega)\}-\frac{c_{i+1}}{m_i}\omega\mathrm{Im}\left\{S_{\ddot{u}_i\ddot{u}_{i+1}}(\omega)\right\}+C. \tag{10.13}$$

Here C stands for the constant term in the regression model. Given the middle node

mass m_i, the stiffness and damping coefficients (i.e. $k_{i,i-1}$, $k_{i,i+1}$, c_{i-1}, c_{i+1}) can be

estimated through regression using Eq. (10.13). To perform this regression on discrete

signals:

$$\mathbf{Y} = \omega_j\mathrm{Re}\left\{\mathbf{S}_{\ddot{u}_i}\left(\omega_j\right)\right\}, \quad j = 1,\ldots,N$$

$$\mathbf{X} = [-\mathrm{Re}\left\{\mathbf{S}_{\ddot{u}_i\ddot{u}_{i-1}}\left(\omega_j\right)\right\}+\mathrm{Re}\left\{\mathbf{S}_{\ddot{u}_i}\left(\omega_j\right)\right\}, -\mathrm{Re}\{\mathbf{S}_{\ddot{u}_i\ddot{u}_{i+1}}\left(\omega_j\right)\}+\mathrm{Re}\left\{\mathbf{S}_{\ddot{u}_i}\left(\omega_j\right)\right\},$$
$$-\omega_j\mathrm{Im}\{\mathbf{S}_{\ddot{u}_i\ddot{u}_{i-1}}\left(\omega_j\right)\}, -\omega_j\mathrm{Im}\left\{\mathbf{S}_{\ddot{u}_i\ddot{u}_{i+1}}\left(\omega_j\right)\right\},\mathbf{1}]/\omega_j,$$

$$\hat{\boldsymbol{\beta}} = \left(\mathbf{X'X}\right)^{-1}\mathbf{X'Y} = \begin{bmatrix}\dfrac{\hat{k}_{i,i-1}}{m_i} & \dfrac{\hat{k}_{i,i+1}}{m_i} & \dfrac{\hat{c}_{i-1}}{m_i} & \dfrac{\hat{c}_{i+1}}{m_i} & \hat{C}\end{bmatrix}^{\mathrm{T}}. \tag{10.14}$$

In Eq. (14), N is the total number of sample points in frequency domain. An

obvious advantage of this method is that it turns the vibration initial conditions into

regression constants, thus eliminating the displacement reconstruction step, and all the

associated computational cost and estimation errors.

10.6 ENHANCED ALGORITHM FORMULATION FOR REGULAR FRAMES

A shear frame is a simplified model that serves as an approximation for certain types

of real structures. Rotational response, though insignificant in many cases, always exists.

This section focuses on the effect of nodal rotation on the stiffness estimators from

TDRM and FDRM.

186

When a frame structure has flexible beams, the responses of each story depend on the responses at non-neighbor nodes as well, since the structural stiffness matrix bandwidth increases. As the beams become more flexible, this dependence becomes greater. For illustration, Figure 10.3 shows four stiffness matrices of five-story frames with different beam stiffness. As the ratio of beam-to-column stiffness gets smaller, the elements distant from the main diagonal of this matrix become larger.

In such cases, the application of previous methodology no longer produces accurate estimators. However, its performance can be improved by introducing a modified regression model. The derivation starts with the classical equation of motion for dynamic systems:

$$\mathbf{m\ddot{u} + c\dot{u} + ku} = \mathbf{p}(t),$$

$$
\begin{bmatrix}
m_1 & & & & & \\
& m_2 & & & & \\
& & \ddots & & & \\
& & & m_i & & \\
& & & & \ddots & \\
& & & & & m_n
\end{bmatrix}
\begin{bmatrix}
\ddot{u}_1 \\ \ddot{u}_2 \\ \vdots \\ \ddot{u}_i \\ \vdots \\ \ddot{u}_n
\end{bmatrix}
+
\begin{bmatrix}
c_{(1,1)} & c_{(1,2)} & c_{(1,3)} & & \cdots & & \\
c_{(2,1)} & c_{(2,2)} & c_{(2,3)} & & c_{(2,4)} & \cdots & \\
& & \ddots & & & & \\
\cdots & c_{(i,i-2)} & c_{(i,i-1)} & c_{(i,i)} & c_{(i,i+1)} & \cdots & \\
& & & & & \ddots & \\
& & & \cdots & c_{(n,n-2)} & c_{(n,n-1)} & c_{(n,n)}
\end{bmatrix}
\begin{bmatrix}
\dot{u}_1 \\ \dot{u}_2 \\ \vdots \\ \dot{u}_i \\ \vdots \\ \dot{u}_n
\end{bmatrix}
$$

$$
+
\begin{bmatrix}
k_{(1,1)} & k_{(1,2)} & k_{(1,3)} & & \cdots & & \\
k_{(2,1)} & k_{(2,2)} & k_{(2,3)} & & k_{(2,4)} & \cdots & \\
& & \ddots & & & & \\
\cdots & k_{(i,i-2)} & k_{(i,i-1)} & k_{(i,i)} & k_{(i,i+1)} & \cdots & \\
& & & & & \ddots & \\
& & & \cdots & k_{(n,n-2)} & k_{(n,n-1)} & k_{(n,n)}
\end{bmatrix}
\begin{bmatrix}
u_1 \\ u_2 \\ \vdots \\ u_i \\ \vdots \\ u_n
\end{bmatrix}
=
\begin{bmatrix}
p_1 \\ p_2 \\ \vdots \\ p_i \\ \vdots \\ p_n
\end{bmatrix},
$$

Assuming that the correlation coefficients outside 1 half-bandwidth (which counts the number of diagonals on either side of the main diagonal) in the **c** and **k** matrices are

187

relatively insignificant compared to the rest, the i th row of the system of equations above can be extracted as

$$m_i \ddot{u}_i + c_{(i,i-1)} \dot{u}_{i-1} + c_{(i,i)} \dot{u}_i + c_{(i,i+1)} \dot{u}_{i+1} + k_{(i,i-1)} u_{i-1} + k_{(i,i)} u_i + k_{(i,i+1)} u_{i+1} = p_i,$$

Comparing it with Eq. (10.2) in Section 10.3 and applying a similar derivation methodology that leads to Eq. (10.8) and (10.13), the following expressions can be obtained for the enhanced TDRM/FDRM formulation:

$$m_i R_{\ddot{u}_i}(\tau) = -k_{(i,i-1)} R_{\ddot{u}_i \iint \{\ddot{u}_{i-1}\}}(\tau) - k_{(i,i+1)} R_{\ddot{u}_i \iint \{\ddot{u}_{i+1}\}}(\tau) - k_{(i,i)} R_{\ddot{u}_i \iint \{\ddot{u}_i\}}(\tau).$$

(10.15)

$$m_i S_{\ddot{u}_i}(\omega) = k_{(i,i-1)} \frac{\text{Re}\{S_{\ddot{u}_i \ddot{u}_{i-1}}(\omega)\} + R_{\ddot{u}_i \dot{u}_{i-1}}(0)}{\omega^2} + k_{(i,i)} \frac{S_{\ddot{u}_i}(\omega) + R_{\ddot{u}_i \dot{u}_i}(0)}{\omega^2}$$
$$+ k_{(i,i+1)} \frac{\text{Re}\{S_{\ddot{u}_i \ddot{u}_{i+1}}(\omega)\} + R_{\ddot{u}_i \dot{u}_{i+1}}(0)}{\omega^2} - c_{(i,i-1)} \frac{\text{Im}\{S_{\ddot{u}_i \ddot{u}_{i-1}}(\omega)\}}{\omega} - c_{(i,i+1)} \frac{\text{Im}\{S_{\ddot{u}_i \ddot{u}_{i+1}}(\omega)\}}{\omega}.$$

(10.16)

Corresponding discrete regression models can be constructed from Eq. (10.15) and (10.16) and then applied for structural stiffness estimation and condition evaluation.

When structures of more complex geometry are monitored, a more general substructuring approach can be used:

$$mf(r_i, r_b) = g(r_i, r_b) + p.$$

(10.17)

where r_i, r_b denotes the vibration response measurements (acceleration, strain etc.) at inner and boundary nodes of the substructural system, respectively. f denotes the average acceleration function of the substructure, g stands for the restoration forces from the rest of the system acting through substructural boundaries, and p is the amount of load directly applied to the substructural system. When the substructure remains in the linear range, f and g are linear functions, and the methodologies used in the

188

formulations of TDRM/FDRM can still be applied through performing regression on auto/cross correlation/spectra functions of r_i and r_b obtained under random external excitation p. The effectiveness of this modeling will be closely related to the accuracy of representation of substructural boundary dynamics through measurements at the boundary nodes. This is an entirely separate topic and will be further expanded in the next chapter.

10.7 NUMERICAL VALIDATION

TDRM and FDRM are applied to the simulated responses from the 5 DOF system described in section 2 (Figure 10.1) and another frame with non-rigid beam links (Figure 10.4) for their performance assessment. Random excitation is applied at each floor level of both systems. In all of the regression processes, it is assumed that all the nodal masses are known. While this assumption may restrict the application of the methods, there are a lot of cases that an estimate of the structural mass could be available using the construction drawings and site visits. In addition, for the damage detection applications and in the cases where properties of the stiffness can be estimated using as-built drawings, the masses can be updated using modal identification of the undamaged/baseline structures. In other cases where no information on the mass is available, the stiffness-to-mass ratio can still be obtained for damage detection and structural evaluation. In fact, for damage detection algorithms based entirely on structural vibration, it is generally not feasible to uncouple the effect from change in mass with that from change in stiffness. The limitation of the method is if no information about either mass or stiffness is available.

189

Results from application of the two regression techniques to the shear frame and the regular frame are presented in the following two subsections.

10.7.1 Performance evaluation of the proposed algorithms for the shear frame

The results from TDRM are summarized in Table 10.2. The algorithm is found to yield reasonable estimates of interstory stiffness as long as the noise level is relatively low (e.g. less than 10%). It underestimates the stiffness in most cases, though, because the damping effect is neglected in the regression model. As the acceleration measurement noise level increases, the displacement reconstruction accuracy decreases (Figure 10.5) and the estimation error becomes larger. In this simulation, the acceleration responses from the 1st-3rd floors have large high frequency contents, which negatively affect the displacement reconstruction accuracy as the method is designed for low-frequency signals (Lee et al., 2010). This is the reason that the regression results associated more with responses from these three nodes tend to have a larger bias.

In this example, TDRM has a tendency to underestimate the stiffness of the upper floors more than that of the lower floors. This is because the omitted viscous damping terms, which depend on the velocities of the stories incorporated in the model, have a stronger correlation with the upper story vibration than the lower story vibration (as a result of the shear frame structure topology and the loading condition; it is always easier to excite a location on a 'stick-type' structure from above than from below, and in this experiment the excitation amplitudes used for the top floors are greater.). Thus there is a 10-15% difference in the estimates of k_{34} from nodal responses 2-4 and nodal responses 3-5. It can also be observed that the difference between the two estimated values of k_{12} is

190

decreasing when the noise level increases because the result from the second regression (123) deviates from the real value faster than that from the first regression (012), as the second model incorporates responses from three nodes, while the first model incorporates only those from two.

Given information in Table 10.1, which indicates that the regression model yields accurate performance with accurate excitation, displacement, velocity, and acceleration measurements of the substructural systems, incorporating velocity information in TDRM will help estimation. Table 10.3 shows that when velocity data is incorporated in the TDRM model, the accuracy of the estimation as a whole increases but there is a tendency to overestimate. The reason for that is because the acceleration measurement is better correlated with the actual velocity than the reconstructed displacement, thus as the model overestimates damping, it also overestimates stiffness.

The implementation of FDRM on the simulated 5 DOF system reveals that the method works best when the number of Fast Fourier Transform points (Welch, 1967) is approximately the same as the length of the vibration signal sequence. Here all of the auto/cross power spectral densities are evaluated from the vibration responses using periodograms. Only half of the responses over the entire frequency range are used for regression, as the rest are comparatively insignificant in value. The sampling frequency for the vibration responses is 200Hz, and the length of every signal is 16,000 samples (80s). For FDRM in the numerical case, the number of FFT points for the Welch periodogram construction is 2^{14}.

191

Table 10.4 contains results from applying FDRM to simulated system responses of different signal qualities. It is seen that this method outperforms TDRM; it produces more accurate stiffness estimates, and is less affected by measurement noise. Figure 10.6 shows that the frequency domain regression model did capture most of the variations in the dependent variable.

10.7.2 Performance evaluation of the proposed algorithms for the regular frame

Table 10.5 summarizes the results of FDRM from responses of simulated 5-story frames with different beam-to-column stiffness ratios (Figure 10.4). The length of the beams for the frame is 6 m, while the column height is 3 m everywhere except for the top floor (2.5 m). The signal-to-noise ratio (dB) for the measurements is 5. For this case, the bias is computed with respect to $12EI_c / L^3$,. When $\frac{EI_b}{EI_c} > 12$, the estimation bias is within 10%, and the system can be very well approximated by a shear frame. TDRM is also used; however, because of its innate tendency to underestimate structural stiffness, it yields more biased results. The estimation error of stiffness of middle stories amount to 20% even when the signal-to-noise ratio is 50 and $\frac{EI_b}{EI_c} > 16$. The results are thus not presented here due to space limitations.

The enhanced formulations of TDRM/FDRM are also applied to the data from this frame and their results are presented in Table 10.6 and Table 10.7. Both tables show that the estimation of $k_{(i,i)}$ is the most accurate of all, which is because given the neighboring nodes responses, the response at the middle node is least affected by responses of far-

192

away nodes. For the time domain method the estimation bias/standard deviation of the

$k_{(4,4)}$ is greater than $k_{(5,4)}$, which is because the reconstructed displacements of

acceleration measurements from the first 3 stories are noisy. The estimated values of $k_{(i,i)}$

can be used as indicators of structural damage; Table 10.8 presents the change in FDRM

stiffness estimates of a frame with initial $\dfrac{EI_b}{EI_c} = 2$ due to a 10% stiffness reduction in the

first floor columns.. The signal-to-noise ratio is set to 5 for measurements used in FDRM,

and 20 for those used in TDRM. Performance of the latter method degrades significantly

for signals with larger noise levels.

Results presented in this section demonstrate that FDRM can still be used for direct

structural stiffness estimation and damage identification/localization even when nodal

rotational responses exist. However, the accuracy of the stiffness estimates from FDRM

decrease as the modeling error increases, and for reliable structural stiffness estimation/

damage identification it is best to pool independent stiffness estimator samples together

for an average (like what is done for Table 10.8).

10.8 EXPERIMENTAL VALIDATION

In many real world applications, the aim of structural property estimation/evaluation

is to identify possible damage within the structure, which is in the form of a stiffness

change. In this section TDRM and FDRM are applied to acceleration responses from two

laboratory specimens that are subjected to random excitations for damage identification

purposes. Such comparison between damage and undamaged state is necessary for

evaluation of the effectiveness and accuracy of the proposed algorithms, as in both case

studies the actual stiffness of the specimens are not known *a priori*. The first specimen is

193

a 5-DOF aluminum-plexiglas model (Figure 10.7), and damage is simulated by adding mass to the 4th floor. The second specimen is a 7-DOF steel mass spring system (Figure 10.8), and damage is introduced through replacing the spring between the 2nd and 3rd masses with a more flexible one. Some basic properties of both specimens are presented in Table 10.9. The damage indices used are the nominal system stiffness estimators produced by the two algorithms. The results from both applications are presented in the form of figures for the ease of comparison and contrast.

10.8.1 Case study 1: a 5-DOF aluminum-plexiglas structure

As shown in Figure 10.7, an accelerometer is mounted to the shaking table and each floor of the test specimen. The total mass of each floor (together with the sensor, clamp etc.) is measured at 1.09 kg (2.4 lb$_m$). Damage is simulated by clamping three additional steel plates to the 4th floor; though the elastic stiffness is not affected, the geometric stiffness for stories below the 4th floor will change because of the P-delta effect incurred by the additional mass. For each structural scenario, 5 sets of acceleration measurements are collected when random excitation is applied at the base of the specimen. The sampling frequency for all datasets is 100 Hz, and each set contains 8,600 samples.

Figure 10.9 and Figure 10.10 present the stiffness estimation results from the proposed algorithms. The circles in the figures indicate stiffness values estimated from undamaged state signals and the crosses are those from damaged state. The dashed line and solid line are their respective averages. Floor No. '0' is used to denote the shaking table surface here. In the title of each plot, the subscripts of k indicate the location of this inter-story connection in the lumped mass structure, and the numbers after the dashed line are the response combination used for each regression. For example, $k_{23} / 123$ refers to

194

the stiffness estimate for the plexiglass plates between floor 2 and 3 based on responses from floors 1,2 and 3. Three estimates of system stiffness are made from each dataset by applying a rectangular time window to the signal at different time points. As expected, the mean of the estimated stiffness values for stories below the 4th floor dropped as a result of damage, as shown in both figures.

Figure 10.10 shows that FDRM produces very consistent stiffness estimators and hence clearly reports the system stiffness loss from the P-delta effect brought by the additional mass. However, the estimates from TDRM vary significantly even when the structural state is not changed (Figure 10.9). This is happening because TDRM as a time-domain method relies on accurate displacement-reconstruction estimates, but as a result of the nonlinear behavior and large damping effect associated with the plexiglas, the time domain regression modeling (without considering damping) is not accurate enough. Thus it is concluded that for stiffness estimation in nonlinear systems, FDRM is a more suitable choice.

10.8.2 Case study 2: a 7-DOF steel mass-spring system

To investigate the performance of the algorithms without concerns for material nonlinearity, TDRM and FDRM are also applied for damage identification in a steel mass-spring system (Figure 10.8). The ends of each spring are attached into two pieces of steel brackets, which are in turn bolted to the masses. The effective mass at each node (steel block together with sensor etc.) is 2.587 lb$_m$. An electro-magnetic shaker with 31.14N (7 lbs) harmonic peak force capacity is connected to the first steel block to provide random excitation for the system. Damage is introduced into the specimen by replacing the original spring between the 2nd and 3rd masses with a more flexible one. Five sets of acceleration responses, each containing 40,000 samples, are collected at each

195

structural state. All data is sampled at 200Hz frequency. It can be seen from Table 10.9 that damage cannot be directly located through modal frequency identification.

The stiffness estimation results are shown in Figure 10.11 and Figure 10.12. The numbering of the steel blocks is from left to right. As in the previous case study, the subscripts of k in the title of each plot indicate the location of this spring connection in the lumped mass structure, and the numbers after the dashed line are the response combination used for each regression. For example, $k_{23}/123$ refers to the stiffness estimate for the spring between masses 2 and 3 based on responses from masses 1, 2 and 3. Nine estimates of system stiffness are made from each dataset by applying a rectangular window to the signal at different time points. The dashed line and solid line are their respective averages. Enhanced TDRM/FDRM is also applied; however, as the problem here is caused mainly by translational motion of the mass blocks, they do not show a superior performance than the originally proposed regression schemes.

Figure 10.12 shows that FDRM successfully identifies a substantial stiffness reduction between masses 2 and 3 in both regression cases 1-2-3 and 2-3-4. Figure 10.11 indicates that TDRM also detects the stiffness loss between masses 2 and 3 in case 1-2-3, but fails in case 2-3-4. Still, both methods in this case have identified the damage location as the spring connection that has the largest stiffness loss after damage.

It is noted from Figure 10.11 and Figure 10.12 that in the application of both algorithms in this experiment, the stiffness values of some connection springs estimated using signals from different mass combinations are different (e.g. $k_{56}/456$ and $k_{56}/567$). In some cases(e.g. k_{45}) a relatively large variance of the stiffness estimators is observed for both algorithms (TDRM yields larger variation in stiffness estimates still).

196

These cases happen because of the out-of-plane motion of the masses caused by the manufacturing error; as observed in Figure 10.13, the two end brackets of each spring are not made exactly parallel during the manufacturing process, and hence some of the mass blocks are in a slightly skewed position and will jiggle and waggle a bit when the system is excited. Another interesting fact is that the stiffness estimators for some undamaged connections (e.g. the spring connection between masses 4 and 5) also undergo a slight change after damage occurred. This is because when switching the spring connection the system geometry is slightly changed – the skew angles of some mass blocks change. This changes the transverse vibration of the masses when subjected to shaker excitation, which increases the overall noise of the system.

The two experiments presented in this section demonstrate that FDRM yields more accurate and stable stiffness estimates than TDRM. Though the performances of the two algorithms are affected by the fact that the systems are not perfect linear elastic MDOF systems, their stiffness estimators are generally effective in identifying the extent and location of damage. The methods can also be applied to identify multiple concurrent damage locations; however, construction of the damage threshold should be determined according to the specific structural geometry and the associated modeling error.

10.9 CONCLUSION

This research investigated stiffness estimation/damage detection in a shear frame structure. Two methods are proposed to detect the interstory stiffness loss from acceleration measurements: regression using reconstructed displacements (TDRM) and regression using the signal auto/cross correlation spectra (FDRM). Both are applied to

responses from two simulated models for stiffness estimation and two lab specimens for damage detection, and their results are presented and their performances compared.

Both algorithms are shown to be effective for the applications. However, it is observed that FDRM is superior in almost every aspect: it is more accurate, more robust to noise, and less computationally intensive. This is because with the initial conditions unknown, displacement reconstruction from acceleration is an *ill-posed* problem (Hansen, 1998). To achieve a unique solution, additional regularization conditions are needed. Besides, the accuracy of such methods will decrease significantly even when the measurements are only slightly corrupted by noise. FDRM circumvented this problem as the initial conditions become constants in the regression model.

When joint rotations exist, the performance of these algorithms degrades. However, the stiffness estimators can still be used as viable damage indexes. In principle the proposed methods can be applied to more complicated structures, as the idea behind them is to use responses from adjacent nodes as inputs for the center node, and to infer the displacement/velocity responses from acceleration signals. In case of applications where the nodal rotations cannot be omitted from consideration, measurements on rotational effects (e.g. strain, or relative element or story rotation) should be acquired and incorporated into modeling to achieve a good performance.

In summary, the main objective of this research is to demonstrate the potential of using acceleration signals for structural damage detection purposes through examples of linear regression modeling for MDOF systems with a linear topology. These partial models based on local responses are more efficient and more sensitive alternatives for damage detection than modal analysis, which often requires output from a large array of

sensors to produce accurate results. Instead of treating all the responses as outputs from an unknown linear system, models presented here use responses at one location as output and those from adjacent locations as input. This is the essence of this approach; however, to make it more generally applicable several additional issues such as joint rotation and adaptation to complicated geometry will need to be addressed.

Table 10.1   Regression results from Eq. (1) using simulated data. The unit for stiffness is kN/m.

Node combination*	012		123		234		345		45
Connection location**	k_{01}	k_{12}	k_{12}	k_{23}	k_{23}	k_{34}	k_{34}	k_{45}	k_{45}
Est. stiffness	839.9	3359.6	3359.7	2519.8	2520.1	1260.1	1260.0	1400.0	1400.1
Actual stiffness	840	3360	3360	2520	2520	1260	1260	1400	1400

* e.g. 123 means the regression is based on responses from nodes 1-3. Node '0' means ground.

**e.g. k_{01} means the stiffness of the story between the ground and the first floor

Table 10.2   Regression results from TDRM: for each case 50 independent and identical simulations are run. The unit for stiffness is kN/m.

Node combination	012		123		234		345		45
Connection location	k_{01}	k_{12}	k_{12}	k_{23}	k_{23}	k_{34}	k_{34}	k_{45}	k_{45}
	Stiffness estimates from noise free signals								
Est. mean ($\bar{\hat{k}}$)	764.0	2885.6	3017.4	2183.6	2247.8	1096.5	1259.7	1304.3	1409.9
Normalized std. ($\sigma_{\hat{k}} / \bar{\hat{k}}$)	1.9%	0.5%	1.9%	1.7%	1.1%	1.7%	1.7%	0.7%	0.7%
Normalized bias ($\bar{\hat{k}} / k - 1$)	-9.0%	-14.1%	-10.2%	-13.3%	-10.8%	-13.0%	0.0%	-6.8%	0.7%
	Stiffness estimates from signals with a 5% noise level								
Est. mean ($\bar{\hat{k}}$)	757.2	2879.2	2966.3	2147.1	2239.1	1088.0	1257.0	1300.5	1404.4
Normalized std. ($\sigma_{\hat{k}} / \bar{\hat{k}}$)	3.4%	1.1%	4.2%	3.7%	2.7%	4.0%	3.8%	1.6%	1.7%
Normalized bias ($\bar{\hat{k}} / k - 1$)	-9.9%	-14.3%	-11.7%	-14.8%	-11.1%	-13.7%	-0.2%	-7.1%	0.3%
	Stiffness estimates from signals with a 10% noise level								
Est. mean ($\bar{\hat{k}}$)	724.2	2733.2	2734.0	2014.7	2149.8	1053.1	1246.7	1287.0	1389.2
Normalized std. ($\sigma_{\hat{k}} / \bar{\hat{k}}$)	7.5%	2.9%	9.0%	8.7%	5.3%	8.5%	6.6%	3.2%	2.8%
Normalized bias ($\bar{\hat{k}} / k - 1$)	-13.8%	-18.7%	-18.6%	-20.1%	-14.7%	-16.4%	-1.1%	-8.1%	-0.8%

Table 10.3   Comparison of performances of models with/without velocity data; results are obtained as average from 50 simulations with 5% additive Gaussian noise

Node combination*	012		123		234		345		45
Connection location**	k_{01}	k_{12}	k_{12}	k_{23}	k_{23}	k_{34}	k_{34}	k_{45}	k_{45}
TDRM results	783.3	2850.0	3008.3	2164.1	2184.6	1141.6	1286.6	1291.0	1409.0
TDRM with velocity data	895.4	3645.9	3510.8	2593. 4	2644.4	1314.3	1296.8	1411.1	1450.0
Actual stiffness	840	3360	3360	2520	2520	1260	1260	1400	1400

Table 10.4   FDRM results: for each case 50 independent and identical simulations are

run. The unit for stiffness is kN/m.

Node combination	012		123		234		345		45
Connection location	k_{01}	k_{12}	k_{12}	k_{23}	k_{23}	k_{34}	k_{34}	k_{45}	k_{45}
	Stiffness estimates from noise free signals								
Est. mean ($\overline{\hat{k}}$)	822.9	3317.9	3257.9	2475.2	2476.6	1201.4	1261.8	1381.0	1411.4
Normalized std. ($\sigma_{\hat{k}}/\overline{\hat{k}}$)	2.5%	0.5%	2.0%	2.9%	1.1%	1.9%	2.5%	1.1%	0.2%
Normalized bias ($\overline{\hat{k}}/k-1$)	-2.0%	-1.3%	-3.0%	-1.8%	-1.7%	-4.7%	0.1%	-1.4%	0.8%
	Stiffness estimates from signals with a 10% noise level								
Est. mean ($\overline{\hat{k}}$)	838.4	3310.1	3236.4	2478.9	2485.6	1196.6	1250.6	1386.6	1411.3
Normalized std. ($\sigma_{\hat{k}}/\overline{\hat{k}}$)	4.6%	0.9%	4.0%	5.6%	2.1%	3.5%	4.7%	1.9%	0.3%
Normalized bias ($\overline{\hat{k}}/k-1$)	-0.2%	-1.5%	-3.7%	-1.6%	-1.4%	-5.0%	-0.7%	-1.0%	0.8%
	Stiffness estimates from signals with a 20% noise level								
Est. mean ($\overline{\hat{k}}$)	841.1	3315.0	3264.8	2434.8	2491.9	1199.9	1269.2	1378.2	1410.3
Normalized std. ($\sigma_{\hat{k}}/\overline{\hat{k}}$)	6.5%	1.3%	4.8%	7.1%	2.7%	4.5%	6.8%	2.9%	0.6%
Normalized bias ($\overline{\hat{k}}/k-1$)	0.1%	-1.3%	-2.8%	-3.4%	-1.1%	-4.8%	0.7%	-1.6%	0.7%
	Stiffness estimates from signals with a 30% noise level								
Est. mean ($\overline{\hat{k}}$)	847.2	3301.7	3192.5	2399.3	2505.8	1190.2	1247.7	1391.0	1405.0
Normalized std. ($\sigma_{\hat{k}}/\overline{\hat{k}}$)	14.2%	2.7%	10.1%	13.8%	6.0%	10.5%	12.7%	5.4%	1.2%
Normalized bias ($\overline{\hat{k}}/k-1$)	0.9%	-1.7%	-5.0%	-4.8%	-0.6%	-5.5%	-1.0%	-0.6%	0.4%

203

Table 10.5   Stiffness estimation results for frames with flexible beams using FDRM;

for each case 50 independent and identical simulations are run. The unit for stiffness is

kN/m.

Node combination	012		123		234		345		45
Connection location	k_{01}	k_{12}	k_{12}	k_{23}	k_{23}	k_{34}	k_{34}	k_{45}	k_{45}
	Stiffness estimates when $EI_b / EI_c = 2$								
Est. mean ($\bar{\hat{k}}$)	1214.8	1457.4	1206.6	1045.2	932.0	1381.9	1184.5	1446.9	1344.5
Normalized std. ($\sigma_{\hat{k}} / \bar{\hat{k}}$)	9.0%	6.0%	9.3%	2.2%	7.2%	6.9%	12.0%	1.4%	1.0%
Normalized bias ($\bar{\hat{k}} / k - 1$)	-24.1%	9.3%	-9.5%	-21.6%	-30.1%	3.6%	-11.2%	-30.2%	-35.2%
	Stiffness estimates when $EI_b / EI_c = 4$								
Est. mean ($\bar{\hat{k}}$)	1393.9	1372.3	1206.3	1140.1	1059.0	1360.5	1193.3	1683.8	1609.6
Normalized std. ($\sigma_{\hat{k}} / \bar{\hat{k}}$)	5.4%	4.3%	9.2%	2.2%	3.7%	6.0%	14.1%	0.8%	0.7%
Normalized bias ($\bar{\hat{k}} / k - 1$)	-14.8%	2.8%	-10.5%	-16.9%	-25.9%	2.0%	-11.7%	-23.1%	-28.8%
	Stiffness estimates when $EI_b / EI_c = 8$								
Est. mean ($\bar{\hat{k}}$)	1494.9	1337.0	1218.8	1242.7	1177.2	1327.3	1259.9	1838.1	1806.6
Normalized std. ($\sigma_{\hat{k}} / \bar{\hat{k}}$)	3.3%	3.1%	5.1%	2.4%	2.9%	6.4%	10.7%	0.9%	0.9%
Normalized bias ($\bar{\hat{k}} / k - 1$)	-7.0%	0.3%	-9.4%	-7.3%	-13.3%	-0.5%	-5.8%	-12.8%	-14.8%
	Stiffness estimates when $EI_b / EI_c = 12$								
Est. mean ($\bar{\hat{k}}$)	1538.1	1326.7	1281.2	1255.3	1200.2	1383.8	1354.5	1913.5	1873.3
Normalized std. ($\sigma_{\hat{k}} / \bar{\hat{k}}$)	2.4%	1.8%	4.7%	1.4%	3.3%	5.3%	10.7%	0.6%	1.0%
Normalized bias ($\bar{\hat{k}} / k - 1$)	-3.9%	-0.5%	-3.9%	-5.9%	-10.0%	3.8%	1.6%	-7.7%	-9.7%

204

Table 10.6   Stiffness estimation results using enhanced TDRM scheme; for each case 50 independent and identical simulations are run. The unit for stiffness is kN/m.

	Stiffness estimates when $EI_b / EI_c = 2$					Stiffness estimates when $EI_b / EI_c = 4$					Stiffness estimates when $EI_b / EI_c = 8$				
i**	1	2	3	4	5	1	2	3	4	5	1	2	3	4	5
$\overline{\hat{k}}_{(i-1,i)}$	--	-1122.5	-926.5	-764.6	-1295.1	--	-1102.0	-1045.4	-808.3	-1537.9	--	-1010.9	-1115.0	-801.9	-1735.3
$\overline{\hat{k}}_{(i,i)}$	2459.7	1982.1	1888.7	2151.0	1267.6	2531.6	2174.7	2102.5	2445.9	1531.0	2634.6	2226.8	2309.2	2614.6	1737.2
$\overline{\hat{k}}_{(i+1,i)}$	-1057.9	-968.0	-985.0	-1357.0	--	-1083.9	-1080.2	-1068.9	-1580.6	--	-1141.0	-1127.4	-1176.0	-1729.1	--
	Normalized bias of the estimates when $EI_b / EI_c = 2$					Normalized bias of the estimates when $EI_b / EI_c = 4$					Normalized bias of the estimates when $EI_b / EI_c = 8$				
i**	1	2	3	4	5	1	2	3	4	5	1	2	3	4	5
$\overline{\hat{k}}_{(i-1,i)} / k_{(i-1,i)} - 1$	--	-17.75%	-29.61%	-43.58%	-18.12%	--	-18.58%	-21.21%	-40.42%	-13.47%	--	-24.84%	-16.24%	-40.61%	-9.06%
$\overline{\hat{k}}_{(i,i)} / k_{(i,i)} - 1$	-9.42%	-13.53%	-16.61%	-21.82%	-8.15%	-9.60%	-10.68%	-13.01%	-18.86%	-6.53%	-7.83%	-12.15%	-8.51%	-18.01%	-4.72%
$\overline{\hat{k}}_{(i+1,i)} / k_{(i+1,i)} - 1$	-22.49%	-26.45%	-27.32%	-14.21%	--	-19.91%	-18.58%	-21.21%	-11.06%	--	-15.16%	-15.31%	-12.90%	-9.38%	--
	Normalized standard deviation of the estimates when $EI_b / EI_c = 2$					Normalized standard deviation of the estimates when $EI_b / EI_c = 4$					Normalized standard deviation of the estimates when $EI_b / EI_c = 8$				
i**	1	2	3	4	5	1	2	3	4	5	1	2	3	4	5
$\text{std}\left(\hat{k}_{(i-1,i)}\right) / \left|\overline{\hat{k}}_{(i-1,i)}\right|$	--	27.77%	7.19%	42.49%	3.32%	--	24.25%	6.65%	55.43%	1.47%	--	28.08%	5.41%	49.26%	1.83%
$\text{std}\left(\hat{k}_{(i,i)}\right) / \left|\overline{\hat{k}}_{(i,i)}\right|$	7.19%	9.89%	9.39%	14.02%	3.12%	4.88%	6.67%	11.18%	17.38%	1.41%	2.52%	7.84%	5.74%	13.97%	1.61%
$\text{std}\left(\hat{k}_{(i+1,i)}\right) / \left|\overline{\hat{k}}_{(i+1,i)}\right|$	11.22%	9.94%	14.48%	3.65%	--	9.04%	6.00%	19.49%	4.75%	--	7.58%	4.42%	10.06%	3.89%	--

**: the number of the middle node in the regression model

Table 10.7   Stiffness estimation results using enhanced FDRM scheme; for each case 50 independent and identical simulations are run. The unit for stiffness is kN/m.

	Stiffness estimates when $EI_b / EI_c = 2$					Stiffness estimates when $EI_b / EI_c = 4$					Stiffness estimates when $EI_b / EI_c = 8$				
i**	1	2	3	4	5	1	2	3	4	5	1	2	3	4	5
$\overline{\hat{k}}_{(i-1,i)}$	--	-1457.4	-1149.7	-1382.5	-1477.4	--	-1382.0	-1229.3	-1372.8	-1697.8	--	-1344.0	-1270.1	-1348.6	-1849.8
$\overline{\hat{k}}_{(i,i)}$	2666.9	2265.4	2240.8	2686.0	1308.3	2761.5	2411.4	2420.8	2916.6	1584.8	2814.9	2501.6	2524.8	3094.7	1789.9
$\overline{\hat{k}}_{(i+1,i)}$	-1441.8	-1127.3	-1289.6	-1368.2	--	-1372.5	-1141.8	-1260.6	-1630.7	--	-1353.7	-1168.5	-1262.0	-1813.5	--
	Normalized bias of the estimates when $EI_b / EI_c = 2$					Normalized bias of the estimates when $EI_b / EI_c = 4$					Normalized bias of the estimates when $EI_b / EI_c = 8$				
i**	1	2	3	4	5	1	2	3	4	5	1	2	3	4	5
$\overline{\hat{k}}_{(i-1,i)} / k_{(i-1,i)} - 1$	--	6.79%	-12.64%	2.01%	-6.60%	--	2.11%	-7.35%	1.19%	-4.47%	--	-0.07%	-4.59%	-0.12%	-3.06%
$\overline{\hat{k}}_{(i,i)} / k_{(i,i)} - 1$	-1.79%	-1.17%	-1.07%	-2.38%	-5.20%	-1.39%	-0.96%	0.16%	-3.24%	-3.25%	-1.52%	-1.31%	0.03%	-2.95%	-1.83%
$\overline{\hat{k}}_{(i+1,i)} / k_{(i+1,i)} - 1$	5.64%	-14.35%	-4.85%	-13.50%	--	1.41%	-13.94%	-7.08%	-8.24%	--	0.65%	-12.23%	-6.53%	-4.96%	--
	Normalized standard deviation of the estimates when $EI_b / EI_c = 2$					Normalized standard deviation of the estimates when $EI_b / EI_c = 4$					Normalized standard deviation of the estimates when $EI_b / EI_c = 8$				
i**	1	2	3	4	5	1	2	3	4	5	1	2	3	4	5
$\mathrm{std}\left(\hat{k}_{(i-1,i)}\right) / \left|\overline{\hat{k}}_{(i-1,i)}\right|$	--	16.07%	7.32%	14.94%	4.27%	--	8.83%	5.55%	10.14%	4.03%	--	7.07%	3.97%	8.13%	3.05%
$\mathrm{std}\left(\hat{k}_{(i,i)}\right) / \left|\overline{\hat{k}}_{(i,i)}\right|$	4.37%	6.38%	7.40%	5.84%	3.27%	2.63%	3.87%	6.02%	7.37%	1.85%	2.62%	3.72%	4.17%	5.40%	1.71%
$\mathrm{std}\left(\hat{k}_{(i+1,i)}\right) / \left|\overline{\hat{k}}_{(i+1,i)}\right|$	14.84%	15.37%	11.66%	3.14%	--	9.31%	11.69%	16.38%	2.12%	--	9.83%	6.76%	11.99%	1.90%	--

**: the number of the middle node in the regression model

Table 10.8   Changes in the estimated stiffness matrix from FDRM after damage

occurs. The unit for stiffness is kN/m. This is the average of results from 10 simulations.

Row No. / Column No.	1	2	3	4	5
1	**184.8**	-22.3	0.0	0.0	0.0
2	-26.5	25.6	-8.4	0.0	0.0
3	0.0	-46.7	29.5	54.9	0.0
4	0.0	0.0	-43.7	55.3	4.5
5	0.0	0.0	0.0	-25.7	-13.8

Table 10.9   Basic properties of Laboratory specimens used

	5 DOF multi-story model	7 DOF mass-spring system
Material	aluminum-plexiglas	Steel
Overall Dimension*(Unit: cm)	H:78.11 W:10.16 L:19.37	H:127 W:35.56 L:78.74
Mass block size* (Unit: cm)	TH:1.91 W:10.16 L:19.37	TH: 2.54 H:5.08 W: 8.89
Effective nodal mass (Unit: kg)	1.09	1.17
Modal frequencies**(Unit: Hz)	0.65(0.5), 2.30(2.00), 3.70(3.35), 4.90(4.45) and 6.20(5.35)	4.12(4.32), 9.23 (9.01), and 13.82 (13.60)

* H—height, W – width, L—length, TH—thickness

** terms outside / inside the brackets are the frequencies from healthy/damaged state; for the 7 DOF system only 3 lowest modal frequencies are listed because the rest cannot be consistently identified
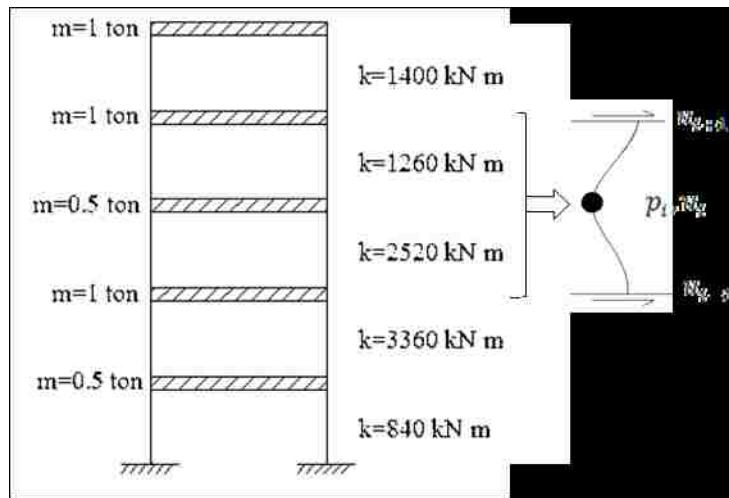
Figure 10.1   A simulated 5 DOF shear frame with its story mass and

interstory stiffness values
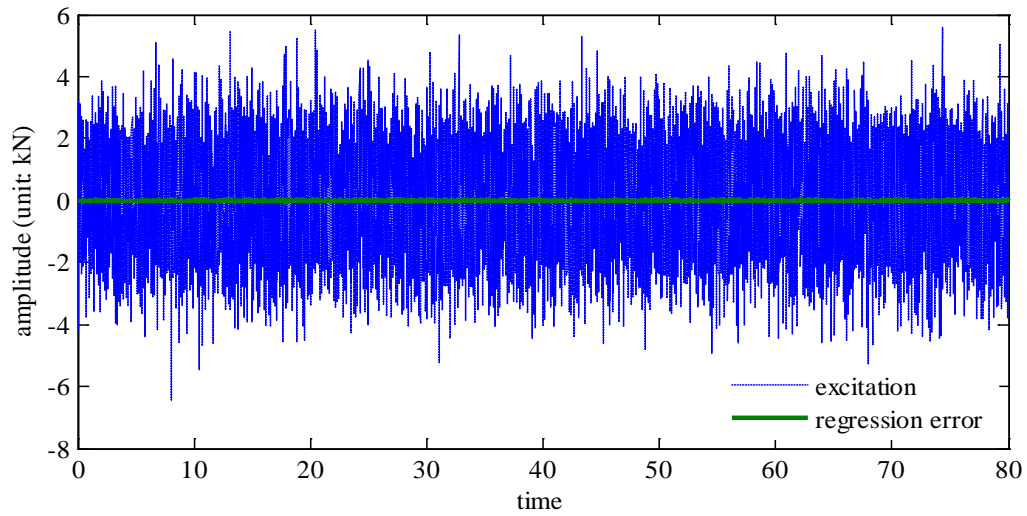
Figure 10.2   A contrast of the amplitude of the excitation and the

regression error from regressing the response from the 3rd

node on those from 2nd and 4th nodes.

$$
\begin{pmatrix}
2933.33 & -1333.33 & 0.00 & 0.00 & 0.00 \\
-1333.33 & 2666.67 & -1333.33 & 0.00 & 0.00 \\
0.00 & -1333.33 & 2666.67 & -1333.33 & 0.00 \\
0.00 & 0.00 & -1333.33 & 3406.93 & -2073.60 \\
0.00 & 0.00 & 0.00 & -2073.60 & 2073.60
\end{pmatrix}
\quad
\begin{pmatrix}
2900.86 & -1338.49 & 31.34 & -0.49 & 0.01 \\
-1338.49 & 2609.23 & -1332.93 & 31.39 & -0.62 \\
31.34 & -1332.93 & 2604.23 & -1341.78 & 39.63 \\
-0.49 & 31.39 & -1341.78 & 3313.30 & -2002.42 \\
0.01 & -0.62 & 39.63 & -2002.42 & 1963.39
\end{pmatrix}
$$

(c)   (d)

$$
\begin{pmatrix}
2837.59 & -1348.07 & 91.77 & -4.23 & 0.23 \\
-1348.07 & 2498.64 & -1329.86 & 92.03 & -5.03 \\
91.77 & -1329.86 & 2485.09 & -1353.20 & 110.40 \\
-4.23 & 92.03 & -1353.20 & 3126.49 & -1861.28 \\
0.23 & -5.03 & 110.40 & -1861.28 & 1755.69
\end{pmatrix}
\quad
\begin{pmatrix}
2715.53 & -1364.75 & 205.24 & -21.17 & 2.33 \\
-1364.75 & 2292.19 & -1316.13 & 204.57 & -22.46 \\
205.24 & -1316.13 & 2265.04 & -1355.30 & 222.02 \\
-21.17 & 204.57 & -1355.30 & 2751.49 & -1581.73 \\
2.33 & -22.46 & 222.02 & -1581.73 & 1380.08
\end{pmatrix}
$$

Figure 10.3   Contrast of the stiffness matrices of frames with different beam-to-column sectional stiffness ratios (EI_b / EI_c) (a) $EI_b / EI_c = \infty$; (b) $EI_b / EI_c = 12$; (c) $EI_b / EI_c = 4$; (d) $EI_b / EI_c = 2$.

211
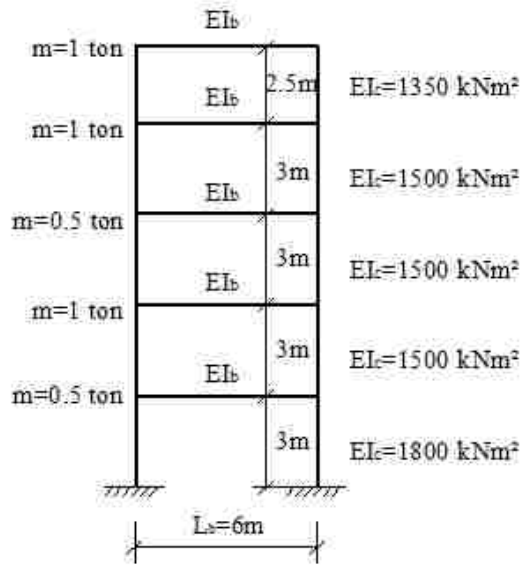
Figure 10.4   A frame with flexible beams
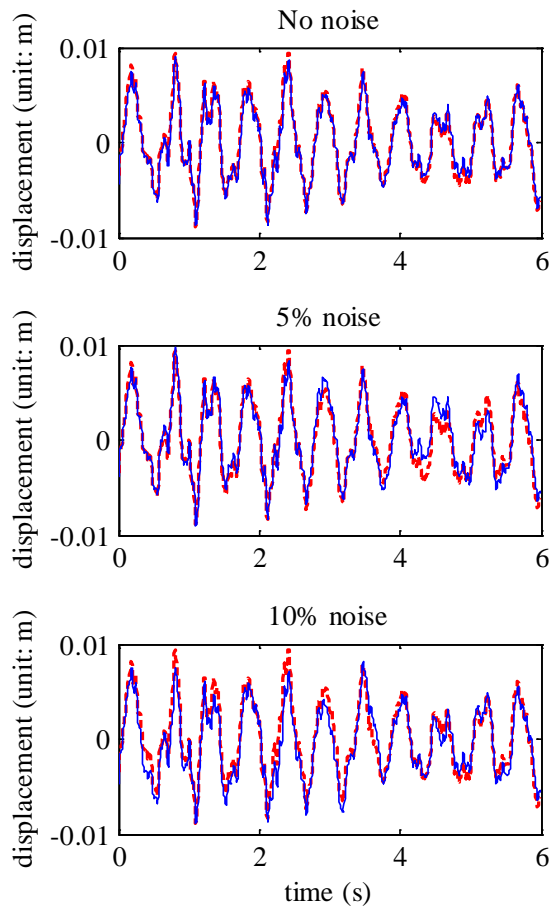
Figure 10.5   Comparison between the reconstructed displacement (blue

solid line) and the real displacement (red dashed line) for

different acceleration measurement noise levels
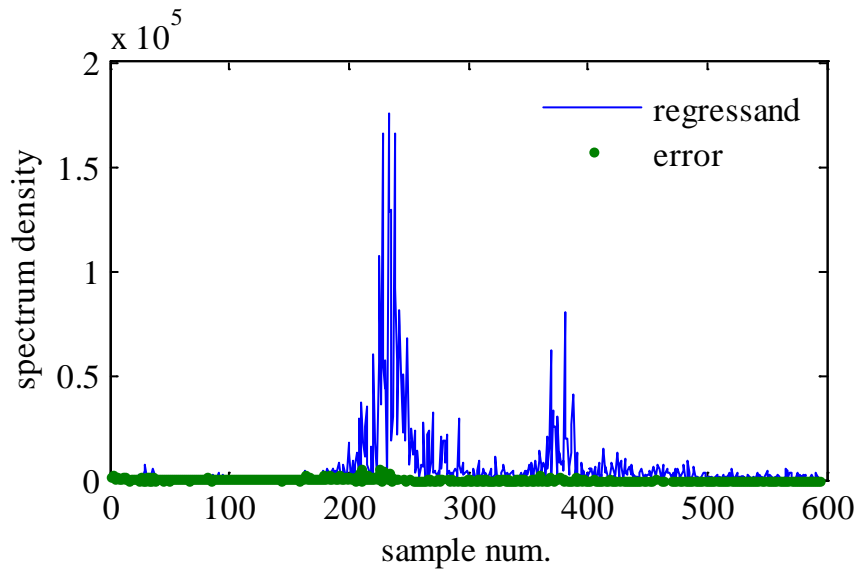
Figure 10.6   The error from FDRM model is insignificant compared to the

regressand spectrum. The acceleration measurements used are

from node 2-4.

Figure 10.7   The 5 DOF plexiglass-aluminum model

Figure 10.8   The 7-DOF steel mass-spring model
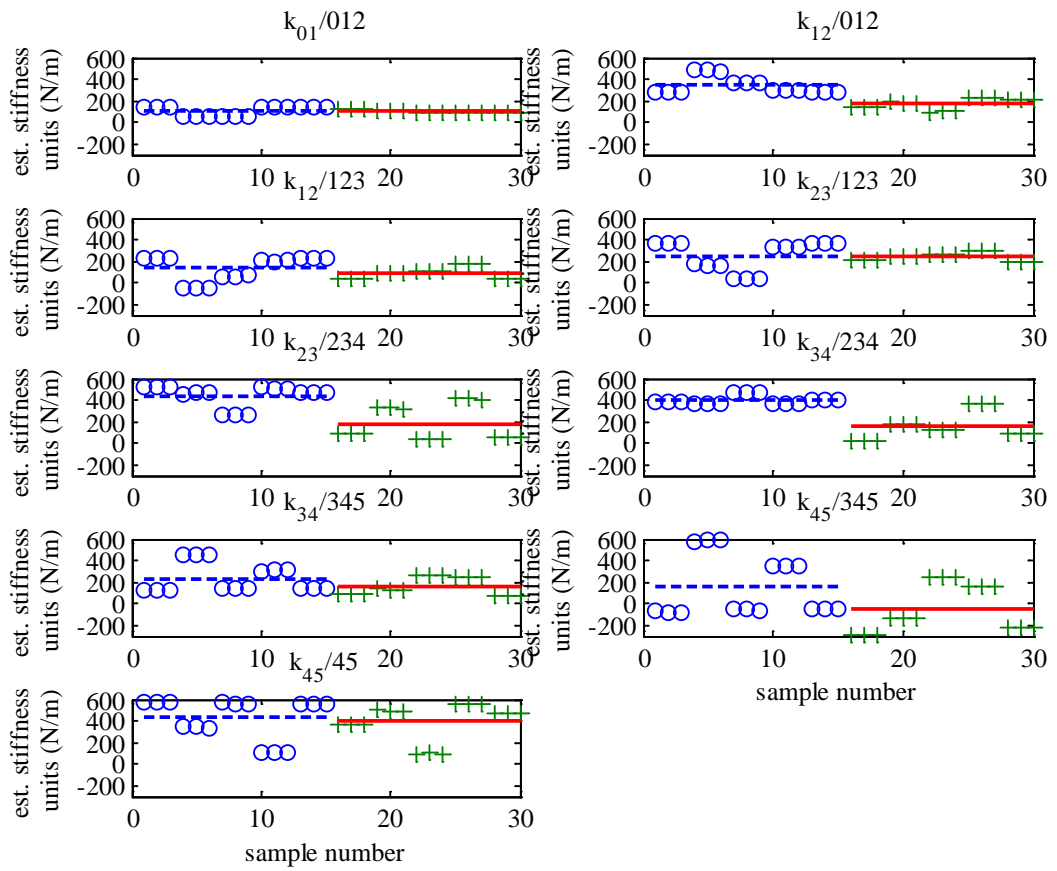
Figure 10.9   Stiffness estimation results for the 5 DOF model using TDRM
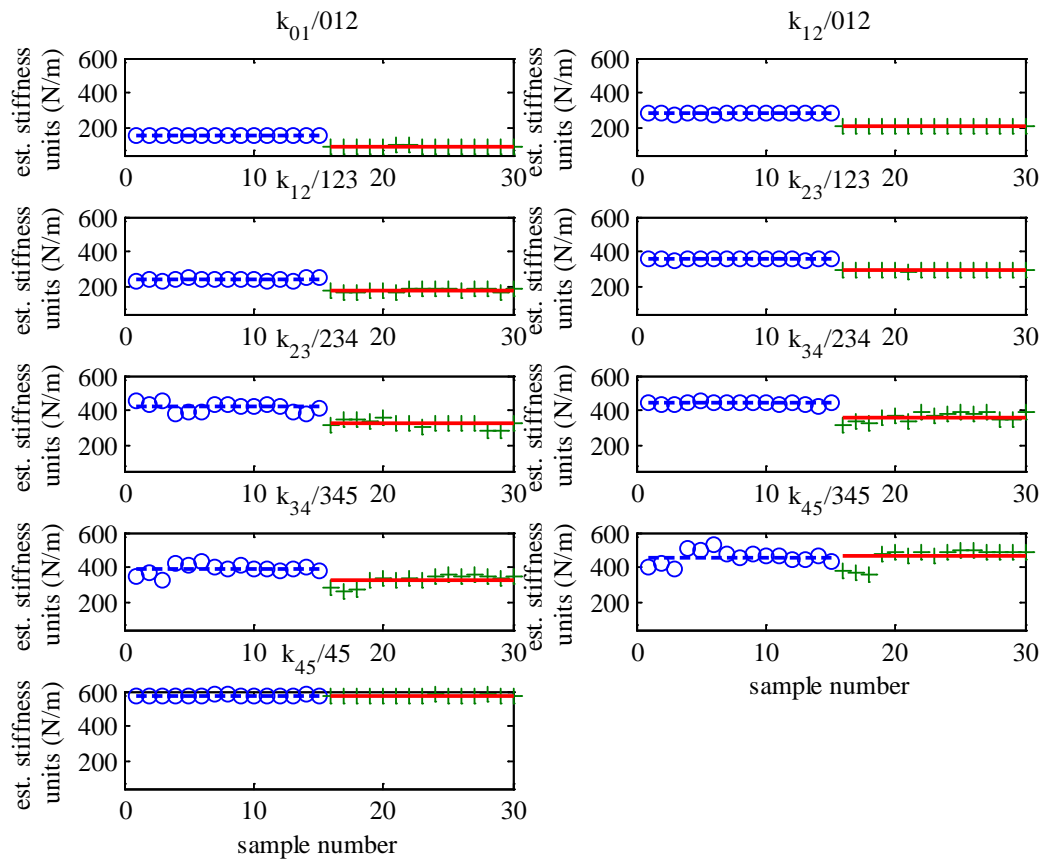
Figure 10.10   Stiffness estimation results for the 5 DOF model using FDRM
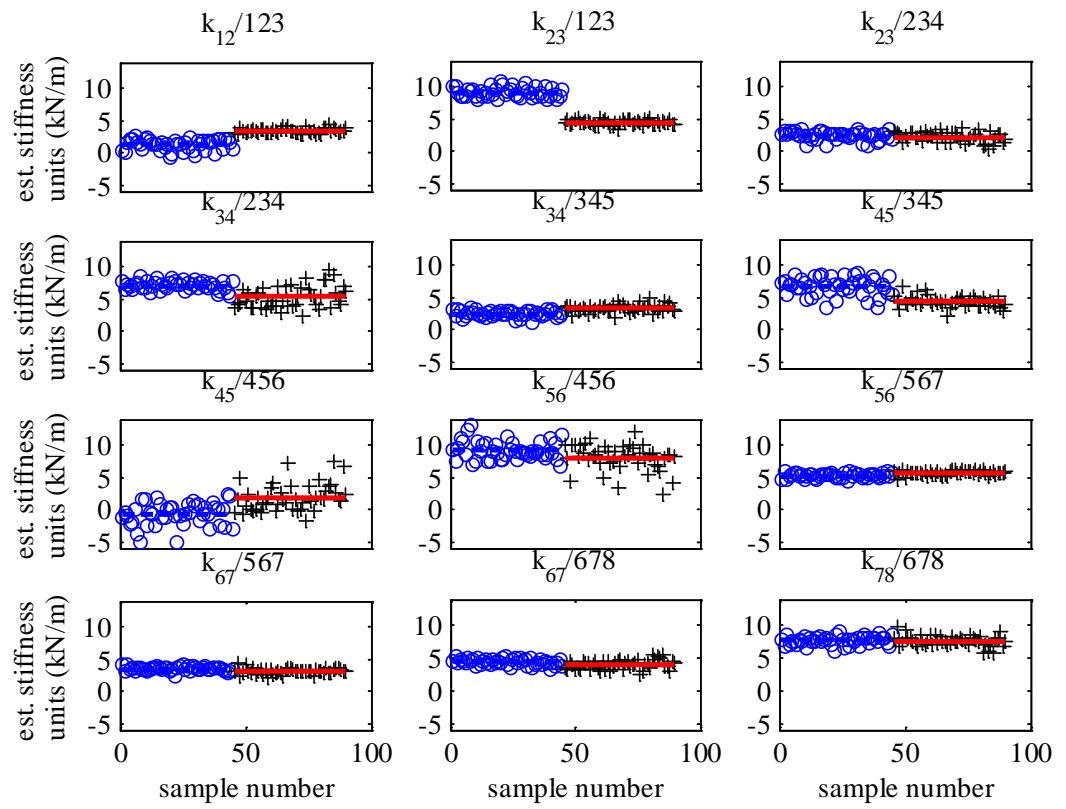
Figure 10.11   Stiffness estimation results for the 7 DOF model using TDRM
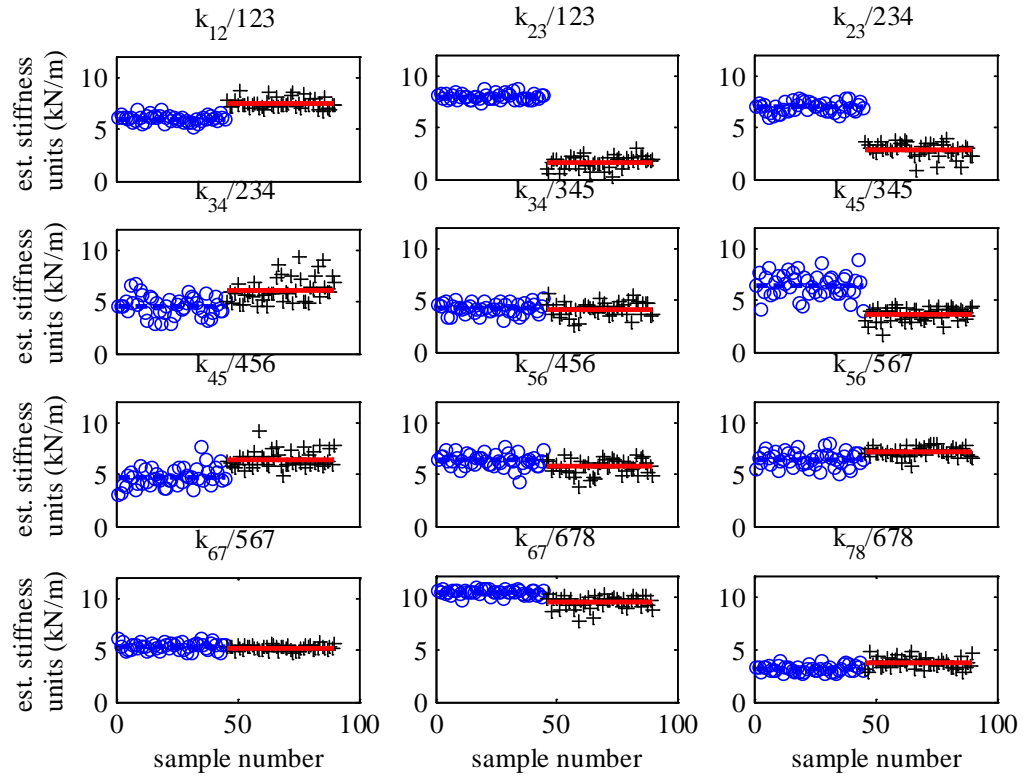
Figure 10.12   Stiffness estimation results for the 7 DOF model using FDRM
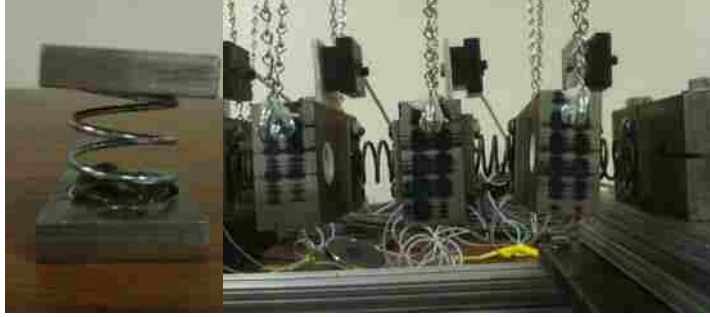
Figure 10.13   Skewed position of the masses as a result of unparallel spring

ends.

Chapter 11 Substructural approach for damage detection in flexible members

11.1 PRELUDE

To form an on-line automatic structural assessment procedure that requires little involvement of technicians/experts (thereby reducing the cost and bias in the decision making process), damage features that indicate damage location/extent and damage thresholds that carry the smallest risk of misclassification are needed.

As noted in above chapters, system identification/modal realization is the classical method used for structural health monitoring purposes(Hassiotis and Jeong, 1995; Pothisiri and Hjelmstad, 2003; Salawu, 1997). While these damage features are theoretically well-grounded, it may take a lot of time and resources for some algorithms to achieve good results, and more importantly, these features are sometimes found to be not responsive to local damage (Doebling et al., 1998). In an effort to overcome these problems, damage detection techniques that adopt statistical analysis on structural responses (Sohn and Farrar, 2001; Zhang, 2007) have been proposed and found to be sensitive to damage, but also to the excitation condition change as a result of the inherent information limitation for this family of methods.

In order to strike a balance between a method's damage sensitivity and performance robustness, Substructural approaches that treat the entire structural system as an assembly of substructures and model each substructure independently have been developed and tested (Gul and Catbas, 2010; Hernandez-Garcia et al., 2010a; Yan et al., 2011). This family of algorithms often uses the response from within the substructure for output and

responses at substructural boundaries for input, and therefore damage features based on the estimated substructural model parameters and model residuals should be conveying information strongly related to physical behavior of the substructures. Gul and Catbas (2010) applied autoregressive with exogenous input (ARX) modeling to measurements collected from clusters of sensors for damage localization in a numerical mass-spring system and a steel grid set up in a laboratory. Their analysis results show that while the test produces false alarms (i.e. detects changes in intact substructures), the damage locations are correctly identified as where the largest fit ratio changes occur. Hou et al. (2011) used the experimental responses to form the impulse response matrix and identify damage through computing the residual strains/ deformations. In addition, Weng et al. (2011) have employed substructure system identification results for model updating.

Compared with the approaches mentioned in the previous paragraph, substructural methods are generally better at damage location detection, less affected by operational condition variations than scalar signal analysis, and less computationally demanding than many global system identification approaches.

11.2 MOTIVATION AND ORGANIZATION

Among the above listed studies on substructural damage identification, several employ black-box models such as numerical ARX model and neural network that cannot be directly related to structural physics. For those literatures listed in previous chapter that explicitly address the damage-induced structural stiffness loss, the algorithms are devised mainly for structures with linear topology (i.e. mass-spring and shear building systems). In order to assess the local stiffness variation for structures with more complex geometry, the TDRM/FDRM proposed in Chapter 11 is extended to substructural beam

223

element models in plane and space. Two types of element models are developed, one of which considers only the static effects, and the other takes into account the dynamic effects through assuming an intermediate concentrated mass. The regression expression for each model can be formed in either time or frequency domain. Damage features based on these regression models are then integrated with change point analysis (CPA) (Brodsky and Darkhovsky, 1993; Nigro et al., 2014) methods and voting schemes for structural damage assessment. The effectiveness of the proposed methodology is validated through numerical and experimental implementations.

The remaining content is organized in 6 sections.

- Section 11.3 contains the discussion on the substructural model in general and the development of substructural beam models for both the 2D and 3D cases.
- Section 11.4 formulates the regression procedure for the substructural models and three damage features.
- Section 11.5 details a voting-based information fusion process to combine the damage detection results from different models/damage features/CPA techniques.
- Section 11.6 uses data from a simulated frame and a simulated truss to demonstrate the proposed 2D and 3D modeling methods, respectively.
- Section 11.7 presents implementation results on a laboratory frame and a real-world truss bridge for the algorithms, and their damage identification and localization performances are compared and contrasted.
- Section 11.8 draws conclusions on the merits and demerits of the methods.

224

11.3 SUBSTRUCTURAL MODEL DEVELOPMENT BASED ON FINITE ELEMENT CONCEPT

To apply the linear regression techniques for damage identification, we need to clarify an input-output linear model for the structure that is to be assessed. Since the goal of this research is to characterize local damage, structures will be divided into substructures and each substructure will be analyzed and modeled independently.

The behavior of a substructure is controlled by two types of influences: those acting directly on the substructure itself and those acting on its 'boundary'. The relation between these inputs and the substructure response reflects certain physical properties of the substructure. When the structural responses collected are structural vibration (the most commonly monitored signal in SHM applications), the relevant structural physical properties are the material constitutive relations.

The displacement response at an internal node of a substructure can be expressed as the following function (Figure 11.1):

$$\mathbf{r}_i = h(S, p, \mathbf{x}_i) \tag{11.1}$$

where S is the boundary force, p is the excitation acting on the substructure, and $\mathbf{x}_i$ is the coordinate vector of the internal node. $h(\cdot)$ is determined from both the substructural constitutive relations and the geometry, while S is a function of the boundary displacement response ($\mathbf{r}_b$) and its higher order derivatives with respect to the system coordinates ($\mathbf{r}_b^{(n)}$):

$$S = g(\mathbf{r}_b, \mathbf{r}_b^{(n)}) \tag{11.2}$$

225

Exact characterization of a substructural system requires continuous measurement of system behavior along the boundaries, which is unfeasible in practice since most of the existing sensing systems are discrete and sparse. Therefore, it is assumed that the boundary responses have a finite number of degree-of-freedoms (DOF) and can be safely inferred from measurements collected at a few locations along the boundary. Also, knowledge of the excitation on the substructure is necessary for model identification. This force generally cannot be measured directly; however, there are cases where it can be either eliminated from consideration or expressed using other measurable quantities. For example, if the excitation is white noise, its effect can be canceled out by taking the autocovariance function of the responses as the system free vibration response (James III et al., 1993). If the excitation is the inertial force of the substructural mass, then it is a function of substructural system mass and acceleration (i.e. $p = p(m, \ddot{\mathbf{r}}_{b}, \ddot{\mathbf{r}}_{i})$).

When the structure is linear and substitution principle can be applied, Eq. (11.3) becomes:

$$\mathbf{r}_{i} = h(S, \mathbf{x}_{i}) + h(p, \mathbf{x}_{i}) = h(g(\mathbf{r}_{b}, \mathbf{r}_{b}^{(n)}), \mathbf{x}_{i}) + h(p, \mathbf{x}_{i})$$
$$= \begin{cases} h(g(\mathbf{r}_{b}, \mathbf{r}_{b}^{(n)}), \mathbf{x}_{i}) \text{ (Static case with no directly applied excitation)} \\ h(g(\mathbf{r}_{b}, \mathbf{r}_{b}^{(n)}), \mathbf{x}_{i}) + h(p(m, \ddot{\mathbf{r}}_{b}, \ddot{\mathbf{r}}_{i}), \mathbf{x}_{i}) \text{ (Dynamic case with no directly applied excitation),} \end{cases}$$
$$(11.3)$$

Here velocity measurements are not considered as damping is assumed negligible, and $\mathbf{r}_{b}$ / $\mathbf{r}_{b}^{(n)}$ terms are, as noted before, referring to the data collected at a few sensing locations. With both internal and boundary responses of the substructure sampled, a model reflecting the underlying structural physics can be identified using one of the existing numerical system identification techniques. The accuracy of the results will depend on

226

how closely the measurements represent the boundary interactions and the inertial forces in the dynamic case. The whole idea bears some similarity to the substructuring method adopted in finite element modeling (FEM); only the latter aims at solving for structural response by assembling substructural stiffness matrices into one global stiffness matrix and forming equilibrium equations, while the former estimates the structural stiffness properties from known structural response and operates separately on individual substructures.

The remainder of this section will be devoted to construction of linear substructural models for beam element, one of the most studied finite element types in the literature. In the first subsection, static and dynamic models for beam elements in planar space are presented and associated input-output relations are defined. The relations are then generalized for modeling of beam members in three-dimensional Euclidean space in the second subsection.

11.3.1 Substructural models for beam in plane
For modeling of in-plane elements with no axial elongation, translation perpendicular to the member axis is the only DOF along the member. Measurements needed at beam ends are the translation and rotational movements.

11.3.1.1 Static beam model in plane
For a continuous Euler-Bernoulli beam model with section stiffness $EI(x)$ when subjected to no intermediate load (Figure 11.2(a)), the displacement $u(x)$ will satisfy the 4$^{\text{th}}$ order differential equation:

$$\frac{d^2\left(EI(x)d^2u(x)\right)}{dx^4} = 0 \tag{11.4}$$

227

Constants for the homogenous solution can be determined using the displacement and slope angles at both beam ends. When the beam remains linear in terms of the stress-strain relationship, conditions of slope can be replaced with conditions of strain (at the upper/lower surface):

$$u(x_C) = f_1(u_A, \varepsilon_A, u_B, \varepsilon_B) \tag{11.5}$$

where $f_1(\cdot)$ denotes a certain functional relation. This expression is useful in cases that the strain instead of slope is measured. When $EI(x)$ satisfies certain conditions so that the solution of Eq. (11.4) is linear with respect to its homogeneous constants, f_1 becomes a linear function.

In vibration monitoring applications that measure the system's acceleration instead of displacements, this model can still be applied by taking the 2nd derivative of Eq. (11.5) with respect to time if the system stiffness-to-mass ratio is large:

$$a_C = \ddot{u}(x_C) = f_1(\ddot{u}_A, \ddot{\varepsilon}_A, \ddot{u}_B, \ddot{\varepsilon}_B) = f_1(a_A, \ddot{\varepsilon}_A, a_B, \ddot{\varepsilon}_B) \tag{11.6}$$

where a_A, a_B and a_C are the acceleration signals measured at different positions indicated by the subscripts. This relation can also be formulated in the frequency domain by taking the one-sided Fourier Transform of Eq.(11.6):

$$\begin{aligned}
\hat{a}_C(i\omega) &= \hat{f}_1(a_A, \ddot{\varepsilon}_A, a_B, \ddot{\varepsilon}_B) \overset{f\ linear}{\Rightarrow} f_1(\hat{a}_A(i\omega), \hat{\ddot{\varepsilon}}_A(i\omega), \hat{a}_B(i\omega), \hat{\ddot{\varepsilon}}_B(i\omega)) \\
&= f_1(\hat{a}_A(i\omega), -\omega^2 \hat{\varepsilon}_A(i\omega) - i\omega \varepsilon_A(t=0) - \dot{\varepsilon}_A(t=0), \hat{a}_B(i\omega), -\omega^2 \hat{\varepsilon}_B(i\omega) - i\omega \varepsilon_B(t=0) - \dot{\varepsilon}_B(t=0)) \\
&= f_1(\hat{a}_A(i\omega), -\omega^2 \hat{\varepsilon}_A(i\omega), \hat{a}_B(i\omega), -\omega^2 \hat{\varepsilon}_B(i\omega)) + Cst_1.
\end{aligned} \tag{11.7}$$

Only the real part of the frequency domain representation will be retained for regression as it contains more power than the imaginary part. For all the derivations

228

herein subscripted *Cst* is a regression constant. When $f_1(\cdot)$ is a linear function, the physical interpretation of the coefficients of the function variables is shown in Figure 11.2(b). In the plot it is assumed that a strain gage is applied to the top surface of the beam element. Here $h_A^{'}$ and $h_B^{'}$ are used to denote the vertical distances from the section centroid at A and B to their respective strain gage locations. The coefficients are numbered in the order in which their corresponding variables appear inside the function bracket of Eq. (11.7). Basically, each interpretation is obtained as the translational displacement at C from setting the corresponding boundary condition to unity and all the rest conditions to zero. This knowledge will be useful in understanding of the substructural behavior, and in light of possible structural damage, identification of the damage location and extent. It can be seen that the coefficients of the acceleration terms (β_1 and β_3) will not be affected by substructural stiffness loss unless a hinge formed somewhere along the beam. However, since this static model is rarely an exact description of real beam members, these coefficients are still retained for structural state evaluation.

11.3.1.2 Beam model in plane, with a lumped mass

The model introduced in the previous subsection addresses only static/quasi-static applications. Here a model that incorporates a part of dynamic effects is constructed by adding a lumped mass on the beam (Figure 11.3(a)). Again assuming linear material constitutive relation and applying the generalized force concept:

$$u(x) = f\left(u_A, \varepsilon_A, m\ddot{u}_C, u_B, \varepsilon_B\right) \tag{11.8}$$

When f is a linear function (the conditions for this to hold are still the same as in part (11.3.2.1)), Eq. (11.8) can be reformulated as:

$$a_C = \ddot{u}_C = f_2\left(u_A, \varepsilon_A, u_C, u_B, \varepsilon_B\right) \tag{11.9}$$

f_2 is another linear function with different coefficients. Its corresponding frequency domain representation is

$$
\begin{aligned}
\hat{a}_C(i\omega) &= \hat{f}_2\left(u_A, \varepsilon_A, u_C, u_B, \varepsilon_B\right) \overset{f\ linear}{\Rightarrow} f_2\left(\hat{u}_A(i\omega), \hat{\varepsilon}_A(i\omega), \hat{u}_C(i\omega), \hat{u}_B(i\omega), \hat{\varepsilon}_B(i\omega)\right) \\
&= f_2\left(\frac{\hat{a}_A(i\omega) + i\omega u_A(t=0) + \dot{u}_A(t=0)}{-\omega^2}, \hat{\varepsilon}_A(i\omega), \frac{\hat{a}_C(i\omega) + i\omega u_C(t=0) + \dot{u}_C(t=0)}{-\omega^2},\right. \\
&\qquad\qquad \left. \frac{\hat{a}_B(i\omega) + i\omega u_B(t=0) + \dot{u}_B(t=0)}{-\omega^2}, \hat{\varepsilon}_B(i\omega)\right) \\
&= f_2\left(\hat{a}_A(i\omega)/-\omega^2, \hat{\varepsilon}_A(i\omega), \hat{a}_C(i\omega)/-\omega^2, \hat{a}_B(i\omega)/-\omega^2, \hat{\varepsilon}_B(i\omega)\right) + Cst_2.
\end{aligned}
$$

$$\tag{11.10}$$

In a manner similar to that of Figure 11.2(b), Figure 11.3(b) illustrates the physical meaning associated with each variable coefficient. Note that here each coefficient is represented with a force instead of a displacement, and when the assumed mass value at C is not unity, all of the force values are divided by the actual mass value to get the linear coefficients ($\{\beta_k\}$). In the definition of this model, coefficients of all variables are affected by beam stiffness variations. The exact relation can be found using standard structural analysis techniques (e.g. virtual work, etc.).

11.3.2 Substructural models for beam in three dimensional (3D) space

Substructural modeling for beams in three-dimensional space is innately a more complex problem, especially when torsional deformation is taken into consideration. Otherwise, it can be done by analyzing the bending about strong/weak axis as a planar

bending problem so that model definitions from the previous subsection can be applied. In this subsection, relations between the internal responses and boundary responses of an arbitrary 3D beam (Figure 11.4) will be derived.

11.3.2.1 Static beam model in 3D space

The homogeneous governing differential equations for the translation (at the centroid) and rotation (with respect to the shear center) of a linear beam in 3D space are examined (without considering second-order effects) in (Seaburg and Carter, 1997):

$$\frac{d^2\left(EI_y(z)d^2u(z)\right)}{dz^4} = 0,$$

$$\frac{d^2\left(EI_x(z)d^2v(z)\right)}{dz^4} = 0,$$

$$\frac{d\left(GK_T(z)d\phi(z)\right)}{dz^2} - \frac{d\left(EI_\omega(z)d^3\phi(z)\right)}{dz^4} = 0. \qquad (11.11)$$

where u, v and ϕ are x-direction translation, y-direction translation and torsion angle at the section centroid. EI_x and EI_y are the section bending stiffness about the x and y axes, respectively. GK_T is the St. Venant torsional stiffness and EI_ω is the warping torsional stiffness. Since these three differential equations are all fourth-order, six boundary conditions are needed at each end of the beam for a unique solution. Three such conditions can be obtained by measuring the translation and axial rotational responses at the beam ends. Because direct measurement of internal forces or derivatives of translation/axial rotation is not feasible, strains measured at three distinct points along the section circumference can be used in their stead. Justification for this comes from the fact that when the system is linear, these strain data are the linearly transformed versions of

231

three components of normal stress: warping normal stress (σ_W), bending normal stress about x axis (σ_{bx}) and bending normal stress about y axis (σ_{by}), which are in turn proportional to second-order derivatives of the rotation and translation along the beam length (i.e. ϕ'', u'', v'').

With the necessary boundary conditions identified, static substructural model can be defined according to Eq. (11.12):

$$\mathbf{r}(z) = \left[u(z), v(z), \phi(z)\right]^T = f_3(\mathbf{r}_A, \mathbf{r}_B, \boldsymbol{\varepsilon}_A, \boldsymbol{\varepsilon}_B) \tag{11.12}$$

where $\boldsymbol{\varepsilon}_A, \boldsymbol{\varepsilon}_B$ are vectors consisting of strain measured at three different locations along the perimeter of Sections A and B, respectively (Figure 11.4). The torsional component accounts for all the coupling between the translational movements in the x and y directions, and thus translational acceleration responses collected from an intermediate location on the beam surface can be expressed using the following functions:

$$\ddot{u}_{C1} = f_4{}'\left(\ddot{u}_A, \ddot{u}_B, \ddot{\phi}_A, \ddot{\phi}_B, \ddot{\boldsymbol{\varepsilon}}_A, \ddot{\boldsymbol{\varepsilon}}_B\right) = f_4\left(\ddot{u}_{A1}, \ddot{u}_{B1}, \ddot{u}_{A2}, \ddot{u}_{B2}, \ddot{\boldsymbol{\varepsilon}}_A, \ddot{\boldsymbol{\varepsilon}}_B\right),$$

$$\ddot{v}_{C1} = f_5{}'\left(\ddot{v}_A, \ddot{v}_B, \ddot{\phi}_A, \ddot{\phi}_B, \ddot{\boldsymbol{\varepsilon}}_A, \ddot{\boldsymbol{\varepsilon}}_B\right) = f_5\left(\ddot{v}_{A1}, \ddot{v}_{B1}, \ddot{v}_{A3}, \ddot{v}_{B3}, \ddot{\boldsymbol{\varepsilon}}_A, \ddot{\boldsymbol{\varepsilon}}_B\right),$$

$$\boldsymbol{\varepsilon}_A = \left[\varepsilon_{A1}, \varepsilon_{A2}, \varepsilon_{A3}\right]^T, \; \boldsymbol{\varepsilon}_B = \left[\varepsilon_{B1}, \varepsilon_{B2}, \varepsilon_{B3}\right]^T. \tag{11.13}$$

In the above two expressions, uppercase letters in the subscripts are the section labels and the numbers following these letters denote a point along the section (Figure 11.4). Assuming f_4 and f_5 are linear in coefficients, the corresponding frequency domain representations of the expressions are:

232

$$\hat{\ddot{u}}_{C1} = \hat{f}_4\left(\ddot{u}_{A1}, \ddot{u}_{B1}, \ddot{u}_{A2}, \ddot{u}_{B2}, \ddot{\boldsymbol{\varepsilon}}_A, \ddot{\boldsymbol{\varepsilon}}_B\right) \overset{f \; linear}{\Rightarrow} f_4\left(\hat{\ddot{u}}_{A1}(i\omega), \hat{\ddot{u}}_{B1}(i\omega), \hat{\ddot{u}}_{A2}(i\omega), \hat{\ddot{u}}_{B2}(i\omega), \hat{\ddot{\boldsymbol{\varepsilon}}}_A(i\omega), \hat{\ddot{\boldsymbol{\varepsilon}}}_B(i\omega)\right)$$

$$= f_4\left(\hat{\ddot{u}}_{A1}(i\omega), \hat{\ddot{u}}_{B1}(i\omega), \hat{\ddot{u}}_{A2}(i\omega), \hat{\ddot{u}}_{B2}(i\omega), -\omega^2 \boldsymbol{\varepsilon}_A, -\omega^2 \boldsymbol{\varepsilon}_B\right) + Cst_4,$$

$$\hat{\ddot{v}}_{C1} = \hat{f}_5\left(\ddot{v}_{A2}, \ddot{v}_{B2}, \ddot{v}_{A3}, \ddot{v}_{B3}, \ddot{\boldsymbol{\varepsilon}}_A, \ddot{\boldsymbol{\varepsilon}}_B\right) \overset{f \; linear}{\Rightarrow} f_5\left(\hat{\ddot{v}}_{A2}(i\omega), \hat{\ddot{v}}_{B2}(i\omega), \hat{\ddot{v}}_{A3}(i\omega), \hat{\ddot{v}}_{B3}(i\omega), \hat{\ddot{\boldsymbol{\varepsilon}}}_A(i\omega), \hat{\ddot{\boldsymbol{\varepsilon}}}_B(i\omega)\right)$$

$$= f_5\left(\hat{\ddot{v}}_{A2}(i\omega), \hat{\ddot{v}}_{B2}(i\omega), \hat{\ddot{v}}_{A3}(i\omega), \hat{\ddot{v}}_{B3}(i\omega), -\omega^2 \boldsymbol{\varepsilon}_A, -\omega^2 \boldsymbol{\varepsilon}_B\right) + Cst_5.$$

$$(11.14)$$

There is a physical interpretation associated with each coefficient of these variables as well, only in this case their relation to structural stiffness quantities is more complicated and it is especially difficult to directly present the physical equivalents of the coefficients of strain terms. Figure 11.5(a) contains schematic illustration on the physical equivalent of coefficients associated with acceleration regressors when the complete strain measurements are available. For clarity purposes only a surface is drawn instead of a 3D beam.

11.3.2.2 Lumped mass beam model in 3D space

The process of developing a lumped mass beam model in 3D space is similar to that in 2D space. The assumption made here is that total inertia effect of the substructure could be accounted for by using the accelerations measured at an intermediate point on the beam. The functions are thus derived as:

$$\ddot{u}_{C1} = f_6\,'\left(u_A, u_B, u_{C1}, \phi_A, \phi_B, \boldsymbol{\varepsilon}_A, \boldsymbol{\varepsilon}_B\right) = f_6\left(u_{A1}, u_{B1}, u_{A2}, u_{B2}, u_{C1}, \boldsymbol{\varepsilon}_A, \boldsymbol{\varepsilon}_B\right),$$

$$v_{C1} = f_7\,'\left(v_A, v_B, v_{C1}, \phi_A, \phi_B, \boldsymbol{\varepsilon}_A, \boldsymbol{\varepsilon}_B\right) = f_7\left(v_{A1}, v_{B1}, v_{A3}, v_{B3}, v_{C1}, \boldsymbol{\varepsilon}_A, \boldsymbol{\varepsilon}_B\right). \qquad (11.15)$$

And their frequency domain counterparts are:

233

$$\hat{\ddot{u}}_{C1}(i\omega) = \hat{f}_6\left(u_{A1}, u_{B1}, u_{A2}, u_{B2}, u_{C1}, \boldsymbol{\varepsilon}_A, \boldsymbol{\varepsilon}_B\right) \stackrel{f\ linear}{\Rightarrow} f_6\left(\hat{u}_{A1}, \hat{u}_{B1}, \hat{u}_{A2}, \hat{u}_{B2}, \hat{u}_{C1}, \hat{\boldsymbol{\varepsilon}}_A, \hat{\boldsymbol{\varepsilon}}_B\right)$$

$$= f_6\left(\hat{\ddot{u}}_{A1}(i\omega)/-\omega^2, \hat{\ddot{u}}_{B1}(i\omega)/-\omega^2, \hat{\ddot{u}}_{A2}(i\omega)/-\omega^2, \hat{\ddot{u}}_{B2}(i\omega)/-\omega^2, \hat{\ddot{u}}_{C1}(i\omega)/-\omega^2, \hat{\boldsymbol{\varepsilon}}_A, \hat{\boldsymbol{\varepsilon}}_B\right) + Cst_6,$$

$$\hat{\ddot{v}}_{C1}(i\omega) = \hat{f}_7\left(v_{A1}, v_{B1}, v_{A3}, v_{B3}, v_{C1}, \boldsymbol{\varepsilon}_A, \boldsymbol{\varepsilon}_B\right) \stackrel{f\ linear}{\Rightarrow} f_7\left(\hat{v}_{A1}, \hat{v}_{B1}, \hat{v}_{A3}, \hat{v}_{B3}, \hat{v}_{C1}, \hat{\boldsymbol{\varepsilon}}_A, \hat{\boldsymbol{\varepsilon}}_B\right)$$

$$= f_7\left(\hat{\ddot{v}}_{A1}(i\omega)/-\omega^2, \hat{\ddot{u}}_{B1}(i\omega)/-\omega^2, \hat{\ddot{v}}_{A3}(i\omega)/-\omega^2, \hat{\ddot{v}}_{B3}(i\omega)/-\omega^2, \hat{\ddot{v}}_{C1}(i\omega)/-\omega^2, \hat{\boldsymbol{\varepsilon}}_A, \hat{\boldsymbol{\varepsilon}}_B\right) + Cst_7.$$

(11.16)

Figs. 4(b) and (c) contain schematic plots showing the physical meaning of coefficients related to acceleration variables. The lumped mass model is a simplified approximation of the real behavior. But to make this approximation more accurate, the model needs to incorporate more variables and may then suffer from overparameterization. This problem will become evident when the whole structure is not very well excited. (i.e. the response only contains a few dynamic modes)

When the substructure is subjected to the ambient/white noise load, the models described in this section will be applicable by using the correlation of the signals with the regressand signal as a free-decay response. The corresponding frequency domain relation will then be defined for the auto/cross power spectral densities, instead of the Fourier transform.

11.4 DAMAGE FEATURE EXTRACTION FROM SUBSTRUCTURAL REGRESSION MODEL FORMULATIONS

The general MISO (multi-input-single-output) linear regression problem can be formulated as:

$$\mathbf{Y} = \mathbf{X}\boldsymbol{\beta} + \boldsymbol{\epsilon}$$

(11.17)

In Eq.(11.17), $\mathbf{Y}$ is the $n \times 1$ regressand vector, $\mathbf{X}$ is the $n \times m$ regressor matrix, β is the $m \times 1$ regression coefficients vector, and ϵ is the $n \times 1$ residual series. In the size

234

definitions *n* stands for the number of observations, and *m* refers to the number of input series. Thus given the input and output observations, the coefficients and the residuals can be estimated through applying standard curve fitting algorithms (often using least squares or maximum likelihood).

The substructural models presented in the previous section can be used to form regression models as outlined in Table 11.1. Note that for all of the regression schemes, only acceleration and strain signals are employed as they are the most commonly measured vibrational responses. In the table, subscript $j=1,...,N$ is a range variable which represents the collection of sample points in time/frequency domain depending on the situation. $\mathbf{a}_b = [a_{b1}, a_{b2}, ..., a_{bd}]$ and $\mathbf{\varepsilon}_b = [\varepsilon_{b1}, \varepsilon_{b2}, ..., \varepsilon_{bd'}]$ are vectors of boundary acceleration and strain measured at a series of discrete locations, with d and d' being the total number of acceleration and strain sensing points, respectively. $\Delta^2\{\cdot\}$ represents the central difference of a signal, $\iint\{\cdot\}$ denotes the reconstructed displacement from the acceleration signal inside the brackets by applying the CFIR filter described in (Hong, Kim, and Lee, 2010), and the macro accent $\overline{\{\cdot\}}$ means the detrended signal. The purpose for detrending is to eliminate from the regression models the regression constant, which is associated with the system static deformations in the time domain signal, and the vibration initial conditions in the one-sided frequency spectrum. In the applications herein, two-sided spectrum is adopted instead of one-sided spectrum because it is easier to estimate the former from data. The estimated regression coefficients (
$\hat{\mathbf{\beta}} = \left(\mathbf{XX}^T\right)^{-1}\mathbf{X}^T\mathbf{Y}$ from the least squares method), the ratio of the variance of regression residuals from baseline model to that of the signal ($RF1 = var(\epsilon_{BL})/var(\mathbf{Y})$,

235

$\epsilon_{BL} = \mathbf{Y} - \mathbf{X}\hat{\boldsymbol{\beta}}_{BL}$), and the ratio of the residual variance from baseline model to that from current state model ($RF2 = var(\epsilon_{BL}) / var(\epsilon_{CS})$, $\epsilon_{BL} = \mathbf{Y} - \mathbf{X}\hat{\boldsymbol{\beta}}_{BL}$, $\epsilon_{CS} = \mathbf{Y} - \mathbf{X}\hat{\boldsymbol{\beta}}_{CS}$) will be used as damage features.

11.5 STATISTICAL INFORMATION SYNTHESIS FOR RELIABLE DAMAGE PROGNOSIS

In the previous section, four substructural models and three damage indices are presented. Two change point analysis (CPA) methods, one based on maximum cumulative sum and one based on minimum deviance (Brodsky and Darkhovsky, 1993; Nigro et al., 2014), will be used to identify the point at which a statistically significant change occur in damage feature sequences extracted from chronologically arranged datasets representing structural baseline state and unknown state. Thereby, $4\times3\times2=24$ combinations for damage detection and localization can be formed by performing all possible arrangements for these three components. In applications, it is found that the algorithms rarely yield unanimous results, which is caused by different levels of sensitivity to measurement and modeling inaccuracies and possible over-parameterization. In light of these limitations, a triple-layer voting scheme will be used to pool the damage identification/localization results from all algorithms for an accurate decision on the current structural state.

Majority voting (Jain et al., 2000) is used for damage existence recognition. The median of all captured change points (implying the time when damage occurred) is selected as the nominal change point in accordance with the median voter theorem, which states that a majority voting system will select the outcome most supported by the median voter and has been widely applied in public decision making research (Congleton, 2004).

236

Voting strategy for damage location is a more complex problem and requires more preliminary preparation. Possible damage locations are found as positions of those substructures with most significant changes in damage features produced via different algorithms. To quantify the significance of variations from CPA, Two indicators are introduced as in Figure 11.6; the normalized damage indication variable (NDIV) and the normalized mean shift (NMS).

Note that because the exact change point location is not known *a-priori*, nominal change point from the second stage of voting is used instead. NDIV indicators from algorithms with different CPA methods but the same other components will be summed up since NMS is not affected by CPA methods and there is no reason to give one indicator more weight than the other in the voting process. Again in the spirit of equal weight voting, NDIV and NMS values from the same substructural models and either of the residual-based features are added up, so that coefficients-based and residual-based features will exert the same amount of influence in the final decision. These measures are taken because voting works best for independent observations but these pooled terms tend to be highly correlated.

The two significance metrics together with the two categories of feature extraction methods and four substructural models, give 16 ways to predict possible damage location(s) which will serve as candidates for the third round of voting. Tie-breaking procedures can be devised for multiple damage locations suggested by coefficients from different substructures by examining the significance of change for other coefficients in their respective substructures. For residual-based features, the weight will be divided evenly among locations that tie for the most significant change (i.e., ½ weight if there are

237

two candidates and 1/3 if there are three, etc.). There is also a subtle difference in the handling of locations indicated via coefficients between the 2D and 3D substructural approach: for the former the voting weight is evenly split between locations of regressand node and regressor node(s) (i.e. ¼ weight for each regressor node if there are two, and ½ if there is only one regressor), while for the latter only the regressand node location is considered because of the more complex boundary conditions and dynamics.

To better illustrate the procedure, Figure 11.7 includes a flow chart on the process of damage detection and characterization using voting. The three stages of voting are clearly marked with a blue background.

11.6 NUMERICAL VALIDATION OF THE DAMAGE DETECTION ALGORITHMS

In this section the proposed damage detection methodology will be applied to a planar frame structure and a space truss model created in commercial finite element modeling software packages for evaluation of its effectiveness. The first simulated structure shall be used to examine substructural models based on in-plane beam elements, and the second one will be employed to evaluate the substructural models based on space beam elements.

11.6.1 Case 1: two-bay planar frame simulated in SAP 2000

A small-scale two-span steel bridge girder simulated in SAP2000 is used here for verification of the proposed damage detection methodology. The girder was modeled as a two-dimensional frame with uneven spans as shown in Figure 11.8. The uneven spans allow for more variety in the results and damage scenarios. The frame model is constructed to resemble a real girder built in the testing lab, which will also be used to

evaluate the performance of the algorithms in the following experimental validation section. The reason to choose the simulated model here is to obtain data at various sensing locations, as not so many strain gages are available on the real specimen. The model has 23 total nodes, which coincide with the accelerometer/strain gage locations.

For vibration data collection, a white noise excitation was applied in the horizontal direction to produce responses at each node. Measurement noise was accounted for by adding 5% random noise to the response. Four damage scenarios are simulated in succession by switching out a 20.32 cm portion at distinct sensor location 6, 15, 17 and 20, respectively. Except that the switched out portion is replaced with another tube with only 50% of the original section stiffness, the rest of the structure maintains the same stiffness properties as the undamaged. For testing of each structural state (undamaged/damaged), acceleration and strain signals are simulated at 500 Hz sampling frequency.

Damage identification--change point histograms

The algorithms have correctly reported existence of damage for all four damage scenarios. For each damage scenario, the algorithms outlined in Section 11.3-11.5 are applied to all the beam substructures that can be formed based the sensing locations. If one end of the beam element is connected to a support, then only strain and acceleration measurements from the other end is utilized to construct the regressor matrix. When applying frequency domain techniques, only samples larger than the median response are used for noise-robust performance. For each type of damage index, the values extracted from 10 sets of signals collected from damaged state are compared with those from 10 sets of baseline signals. Thus the ideal case is that all damage indices that reports damage

239

though CPA shows a change point at 10. However, in the results acquired from applying the damage localization algorithm to the data, the histogram of change points(Figure 11.9) have a wide spread, and the correct change point location needs be recognized through taking the median. The errors are caused by both by model error and noise from sensing measurements. A way to counter the interference of large noise variance is to collect more vibration signals so as to have more estimated damage feature samples for the CPA.

Damage localization – identification of the location where the most significant change occurs

Table 11.2 summarizes the damage localization results for all 4 different damage states for the ease of comparison and contrast. Basically, the sensor (or sensor pair) location that corresponds to the largest change in damage location indicator values are identified as the damage location. None of the methods proposed has a 100% correct performance as the simulated structure is different from the models presented. It can be seen that overall the residual-based methods perform better than the coefficient based damage methods in damage localization, and that the dynamic models outperform the static models for longer/suppler beam substructural models because the inertia force is accounted for, but underperform for shorter/stiffer beam models because their dynamic behavior is not significant. Therefore it is concluded that there is a trade-off between model accuracy and over-parameterization when designing damage detection algorithms. Also, it is noticed that the results would also improve for damaged locations closer to the excitation source (such as location 6) for the larger signal-to-noise ratios.

In accordance to the procedure outlined in Section 11.5, a direct voting scheme among the results from different type of methods is used to decide on the most probable location of damage. When there are two regressor nodes in the results from coefficient-based methods, assign 0.5 and 0.25 weight to each regressand and each regressor node; otherwise, assign both the regressor and regressand node 0.5 weight. The votes are then pooled together to select three locations with the top scores. Number 3 is used as theoretically this is the maximum number of substructural models that will be affected by a potential damage. The results are shown in Figure 11.10.

Damage characterization through examining the coefficients change

Figure 11.11 shows the plots of coefficients from substructural modeling at the most probable damage locations (for the 4 scenarios) from the voting scheme. One of the four available models is chosen depending on which one produces indices with maximum NMS. Grey background in a subplot indicates that a change has been identified using CPA algorithms, and each bracketed arrow at the end of a subplot title represents the mean shift direction after damage. The blue and red dashed line show the mean values for the first and last 10 datasets, respectively. As in Table 11.2, coefficients are represented using hyphenated regressand and regressor locactions. The regressor from acceleration is denoted by the sensing location, while the regressor from strain data is denoted by the sensing location appended with an 's'. Figure 11.3(b) and Figure 11.4(b) in Section 11.3 can be referred to for the physical implications of these coefficients. For the first damage scenario, the absolute values of the coefficients that experienced a statistically significant change (i.e. 6-6 and 6-3) increases, suggesting that the regression model is affected more by the mass reduction from the damage than the resulted stiffness reduction. For the

241

second scenario the damage-reporting coefficient values dropped after damage, implying that here stiffness reduction outweighs the dynamic mass reduction in this case. Note that the coefficients using measurements at sensing node 15 (the true damage location) underwent more significant change. For the third scenario, the regression coefficient between acceleration measurements at node 16 and 15 increased significantly, hinting a modeling error as in the static model this coefficient is determined by substructural geometry. This could be because this relatively long beam substructure has significant dynamic response. Still, the coefficient between acceleration at node 16 and strain measurements at node 17 reduces as a result of damage, indicating stiffness loss. For the fourth damage scenario, the regression model assumes that one side of the beam is fixed (cantilever type). As such, a drop in the value of coefficient 21-20 points to a sectional stiffness reduction.

In the following validation examples the results will all be presented in the same order of damage identification-localization-characterization, though the subheadings will be omitted to preserve the flow of the text.

11.6.2 Case 2: steel truss structure simulated in ABAQUS

To evaluate the effectiveness of proposed space beam substructural models, a truss structure is simulated in ABAQUS using its space beam elements (Figure 11.12(a)). Damage is introduced in one of its vertical members by assigning a smaller section to a portion of the component between sections 5 and 6 (Figure 11.12(b)). The replacement section has a 16.7% narrower flange width and 25% thinner web thickness. Concentrated random translational force in both directions and torsional moment excitation are applied at 1/6 height, mid-height and 5/6 height of the member, respectively. For each structural

scenario, five datasets are simulated at a sampling rate of 1000 Hz from seven sections as illustrated. Each dataset lasts 19 seconds. The sensing plan for each section is given in Figure 11.12(c). Since ABAQUS does not directly provide strain/translation information for specific points on a beam element section, sectional moments (i.e. bending moments around the two axes and torsion moment) are employed to calculate the strain, and section rotational and centroidal translational accelerations are used to compute the acceleration measurements at the sensing points. 5% white noise is added to the signals to simulate measurement noise.

The change point histogram is shown in Figure 11.13. The median of all the detected change points matches the true change point value. Table 11.3 contains the damage locations identified from the algorithms; notice here that tie-breaking did not completely eliminate multiple choices for the NDIV- coefficient method. The numbering of sensing locations in the table is a combination of section labels and sensing point labels on each section (Figure 11.12(b) & (c)). The algorithms here very accurately predict the damage location. Also included is a ranking of the most possible damage locations from the voting scheme. It should be noted that only those locations with more than one vote are listed. All of the ranked damage locations are around the real damaged portion.

Figure 11.14 displays plots of coefficients from regression models with maximum NMS at two ranked damage locations 54 and 61. Only those coefficients associated with acceleration regressors are included. In the title for each plot, the number before the hyphen is the regressand while that after the hyphen is the regressor. The bracketed arrow points the mean shift direction after change point. The shaded backgrounds indicate a statistically significant change for the coefficient sequences, and the blue/red lines

243

represent the average values of coefficients before/after the change point. For substructural modeling results at node 54, coefficient 54-54 has a decrease in its absolute value as a result of structural change, suggesting that the effect of mass loss on this model outweighs the effect from stiffness loss. The absolute values of coefficients 54-43 and 54-44 increase after damage, implying strengthened correlation between responses at Section Location 4 and Location 5. The values of coefficient 54-64 drop below zero, which is because the substructural model is not an exact representation of the simulation and also because the model, which uses 10 regressors, can be overparameterized if the structure is not well excited over a wide range of modes. For substructural model with sensing point 61 as the regressand node, the regression coefficient of responses from node 61 on those from 72 (61-72) is always zero because responses at 71 and 72 are negatively correlated as Section Location 7 only has torsional responses. Among the two sets of identified coefficients, coefficient 61-71 shows an increasing trend in its absolute value while 61-52 shows a decrease. This indicates that the responses at node 61 become more dependent on responses from 71 and less on those from 52 after the structural change. Thus overall behavior of the coefficient sets that have been identified by CPA evinces a loss of correlation between responses at Section Location 6 and Section Location 7 in both translational directions, implying that stiffness reduction for the portion between Section Location 6 and Location 7 around both the strong and weak axis.

11.7 EXPERIMENTAL VALIDATION OF THE DAMAGE DETECTION ALGORITHMS

To further test the accuracy of the algorithms, they are applied to detect and locate damage in a real two-bay frame specimen in the laboratory and structural change in a steel truss bridge using vibration measurements collected from these structures. The two-

bay frame is used to authenticate the algorithms based on in-plane substructural beam element. The truss bridge members have vibration in the three-dimensional space, and thus serve as a testbed for the algorithms based on substructural beam model in 3D space.

11.7.1 Case 1: the planar steel frame specimen tested in the laboratory

Three different damage scenarios were set up on the two-bay frame laboratory specimen constructed from steel tubes used in Chapter 5 (Figure 5.4). A description of the structure and the sensing scheme can be found in Section 9.7. The sensing and damage schemes are illustrated in Figure 9.5.

Since here only a limited number of sensing locations has strain gages, results on damage identification/localization using the proposed algorithms are only obtained for the beam substructures with strain gages at their ends. It can be seen from Figure 11.15 that the identified change points for three damage scenarios all have a relatively dispersed distribution. This is especially evident for the 3rd damage scenario case, where there are fewer available datasets. Still, the median change point values coincide with the real change points.

Damage locations predicted by algorithms based on different models and/or different damage indices are listed in Table 11.4. It is noticed that while for the 3rd damage state the damage location is very clearly indicated by almost all algorithms, for the other two damage states the algorithms are suggesting quite a few distinct locations (with the correct damage location among them), thus making direct determination of damage location difficult. This is because the replacement of the switch-out portions to simulate damage tends to affect the whole frame (the frame needs to be effectively disassembled and assembled again).To select the most probable damage locations, the voting scheme is

245

applied to pick the top three sites with the highest votes (Figure 11.16). Three sites are chosen because theoretically that is the largest number of locations that can be affected by a single damage. The results agree well with the actual damage locations, with the latter identified as either the first or second choice from voting in each damage scenario. Therefore, it is concluded that regression models based on beam elements are effective in damage localization applications for the steel frame structure.

Model coefficients that reported the most significant change at the suggested damage locations from the voting scheme are plotted in Figure 11.17. The usage of grey background, dashed line, and parenthetical arrows is the same as in Figure 11.14, and the suffix 's' represents coefficients associated with strain. For the first damage case, the regression coefficients between acceleration channels demonstrate significant change, which is resulted from ignoring system mass and nonlinearity brought by bolt connections. On the other hand, absolute values of the coefficients of both strain regressors shift towards zero after damage, signaling a stiffness reduction that can be attributed to a connection loosening. Analysis of coefficients from beam element modeling about location 6 also reveals a similar trend. Note here the coefficients pertaining to strain have small magnitudes because the data is recorded in micro-strain. For the second damage scenario, the coefficient 15-16s showed a significant decrease, suggesting that a stiffness reduction occurred between location 15 and 16. For the third damage scenario, again the coefficients from acceleration regressors are reporting changes due to model inexactness. The coefficient 17-18s has a significant drop in its values for the last 6 datasets, indicating section stiffness loss.

246

11.7.2 Case 2: members of a steel truss bridge under ambient conditions

The damage detection algorithms based on substructural modeling for beam in 3D space are applied to identify structural change for a vertical truss member in a steel truss bridge over the Allegheny River in western Pennsylvania. The bridge structure is a continuous deck truss with spans of 420 feet, 540 feet, and 420 feet, as shown in Figure 6.7. The truss is 40 feet in depth and is haunched to 84 feet at the two intermediate piers.

During an inspection in June 2010, it was found that vertical members at Panel Points (PP) 20' and 22 (Figure 6.7) on the north side of truss had excessive wind-induced vibration. The two members were then retrofitted by bolting a steel wide-flange member to the web of each of them over their full height.

In a subsequent field test, ambient vibration measurements are collected for vertical PPs 22 and 22'. These two members were identical before the retrofit of PP22. Each member is instrumented with four accelerometers at the mid-span cross section and another four at ¾ height cross section (Figure 11.18(a) & (b)). Besides, at each end of each member two accelerometers and one strain gage is mounted (Figure 11.18(c) & (d)). Five datasets are collected at a frequency of 1000 Hz for 100 seconds respectively from the retrofitted member PP22 and the unretrofitted PP22'. The damage indices will be applied to these measurements in order to identify the difference between these two members.

A preliminary examination of collected data reveals that accelerometers mounted at the top of vertical PP22 are dysfunctional, and thus these two channels cannot be incorporated in the substructural models. Therefore, it is assumed that the translations occurring at the top of the PPs are of relatively small amplitude and can be omitted from

247

consideration without causing much error. This assumption is supported by comparing the Power Spectral Density (PSD) plots of acceleration measurements from the middle of PP22 and the top of PP 22'; acceleration from the latter location carries more high frequency contents and a lot less low frequency contents, and because dynamic displacements are primarily resulted from lower frequency vibrations, the level of displacement amplitude at the top of PP22' should be much lower than that in the middle of PP22. Since the bridge is symmetric on the whole, the displacements of the top of the two members will have similar amplitude. As such, it can be inferred that the dynamic displacements at the top of PP22' is insignificant compared to local vibrational displacements of the vertical member. Similar examination is performed for acceleration measurements collected at the bottom of the verticals and same conclusion is made.

In this experiment only two strain gages are instrumented at the mid-section and one at the top/bottom of the members. These are not theoretically sufficient for beam element modeling in 3D space, which requires three distinct channels of strain measurements at each end of the element. Assuming the gusset plate completely restrains rotation around the weak axis, additional independent boundary conditions are still needed for a solution to the substructural problem. But as no more data is available from the tests on this bridge, regression models will be constructed from the available data in this case. Table 11.5 presents a list of the regressand-regressor pairs used for substructural modeling based damage detection in this case. Two substructures are formed from measurements made at four levels of the vertical member and four input-output formulations are established for each substructure. There are several points meriting clarification regarding determination of regressor and regression channels shown in the table: 1) Because strain

248

measurements are not available at the lower interface of the upper substructure (the ¾ height cross section), strain measurements within the substructure (i.e. at the mid span of vertical member) is used. This substitution is plausible as construction of linear regression model for substructures implicitly assumes that responses at any point within the substructure is a linear combination of certain boundary responses, and thereby the boundary responses can be replaced by the same number of non-correlated responses within the substructure. A drawback of this approach is that physical interpretations of the regression coefficients become more obscure. 2) Since the strain at location SG2 cannot be induced by bending around the weak axis and torsion of an I-section, here the difference of measurements at SG1 and SG2 are used as a regressor for models associated with transverse vibration to avoid redundancy in parameterization. 3) For the lower substructure the translational measurements at bottom can either be included or excluded in the regression models for structural change identification. Here both options are explored and their results will be presented and contrasted in the rest of this section.

Histograms of the identified change points from damage detection algorithms are displayed in Figure 11.19. Regardless of whether the lower cord acceleration is included or not, the graph peaks at six, which is the correct change point as the first five datasets used are from retrofitted member and the rest are from the unretrofitted one. In order to obtain further details on this structural change, the physical locations that report the largest change in different damage indices, together with their voting results, are summarized in Table 11.6. Here all the locations are presented as there are only two overlapping substructures and one damage location can very well affect all nodes. The locations obtained from the models including and neglecting lower cord acceleration are

similar, though in the former case the changes in the lower substructure (represented by location 5-8) are more prominent, a result of more accurate modeling. For both types of modeling, regression based on longitudinal vibration tends to report more significant change than that based on transverse vibration, indicating that section stiffness properties about the weak axis are affected relatively more than that about the strong axis. Figure 11.20 shows the coefficients from regression models with maximum NMS at the top two ranking damage locations (namely, location 5 and 8). As in the ABAQUS example, only the coefficients corresponding to acceleration measurements are plotted. It can be seen that for modeling of the longitudinal vibration, the absolute values of coefficients 5-5 and 5-11 decreases, signifying substructural stiffness loss about the weak axis. For modeling of the transverse vibration, the negative correlation between acceleration from node A3 and A8 increases after the structural change, suggesting that the substructural torsion behavior is affected more than flexural behavior about the strong axis. The other two coefficients, 8-4 and 8-12 did not report a statistically significant variation, because the data insufficiency here has caused the modeling error to increase.

11.8 CONCLUSION

For damage detection purposes, two types of substructural beam elements are investigated both in plane and in three-dimensional space. One element ignores the substructural dynamic behavior; the other takes it into account via a concentrated mass at the intermediate sensing location. Based on each element definition regression models using strain and acceleration measurements can be constructed in either time or frequency domain, and regression coefficients and two functions of model residuals are adopted as damage indices. A heuristic voting scheme is devised to combine the damage existence

250

and location identification results from the 24 algorithms obtained by coupling the four substructural models, three damage indices and two change point analysis methods together. This substructural methodology is applied to detect and localize damage in a laboratory 2-bay planar frame structure for validation of the in-plane beam model, and also structural change in vertical members of a simulated space truss and a steel truss bridge for validation of the space beam model. On the whole, results from the applications here support the effectiveness of the proposed damage detection and localization scheme.

It is observed that different algorithms tend to yield different damage identification and localization results, and the performance of each algorithm varies by application. For example, the static model outperforms the dynamic model when the in-plane beam segment is shorter, while the reverse is true as the segment becomes more slender. This is because different models implemented in different settings have modeling errors to various degrees. Since beam elements in actual structures have continuous mass and those in FEM software can have more complex lumped mass pattern than those from substructural modeling, the beam elements proposed here are only approximations of the experimental and simulational beam components. Material and system nonlinearities in real structures could also contribute to the observed discrepancies. Other sources of modeling error include neglect of damping effects and, for space beam elements, the omission of torsional inertia in the model. These simplifications are done to avoid model overparameterization, and to limit the regressors, where possible, to substructural boundary measurements so that the regression coefficients would reflect the structural condition between the interior node and boundary. The information synthesis procedure

251

has helped to 'average' out the model errors from distinct algorithms and achieve an accurate decision in most of the applications.

On a cross-comparison note, the coefficient estimates in the applications here generally demonstrate larger variations than those in Chapter 10, where regression is carried out for consecutive three stories within a shear frame structure. This is probably because substructural beam elements are less well-excited than mass-spring subsystems, yet can have more parameters to estimate if the elements are in 3D space. Also noticed is that the residual-based methods are often more sensitive than their coefficients-based counterparts in the experimental implementations. This observation is in line with the fact that the change in residuals properties is related to changes in all regression coefficients. On the other hand, when the excitation conditions are varying, the residual-related features will have a larger chance to be affected. These observations evince the importance of signal-to-noise ratio in structural damage detection applications.

The substructural concept can be applied to form elements of different geometry; the key issue is the identification of boundary reactions, the external input and the environmental factors. Measurements that best represent these influences should be made with an adequate signal-to-noise ratio, and appropriate substructural models can then be constructed by expressing the substructural intermediate responses as functions of these measurements. Functions of the model parameters and residuals will then be used as substructural state indices. This method could prove useful for monitoring of certain important parts of a large scale structure, where sensors of different nature can be implemented to obtain high information density in that particular region. For other parts

252

of the structure with less sensing density, existing macro-scale system identification and

monitoring schemes can still be applied.

Table 11.1 The linear regression models derived from substructural beam models

Model type	Choice of regressors/regressand
1. Static beam model (Time domain)	$\mathbf{Y} = \mathbf{a}_C\left(t_j\right),\ \mathbf{X} = \left[\mathbf{a}_b\left(t_j\right), \Delta^2\left\{\overline{\boldsymbol{\varepsilon}}_b\left(t_j\right)\right\}\right],$
2. Static beam model (Frequency domain)	$\mathbf{Y} = Re\left\{\overline{\hat{\mathbf{a}}}_C\left(i\omega_j\right)/\omega_j\right\}, \mathbf{X} = Re\left\{\left[\overline{\hat{\mathbf{a}}}_b\left(i\omega_j\right)/\omega_j, -\omega_j\overline{\hat{\boldsymbol{\varepsilon}}}_b\left(i\omega_j\right)\right]\right\},$
3. Beam model with lumped mass (Time domain)	$\mathbf{Y} = \mathbf{a}_C\left(t_j\right), \mathbf{X} = \left[\iint\mathbf{a}_b\left(t_j\right), \overline{\boldsymbol{\varepsilon}}_b\left(t_j\right), \iint\mathbf{a}_C\left(t_j\right)\right],$
4. Beam model with lumped mass (Frequency domain)	$\mathbf{Y} = Re\left\{\omega_j\overline{\hat{\mathbf{a}}}_C\left(i\omega_j\right)\right\}, \mathbf{X} = Re\left\{\left[\dfrac{\overline{\hat{\mathbf{a}}}_b\left(i\omega_j\right)}{-\omega_j}, \omega_j\overline{\hat{\boldsymbol{\varepsilon}}}_b\left(i\omega_j\right), \dfrac{\overline{\hat{\mathbf{a}}}_C\left(i\omega_j\right)}{-\omega_j}\right]\right\}.$

Table 11.2   Damage locations as determined from multiple algorithms for the frame

simulation

	Model 1	Model 2	Model 3	Model 4	Model 1	Model 2	Model 3	Model 4
	Damage scenario 1 (at location 6)				Damage scenario 2 (at location 15)			
NDIV from regression coefficients*	6-7	6-7	3-6-7	3-6-7	3-2	7-8	12-15	17-16
NMS from regression coefficients*	3-6	6-7	3-6-7	3-6-7	3-2	7-8	12-15	5-5
NDIV from RF1and RF2	7	6	6	6/11	16	12	12	15
NMS from RF1and RF2	7	6	6	6	16	12	12/15	17
	Damage scenario 3 (at location 17)				Damage scenario 4 (at location 20)			
NDIV from regression coefficients*	16-17-18	16-17	6-7	12-15	21-20	21-20	14-13	10-11-12
NMS from regression coefficients*	16-17	16-17	16-17	15-16	21-20	21-20	12-11	11-10
NDIV from RF1and RF2	16/17	16/17	21	15/16	21	2	21	21
NMS from RF1and RF2	16	16	21	15	21	21/12	21	21

* when two numbers are hyphenated, the first number denotes the regressand node;

when three numbers are hyphenated, the middle number denotes the regressand node.

254

Table 11.3   Damage locations in the middle vertical of the simulated truss as suggested

by proposed algorithms

Sensing locations associated with largest change in a damage index	Model 1		Model 2		Model 3		Model 4	
NDIV from regression coefficients	63/64		31/54		54		53	
NMS from regression coefficients	63		64		54		61	
NDIV from RF1and RF2	23/24/61/62		22/31/32/41/ 42/51/52/61/63		31/32/34/41/42/51/ 52/53/54/61/62/63/64		32/41/42/51/ 61/62/63/64	
NMS from RF1and RF2	62		52		51		51	
Damage locations ranked by the voting scheme	#1	#2	#3	#4	#5	#6	#7	#8
Sensor number	54	*51**	63	64	*61*	*62*	*52*	53

* Italic font is used to highlight locations associated with longitudinal vibration

Table 11.4   Damage locations as determined from multiple algorithms for the frame

experiment

	Model 1	Model 2	Model 3	Model 4	Model 1	Model 2	Model 3	Model 4
	Damage scenario 1 (at location 6)				Damage scenario 2 (at location 15)			
NDIV from regression coefficients*	16-17-18	16-17-18	8-9	19-20-21	19-20-21	17-16	7-8-9	16-17-18
NMS from regression coefficients*	6-7	8-7	8-9	20-21	20-21	17-16	8-7	8-9
NDIV from RF1and RF2	8/20	8/17/20	6/8/17/20	6/17/20	15	17	15	6/15/17
NMS from RF1and RF2	8	8	6	6	20	17	15	15
	Damage scenario 3 (at location 17)				* when two numbers are hyphenated, the 1st number denotes the regressand node; when three numbers are hyphenated, the 2nd number denotes the regressand node.			
NDIV from regression coefficients*	17-18	17-18	16-17-18	17-18				
NMS from regression coefficients*	17-18	17-18	17-18	17-18				
NDIV from RF1and RF2	20	17	17	17				
NMS from RF1and RF2	20	17	17	17				

Table 11.5   Regression models formed for 3D beam substructures found in PP22/PP22'

Substructure location	Translation direction	Regressor signal*	Regressand signal*
Between the top gusset and ¾ height cross section	Longitudinal	A5, A6, (SG1-SG2), SG3	A1
			A 2
	Transverse	A7, A8, SG1, SG2, SG3	A 3
			A 4
Between mid-height cross section and the bottom gusset	Longitudinal	A1, A2, (SG1-SG2), SG4, A11**	A 5
			A 6
	Transverse	A3, A4, SG1, SG2, SG4, A12**	A 7
			A 8

*: For signal names, the letter 'A' preceding a number denotes acceleration, and the

letters 'SG' denotes strain measurements.

**: Optional

257

Table 11.6   Structural change characterization results for truss bridge member

PP22/PP22'

Sensing locations* associated with largest change in a damage index	Including translations at A11, A12				Excluding translations at A11, A12			
	Model 1	Model 2	Model 3	Model 4	Model 1	Model 2	Model 3	Model 4
NDIV from regression coefficients	1	8	8	5	1	8	8	5
NMS from regression coefficients	1	8	6	2	1	8	2	2
NDIV from RF1and RF2	1/4-8	5	2/3/6	5	1/4-8	5	2-6	5
NMS from RF1and RF2	6	5	2	5	6	5	2	5
Damage locations* ranked by the voting scheme	#1	#2	#3	#4	#5	#6	#7	#8
Including translations at A11, A12	*5***	8	*6*	*2*	*1*	3	4	7
Excluding translations at A11, A12	*5*	8	*2*	*1*	*6*	4	3	7

* The numbering of these locations coincides with the numbering of accelerometers

in Figure 11.18

** Italic font is used to highlight locations associated with longitudinal vibration
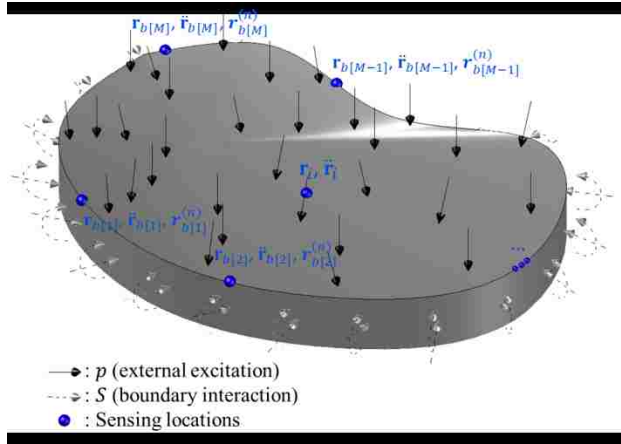
Figure 11.1   Illustration of the substructural concept. Annotations explain

the type of measurements made at the sensing locations (total

number: M+1).
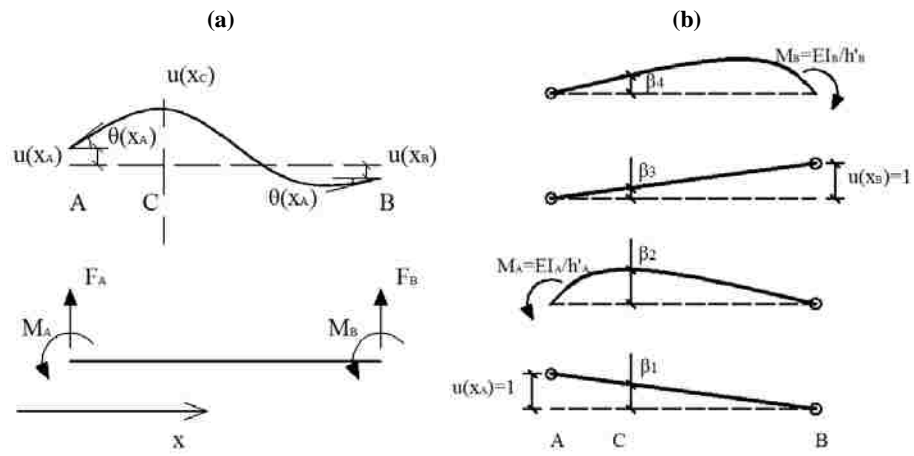
Figure 11.2   (a) the deflected shape and free body diagram of the static

beam element model, (b) coefficients of each variable when

the static model function is linear.
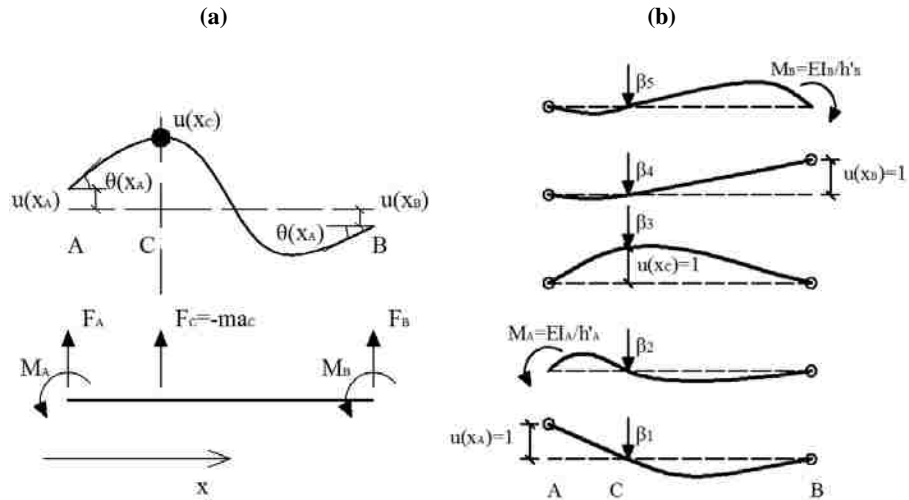
Figure 11.3   (a) the deflected shape and free body diagram of the lumped

mass beam model, (b) coefficients of each variable when the

lumped mass model function is linear (assuming unit mass at

C).
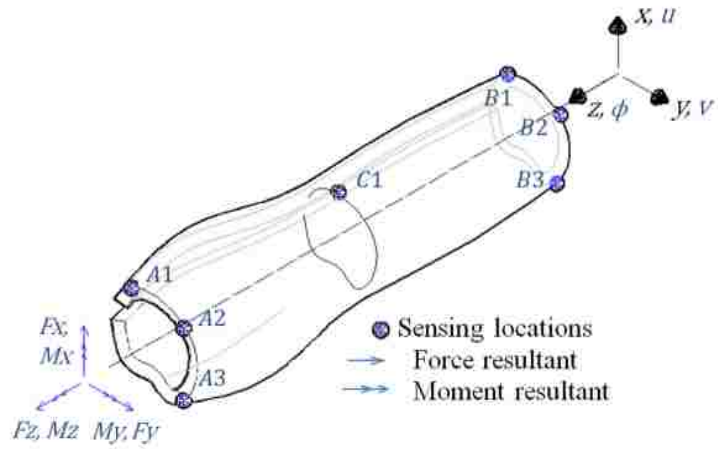
Figure 11.4   Space beam substructure with arbitrary section shape along

the length. The arrows at the front are internal force resultants,

while those at the rear show the coordinates and the associated

deformation variables.
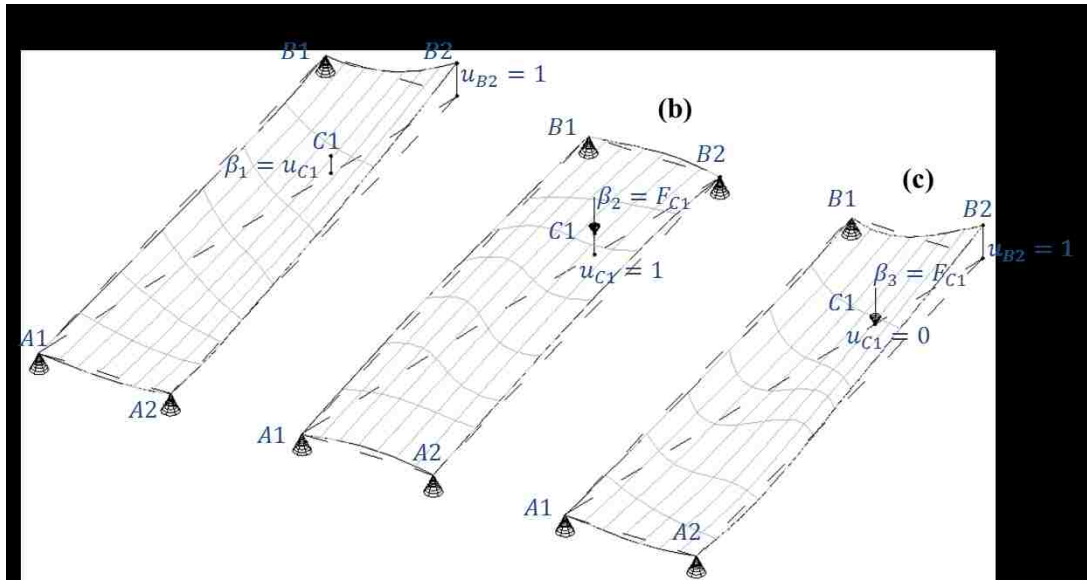
Figure 11.5   Physical interpretations of regression coefficient between (a)

$\ddot{u}_{C1}$ and $\ddot{u}_{B2}$ in the static model; (b) $\ddot{u}_{C1}$ and u_{C1} in the

dynamic model; (c) $\ddot{u}_{C1}$ and u_{B2} in the dynamic model

(Assuming unit mass at C1 for dynamic model)
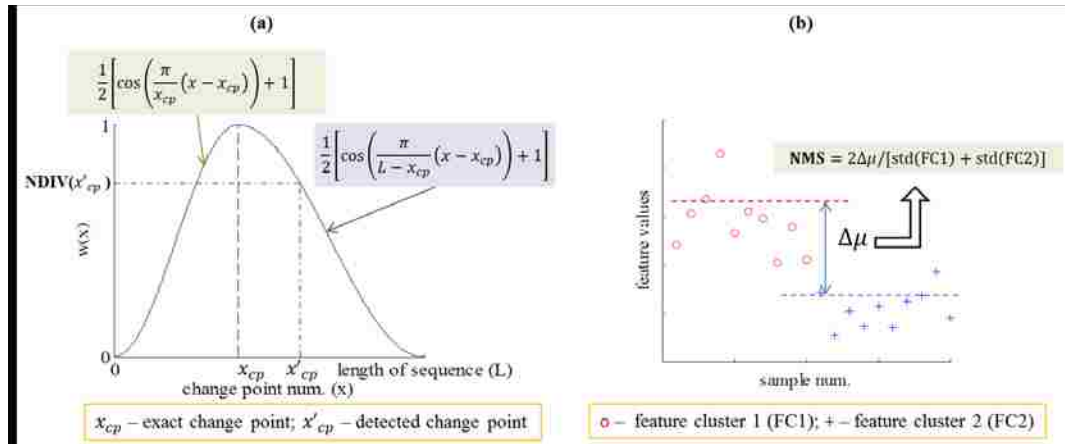
Figure 11.6   Illustration on calculation of the two significance of change indicators (a)NDIV and (b)NMS; in (b) std(·) stands for the standard deviation of the bracketed sequence.
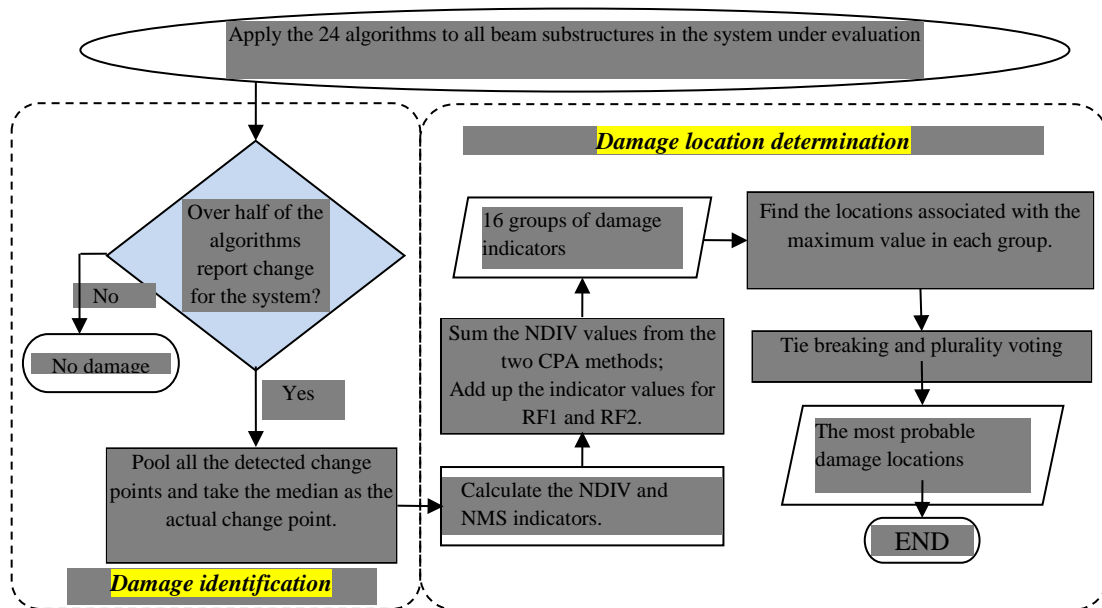
Figure 11.7   Information synthesis from different algorithms based on

voting concept.

www.manaraa.com
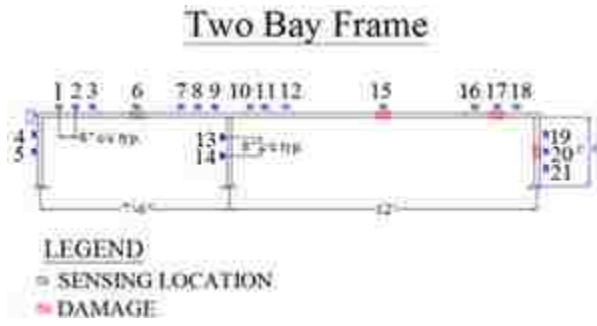
Figure 11.8   The sensing scheme for the two-bay frame model
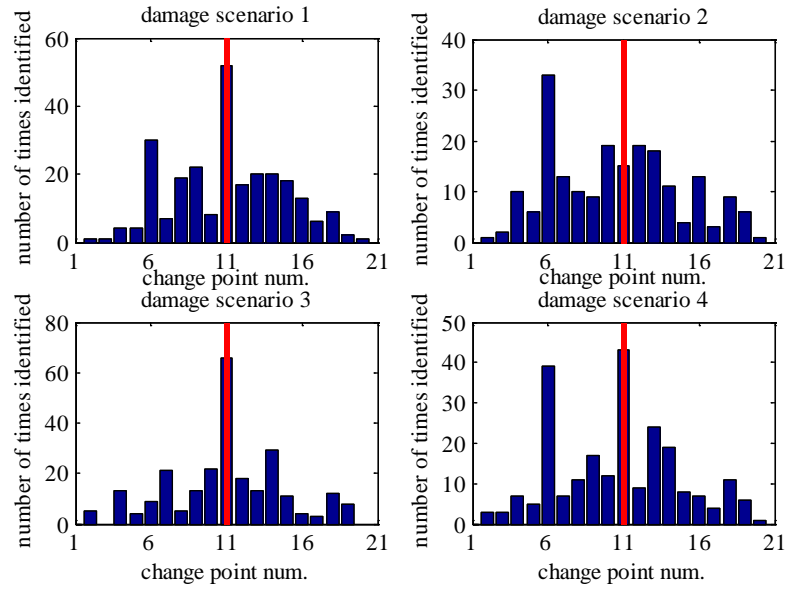
Figure 11.9   Change point histograms for the four damage scenarios of the

simulated truss; red bar shows the change point median
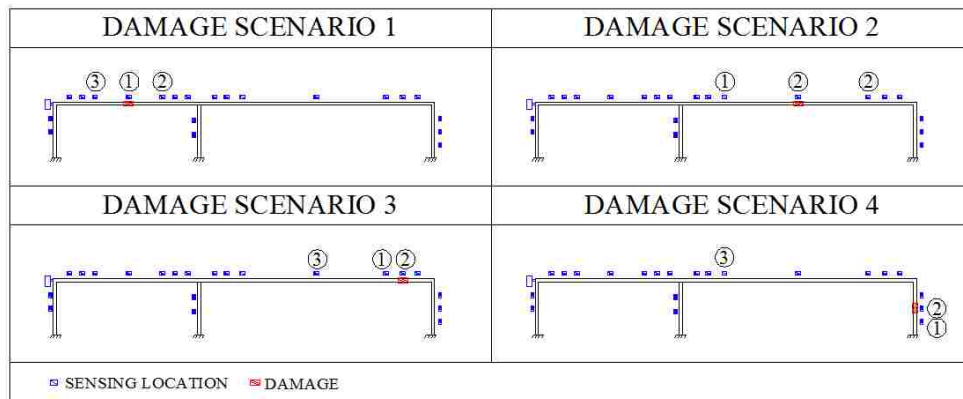
Figure 11.10   Contrast of simulated damage locations on the simulated

frame and suggested locations from the voting scheme

267
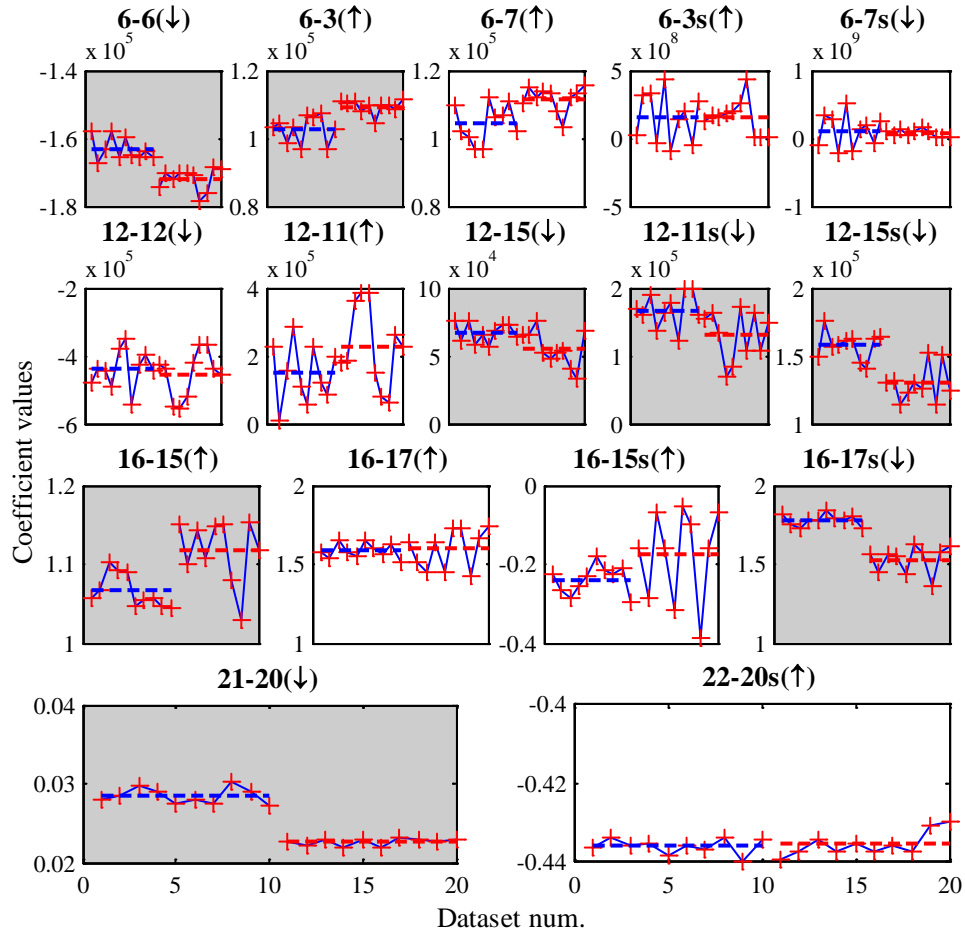
Figure 11.11   Plots of selected model coefficients extracted from the 20 datasets in the frame simulation. 1st row is from Model 4, Damage state 1; 2nd row is from Model 3, Damage state 2; 3rd row is from Model 1, Damage state 3, 4th row is from Model 1, Damage state 4. Any row without x tick marks has same x tick labels the row below (or the closest row with x ticks).

268
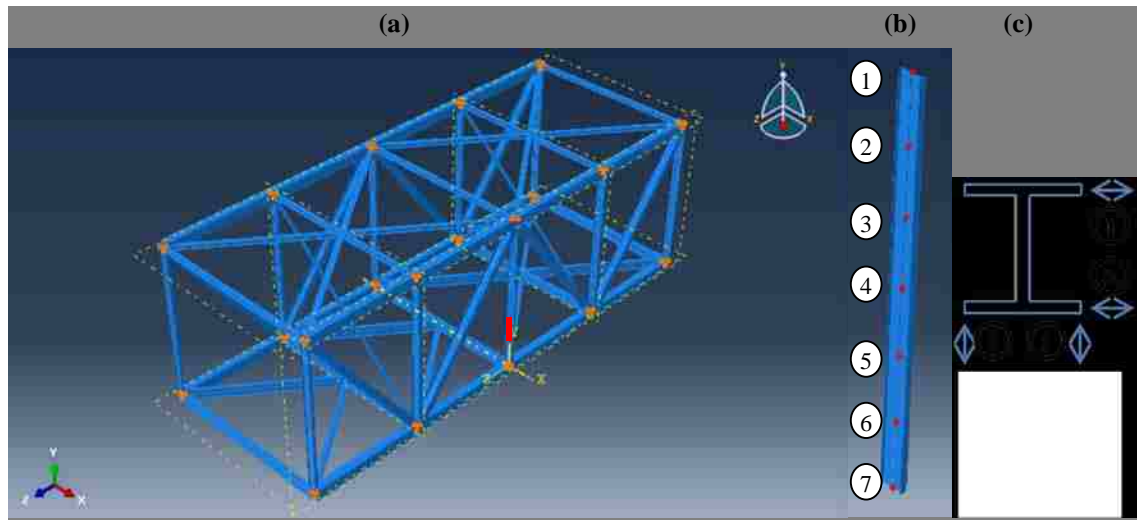
Figure 11.12   (a) Snapshot of the truss in ABAQUS; the damaged portion of

the middle vertical member is highlighted in red. (b) Sections

being monitored along the vertical; (c) acceleration sensor

labels per each section
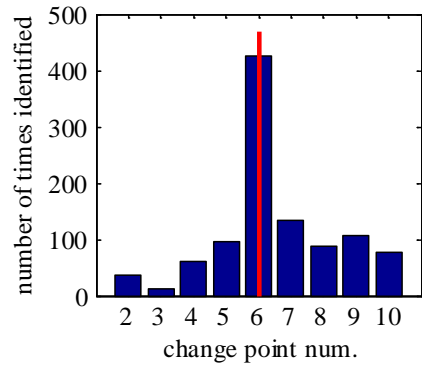
Figure 11.13   Change point histograms for the truss simulation example.
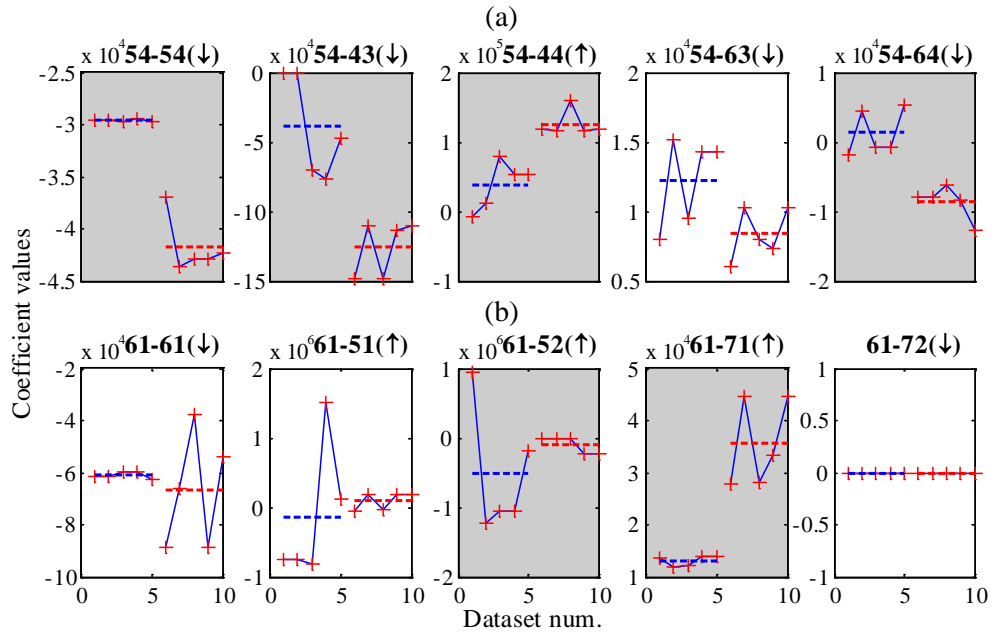
Figure 11.14   Acceleration-related coefficients of the regression models. (a)

is from Model 3 with regressand node 54 and (b) is from

Model 4 with regressand node 61.

271
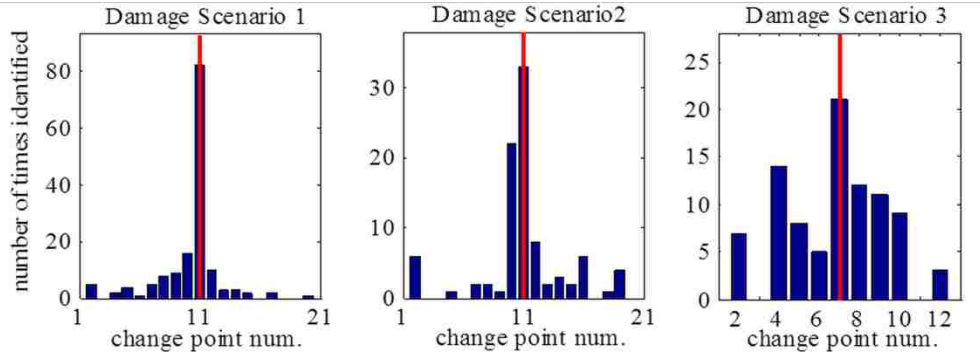
Figure 11.15   Histograms of change point locations for the three damage

scenarios created in the frame experiment; the median change

point for each case is indicated as the red thin bar.
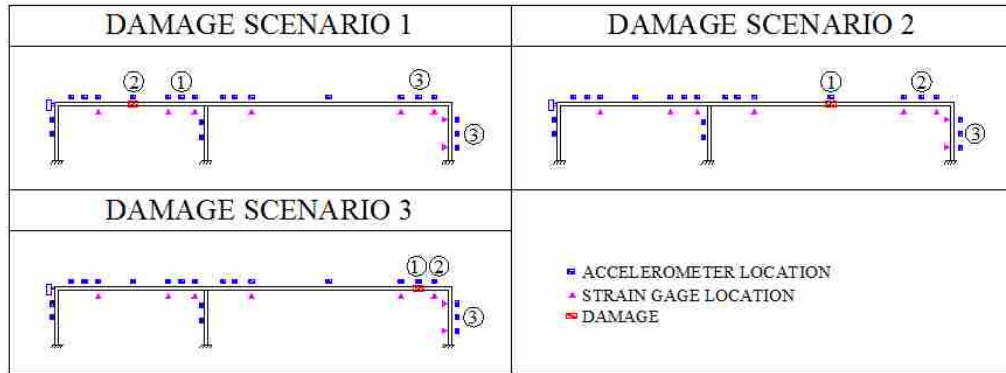
Figure 11.16   Contrast of real damage locations on the frame and suggested

locations from the voting scheme in the experiment

273
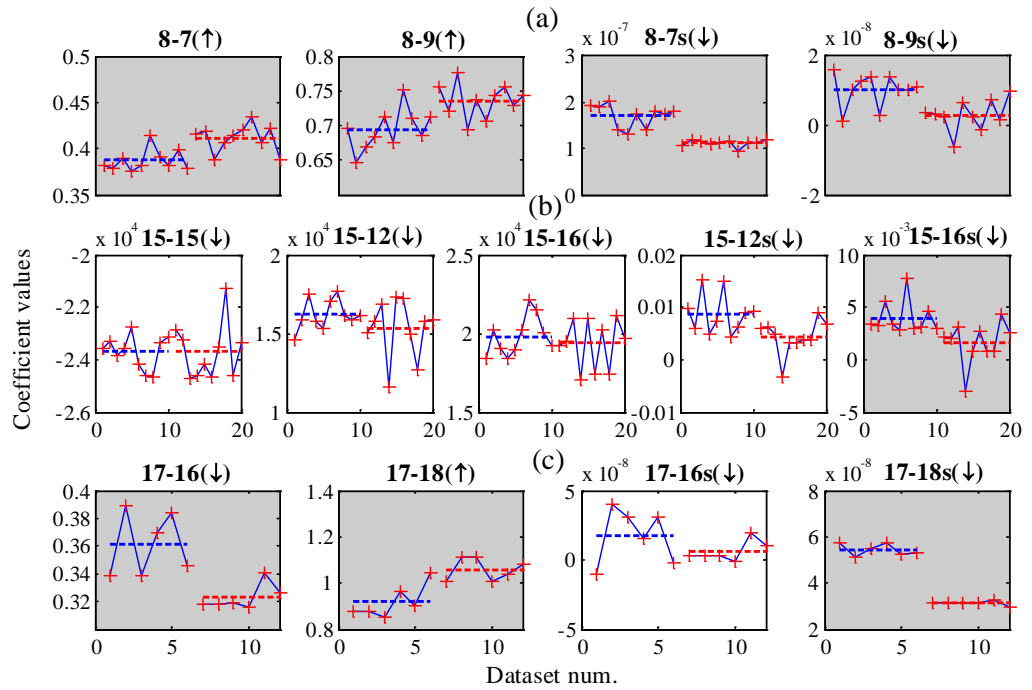
Figure 11.17   Plots of selected model coefficients extracted from datasets

from the frame experiment. (a) is from Model 2, Damage state

1; (b) is from Model 3, Damage state 2; (c) is from Model 2,

Damage state 3.
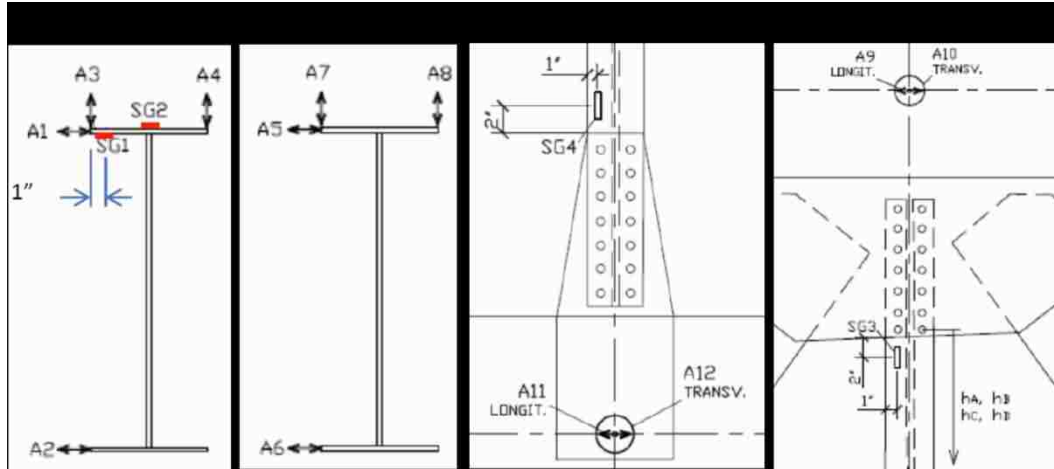
Figure 11.18 Installation of accelerometers(A) and strain gages (SG) at (a)

the middle height; (b) the ¾ height; (c) the bottom gusset

connection; (d) the top gusset connection.
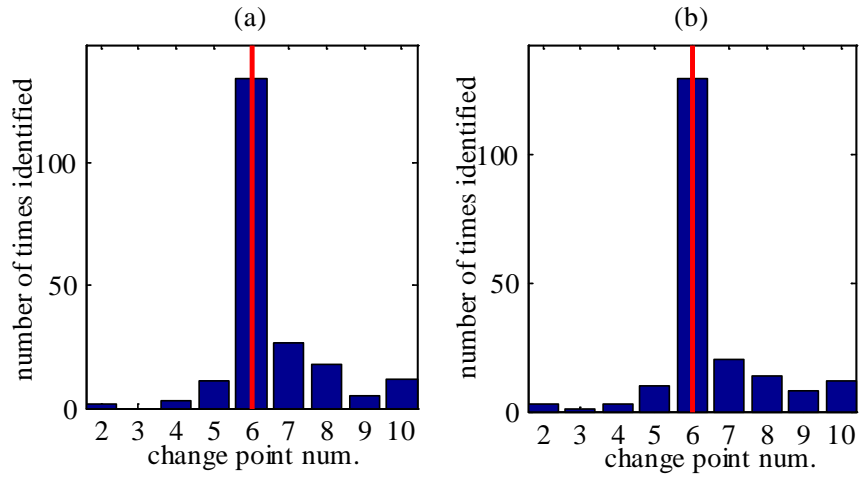
Figure 11.19   Histograms of change points (a) from models excluding the

lower cord translations, (b) from models including those

translations. The median change point for each case is

indicated as the red thin bar.
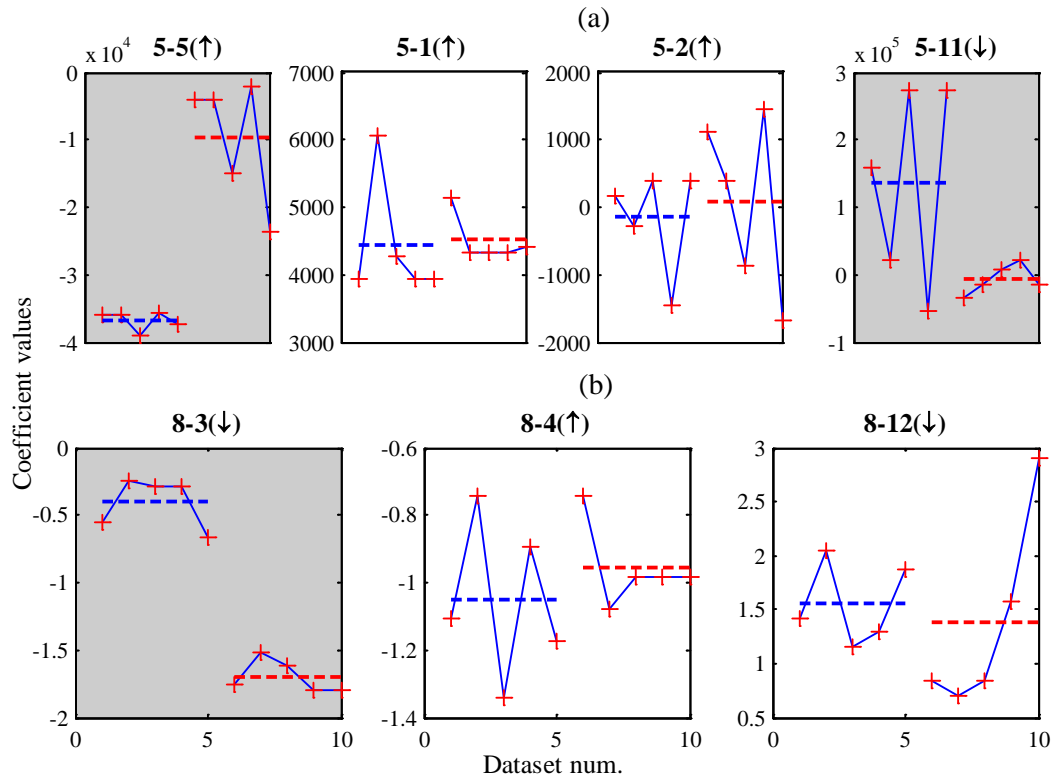
Figure 11.20   Acceleration-related coefficients of the regression models for

the longitudinal and transverse vibration. (a) is from Model 3

with location 5 as the regressand node, (b) is from Model 1

with location 8 as the regressand node.

Chapter 12 **Summary and Conclusions**

12.1 BACKGROUND AT A GLANCE

There are many types of sensors available for SHM; and similarly many types of algorithms are devised for data processing. Apart from system identification, scalar time series analysis and multivariate substructural modeling that were discussed herein, other time-frequency domain techniques such as wavelet decomposition for transient response analysis (Okafor and Dutta, 2000), frequency response function evaluation (Maia, Silva, Almas, and Sampaio, 2003) are also being actively investigated by researchers.

The choice of data analysis method depends largely on the monitoring context. Modeling procedures for mechanical vibration measurements is certainly different than those for acoustic waves. And for vibration analysis, depending on whether the structural system is under ambient load or under known artificial excitation, whether the environment is stable or varying, the accordingly devised algorithms will have different complexities.

Here since damage detection is performed using acceleration/strain measurements from structures subjected to ambient/random (sometimes impulse) excitation, time series analysis and statistical regression approaches on stationary signals are the chief research interest of this dissertation.

12.2 SUMMARY OF PAST RESEARCH DIRECTIONS AND JUSTIFICATIONS

As reiterated in the previous chapters, effective damage detection relies on damage features that are sensitive to damage while robust to environmental/operational change

and damage feature thresholds that minimizes both Type I (false alarm) and Type II (missed case) errors. At the meantime it is important to have damage indices that reflect structural damage location and extent. Part I and II of this dissertation addresses these two tasks, respectively. In **Part I**, scalar time series analysis methods (Brockwell and Davis, 2002, 2009) is the focus of studies. This family of methods makes use of parametric/ non-parametric estimation techniques to examine certain aspects of collected signal. The features produced by them are very suitable for statistical processing as they are often in large quantities. Also, many of these methods rely only on signal from a single sensor node, and thus are computationally efficient. However, it is found during several investigations that these features based on modeling on a single node response can demonstrate large fluctuations in cases where operational conditions is subjected to change, e.g., the input is ambient instead of artificial. This feature 'fragility' may be resulted from information limitation, as only single node output is used. Therefore, careful consideration should be given to feature damage threshold construction, and investigations are needed for accurate evaluation of their damage sensitivity/noise robustness.

To devise vibration-based features that are more robust to changes of irrelevant factors, it is necessary to incorporate response from several nodes to form a substructural model. As noted in Part II, such models often uses the response from within the substructure for output and responses at substructural boundaries for input, and therefore damage features based on the estimated substructural model parameters and model residuals should convey information strongly related to physical behavior of the substructures. The substructural algorithms can be regarded as inverse Finite Element

279

Modeling approaches, because here substructural properties are inferred from substructural nodal responses instead of the other way around. Since this family of approaches is input-output based, it enjoys better stability than the output-only scalar TSA techniques and still computationally advantageous compared to global scale modeling and updating methods.

12.3 SUMMARY OF FINDINGS

Part I details my research on ***univariate TSA approach (mainly autoregressive (AR) modeling) for damage existence identification***.

Damage thresholds

Ideally, damage features should be devised so that it is highly sensitive only to changes in structural properties but unaffected by other environmental and operational factors. However, in practices it is often difficult to eliminate the influences of the latter from the data extraction results. As such, special attention needs to be paid to the damage threshold construction for the indicators. For this purpose I introduce thresholds created from resampling methods such as bootstrapping and cross-one-validation (Chapter 3). These thresholds generally deliver good performances on balancing the false-positive (identifying non-relevant change) and false-negative (neglecting structural damage) risks.

Damage features

My contribution is mainly on improving and quantifying the damage sensitivity and robustness of the AR indicators/features: Ljung-Box statistic, a metric that evaluates the change in the autocorrelation function of the model residuals, is proposed as a more responsive feature than residual standard deviation ratio; a distance measure (namely,

Cosh distance) between AR model spectra is used to yield more stable performance than the Mahalanobis distance feature between AR model coefficients (Section 4.4, Chapter 4). The performance of the proposed features have been validated through application to wired/wireless sensor measurements from a variety of structures including a simulated mass spring system, a steel truss, a two-bay frame specimen and reinforced concrete bridge slab (Section 4.5-4.6, Chapter 4). And they are also compared to other existing features such as influence coefficients (Chapter 5).

Theoretical sensitivity evaluation of damage featues

In an effort to provide more theoretical support for the AR-based damage detection methodology, I have developed a proof on the vectorial autoregressive nature of responses from MDOF system nodes under random excitation and the autoregressive property of single channel response (Section 6.3.1, Chapter 6). Analytical sensitivity expressions for the Cosh distance and Mahalanobis distance feature to damage/ measurement noise are also derived(Section 6.4, Chapter 6), results from a simulated beam structure shows agreement between the sensitivity analysis results and those from simulation (Section 6.6, Chapter 6). AR modeling on signal auto-covariance function is also examined theoretically(Section 6.5, Chapter 6) and experimentally (Section 6.7, Chapter 6) on a steel bridge, and it is found that compared to features from ambient series modeling, features from this approach are more robust to noise, but in the meantime also lose some damage sensitivity.

281

Part II describes my effort on improving ***multivariate substructural approaches, which utilize responses from several adjacent locations to form input/output algorithms for higher-level damage detection (damage location/extent determination)***.

Heuristic methods – damage indices have no explicit physical meaning

Heuristic methods here refer to the approaches that do not stem from strict theoretical derivation, and thereby do not produce parameters with an explicit relation to the structural properties. Within this category there are two types of measures that I have contributed: the mutual information statistic, and the direct multivariate regression.

Mutual information statistic is based on the temporal correlation between data from two adjacent sensing channels(Section 9.4, Chapter 9). The damage identification/localization results(Section 9.6, Chapter 9) in a 3D steel truss obtained from this method and the available ARX modeling technique (Section 8.2.1.2, Chapter 8) are then compared to those from univariate AR modeling, and it is observed that the multivariate time series analysis produces viable damage indices and in the meanwhile is able to predict damage location with greater accuracy.

In Section 9.5, Chapter 9, Coefficients from multivariate linear regression (IIC) between the acceleration collected at one location and those at adjacent nodes are also used as damage indicators. This regression model is further refined by incorporating strain measurements at the adjacent locations to produce coefficients denoted as ICHVR. Damage recognition and localization performances of these two types of coefficients are compared with the pair-wise regression coefficients(IC) through applying the algorithms to a two-span steel girder in the lab (Section 9.7, Chapter 9). It is found that for this case

study the model performance levels are positively correlated with their respective complexities. In other words, ICHVR yields the best overall results while the IC tends to be less sensitive and accurate in damage reporting. The example suggests that damage identification can be improved to an extent by tuning the model to include more independent information sources.

Proven approaches– damage indices have explicit physical meaning

Heuristic approaches have the merit of being straightforward to implement and intuitive to understand, but their results do not have explicit physical interpretations, and they are not supported by rigorous derivations. Thus, two novel regression-based techniques that use local acceleration responses of a shear frame structure to estimate its local stiffness are proposed by me in Section 10.4-10.5, Chapter 10. The substructure here is defined as a single story (denoted as 'middle story') along with all its adjacent stories. The basic idea is that the acceleration at middle story is proportional to the restoration forces generated by the connections from this story to neighboring stories, which are in turn functions of their interstory drifts and velocities. In the case of linear structures, the regression functions are linear and the coefficients associated the interstory drifts are the ratios of interstory stiffness values to middle story mass. One time domain method (TDRM) regress the story acceleration on to interstory displacements reconstructed from acceleration signals; the other re-interpret this relation in the frequency domain (FDRM) to get a more neat and efficient regression formula. Both methods are proved effective in their application to acceleration data from a simulated 5DOF system for stiffness estimation (Section 10.7, Chapter 10), and to acceleration from a five degree-of-freedom aluminum-plexiglas model and a steel mass-spring system

283

that are subjected to white noise excitation(Section 10.8, Chapter 10). FDRM shows a more reliable performance since it considers the effect of damping in its formulation, and also because it does not involves displacement reconstruction, which is an ill-posed problem as vibration initial conditions are not available. FDRM can also be used for stiffness estimation for regular frame structures (Section Section 10.6 and 10.7.2, Chapter 10) given that the beam-to-column stiffness ratio exceeds a certain limit (12 for the regular FDRM, and 4 for the modified FDRM).

To extend the TDRM/FDRM approaches to applications on structures with more complex geometry, Euler-Bernoulli beam elements are adopted as another form of substructure in Chapter 11. The beam elements in plane and three-dimensional (3D) space are examined, and the regression can be again formulated in either the time or frequency domain between responses from within the substructure and responses at both ends of the element. For in-plane members strain needs to be measured only at one point along the section of each element end to account for in-plane rotation, while for 3D space members strain measurements are needed at three distinct points for each section to characterize the biaxial bending and torsional effects. Also, for 3D space members the biaxial transverse acceleration measurements are required (Section 11.3, Chapter 11). Regression coefficients here are functions of element section stiffness and have their physical interpretations. Three damage indices are defined from the regression model characteristics, and two change point analysis methods are adopted to capture the changes occur in damage index sequences extracted from structural monitoring datasets from healthy state and current state. Damage location is identified as where the most significant change in damage indices occurs, and a voting scheme is used to synthesize

284

the results from different algorithms introduced. Algorithms thus formulated are applied to detect and locate damage in the aforementioned 2-bay steel frame specimen and the vertical member of a steel truss bridge in western Pennsylvania (Section 11.7, Chapter 11). The results are satisfactory in that damage location and nature is properly recognized for most of the damage scenarios.

Generalized substructural modeling

For effective substructural modeling it is important to clarify an independent input-output linear model for each substructure within a structural system. The behavior of a substructure is controlled by two types of influences: those acting within the substructure itself and those acting on its 'boundary'. The two sources must achieve equilibrium to hold a substructure in place, and the relation between these forces and the substructure response reflects certain physical properties of the substructure. When the structural responses collected are structural vibration (the most commonly monitored signals in SHM applications), the structural physical properties that affect the responses are the material constitutive relations (Hook's Law etc.). As such, structural stiffness properties can be inferred from the substructural model characteristics estimated from monitoring data.

12.4 ORIGINAL CONTRIBUTIONS: A BRIEF DESCRIPTION

My contributions, as indicated by the structure of this thesis, can be classified into two categories: 1) development and validation of damage existence detection methods using univariate time series analysis; 2) formulation and verification of higher-level damage detection methods using regression analysis on signal transforms.

285

My work in the first category concerns both the damage feature extraction and damage threshold construction. For the first part I devised damage features using Cosh distance of autoregressive (AR) spectra and Ljung-Box statistic of AR residuals, and compared them with existing AR model coefficients and residual based damage detection approaches through various implementations. The Cosh distance feature is proposed in hope of better noise robustness, while the Ljung-Box statistic feature is brought forward with an expectation of higher damage sensitivity. Results of the applications validated the results to certain extents. Also, theoretical damage/noise sensitivity of the AR coefficients based features are derived and presented. For damage threshold construction, data-driven approaches are proposed in place of the theoretical hypothesis testing to reduce statistical modeling errors that will occur when the actual feature distribution deviates from the assumed one.

My research in the second category involves mainly the damage feature extraction. Multivariate analysis (i.e. analysis on measurements from multiple sensors) is used here, and damage indices are expected to yield light not only on structural damage existence but also on damage location and extent. Heuristic damage indicators, including adjacent channel mutual information and multivariate regression coefficients (modified influence coefficients), are first proposed and tested to evaluate the potential of this family of methods. After that, substructure models based on shear frame and beam substructures are derived in an analytically rigorous manner and evaluated through numerical and real-world applications. The corresponding threshold construction methodology used here is cumulative sum and variance reduction based change point analysis, and application

286

results show that the proposed methods are capable of damage localization and extent quantification.

To sum up, my contributions have been in developing and testing different damage detection techniques and apply them to different kinds of civil structures. The method formulations are based on either theoretical derivations or experiential judgments, and they are validated using applications and/or analytical sensitivity analysis. Generally, the optimal damage detection method varies by application, and as such it is important to propose different features and study their pros and cons so that features best suits the purpose will be selected for a certain sensing and structural setting. The content of this dissertation serves to advance the research on adaptive damage detection.

12.5 GENERAL CONCLUSIONS, FUTURE WORK

Data-driven SHM can bring in massive amount of data through continuous system monitoring. The aim of all SHM data compression strategies is to gaze through the uncertainties and disturbances contained with the measurements to discover information pertaining to the current structural condition and other operational parameters of interest. Within the area of damage identification, I have worked on exploring the capabilities of different SHM vibration sensors, proposing and testing new features/thresholds for damage identification, cross-comparing the proposed features/thresholds with existing ones through applications to various types of civil structures, and developing theoretical models regarding the validity/sensitivity/robustness of several damage features. These aspects are interrelated as in improvement in one will benefit others. In the end, they all contribute to the search and development for optimal damage detection method for a certain application.

Vibration-based system monitoring is relatively economical and convenient, but its success is not always guaranteed because environmental conditions can vary and potential damage form is largely unknown. Sometimes its local damage detection performance can be poor because of the low signal-to-noise ratio. As such, in future work sensors of various types should be examined and combined to make best possible use of their advantages. Specifically, digital image correlation systems have found use in detecting surface cracks, while ultrasonic testing methods are effective at evaluating unobvious damage such as delamination and internal fracture. Accelerometer sensor networks are often employed for modal realization, while fiber and nanotube based sensors can be applied for strain/pressure sensing and internal force estimation. Because each sensor has its own distinct characteristics, there is huge potential in increasing structural state identification accuracy by synthesizing information from multiple types of sensors, just like a more vivid and truthful representation of an object can be given by combining pictures taken at different angles. This topic has been briefly touched in substructural modeling of beam elements (Chapter 11), where both strain and acceleration signals are used for high-level damage detection. To improve monitoring quality of real structures, excitation records (wind, traffic etc.) environmental conditions should be incorporated where available. On the other hand, active sensing methods should come into play when passive sensing based algorithms are unable to identify the current structural state. My interest is in devising and optimizing combination models for these measurement types. The guiding philosophy is to proportion the amount of useful information sensed according to the relative importance of structural components; Correlation among separate kinds of measurements and their relation to the structural

288

condition needs to be clarified and analyzed for different applications, and laboratory and field experiments can help examine, improve and validate the models so that the theoretical model can serve as a valid approximation of the real situation. The models can then also be used to provide lower/upper bounds on the identification accuracy. I would like to first apply these concepts to the monitoring and analysis to steel structures, not only because they are the objects of many of my past research projects, but also because their material constitutive relation can be more accurately defined than those of concrete and composite structures, thus promising less modeling error regarding the relation between external influences and structural response.

References

Abdel Wahab, M. M., de Roeck, G., and Peeters, B. (1999). Parameterization of Damage in Reinforced Concrete Structures Using Model Updating. *Journal of Sound and Vibration*, *228*(4), pp. 717–730. doi:10.1006/jsvi.1999.2448

Atamturktur, S., Bornn, L., and Hemez, F. (2011). Vibration Characteristics of Vaulted Masonry Monuments Undergoing Differential Support Settlement. *Engineering Structures*, *33*(9), pp. 2472–2484.

Barroso, L. R., and Rodriguez, R. (2004). Damage Detection Utilizing the Damage Index Method to a Benchmark Structure. *Journal of Engineering Mechanics*, *130*(2), pp. 142–151.

Beck, J. L., and Katafygiotis, L. S. (1998). Updating Models and Their Uncertainties. Part I: Bayesian Statistical Framework. *Journal of Engineering Mechanics*, *124*(4), pp. 455–461.

Berk, K. N. (1974). Consistent Autoregressive Spectral Estimates. *The Annals of Statistics*, *2*(3), pp. 489–502.

Bernal, D. (2002). Load Vectors for Damage Localization. *Journal of Engineering Mechanics*, *128*(1), pp. 7–14. doi:10.1061/(ASCE)0733-9399(2002)128:1(7)

Bodeux, J., and Golinval, J. (2001). Application of ARMAV Models to the Identification and Damage Detection of Mechanical and Civil Engineering Structures. *Smart Materials and Structures*, *10*(3), pp. 479–489.

Brockwell, P. J., and Davis, R. A. (2002). Introduction to Time Series and Forecasting (2nd ed.). NY: Springer.

Brockwell, P. J., and Davis, R. A. (2009). Time Series: Theory and Methods (2nd ed.). NY: Springer.

Brodsky, B., and Darkhovsky, B. (1993). Nonparametric Methods in Change Point Problems. Vol. 243, Springer.

Brownjohn, J., Xia, P., Hao, H., and Xia, Y. (2001). Civil Structure Condition Assessment by FE Model Updating:: Methodology and Case Studies. *Finite Elements in Analysis and Design*, *37*(10), pp. 761–775.

Campbell Scientific Inc. (2005). Anti-Alias Filter & FFT Spectrum Analyzer Modules.

Campbell Scientific Inc. (2009). CR9000X & CR9000XC Specifications.

Chang, M., and Pakzad, S. (2012). Modified Natural Excitation Technique for Stochastic Modal Identification. *Journal of Structural Engineering*, *139*(10), pp. 1753–1762.

Chang, P., Flatau, A., and Liu, S. (2003). Review Paper: Health Monitoring of Civil Infrastructure. *Structural Health Monitoring*, *2*(3), pp. 257–267.

Chopra, A. (2006). Dynamics of Structures: Theory and Applications to Earthquake Engineering. Prentice-Hall. Upper Saddle River, NJ.

Congleton, R. (2004). The Median Voter Model. *The encyclopedia of public choice* (pp. 707–712). Springer.

Cover, T., and Thomas, J. (2006). Elements of Information Theory (2nd ed.). John Wiley & Sons.

Crossbow Technology Inc. (2006). Imote2 Datasheet, pp. 2–4.

De Lautour, O. R., and Omenzetter, P. (2010). Nearest Neighbor and Learning Vector Quantization Classification for Damage Detection Using Time Series Analysis. *Structural Control and Health Monitoring*, *17*(6), pp. 614–631. doi:10.1002/stc.335

Dharap, P., Koh, B., and Nagarajaiah, S. (2006). Structural Health Monitoring Using ARMarkov Observers. *Journal of Intelligent Material Systems and Structures*, *17*(6), pp. 469–481.

Digitexx Data Systems. (2010). PDAQ (Portable Data Acquisition Systems) Product Family Brochure.

Doebling, S. W. (1995). *Measurement of Structural Flexibility Matrices for Experiments with Incomplete Reciprocity*. Department of Aerospace Engineering Sciences, University of Colorado, Boulder, CO.

Doebling, S. W., and Farrar, C. R. (1998). Statistical Damage Identification Techniques Applied to the I-40 Bridge over the Rio Grande River. *Proceedings of the International Modal Analysis Conference*, *16*, pp. 1717–1724.

Doebling, S. W., Farrar, C. R., and Prime, M. B. (1998). A Summary Review of Vibration-Based Damage Identification Methods. *Shock and Vibration Digest*, *30*(2), pp. 91–105.

Dorvash, S., and Pakzad, S. (2012). Effects of Measurement Noise on Modal Parameter Identification. *Smart Materials and Structures*, *21*(6), pp. 065008.

Duan, Z., Yan, G., Ou, J., and Spencer, B. (2007). Damage Detection in Ambient Vibration Using Proportional Flexibility Matrix with Incomplete Measured DOFs. *Structural Control and Health Monitoring*, *14*(2), pp. 186–196.

291

Duda, R. O., Hart, P. E., and Stork, D. G. (2012). Pattern Classification (2nd ed.). Wiley-Interscience.

Farrar, C. R., Duffey, T. A., Doebling, S. W., and Nix, D. A. (1999). A Statistical Pattern Recognition Paradigm for Vibration-Based Structural Health Monitoring. In *Proceedings of 2nd International Workshop on Structural Health Monitoring*. Stanford, CA.

Farrar, C. R., and Worden, K. (2007). An Introduction to Structural Health Monitoring. *Philosophical Transactions. Series A, Mathematical, Physical, and Engineering Sciences*, *365*(1851), pp. 303–15. doi:10.1098/rsta.2006.1928

Fassois, S. D., and Sakellariou, J. S. (2007). Time-Series Methods for Fault Detection and Identification in Vibrating Structures. *Philosophical Transactions of the Royal Society A: Mathematical, Physical and Engineering Sciences*, *365*(1851), pp. 411–448.

Friswell, M., and Mottershead, J. (1995). Finite Element Model Updating in Structural Dynamics (1st ed.). Springer: Berlin.

Fugate, M. L., Sohn, H., and Farrar, C. R. (2001). Vibration-Based Damage Detection Using Statistical Process Control. *Mechanical Systems and Signal Processing*, *15*(4), pp. 707–721.

Good, P. I. (2001). Resampling Methods. Birkhäuser.

Gray Jr, A., and Markel, J. (1976). Distance Measures for Speech Processing. In *Acoustics, Speech and Signal Processing, IEEE Transactions on,* (Vol. 24, pp. 380–391).

Gul, M., and Catbas, F. (2010). Damage Assessment with Ambient Vibration Data Using a Novel Time Series Analysis Methodology. *Journal of Structural Engineering*, *137*(12), pp. 1518–1526.

Gul, M., and Catbas, F. N. (2009). Statistical Pattern Recognition for Structural Health Monitoring Using Time Series Modeling: Theory and Experimental Verifications. *Mechanical Systems and Signal Processing*, *23*(7), pp. 2192–2204.

Hansen, P. C. (1998). Rank-Deficient and Discrete Ill-Posed Problems: Numerical Aspects of Linear Inversion.

Haritos, N., and Owen, J. S. (2004). The Use of Vibration Data for Damage Detection in Bridges: A Comparison of System Identification and Pattern Recognition Approaches. *Structural Health Monitoring*, *3*(2), pp. 141–163. doi:10.1177/1475921704042698

Hassiotis, S., and Jeong, G. D. (1995). Identification of Stiffness Reductions Using Natural Frequencies. *Journal of Engineering Mechanics*, *121*(10), pp. 1106–1113.

Hernandez-Garcia, M. R., Masri, S. F., Ghanem, R., Figueiredo, E., and Farrar, C. R. (2010a). A Structural Decomposition Approach for Detecting, Locating, and Quantifying Nonlinearities in Chain-like Systems. *Structural Control and Health Monitoring*, *17*(7), pp. 761–777. doi:10.1002/stc.396

Hernandez-Garcia, M. R., Masri, S. F., Ghanem, R., Figueiredo, E., and Farrar, C. R. (2010b). An Experimental Investigation of Change Detection in Uncertain Chain-like Systems. *Journal of Sound and Vibration*, *329*(12), pp. 2395–2409. doi:10.1016/j.jsv.2009.12.024

Hong, Y. H., Kim, H.-K., and Lee, H. S. (2010). Reconstruction of Dynamic Displacement and Velocity from Measured Accelerations Using the Variational Statement of an Inverse Problem. *Journal of Sound and Vibration*, *329*(23), pp. 4980–5003. doi:10.1016/j.jsv.2010.05.016

Hou, J., Jankowski, Ł., and Ou, J. (2011). A Substructure Isolation Method for Local Structural Health Monitoring. *Structural Control and Health Monitoring*, *18*(6), pp. 601–618.

Illinois Structural Health Monitoring Project. (2011). Imote2 for Structural Health Monitoring: User's Guide, (January).

Intel Corporation Research. (2005). *Intel Mote2 Overview, Version 3.0*. Santa Clara, CA, United States.

ISHMP. (2009). Retrieved from http://shm.cs.uiuc.edu/software.html

Jain, A. K., Duin, P. W., and Mao, J. (2000). Statistical Pattern Recognition: A Review. *IEEE Transactions on Pattern Analysis and Machine Intelligence*, *22*(1), pp. 4–37. doi:10.1109/34.824819

James III, G., Carrie, T., and Lauffer, J. (1993). The Natural Excitation Technique (NExT) for Modal Parameter Extraction From Operating Wind Turbines. *Sandia National Labs Report SAND-92-1666*.

Johnson, N., Ranf, R., and Saiidi, M. (2008). Seismic Testing of a Two-Span Reinforced Concrete Bridge. *Journal of Bridge Engineering*, *13*(2), pp. 173–182.

Juang, J., and Pappa, R. (1985). An Eigensystem Realization Algorithm for Modal Parameter Identification and Model Reduction. *Journal of Guidance, Control, and Dynamics*, *8*(5), pp. 620–627.

Koch, K. (1999). Parameter Estimation and Hypothesis Testing in Linear Models (2nd ed.). Springer.

Kuwabara, M., Yoshitomi, S., and Takewaki, I. (2013). A New Approach to System Identification and Damage Detection of High-Rise Buildings. *Structural Control and Health Monitoring*, *20*(5), pp. 703–727.

Labuz, E. L., Chang, M., and Pakzad, S. N. (2010). Local Damage Detection in Beam-Column Connections Using a Dense Sensor Network. In *Proceedings of the 19th Annual Structures Congress* (pp. 3143–3154). ASCE.

Labuz, E. L., Pakzad, S. N., and Cheng, L. (2011). Damage Detection and Localization in Structures: A Statistics Based Algorithm Using a Densely Clustered Sensor Network. In *Proceedings of the 20th Annual Structures Congress* (pp. 53–64). ASCE.

Lee, H., Hong, Y., and Park, H. (2010). Design of an FIR Filter for the Displacement Reconstruction Using Measured Acceleration in Low-Frequency Dominant Structures. *International Journal for Numerical Methods in Engineering*, *82*, pp. 403–434.

Ljung, G. M., and Box, G. E. P. (1978). On a Measure of Lack of Fit in Time Series Models. *Biometrika*, *65*(2), pp. 297–303.

Ljung, L. (1987). System Identification: Theory for the User. Information and System Sciences Series. Englewood Cliffs, NJ: Prentice-Hall.

Lu, Y., and Gao, F. (2005). A Novel Time-Domain Auto-Regressive Model for Structural Damage Diagnosis. *Journal of Sound and Vibration*, *283*(3-5), pp. 1031–1049.

Lynch, J., and Loh, K. (2006). A Summary Review of Wireless Sensors and Sensor Networks for Structural Health Monitoring. *Shock and Vibration Digest*, *38*(91), pp. 91–128.

Mahalanobis, P. C. (1936). On the Generalized Distance in Statistics. In *Proceedings of the National Institute of Sciences, 2* (pp. 49–75). India.

Maia, N. M. M., Silva, J. M. M., Almas, E. A. M., and Sampaio, R. P. C. (2003). Damage Detection in Structures: From Mode Shape to Frequency Response Function Methods. *Mechanical Systems and Signal Processing*, *17*(3), pp. 489–498. doi:10.1006/mssp.2002.1506

Mottershead, J., and Friswell, M. (1993). Model Updating in Structural Dynamics: A Survey. *Journal of Sound and Vibration*, *167*(2), pp. 347–375.

Nagarajaiah, S., Dyke, S., Lynch, J., Smyth, A., Agrawal, A., Symans, M., and Johnson, E. (2008). Current Directions of Structural Health Monitoring and Control in USA. *Advances in Science and Technology*, *56*, pp. 277–286.

Nair, K., Kiremidjian, A., and Law, K. (2006). Time Series-Based Damage Detection and Localization Algorithm with Application to the ASCE Benchmark Structure. *Journal of Sound and Vibration*, *291*(1-2), pp. 349–368.

Nigro, M. B., Pakzad, S. N., and Dorvash, S. (2014). Localized Structural Damage Detection: A Change Point Analysis. *Computer-Aided Civil and Infrastructure Engineering*, pp. in press. doi:10.1111/mice.12059

Noh, H., Nair, K., Kiremidjian, A., and Loh, C. (2009). Application of Time Series Based Damage Detection Algorithms to the Benchmark Experiment at the National Center for Research on Earthquake Engineering (NCREE) in Taipei, Taiwan. *Smart Structures and Systems*, *5*(1), pp. 95–117.

Okafor, A., and Dutta, A. (2000). Structural Damage Detection in Beams by Wavelet Transforms. *Smart Materials and Structures*, *9*(6), pp. 906.

Omenzetter, P., and Brownjohn, J. (2006). Application of Time Series Analysis for Bridge Monitoring. *Smart Materials and Structures*, *15*(1), pp. 129–138.

Oppenheim, A. V., and Schafer, R. W. (2009). Discrete-Time Signal Processing (3rd ed., p. 1120). Upper Saddle River: Prentice Hall.

Overschee, P. Van, and Moor, B. De. (1994). N4SID: Subspace Algorithms for the Identification of Combined Deterministic-Stochastic Systems. *Automatica*, *30*(1), pp. 75–93.

Pakzad, S. (2010). Development and Deployment of Large Scale Wireless Sensor Network on a Long-Span Bridge. *Smart Structures and Systems*, *6*(5-6), pp. 525–543.

Pakzad, S., Dryden, M., and Fenves, G. (2009). Parametric Bootstrap for System Identification of a Scaled Reinforced Concrete Bridge. In *Proceedings of the Structures Congress* (pp. 397–405). Austin, TX.

Pakzad, S., and Fenves, G. (2009). Statistical Analysis of Vibration Modes of a Suspension Bridge Using Spatially Dense Wireless Sensor Network. *Journal of Structural Engineering*, *1359*(7), pp. 863–872.

Pakzad, S., Kim, S., Fenves, G., and Glaser, S. (2005). Multi-Purpose Wireless Accelerometers for Civil Infrastructure Monitoring. In *Proceedings of the 5th Int. Workshop on Structural Health Monitoring*. Stanford, CA.

Park, K. C., Reich, G. W., and Alvin, K. F. (1998). Structural Damage Detection Using Localized Flexibilities. *Journal of Intelligent Material Systems and Structures*, *9*(11), pp. 911–919. doi:10.1177/1045389X9800901107

PCB Piezotronics. (2009). Model 3701G3FA3G Capacitive Accelerometer Installation and Operating Manual. Retrieved from http://pcbpiezotronics.co.uk/contentstore/docs/PCB_Corporate/Vibration/products/Manuals/3701G3FA3G.pdf

Peeters, B., and Ventura, C. E. (2003). Comparative Study of Modal Analysis Techniques for Bridge Dynamic Characteristics. *Mechanical Systems and Signal Processing*, *17*(5), pp. 965–988. doi:10.1006/mssp.2002.1568

Porat, B. (1994). Digital Processing of Random Signals: Theory and Methods. Englewood Cliffs, NJ: Prentice-Hall.

Pothisiri, T., and Hjelmstad, K. D. (2003). Structural Damage Detection and Assessment from Modal Response. *Journal of Engineering Mechanics*, *129*(2), pp. 135–145.

Prevosto, M. (1982). *Algorithmes D'identification Des Caractéristiques Vibratoires de Structures Mécaniques Complexes*. PhD Thesis, Université de Rennes I, France.

Rahai, A., Bakhtiari-Nejad, F., and Esfandiari, A. (2007). Damage Assessment of Structure Using Incomplete Measured Mode Shapes. *Structural Control and Health Monitoring*, *14*(5), pp. 808–829.

Ren, W.-X., and Chen, H.-B. (2010). Finite Element Model Updating in Structural Dynamics by Using the Response Surface Method. *Engineering Structures*, *32*(8), pp. 2455–2465. doi:10.1016/j.engstruct.2010.04.019

Rice, J. A., and Spencer, Jr., B. F. (2008). Structural Health Monitoring Sensor Development for the Imote2 Platform. In *Proceedings of the SPIE - The International Society for Optical Engineering* (Vol. 6932, pp. 693231–693234). SPIE - The International Society for Optical Engineering. doi:10.1117/12.776695

Rytter, A., and Kirkegaard, P. (1994). *Vibration Based Inspection of Civil Engineering Structures*. Aalborg Universitetsforlag.

Saito, T., Mase, S., and Morita, K. (2005). A Probabilistic Approach to Structural Damage Estimation. *Structural Control and Health Monitoring*, *12*(3-4), pp. 283–299.

Sakellariou, J. S., and Fassois, S. D. (2006). Stochastic Output Error Vibration-Based Damage Detection and Assessment in Structures under Earthquake Excitation. *Journal of Sound and Vibration*, *297*(3), pp. 1048–1067.

Salawu, O. (1997). Detection of Structural Damage through Changes in Frequency: A Review. *Engineering Structures*, *19*(9), pp. 718–723.

Salawu, O., and Williams, C. (1993). Structural Damage Detection Using Experimental Modal Analysis A Comparison of Some Methods. In *Proceedings of 11th International Modal Analysis Conference* (pp. 254–260). Orlando, FL.

Seaburg, P. A., and Carter, C. J. (1997). Torsional Analysis of Steel Members. Monograph: American Institute of Steel Construction.

Shao, J., and Tu, D. (1995). The Jackknife and Bootstrap. NY: Springer-Verlag.

Silicon Designs Inc. (2013). Model 2210 Analog Accelerometer Module Specification Sheet. Retrieved from http://www.silicondesigns.com/pdfs/2210.pdf

Sohn, H., and Farrar, C. R. (2001). Damage Diagnosis Using Time Series Analysis of Vibration Signals. *Smart Materials and Structures*, *10*(3), pp. 446–452.

Sohn, H., Farrar, C. R., Hunter, N. F., and Worden, K. (2001). Structural Health Monitoring Using Statistical Pattern Recognition Techniques. *Journal of Dynamic Systems, Measurement, and Control*, *123*(4), pp. 706–711.

Sohn, H., Worden, K., and Farrar, C. R. (2002). Statistical Damage Classification under Changing Environmental and Operational Conditions. *Journal of Intelligent Material Systems and Structures*, *13*(9), pp. 561–574.

Takewaki, I., and Nakamura, M. (2005). Stiffness-Damping Simultaneous Identification under Limited Observation. *Journal of Engineering Mechanics*, *131*(10), pp. 1027–1035.

Taylor, W. A. (2000). Change-Point Analysis: A Powerful New Tool for Detecting Changes. *Preprint, Available as Http://www.variation.com/cpa/tech/changepoint.html*.

Teräsvirta, T. (1977). The Invertibility of Sums of Discrete MA and ARMA Processes. *Scandinavian Journal of Statistics*, *4*(4), pp. 165–170.

TinyOS. (2005). Retrieved from http://www.tinyos.net

Van den Hof, P. M. J., De Vries, D. K., and Schoen, P. (1992). Delay Structure Conditions for Identifiability of Closed Loop Systems. *Automatica*, *28*(5), pp. 1047–1050. doi:10.1016/0005-1098(92)90161-8

Vishay Precision Group. (2010a). Datasheet for General Purpose Strain Gages - Linear Pattern - 250 UW, pp. 11312.

Vishay Precision Group. (2010b). Datasheet for Standard Weldable Patterns Special Use Sensors - Weldable Strain Gages, pp. 118–120.

Wang, Y., Lynch, J. P., and Law, K. H. (2007). A Wireless Structural Health Monitoring System with Multithreaded Sensing Devices: Design and Validation. *Structure and Infrastructure Engineering*, *3*(2), pp. 103–120. doi:10.1080/15732470600590820

Wei, B., and Gibson, J. (2000). Comparison of Distance Measures in Discrete Spectral Modeling. In *Proceedings of the IEEE Digital Signal Process* (pp. 1–4).

Welch, P. (1967). The Use of Fast Fourier Transform for the Estimation of Power Spectra: A Method Based on Time Averaging over Short, Modified Periodograms. *IEEE Transactions on Audio and Electroacoustics*, *AU-15*, pp. 70–73.

Weng, S., Xia, Y., Xu, Y., and Zhu, H. (2011). Substructure Based Approach to Finite Element Model Updating. *Computers & Structures*, *89*(9-10), pp. 772–782.

Worden, K., and Manson, G. (2007). The Application of Machine Learning to Structural Health Monitoring. *Philosophical Transactions of the Royal Society A: Mathematical, Physical and Engineering Sciences*, *365*(1851), pp. 515–537.

Worden, K., Manson, G., and Fieller, N. (2000). Damage Detection Using Outlier Analysis. *Journal of Sound and Vibration*, *229*(3), pp. 647–667.

Xie, L., Mita, A., and Carden, P. (2010). Identifiability of Linear Superstructures under feedback—Taking Base-Isolated Structures as Example. *Structural Control and Health Monitoring*, *17*(4), pp. 355–367.

Xing, Z., and Mita, A. (2012). A Substructure Approach to Local Damage Detection of Shear Structure. *Structural Control and Health Monitoring*, *19*(2), pp. 309–318.

Yan, L., Elgamal, A., and Cottrell, G. W. (2011). Substructure Vibration NARX Neural Network Approach for Statistical Damage Inference. *Journal of Engineering Mechanics*, *139*(6), pp. 737–747.

Zhang, Q. W. (2007). Statistical Damage Identification for Bridges Using Ambient Vibration Data. *Computers & Structures*, *85*(7), pp. 476–485.

Zheng, H., and Mita, A. (2009). Localized Damage Detection of Structures Subject to Multiple Ambient Excitations Using Two Distance Measures for Autoregressive Models. *Structural Health Monitoring*, *8*(3), pp. 207–222.

Appendix A

Calculation of the first and second order derivative of the covariance matrix of AR coefficient vectors with respect to the ACovF

The first-order derivative of the covariance matrix of the unknown state AR coefficients is first expressed as a function of the derivatives of the AR residual variance σ_e and that of the inverse of the ACovF Toeplitz matrix $\mathbf{\Gamma}$:

$$\frac{d\Sigma_u}{dR(\tau)} = \frac{d\sigma_e}{dR(\tau)}\mathbf{\Gamma}^{-1} + \sigma_e\frac{d\mathbf{\Gamma}^{-1}}{dR(\tau)}. \tag{A.1}$$

According to their respective definitions, specific expressions for $\dfrac{d\sigma_e}{dR(\tau)}$ and $\dfrac{d\mathbf{\Gamma}^{-1}}{dR(\tau)}$ are derived as follows:

$$\frac{d\sigma_e}{dR(\tau)} = \begin{cases} 1 + \boldsymbol{\gamma}^T\mathbf{\Gamma}^{-1}\mathbf{\Gamma}^{-1}\boldsymbol{\gamma}, & \tau = 0 \\ \boldsymbol{\gamma}^T\mathbf{\Gamma}^{-1}toeplitz(\mathbf{e}_{\tau+1})\mathbf{\Gamma}^{-1}\boldsymbol{\gamma} - 2\mathbf{e}_\tau^T\mathbf{\Gamma}^{-1}\boldsymbol{\gamma}, & 1 \le \tau \le p-1. \\ -2\mathbf{e}_\tau^T\mathbf{\Gamma}^{-1}\boldsymbol{\gamma}, & \tau = p \end{cases} \tag{A.2}$$

$$\frac{d\mathbf{\Gamma}^{-1}}{dR(\tau)} = \begin{cases} -\mathbf{\Gamma}^{-1}toeplitz(e_{\tau+1})\mathbf{\Gamma}^{-1}, & 0 \le \tau \le p-1 \\ \mathbf{0}, & \tau = p \end{cases}. \tag{A.3}$$

Likewise the second-order derivative of Σ_u can be obtained as a function of the first/second order derivatives of σ_e and $\mathbf{\Gamma}^{-1}$:

$$\frac{d^2\Sigma_u}{dR(\tau)^2} = \frac{d^2\sigma_e}{dR(\tau)^2}\mathbf{\Gamma}^{-1} + 2\frac{d\sigma_e}{dR(\tau)}\frac{d\mathbf{\Gamma}^{-1}}{dR(\tau)} + \sigma_e\frac{d^2\mathbf{\Gamma}^{-1}}{dR(\tau)^2}. \tag{A.4}$$

299

The second-order derivatives of σ_e and $\mathbf{\Gamma}^{-1}$ are computed by taking the derivatives of Eq. (A.2) and Eq. (A.3). Note that application of these formulas requires substituting in values of first-order derivative of $\mathbf{\Gamma}^{-1}$:

$$\frac{\mathrm{d}^2\sigma_e}{\mathrm{d}R(\tau)^2} = \begin{cases} 2\mathbf{\gamma}^T \dfrac{\mathrm{d}\mathbf{\Gamma}^{-1}}{\mathrm{d}R(0)} \mathbf{\Gamma}^{-1}\mathbf{\gamma}, \ \tau = 0 \\ 2\mathbf{\gamma}^T \dfrac{\mathrm{d}\mathbf{\Gamma}^{-1}}{\mathrm{d}R(\tau)} toeplitz(\mathbf{e}_{\tau+1})\mathbf{\Gamma}^{-1}\mathbf{\gamma} - 2\mathbf{\gamma}^T \dfrac{\mathrm{d}\mathbf{\Gamma}^{-1}}{\mathrm{d}R(\tau)}\mathbf{e}_\tau - 2\mathbf{e}_\tau^T \dfrac{\mathrm{d}\mathbf{\Gamma}^{-1}}{\mathrm{d}R(\tau)}\mathbf{\gamma} - 2\mathbf{e}_\tau^T\mathbf{\Gamma}^{-1}\mathbf{e}_\tau, \ \ 1 \le \tau \le p-1. \\ -2\mathbf{e}_p^T\mathbf{\Gamma}^{-1}\mathbf{e}_p, \ \tau = p \end{cases} \text{(A.5)}$$

$$\frac{\mathrm{d}^2\mathbf{\Gamma}^{-1}}{\mathrm{d}R(\tau)^2} = \begin{cases} -\dfrac{\mathrm{d}\mathbf{\Gamma}^{-1}}{\mathrm{d}R(\tau)} toeplitz(e_{\tau+1})\mathbf{\Gamma}^{-1} - \mathbf{\Gamma}^{-1}toeplitz(e_{\tau+1})\dfrac{\mathrm{d}\mathbf{\Gamma}^{-1}}{\mathrm{d}R(\tau)}, \ 0 \le \tau \le p-1 \\ \mathbf{0}, \quad \tau = p \end{cases}. \quad \text{(A.6)}$$

Appendix B

Sensitivity of the global stiffness matrix of the simply supported bridge system with respect to changes in the element sectional stiffness

To form the global stiffness matrix, the FEM nodes should be identified, and the 11 element stiffness matrices be assembled by placing the terms associated with the same nodal DOF together and summing them. Here beam elements with no axial elongation are employed.

Thus for the 10 DOF case the global stiffness matrix is first formed as a 24×24 matrix (Figure B1), corresponding to the 12 nodes of the system (including the boundary nodes). Static condensation is performed on $\mathbf{K}_{24}$ to eliminate the massless rotational DOFs to get the final stiffness matrix $\mathbf{K}_f$. Define ξ and η to be sets of certain indices of the rows and columns of the matrix $\mathbf{K}_{24}$, the notation $\mathbf{K}_{24}(\xi, \eta)$ stands for the submatrix that consists of the terms in rows ξ and columns η. Since the translational displacements at beam ends are zero, the 1st and 23rd row and column of $\mathbf{K}_{24}$ will be left out of consideration:

$$\mathbf{K}_f = \mathbf{K}_{mm} - \mathbf{K}_{m0}\mathbf{K}_{00}^{-1}\mathbf{K}_{0m}, \tag{B.1}$$

$$\mathbf{K}_{mm} = \mathbf{K}_{24}(\mathbf{i},\mathbf{i}); \mathbf{K}_{m0} = \mathbf{K}_{24}(\mathbf{i},\mathbf{j}); \mathbf{K}_{00} = \mathbf{K}_{24}(\mathbf{j},\mathbf{j}); \mathbf{K}_{0m} = \mathbf{K}_{m0}{}^T = \mathbf{K}_{24}(\mathbf{j},\mathbf{i}).$$

$$\mathbf{i} = 3, 5, \ldots, 21 \text{ (odd number collection)}, \mathbf{j} = 2, 4, \ldots, 24 \text{ (even number collection)}. \tag{B.2}$$

To calculate the derivative of $\mathbf{K}_{24}$ with respect to element sectional stiffness $(EI)_i$ (i is the label of the element), take the derivative of element stiffness matrix $(\mathbf{K}_e)_i$ over

301

$(EI)_i$ and use a congruent transformation to map the local coordinates to the global

coordinates:

$$\frac{d\mathbf{K}_{24}}{d(EI)_i} = \begin{bmatrix} \mathbf{0}_{(2i-2)\times4} \\ \mathbf{I}_{4\times4} \\ \mathbf{0}_{(22-2i)\times4} \end{bmatrix}_{24\times4} \frac{d(\mathbf{K}_e)_i}{d(EI)_i} \Big[\mathbf{0}_{4\times(2i-2)}, \mathbf{I}_{4\times4}, \mathbf{0}_{4\times(22-2i)} \Big]_{4\times24}, i = 1:11, \quad (B.3)$$

The sensitivities of $\mathbf{K}_{mm}, \mathbf{K}_{m0}, \mathbf{K}_{0m}$ and $\mathbf{K}_{00}$ can be obtained by substitute Eq. (B.3)

into Eq. (B.2):

$$\therefore \frac{d\mathbf{K}_{mm}}{d(EI)_i} = \begin{cases} \begin{bmatrix} [0010] \\ \mathbf{0}_{9\times4} \end{bmatrix}_{10\times4} \frac{d(\mathbf{K}_e)_1}{d(EI)_1} \begin{bmatrix} [0010] \\ \mathbf{0}_{9\times4} \end{bmatrix}_{10\times4}^T, i = 1 \\ \begin{bmatrix} \mathbf{0}_{(i-2)\times4} \\ [1000] \\ [0010] \\ \mathbf{0}_{(10-i)\times4} \end{bmatrix}_{10\times4} \frac{d(\mathbf{K}_e)_i}{d(EI)_i} \begin{bmatrix} \mathbf{0}_{(i-2)\times4} \\ [1000] \\ [0010] \\ \mathbf{0}_{(10-i)\times4} \end{bmatrix}_{10\times4}^T, i = 2:10, \\ \begin{bmatrix} \mathbf{0}_{9\times4} \\ [1000] \end{bmatrix}_{10\times4} \frac{d(\mathbf{K}_e)_{11}}{d(EI)_{11}} \begin{bmatrix} \mathbf{0}_{9\times4} \\ [1000] \end{bmatrix}_{10\times4}^T, i = 11 \end{cases} \quad (B.4)$$

302

$$\frac{d\mathbf{K}_{m0}}{d\left(EI\right)_i} = \left(\frac{d\mathbf{K}_{0m}}{d\left(EI\right)_i}\right)^T = \begin{cases} \begin{bmatrix} \begin{bmatrix} 0010 \end{bmatrix} \\ \mathbf{0}_{9\times4} \end{bmatrix}_{10\times4} \dfrac{d(\mathbf{K}_e)_1}{d\left(EI\right)_1} \begin{bmatrix} \begin{bmatrix} 0100 \end{bmatrix} \\ \begin{bmatrix} 0001 \end{bmatrix} \\ \mathbf{0}_{10\times4} \end{bmatrix}_{12\times4}^T & ,i=1 \\[3em] \begin{bmatrix} \mathbf{0}_{(i-2)\times4} \\ \begin{bmatrix} 1000 \end{bmatrix} \\ \begin{bmatrix} 0010 \end{bmatrix} \\ \mathbf{0}_{(10-i)\times4} \end{bmatrix}_{10\times4} \dfrac{d(\mathbf{K}_e)_i}{d\left(EI\right)_i} \begin{bmatrix} \mathbf{0}_{(i-1)\times4} \\ \begin{bmatrix} 0100 \end{bmatrix} \\ \begin{bmatrix} 0001 \end{bmatrix} \\ \mathbf{0}_{(11-i)\times4} \end{bmatrix}_{12\times4}^T & ,i=2:10, \\[3em] \begin{bmatrix} \mathbf{0}_{9\times4} \\ \begin{bmatrix} 1000 \end{bmatrix} \end{bmatrix}_{10\times4} \dfrac{d(\mathbf{K}_e)_{11}}{d\left(EI\right)_{11}} \begin{bmatrix} \mathbf{0}_{10\times4} \\ \begin{bmatrix} 0100 \end{bmatrix} \\ \begin{bmatrix} 0001 \end{bmatrix} \end{bmatrix}_{12\times4}^T & ,i=11 \end{cases} \qquad (B.5)$$

$$\frac{d\mathbf{K}_{00}}{d\left(EI\right)_i} = \begin{bmatrix} \mathbf{0}_{(i-1)\times4} \\ \begin{bmatrix} 0100 \end{bmatrix} \\ \begin{bmatrix} 0001 \end{bmatrix} \\ \mathbf{0}_{(11-i)\times4} \end{bmatrix}_{12\times4} \frac{d(\mathbf{K}_e)_i}{d\left(EI\right)_i} \begin{bmatrix} \mathbf{0}_{(i-1)\times4} \\ \begin{bmatrix} 0100 \end{bmatrix} \\ \begin{bmatrix} 0001 \end{bmatrix} \\ \mathbf{0}_{(11-i)\times4} \end{bmatrix}_{12\times4}^T \qquad ,i=1:11 , \qquad (B.6)$$

Finally, the sensitivity of the condensed global stiffness matrix $\mathbf{K}_f$ to stiffness reduction for element i is computed by differentiating both sides of Eq. (B.1) with respect to $\left(EI\right)_i$ and substituting Eq. (B.4-B.6) into that expression:

$$\frac{d\mathbf{K}_f}{d\left(EI\right)_i} = \frac{d\mathbf{K}_{mm}}{d\left(EI\right)_i} - \mathbf{K}_{m0}\mathbf{K}_{00}^{-1}\frac{d\mathbf{K}_{0m}}{d\left(EI\right)_i} - \frac{d\mathbf{K}_{m0}}{d\left(EI\right)_i}\mathbf{K}_{00}^{-1}\mathbf{K}_{0m} + \mathbf{K}_{m0}\mathbf{K}_{00}^{-1}\frac{d\mathbf{K}_{00}}{d\left(EI\right)_i}\mathbf{K}_{00}^{-1}\mathbf{K}_{0m}. \qquad (B.7)$$
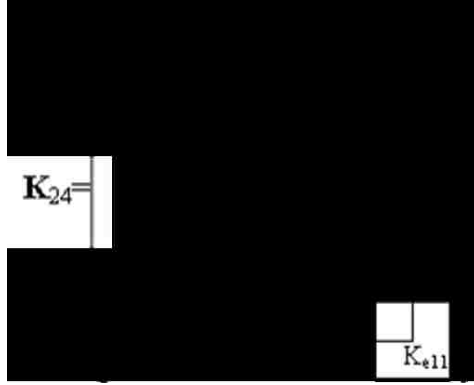
Figure B1. The global stiffness matrix $\mathbf{K}_{24}$

Vita

Ruigen Yao was born in Hubei, China on July 11, 1989. She graduated in July, 2009 with a Bachelor of Science Degree in Civil Engineering (Specialization: Building Engineering) from Tongji University, Shanghai, China. Subsequently she came to Lehigh University, Bethlehem, PA for graduate studies, and earned a Master of Science degree in Structural Engineering in September, 2011. She expects to complete her PhD program in May/September 2014.

305